

BULGARIAN CHEMICAL COMMUNICATIONS

2016 Volume 48 / Special Issue B

Proceedings of the 10th International Symposium on Electrochemical Impedance
Analysis, Borovetz, Bulgaria, June 1-5, 2014

Proceedings of the Sofia Electrochemistry Days, Pravetz, Bulgaria, June 10, 2015

*Journal of the Chemical Institutes
of the Bulgarian Academy of Sciences
and of the Union of Chemists in Bulgaria*

Proceedings of the
10th International Symposium on Electrochemical Impedance Analysis
Borovetz, Bulgaria, 1-5 June 2014

Visiting editor:

G. Raikova

Editorial

The present volume consists papers based on oral and posters presentations from the 10th International Symposium on Electrochemical Impedance Analysis organized in Borovetz, Bulgaria, 1-5 June 2014.

Maintaining the tradition of previous conferences, EIA10 provided a common platform for scientists and experts from various institutions to share knowledge, ideas, and achievements, to discuss impedance data analysis in a friendly environment. The symposium was enhanced with a technical exhibition and a session dedicated to recent developments of the equipment producers. A new topic was the special session organized by the „Fuel Cells and Hydrogen Technologies” Joint Programme of the European Energy Research Alliance (EERA) contributed to the understanding of the impedance analysis role and prospects in the development of next-generation fuel cells.

We would like to express our gratitude to the members of the scientific committee for their expertise and professional support, to all participants for their eager interest, scientific contributions and submitted papers, as well as to the reviewers for their effort to ensure valuable publications.

We would like to acknowledge the support of the International Society of Electrochemistry, the Ministry of Education and Science (Program “Support of International Scientific Events Organized in the Republic of Bulgaria”) and the Bulgarian Academy of Sciences.

It was our great pleasure to welcome you to Bulgaria.

Conference co-chairs:

Daria Vladikova

Zdravko Stoynov

Guest editor:

Gergana Raikova

Academician Evgeni Budevski Institute of Electrochemistry and Energy Systems, Bulgarian Academy of Sciences

Can a form of electrode/electrolyte interface change the ranges of dynamic instabilities?

O.I. Gichan^{1*}, V.V. Pototskaya²

¹Chuiko Institute of Surface Chemistry of National Academy of Sciences of Ukraine, 17 Heneralna Naumova Str., Kiev 03164, Ukraine

²Vernadskii Institute of General & Inorganic Chemistry of National Academy of Sciences of Ukraine, 32-34 Palladina Prosp., Kiev 03142, Ukraine

Received September, 24, 2014; Revised February, 4 2015

Based on the theory of electrochemical impedance spectroscopy the ranges of dynamic instabilities leading to oscillatory and bistable behaviour in a model electrocatalytic process with a preceding chemical reaction in the Nernst diffusion layer and the potential-dependent adsorption/desorption of electroactive species under potentiostatic conditions were compared for a case of spherical, cylindrical and planar electrode.

Keywords: Electrochemical impedance spectroscopy, Electrode geometry, Electrocatalytic mechanism, Oscillations, Bistability

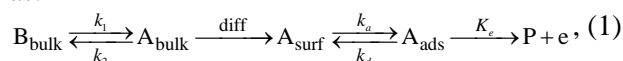
INTRODUCTION

The frequent appearance of oscillations and pattern formation at electrolyte/electrode interface can be explained by the inherently nonlinear electrochemical kinetics and far from equilibrium performance of electrochemical experiments [1-14]. In impedance spectroscopy [15, 16], bifurcations leading to oscillatory and bistable dynamics can be represented by zero of impedance or admittance [9-14]. By instabilities, or bifurcations, we mean a qualitative change in the dynamical states of a system, occurring with the attainment of a certain critical, bifurcation value of the control parameter.

In the paper, we will answer the question whether a simple change in a form of electrode/electrolyte interface at fixed values of other parameters of the electrochemical system can influence its dynamic behaviour. In a model process, the electroactive species of one sort are produced by a preceding chemical reaction, diffuse from the Nernst diffusion layer to the electrode surface, where they are adsorbed and electrochemically oxidized. We consider in detail derivation of necessary conditions for the Hopf and saddle-node instabilities in this electrocatalytic process on a surface of cylindrical electrode and compare these results with those obtained for the planar and spherical ones [5-8].

THEORY

The scheme of the model process can be written as:



where k_1 , k_2 are the rate constants of chemical reaction in the bulk solution, k_a , k_d , K_e are the rate constants of adsorption, desorption and electron transfer. The last step of the reaction is considered to be irreversible.

Neglecting the ohmic losses and double layer influence, the main kinetic equations are:

$$\frac{\partial c(r,t)}{\partial t} = D \frac{1}{r} \frac{\partial}{\partial r} \left(r \frac{\partial c(r,t)}{\partial r} \right) - kc(r,t), \quad (2)$$

$$\Gamma \frac{d\theta}{dt} = v_1(t) - v_2(t, E(t)). \quad (3)$$

Here, $c(r, t)$ is the electroactive species A concentration, $c(r, t) = c_0 + u$ (u is the concentration deviation from the equilibrium value c_0 coinciding with the bulk concentration of species), t – time, r – distance from the origin of coordinates which coincides with the center of the cylinder, $k = k_1 + k_2$ is the effective rate of a preceding homogeneous chemical reaction, $\theta(t)$ is the electrode surface coverage by the adsorbate, Γ is the maximum surface concentration at $\theta=1$, $v_1(t)$ and $v_2(t)$ – the adsorption-desorption rate and the electron transfer rate, that satisfy the equations

$$v_1(t) = \Gamma k_a \exp(\gamma\theta(t)/2) c(r_0, t) (1 - \theta(t)) - \Gamma k_d \exp(-\gamma\theta(t)/2) \theta(t), \quad (4)$$

$$v_2(t) = \Gamma K_e(t) \theta(t) = \Gamma k_e \exp(\alpha b E(t)) \theta(t), \quad (5)$$

* To whom all correspondence should be sent:
E-mail: gichan@meta.ua

where r_0 is the electrode radius, α is the symmetry factor of electron transfer in the direction of oxidation, E is the electrode potential, k_e is the rate constant of electron transfer at $E(t)=0$, $b = F/(RT)$, F is the Faraday's number, R is the gas constant, T is the absolute temperature, γ is the attraction constant. Positive values of the attraction constant γ correspond to the attraction between adsorbed species, and its negative values correspond to the repulsion between adsorbed species. If attraction is small ($\gamma = 0$) the Frumkin isotherm passes in the Langmuir isotherm. Only positive value of the attraction constant leads to instability [9, 11].

As follows from eqn. (4), for the adsorption-desorption rate $\nu_1(t) = 0$, the adsorption-desorption of species A on the electrode surface under steady-state conditions is described by the Frumkin isotherm.

The boundary conditions allow for the fact that at the electrode surface diffusion flux is equal to the adsorption-desorption rate, and at the distance that exceeds δ the bulk concentration of species A is constant and equal to c_0

$$J_c(r_0, t) = -D \frac{\partial c(r, t)}{\partial r} \Big|_{r=r_0} = -\nu_1(t), \quad (6)$$

$$c(\delta, t) = c_0. \quad (7)$$

Here J_c is the diffusion flux, D is the diffusion coefficient, $\delta = r_0 + d$, d is the Nernst diffusion layer thickness.

In eqn. (2), we take into account the variation of the concentration only in the radius line. The dependence on the z and φ coordinates is absent.

The faradaic current density was determined according to the following equation

$$j_f(t) = F\nu_2(t) = F\Gamma k_e \exp[\alpha b E(t)] \theta(t). \quad (8)$$

Steady-State Conditions

Under steady-state conditions, i.e. when $d\theta/dt = 0$, $\partial c(r, t)/\partial t = 0$, from eqns. (2, 3) with boundary conditions (6, 7) one can obtain the steady-state concentration at the electrode surface $c_{st}(r = r_0)$, the steady-state electrode potential E_{st} and steady-state faradaic current density j_{fst}

$$c_{st}(r_0) = \frac{m_c c_0 + \Gamma k_d \theta_{st} \Omega_0 e^{-\gamma \theta_{st}/2}}{m_c + (1 - \theta_{st}) \Omega_0 \Gamma k_d e^{\gamma \theta_{st}/2}}, \quad (9)$$

$$E_{st} = (\alpha b)^{-1} \ln \left[\frac{m_c (c_0 - c_{st}(r_0))}{\Gamma k_e \theta_{st} \Omega_0} \right], \quad (10)$$

$$j_{fst} = \frac{F m_c (c_0 - c_{st}(r_0))}{\Omega_0}. \quad (11)$$

Here $m_c = D/d$, $\lambda = \sqrt{k/D}$,

$$\Omega_0 = \frac{1}{\lambda d} \left(\frac{K_0(x_0) I_0(x_\delta) - K_0(x_\delta) I_0(x_0)}{I_0(x_\delta) K_1(x_0) + I_1(x_0) K_0(x_\delta)} \right),$$

$$x_0 = r_0 \sqrt{k/D}, \quad x_\delta = (r_0 + d) \sqrt{k/D},$$

$I_0(x)$, $K_0(x)$ are modified zero-order Bessel functions, $I_1(x)$, $K_1(x)$ are first-order modified Bessel functions of first and second kind, respectively.

The potential is counted off from the zero-charge potential of the electrode free from species.

Impedance Spectra and System Dynamic Instabilities

Under potentiostatic experimental conditions, the studies of linear stability of the electrochemical system near the steady state are based on analysis of variation of the impedance zero values under variation of the electrode potential [9-14]. A *Hopf bifurcation* can be realized in the system when its complex impedance is equal to zero at nonzero frequency, $Z(\omega) = 0$ at $\omega = \omega_H \neq 0$ ($\omega = 2\pi f$, f – frequency). At Hopf bifurcation point the system can produce its own undamped periodic oscillations with frequency ω_H , so in the case of influence on the system of an external signal with a frequency exactly coinciding with this value, the external signal will pass through the system without resistance [11].

A *saddle-node bifurcation* can appear when $Z(\omega) = 0$ at $\omega = 0$, i.e. in points where polarization resistance of an electrochemical system $Z_P = \lim_{\omega \rightarrow 0} Z_f(\omega)$ is equal to zero [9-11]. This bifurcation initiates in a non-equilibrium system bistability – the coexistence of two stable steady states at the same values of the parameters. Which one is chosen depends on where the system comes from, i.e. on initial conditions. In this sense the bistable system has a memory. The saddle – node bifurcations always come in pairs and lead to hysteresis.

Calculation of Faradaic Impedance

To calculate faradaic impedance of the system, its behavior was analyzed under a low periodical signal $\Delta E(t) = \Delta E_0 e^{i\omega t}$ applied in a given point of the steady-state voltammetric curve

$$E(t) = E_{st} + \Delta E_0 e^{i\omega t}, \quad (12)$$

where $i = \sqrt{-1}$, ΔE_0 is the amplitude of a low periodical signal.

In response to this excitation, the electrode surface coverage $\theta(t)$, faradaic current density $j_f(t)$, and surface concentration $c(r_0, t)$ will oscillate near the steady – state values, namely

$$\begin{aligned} \theta(t) &= \theta_{st} + \Delta\theta_0 e^{i\omega t}, \\ j_f(t) &= j_{fst} + \Delta j_f(E, \theta), \\ c(r_0, t) &= c_{st}(r_0) + \Delta c(r_0, \theta). \end{aligned} \quad (13)$$

The expression for faradaic impedance in the Laplace image space $\bar{F}(s) = \int_0^\infty f(t)e^{-st} dt$ as a function of complex frequency $s = \sigma + j\omega$ takes the form of

$$\bar{Z}(s) = \frac{\Delta \bar{E}(s)}{\Delta \bar{j}_f(s)}. \quad (14)$$

Omitting some mathematical computations, let us write the resultant expression for faradaic impedance in the Laplace image space

$$\bar{Z}_f(s) = R_{ct} \left\{ 1 + \frac{\partial_\theta v_2 (1 + \Omega_s \partial_c v_1)}{\Gamma s (1 + \Omega_s \partial_c v_1) - \partial_\theta v_1} \right\}, \quad (15)$$

where partial derivatives are designated here as $\partial_x u = \partial u / \partial x$ and the following notations are introduced:

$$\begin{aligned} \Omega_s &= \frac{1}{\lambda_s D} \left(\frac{K_0(x_{0s}) I_0(x_{\delta s}) - K_0(x_{\delta s}) I_0(x_{0s})}{I_0(x_{\delta s}) K_1(x_{0s}) + I_1(x_{0s}) K_0(x_{\delta s})} \right), \\ \partial_\theta v_2 &= \Gamma k_e \exp(\alpha b E_{st}), \quad \lambda_s = \sqrt{(k+s)/D}, \\ x_{0s} &= r_0 \sqrt{(k+s)/D}, \quad x_{\delta s} = (r_0 + d) \sqrt{(k+s)/D}, \\ \partial_\theta v_1 &= \Gamma \{ k_d \exp(-\gamma \theta_{st}/2) [\gamma \theta_{st}/2 - 1] + \\ &\quad + k_a \exp(\gamma \theta_{st}/2) c_{st}(r_0) [\gamma (1 - \theta_{st})/2 - 1] \}, \\ \partial_c v_1 &= \Gamma k_a (1 - \theta_{st}) \exp(\gamma \theta_{st}/2), \\ R_{ct} &= 1 / \frac{\partial i_{fst}}{\partial E_{st}} = 1 / F \Gamma \alpha b k_e \exp(\alpha b E_{st}) \theta_{st} \text{ is the} \end{aligned}$$

charge transfer resistance.

In our calculations we ignored the electrolyte resistance and the double-layer impedance. In this case, the impedance of the model system under consideration is equal to faradaic impedance, $Z = Z_f$.

Assuming that the double-layer charging and the faradaic process are not coupled and that the double-layer capacitance C_{dl} is associated in parallel with the faradaic impedance, the interfacial impedance is given by

$$Z_{int} = \left(\frac{1}{Z_f} + i\omega C_{dl} \right)^{-1}. \quad (16)$$

The impedance Z of the cell is the sum of the series resistance R_s and the interfacial impedance Z_{int}

$$Z = R_s + Z_{int}, \quad (17)$$

where R_s is the sum of the electrolyte and external resistance.

It is known that the effect of ohmic resistance on the impedance spectrum is reduced to a horizontal shift of impedance diagrams in the complex plane [10]. This can result in a change in the number of bifurcation points in the system.

It was shown that the parameter R_s can regulate the ranges of Hopf and saddle – node instabilities in an opposite way [7, 8]. Its increase results in a Hopf instability region decrease and a saddle – node instability region increase. There are threshold values of the parameter R_s critical for appearance and disappearance of the instabilities in question. The threshold values of the ohmic resistance depend on the preceding chemical reaction rate in bulk solution.

Double layer capacitance does not affect either Hopf or saddle-node bifurcation points. The effect of this parameter on the impedance spectrum is manifested only in the high–frequency region [7, 8].

Determination of Hopf Bifurcation Points

To determine the Hopf bifurcation points, impedance zero points were studied under electrode potential variation. The impedance zero points were found according to the following equation:

$$Z = R_s + Z_{int} = 0. \quad (18)$$

In order to satisfy condition (18), it is necessary that

$$\begin{cases} \text{Re}[Z] = 0 \\ \text{Im}[Z] = 0. \end{cases} \quad (19)$$

One can solve the system of equations only numerically.

Determination of Saddle-Node Bifurcation Points

To determine saddle – node bifurcation points, the solutions of the following equation were studied numerically:

$$Z_p + R_s = 0, \quad (20)$$

where polarization resistance of the electrochemical system is

$$Z_P = R_{ct} \left\{ 1 - \frac{\partial \theta v_2 (1 + \Omega_0 \partial_c v_1)}{\partial \theta v_1} \right\}. \quad (21)$$

In order to pass from the Laplace space to the Fourier space, it is necessary to perform a substitution $s = i\omega$.

In the model calculation, the following values of system parameters were assumed: $\Gamma = 10^{-9}$ mol/cm²; $\gamma = 8$; $\Gamma k_a = 0.1$ cm s⁻¹; $\Gamma k_d = 10^{-5}$ mol/cm² s; $k_e = 10$ s⁻¹; $D = 10^{-5}$ cm²/s; $\alpha = 0.5$; $d = 10^{-3}$ cm; $c_0 = 7.5 \cdot 10^{-6}$ mol/cm³; $r_0 = 10^{-4}$ cm (for spherical and cylindrical electrodes); $C_{dl} = 2.5 \cdot 10^{-5}$ F cm⁻²; $F = 96484$ C/mol; $T = 300$ K; $R = 8.314$ J/mol K; $b = F/(RT) = 38.7$ V⁻¹; $k = 10$ s⁻¹; $R_s = 0.3$ Ohm cm².

All numerical calculations were performed on the basis of the mathematical package Mathematica™.

RESULTS AND DISCUSSION

Fig. 1 schematically presents a cylindrical electrode of radius r_0 and the Nernst diffusion layer with thickness d , where concentration of electroactive species varies. At the distance that exceeds δ the bulk concentration of species is constant. The variation of the concentration is taken into account only in the radius line. The dependence on the z and φ coordinates is absent.

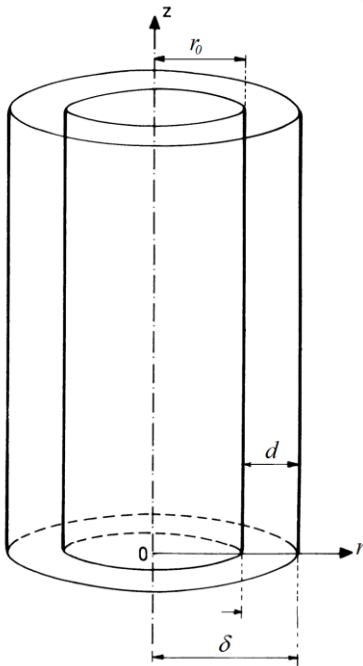


Fig. 1. Schematic presentation of cylindrical electrode of radius r_0 and Nernst diffusion layer of d value.

As shown by the performed calculations, the steady-state polarization j_{fct} , E_{st} - curves are N-shaped form with the negative differential resistance (NDR) region. Two opposite factors

determine the current value in the model process: the increase in the potential and the decrease in the concentration of electroactive species in the near-electrode layer due to the adsorption. The later depends on the potential in the non-linear fashion. When the diffusion rate of electroactive species is equal to the rates of processes occurring on the electrode, the voltammogram contains a maximum. If the rate of consumption of reacting species is predominant, the faradaic current decreases due to the insufficient rate of their delivery from diffusion layer, while the potential increases.

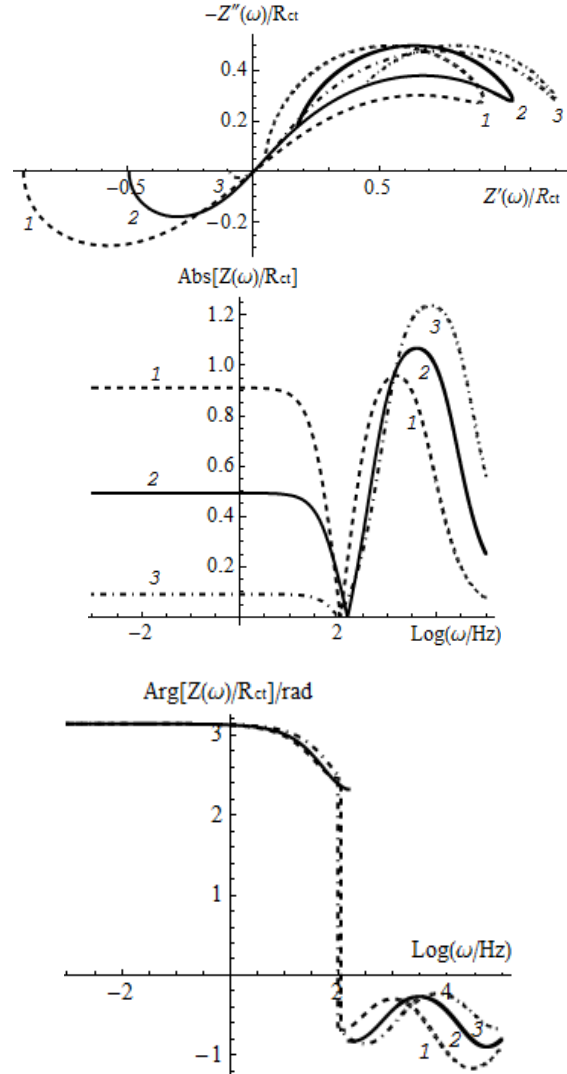


Fig. 2. (a) Nyquist diagrams of the behavior of total cell impedance normalized on charge transfer resistance in a complex plane at the Hopf bifurcation points (H_1) for the case of planar (1), cylindrical (2) and spherical (3) electrodes. Dependences of (b) absolute impedance and (c) impedance phase angle on $\log \omega$ at the bifurcation points.

This is the range of the NDR. The Hopf and saddle-node bifurcation points are in this region. The current density value is the smallest for the

case of a planar electrode; it is the largest for the case of a spherical electrode.

Figs. 2a–2c and Figs. 3a–3c show the Nyquist and Bode diagrams for total cell impedance calculated according to formula (16) in the Hopf (H_1) and saddle-node (SN_1) bifurcation points for a planar, cylindrical and spherical electrode (table).

Table 1. Parameter values of the electrochemical system at the bifurcation points.

Electrode form	Bifurcation point	ω/Hz	θ	$i_{fst}/\text{A cm}^{-2}$	E_{st}/V
plane	H_1	110	0.583	0.00760	0.13455
	SN_1	0	0.374	0.00545	0.14028
	SN_2	0	0.232	0.00330	0.13901
cylinder	H_1	152	0.565	0.02427	0.19618
	SN_1	0	0.442	0.02016	0.19927
	SN_2	0	0.214	0.00916	0.19606
sphere	H_1	97	0.567	0.05239	0.23575
	SN_1	0	0.544	0.05080	0.23629
	SN_2	0	0.198	0.01622	0.22953
	H_2	59	0.196	0.01605	0.22959

For chosen values of the system parameters there are two Hopf bifurcation points for all electrodes. Let's consider the behavior of impedance in a complex plane at the Hopf bifurcation points H_1 (Figs. 2a). At the low-frequency range in the Nyquist diagram, there is a loop with a negative real part of impedance that indicates the existence of instability in the system. This inductive loop decreases as symmetry of electrode increases, i.e. for a planar electrode this loop is the largest, for a spherical electrode it is the smallest. Such change in electrode form leads to a change in a form of conductive loop with positive real part of impedance. The absolute impedance, $Abs[Z(\omega)/R_{ct}]$, turns to zero in the Hopf

bifurcation point at $\omega=\omega_H$ (Figs. 2b, 2c). This bifurcation frequency is different for case of planar, cylindrical and spherical electrode. In the Hopf bifurcation point the functional dependence of the impedance phase angle $Arg[Z(\omega)/R_{ct}]$ on $\log \omega$ changes drastically.

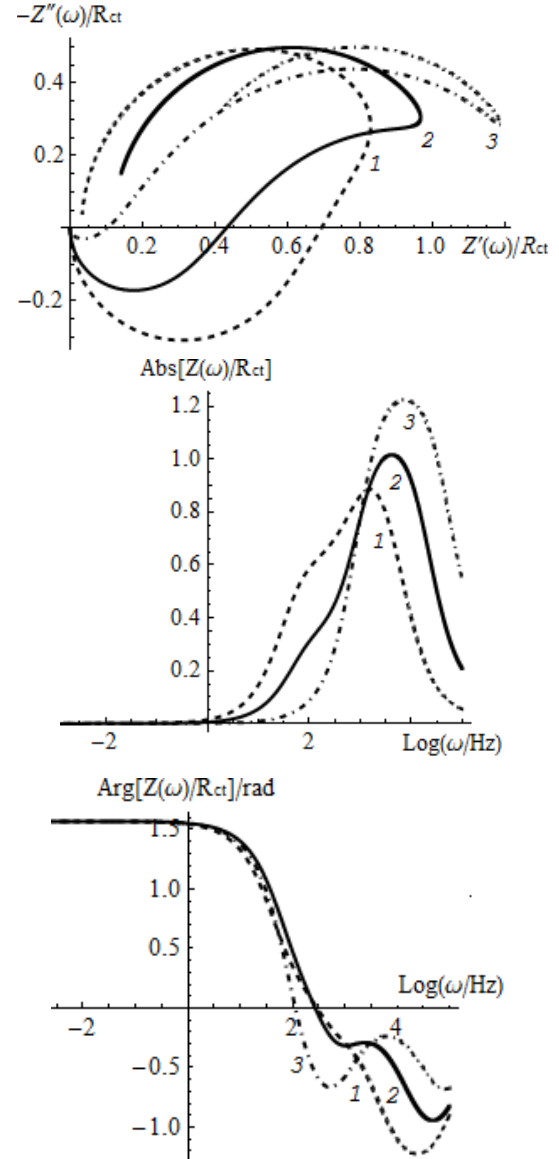


Fig. 3. (a) Nyquist diagrams of the behavior of total cell impedance normalized on charge transfer resistance in a complex plane at the saddle-node bifurcation points (SN_1) for the case of planar (1), cylindrical (2) and spherical (3) electrodes. Dependences of (b) absolute impedance and (c) impedance phase angle on $\log \omega$ at the bifurcation points.

The Nyquist diagrams in the saddle-node bifurcation points SN_1 are presented in Fig. 3a. An inductive loop with a positive real part of impedance increases as the symmetry of electrode decreases from spherical electrode to planar one. A conductive loop with a positive real part of impedance also changes. A decrease in the

symmetry of electrode results in a decrease in absolute impedance and change in its phase angle for bifurcation points under consideration.

CONCLUSIONS

Thus, we can conclude that a simple change in a form of electrode/electrolyte interface can change the dynamic stability of the model electrocatalytic process with a preceding homogeneous chemical reaction in the Nernst diffusion layer and the potential-dependent adsorption/desorption of electroactive species on the electrode surface under potentiostatic conditions. The analytically derived expression for total cell impedance allows us to investigate the possible realization of the Hopf and saddle-node instabilities in the electrochemical system in case of a spherical, cylindrical and planar electrode.

The region of bistability is wider for a spherical electrode than for a planar electrode. In contrast to this a decrease in the electrode symmetry is the reason for the Hopf instability region increase. Varying a form of electrode we can vary frequency of spontaneous current oscillations ω_H . This presents the way of possible control of dynamic behavior of real electrochemical systems.

REFERENCES

1. J. Eshkult, C. Ulrich, F. Björefors, L. Nyholm, *Electrochim. Acta*, **53**, 2188 (2008).
2. D. Sazou, M. Pavlidou, M. Pagitsas, *J. Electroanal. Chem.* **675**, 54 (2012).
3. Ts. Dobrovolska, D.A. López-Sauri, L. Veleva, I. Krastev, *Electrochim. Acta*, **79**, 162 (2012).
4. H. Okamoto, T. Gojuki, N. Okano, T. Kuge, M. Morita, A. Maruyama, Y. Mukouyama, *Electrochim. Acta*, **136**(1), 385 (2014).
5. V.V. Pototskaya and O.I. Gichan, *Russ. J. Electrochem.*, **47**(3), 336 (2011).
6. V.V. Pototskaya and O.I. Gichan, *Russ. J. Electrochem.*, **48**(2), 154 (2012).
7. O.I. Gichan and V.V. Pototskaya, *Electrochimica Acta*, **112**, 957 (2013).
8. V.V. Pototskaya and O.I. Gichan, *Russ. J. Electrochem.*, **50**(11), 1009 (2014).
9. M.T.M. Koper and J.H. Sluyters, *J. Electroanal. Chem.*, **371**, 149 (1994).
10. M.T.M. Koper, *Adv. Chem. Phys.*, **92**, 161 (1996).
11. M.T.M. Koper, *J. Chem. Soc. Faraday Trans.*, **94**, 1369 (1998).
12. M. Naito, N. Tanaka, H. Okamoto, *J. Chem. Phys.*, **111**, 9908 (1999).
13. A. Sadkowsky, *J. Electroanal. Chem.*, **485**, 119 (1999).
14. F. Berthier, J.P. Diard, C. Montella, *Electrochim. Acta*, **44**, 2397 (1999).
15. Z.B. Stoynov, B.M. Grafov, B. Savova-Stoynova, V.V. Elkin, *Elektrokhimicheski impedans (Electrochemical Impedance)*, Nauka, Moscow, 1991.
16. E. Barsoukov, J.R. Macdonald, *Impedance Spectroscopy: Theory, Experiment, and Applications (2nd ed.)*, Wiley Interscience, New York, 2005.

МОЖЕ ЛИ ФОРМАТЪТ НА ИНТЕРФЕЙСА ЕЛЕКТРОД/ЕЛЕКТРОЛИТ ДА ПРОМЕНИ ОБХВАТИТЕ НА ДИНАМИЧНИТЕ НЕСТАБИЛНОСТИ?

О.И. Гичан¹ и В.В.Потоцкая²

¹Чуйко институт по повърхностна химия към националната академия на науките на Украйна, 17 ул. Генерала Наумова 17, Киев 03164, Украйна

²Вернадски институт по обща и неорганична химия към националната академия на науките на Украйна, 32-34 Палладина Просп., Киев 03142, Украйна

Постъпила на 24 септември, 2014 г.; коригирана на 4 февруари, 2015 г.

(Резюме)

На базата на теорията на електрохимичната импедансна спектроскопия обхватите от динамични нестабилности водещи до осцилиращо и бистабилно поведение в модел на електрокаталитичен процес предшестван от химическа реакция в дифузионния слой на Нернст и потенциално зависимата адсорбция/десорбция на електроактивни видове при потенциостатични условия.

Multispectral impedance measurement in embedded systems

T. Günther*, P. Büschel, O. Kanoun

Technische Universität Chemnitz, Reichenhainer Straße 70, 09126 Chemnitz, Germany

Received October 15, 2014; Revised April 4, 2015

The data basis available for Battery management systems (BMS) is mandatory for a proper operation. For now high dimensional and offline gathered datasets describing the batteries behavior are the basis of algorithms implemented in BMS. In the laboratory, Impedance Spectroscopy (IS) for battery characterization is used for many years. As this method requires a high effort in both, hardware and software, Impedance spectroscopy was limited to laboratory applications. In this paper an approach to provide IS for online battery characterization as support for BMS is presented. Thereby challenges related to hardware and signal processing are considered. The developed approach is capable of doing IS measurements for each of the batteries in a stack of four.

Keywords: battery management, battery diagnosis, digital signal processing, cyber-physical system, impedance spectroscopy

INTRODUCTION

In different applications like electric vehicles and stationary energy storage, high power/energy cells are the most expensive part. For proper and safe usage, extensive knowledge about the batteries and their current state is necessary for both management hardware and system designers. In the laboratory Impedance Spectroscopy (IS) is an adequate method to investigate internal electrochemical processes as charge transfer and diffusion [1]. Thus the complex transfer function is fitted to a model and used to rate the state of the battery [2], [3].

For batteries the measurement is usually done in a frequency range from about 10 mHz to 1 kHz [2]. IS has been prevented to be applied to mobile applications for several reasons: the required measurement time in combination of the wide frequency range needed to be covered with the measurement, the drift of the battery voltages as well as high cost for measurement equipment.

To overcome the mentioned challenges multiple problems needed to be faced: a proper perturbation sequence with minimal hardware requirements as well as a data analysis with low effort in memory consumption and computational power.

Other approaches do not provide measurement of impedance spectra in a wide frequency range from a few mHz to kHz for low ohmic test items. Usually one or more of the following aspects are required: a complex hardware for pulse forming i.e.

using the AD593 [4], [5] or other DAC hardware like presented from TI [6], a measurement time of more than 5 minutes in the case of not using multispectral perturbation, a high memory load for data processing using FFT based determination of spectral components. The presented approach omits all of these issues.

APPROACH

Impedance spectroscopy on batteries

Fundamental for Impedance Spectroscopy on batteries is their interpretation as systems described by a transfer function as the complex frequency dependent impedance. Effects present in batteries like contacts, electrode reactions, diffusion show different reaction rates. They have a different impact on the transfer function depending on the investigated frequency. By applying a frequency varying perturbation signal to the investigated system a differentiated view on the effects of interest [1] is performed. For low ohmic systems like batteries perturbation by modulated current is used. Therefore, the superimposed current acting as the perturbation signal as well as the corresponding voltage, the response signal is measured and transformed into the frequency domain. Division of the voltage and current in the frequency domain yields the complex impedance.

In laboratory applications usually AD/DA hardware in combination with power amplifiers are used to do IS measurements. Sampling rates of several kHz as well as resolutions up to 24bit for commercially available devices like NI4461 fulfill all technical requirements for IS measurements on

* To whom all correspondence should be sent:
E-mail: thomas.guenther@etit.tu-chemnitz.de

batteries in the target frequency range. Further signal processing i.e. using Matlab as well as model based system identification are state of the art on PC based post processing. The need of partially saving measurement data as well as the complexity of the measurement and pulse forming hardware for the current perturbation has limited this approach to the laboratory. Consequentially a modified approach regarding the used perturbation sequence lowering the effort for HW and SW and an alternative for FFT based methods is required to provide IS measurements in embedded systems.

Signals for system identification

Besides perturbation sequences with one spectral component other signals like noise, mixed sine, or multilevel signals are available for system identification [7] see Fig. 1. Depending on the requirements of the target device under test and the target application a proper signal needs to be selected for perturbation.

The following main aspects are critical for the selection of a proper perturbation sequence: coverage of the target frequency range, the signal to noise ratio (SNR), the maximum magnitude, fluctuation and the overall time needed for the measurement.

Noise has a continuous spectrum with a flat or frequency proportional dependency of the magnitude in the frequency domain. This provides a high dense observation of the transfer functions characteristics. Other signals like stepped sine or multisine concentrate the energy on selected spectral components. This is positive in terms of the SNR for the measurement. For a proper observation of effects in the battery, a linear distribution of the spectral components in the logarithmic frequency representation is required. This can be achieved by steppedsine and multisine signals easily.

Further optimization for the requirements of system identification is the criterion of linearity having a small magnitude of the perturbation

sequence consequently. Tuning the spectral properties of a multisine signal the maximum value can be optimized using the method called “Frequency domain swapping algorithm” [8], [9]. Other empirical approaches also exist to optimize multispectral signals [10]. Time consuming optimization of the parameters describing the perturbation sequence can be done offline on a PC. Either the optimized signal or the set of parameters is stored in the target application later.

Optimizing criteria of the perturbation sequence are the maximum magnitude and fluctuation. Both of them are improved as the crest factor (CF) of multispectral signals is minimized. The better multisine signals are optimized for the CF the more they behave like a multilevel signal in the time domain having adjusted spectral properties matching the required spectral properties (distribution and magnitudes) at the same time. By limiting the available magnitude levels the optimized multisine signal becomes a binary switching signal.

For binary signals high compression in the data representation allows an offline optimization of the signal properties and save the optimized signal in the program code of the target application. By this approach the effort during perturbation for the software can be reduced to a minimum as the sequence is iteratively used to set the superimposed current to be on or off.

The perturbation of the device under test needs to be realized using a hardware as simple as possible. In embedded applications powerful pulse forming hardware i.e. for sine pulse forming is too complex. The most suitable approach according to the binary switching state signal for excitation is a pulsed current. In combination with a simple switch using one MOSFET and a load resistance a multispectral excitation of a battery can be realized at minimum effort in hardware and software.

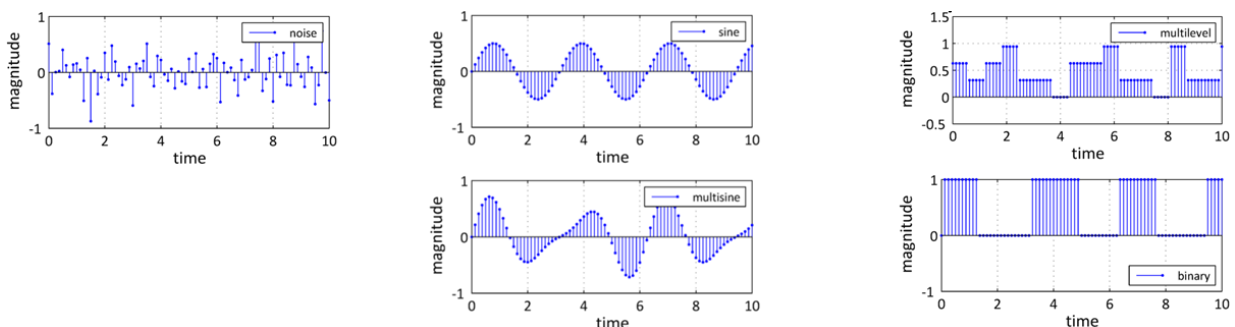


Fig. 1. Commonly used signal types for system identification; noise left, sine based center and amplitude modulated right.

Signal processing

Multispectral signals reduce the overall measurement time by packing the information into parallel information paths, the frequencies. A well-known method to separate the information is the Fourier transformation. For a system of four batteries about 10 MByte of measurement data arise during the measurement. The FFT needs to save and reorder the measured data. Therefore the data analysis using FFT implementation is performed after the measurement only on saved data.

An alternative approach to compute the spectral properties of a signal is the GOERTZEL algorithm[12]. The GOERTZEL algorithm describes an IIR-filter approach to act like a single bin DFT. In the case of a known set of frequencies multiple GOERTZEL filters can be used to detect the frequency components a measured signal.

Further optimization have been found to split the computations needed for the GOERTZEL filter into a recursive part (see Fig. 2) updated with each new measured value and a feed forward part to correct the phase angle of the calculated spectral property of the tuned frequency. The non-recursive part needs to be calculated only once after the measurement is finished. This approach is called sliding GOERTZEL algorithm [13], [14]. As the frequencies contained in the perturbation sequence are known, domain transformation can be limited to those frequencies.

Tuning the Feedback parameters of the IIR filter the resonant frequency of the filter stage is matched to the frequency of interest. Using filter banks consisting of multiple parallel operating filters tuned to different spectral components a filterbank

is constructed. Modern DSP cores with their MAC/SIMD extensions [15] allow fast and efficient transformation of the measurement data from time to frequency domain with low effort in computation time and memory consumption using the filterbank approach.

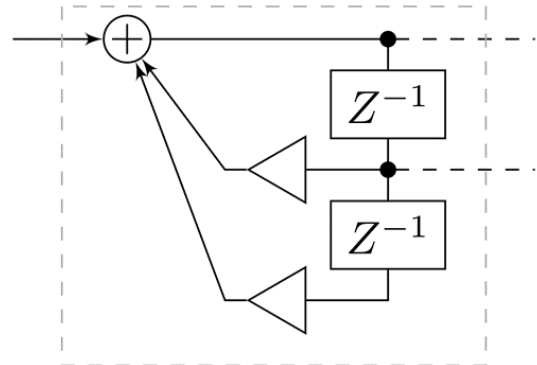


Fig. 2. Recursive part of the GOERTZEL filter acting as single bin dft calculator; the no recursive part is not shown

Comparing both approaches, the FFT and GOERTZEL filter based time to frequency domain transformation the calculated phases as well as the magnitudes show very small relative deviations of less than $5 \cdot 10^{-5}$. The analyzed multispectral signal has been designed to have equivalent magnitudes of target spectral components with tuned phase angles (see Fig. 3). The spectral components are shown versus frequency index. The GOERTZEL filter bank approach can be used to perform domain transformation instead of using FFT algorithms consequentially having a reduced effort in memory consumption and a simultaneous calculation of the spectral properties as benefits.

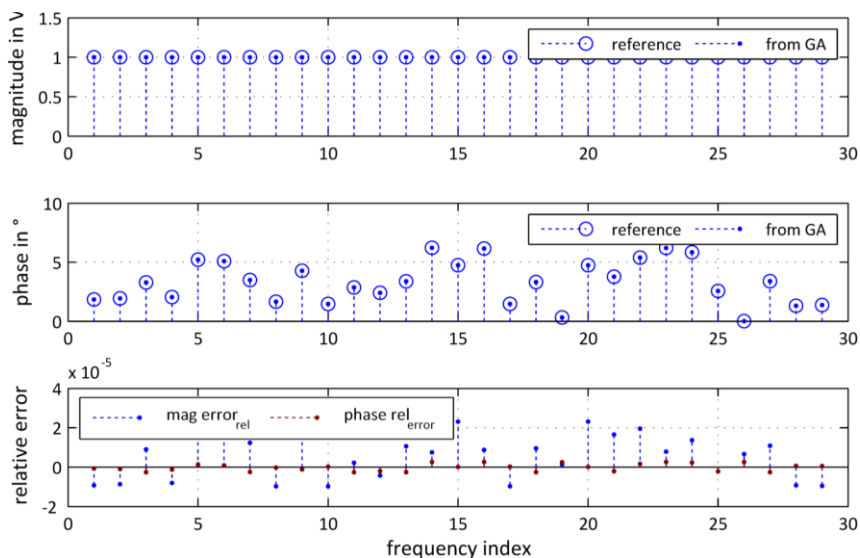


Fig. 3. Comparison of the determined spectral properties of a multisine signal for the FFT(reference) and GOERTZEL(GA) filter bank approach

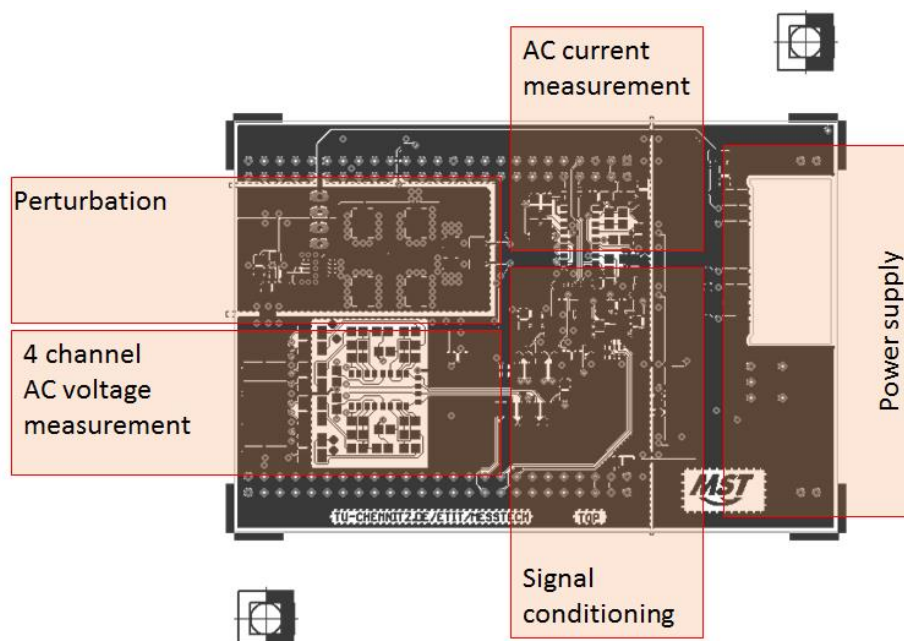


Fig. 4. Developed frontend to perform broadband multispectral impedance measurements using a standard development kit from ST.

Hardware

The developed Hardware (Fig. 4) covers all required aspects to perform IS measurements for perturbation, measurement, signal conditioning and signal processing. Basis is the STM32f4 discovery board [16].

It provides MAC/SIMD extensions for signal processing, multiple AD-converters as well as integrated timers for controlling the perturbation, channel selection and the measurement. The PCB is designed to be a frontend to the development board performing IS measurement being stacked to it.

Components for perturbation of the batteries connected to this board are placed in the upper left part. A MOSFET is used for discharging the batteries over a current limiting resistor and a shunt for current measurement. The offline optimized binary sequence is used to control the current flow by setting the MOSFET's conduction state. As the batteries are in series, all of them are perturbed simultaneously.

The AC components for both the current and voltages for each cell is decoupled using differential operational amplifiers. For voltage measurement an analog multiplexer is used to reduce the number of components for further signal conditioning. This implies programmable amplification and level shift to match the ADC input voltage range of the development board. For current signal conditioning there is no need for a programmable gain as the dynamic range of the current during perturbation is fixed to the cell voltage in contrast to the temperature dependent voltage response of the batteries.

CONCLUSION

The presented approach provides broadband multispectral impedance measurement on a low cost hardware with limited computation power. Key features of the presented approach are: binary sequence for fast and broadband impedance measurement, simple HW for perturbation using a switching MOSFET, no separate current source by using the battery stack as source and DUT at the same time, adapted algorithm for signal processing by using GOERTZEL. Thus i.e. battery management systems can be supported by online measured data describing the dynamic characteristics of batteries.

Acknowledgements: This work has been supported by "SmartLIC", Projekt Nr.: 284879 as by the Adaptive Antriebe in der Elektromobilität, „AdAntE“, Projekt Nr.: 100098113.

REFERENCES

1. C. H. Hamann, W. Vielstich, *Elektrochemie*. John Wiley & Sons Australia, Limited, 2005, p. 662
2. U. Tröltzsch, O. Kanoun, H.R. Tränkler, *Electrochim. Acta*, **51**, 1664 (2006).
3. P. Büschel, U. Tröltzsch, O. Kanoun, *Electrochim. Acta*, **56**, 8069 (2011).
4. J. Hoja, G. Lentka, *Metrol. Meas. Syst.*, **20**, 1 (2013).
5. J. Hoja, G. Lentka, in IMEKO XIX World Congress, (2009), p. 140.
6. <http://www.ti.com.cn/cn/lit/wp/spry215/spry215.pdf>.
7. R. Pintelon, J. Schoukens, *System Identification: A Frequency Domain Approach*, 2nd ed. Hoboken, NJ, USA: John Wiley & Sons, Inc., 2012.

8. E. Van der Ouderaa, J. Schoukens, J. Renneboog, *IEEE Trans. Instrum. Meas.*, **37**(2), 207, (1988).
9. M. Schroeder, *IEEE Trans. Inf. Theory* **16**(1), 85 (1970).
10. J. Ojarand, M. Min, P. Annus, *Physiol. Meas.*, **35**(6), 1019 (2014).
11. J. Schoukens, J. Swevers, R. Pintelon, H. Van der Auweraer, *Mech. Syst. Signal Process.*, **18**(4), 727 (2004).
12. G. Goertzel, An algorithm for the evaluation of finite trigonometric series, *Am. Math. Mon.*, 1958.
13. J. F. Chicharo, M. T. Kilani, *Signal Processing*, **52**(3), 283 (1996).
14. Streamlining Digital Signal Processing: A Tricks of the Trade Guidebook. John Wiley & Sons, (2012), p. 480
15. http://www.keil.com/pack/doc/CMSIS/DSP/html/group__f_i_r.html.
16. <http://www.st.com/web/catalog/tools/FM116/SC959/SS1532/PF252419>.

Мултиспектрални импедансни измервания във вградени системи

Т. Гюнтер*, П. Бюшел, О. Каноун

Технически университет Кемниц, Райхенхайнер щрасе 70, Кемниц, Германия

Постъпила на 15 октомври, 2014 г.; коригирана на 4 април, 2015 г.

(Резюме)

Базата данни достъпна за системи за управление на батерии (СУБ) е задължителна за установяване на подходящ режим на работа. За сега много-мерни офлайн системи за събиране на бази данни описващи поведението на батериите са основния източник на алгоритмите използвани в СУБ. Импедансната спектроскопия (ИС) за характеризирание на батерии се използва в лабораторията от много години. Тъй като този метод изисква значителни хардуерни и софтуерни усилия, използването на Импедансна спектроскопия беше ограничено до лабораторните приложения. В тази статия е представен подход за предоставяне на онлайн характеризирание с помощта на ИСв подкрепа на СУБ. Разгледани са предизвикателствата свързани с хардуера и обработката на сигнали. Разработеният подход е в състояние да помогне при осъществяването на ИС измервания за всяка от батериите в стак от четири на брой батерии.

Equivalent circuits for electrochemical reaction involving consecutive charge transfer steps

A. Survila

Center for Physical Sciences and Technology, Institute of Chemistry, A. Goštauto 9, LT 01108 Vilnius, Lithuania

Received October 24, 2014; Revised February 4, 2015

Two different equivalent circuits can be derived from kinetic equations obtained for consecutive charge transfer with the formation of soluble intermediate. Their description codes are: $R_{\infty}(R_1W_1)(C_2W_2)$ and $([R_3W_3][R_4W_4])$ (elements in series are given in square brackets, and elements in parallel are enclosed in parentheses). Both circuits are indistinguishable, if and only if a certain interrelation between R_1, W_1, W_2 and C_2 is satisfied. Then, upon a proper choice of parameters, both EC display the same impedance spectrum at all frequencies. All faradaic elements are interrelated and each of them depends on the characteristics of the overall process. Neither of EC elements can be attributed to the separate charge transfer step. Though the EIS data obtained for the Cu|Cu(II) system can be described by either of the two EC, the second EC is preferred due to its simplicity and more clear physical sense.

Keywords: Electrochemical impedance spectroscopy, consecutive charge transfer, equivalent circuit, copper(II) reduction.

INTRODUCTION

Consecutive charge transfer steps are typical of the most electrochemical processes including deposition and dissolution of metals. To study processes of this kind, different transient techniques were applied, including the electrochemical impedance spectroscopy (EIS). A proper analysis of impedance spectra makes it possible to determine the kinetic parameters simultaneously with the characteristics of the double electric layer. In so doing, the adequate equivalent circuits (EC), comprising characteristic features of the system, are commonly employed. However, sometimes they lack substantiation and, as a consequence, the physical meaning of EC elements is treated at random. Recently the utility and limitations of using equivalent circuits to analyse EIS data for electrochemical reaction mechanisms have been reviewed [1]. We sustain the position [1, 2] that the preferable circuits should follow from the mathematical expressions derived for the appropriate theoretical models.

In this communication, we focus on the case of step-wise charge transfer processes involving the formation of stable, solution-soluble intermediate that is capable of diffusing from/towards the bulk of solution.

The consecutive charge transfer involving adsorption steps has been considered by Grafov [3] and a rather complicated EC containing 11 elements was obtained. More simple cases arise when the electrochemical process is controlled by charge transfer and diffusion and adsorption steps are ignored. In previous studies, a theoretical analysis of the faradaic impedance has been performed provided that the final product is also soluble [4-6]. Next, the relationships obtained in Ref. [4] have been extended for the case when an insoluble final product (e.g., metal deposit) is formed [7]. No EC was proposed in the previous investigations [4, 5] until it was found [6] that the general impedance expression corresponds to an equivalent circuit consisting of five elements that, according to the authors, "have no sensible physical meaning". At the same time, we proposed another EC [8], which rigorously followed from analytical expressions and contained less sub-circuits. So, two different EC have been proposed for description of the same mechanism.

To avoid confusion in this situation, we made an attempt to analyze both EC so as to clarify their possible interrelation. Theoretical regularities are compared with EIS data obtained for real Cu|Cu(II) system capable of generating stable intermediate Cu^+ ions. Surfactant-free Cu(II) solutions were selected in an effort to minimize adsorption effects. EIS characteristics of the processes involving adsorption of intermediates are available elsewhere [9].

* To whom all correspondence should be sent:
E-mail: arvydass@ktl.mii.lt

EXPERIMENTAL

Solutions were prepared using thrice-distilled water, $\text{CuSO}_4 \cdot 5\text{H}_2\text{O}$ (Mallinckrodt, USA, chlorides less than 0.005%), and H_2SO_4 (high purity, Reakhim Russia) as a supporting electrolyte. They were deaerated before experiments with argon stream over 0.5 h. To prepare the working electrodes, a Pt wire of 0.36 cm^2 surface area was coated with 5–7 μm thick copper in the solution containing (g dm^{-3}): $\text{Cu}_2\text{SO}_4 \cdot 5 \text{H}_2\text{O} - 250$, $\text{H}_2\text{SO}_4 - 50$. Polycrystalline layer with well-exhibited crystallographic edges and faces was formed. Copper crystallites as large as 1–4 μm imparted a particular roughness of the surface.

Impedance measurements were carried out under potentiostatic conditions at the open-circuit potential within the frequency (f) range from 0.05 to 5×10^4 Hz, using a Zahner Elektrik (Germany) IM6 impedance spectrum analyzer. The amplitude of the imposed sinusoidal perturbation of the electrode potential was 5 mV. Computer programs elaborated by Boukamp [10] were used for analyzing impedance spectra.

The electrode potential E was measured in reference to the $\text{Ag} | \text{AgCl} | \text{KCl}(\text{sat})$ electrode and was converted to the standard hydrogen scale. All experiments were performed at 20 °C.

RESULTS AND DISCUSSION

As has been reported [6], the faradaic admittance, derived by Armstrong and Firman [5] for the mechanism $\text{O} + e \rightleftharpoons \text{Y}$, $\text{Y} + e \rightleftharpoons \text{R}$, can be expressed as

$$Y_F = Z_F^{-1} = R_\infty^{-1} \left(1 + b/\sqrt{s} \right) / \left(1 + c/\sqrt{s} + d/s \right), \quad (1)$$

where the complex variable $s = i\omega$; i and ω stand for the imaginary unit and angular frequency, respectively. Notice that the general relationship obtained by Despić et al [4] also takes this form.

Generally, equivalent circuits contain constant phase elements (CPE) with the admittance $Y = Y_0 s^n$. The CPE transforms into resistance (R), Warburg impedance (W), capacitance (C), or inductance (L), when the exponent n takes the value of 0, 0.5, 1 or -1 respectively [9]. Accordingly, the admittance of the specified circuit elements may be written as $1/R$, $Y_0 \sqrt{s}$, Cs or $1/Ls$. When analogous terms are found in the impedance expression, there is no difficulty in understanding the structure of the adequate EC. Hence, to discover the EC compatible with Eq. (1), the certain its rearrangements should be made.

The analysis performed shows (for details see Appendix) that two different EC follow from Eq. (1). The faradaic subcircuit of the first EC was composed by Rueda et al [6]. Upon supplementing with non-faradaic elements, this EC N1 takes form shown in the upper part of Fig. 1. According to Boukamp [10], its description code may be written as: $R_\square([R_\infty(R_1 W_1)(C_2 W_2)]Z_{\text{dl}})$. Here, elements in series are given in square brackets, and elements in parallel are enclosed in parentheses.

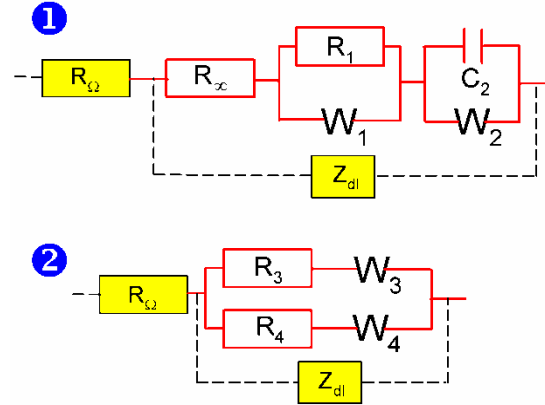


Fig. 1. Two equivalent circuits for consecutive transfer of two electrons. Faradaic elements are connected with solid lines. The ohmic resistance of the solution, R_Ω , and the double-layer impedance, Z_{dl} , are the non-faradaic elements

Though the magnitude and the frequency dependence of Y_F are essentially controlled by four parameters (see Eq. (1)), the faradaic subcircuit contains more (five) elements. For this reason, the specific link between faradaic EC elements occurs:

$$C_2 = R_1 Y_{01} Y_{02}, \quad (2)$$

where Y_{01} and Y_{02} are constants of the respective Warburg admittances (see above).

The faradaic circuit of another alternative EC N2 (lower part of Fig. 1) contains less (four) elements displaced in two parallel $[RW]$ subcircuits. Both foregoing EC yield the same impedance spectra, if and only if the condition (2) is satisfied. As this takes place, the interrelation between elements of the two EC is given by equations (A.4)-(A.8). Besides, as the analysis shows, both circuits follow from Grafov's EC [3], when the adsorption states are neglected,

The ambiguity of EC is well known in the EIS theory. For instance, two different EC are also possible in the case of two sequential one-electron reaction steps with an adsorbed intermediate, in the absence of mass transport control [11]. They are completely interchangeable and can be transformed into each other. However, the case discussed in the present article is somewhat different owing to the constraint given by Eq. (2).

We made use of both EC in fitting experimental impedance spectra, obtained for Cu|Cu(II) system, where quite stable intermediate Cu^+ ions are formed. Considering the non-ideality of the working electrode, the CPE Q_{dl} was applied for representing the properties of the double layer. At the same time, to employ Eqns. (A.4)-(A.8), we tried to retain ideal faradaic elements W and C . Typical experimental result is shown in Fig. 2. The most part of Nyquist plot presents an arc centred below abscissa axis. On the elimination of non-faradaic elements, this arc constitutes a quarter of circle.

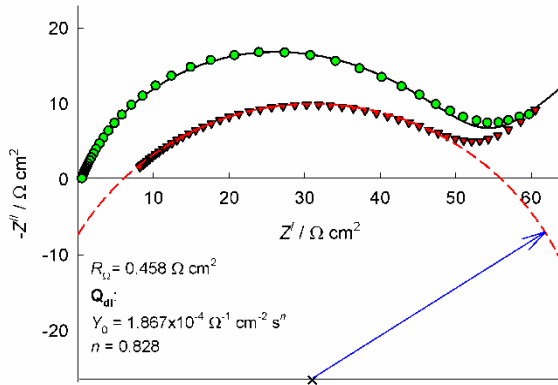


Fig. 2. Nyquist plots of total impedance (circles) obtained for 0.01 M CuSO_4 and 0.6 M H_2SO_4 solution at the open-circuit potential equal to 0.245 V vs. SHE. The residual plot (triangles) was obtained on the elimination of displayed non-faradaic elements

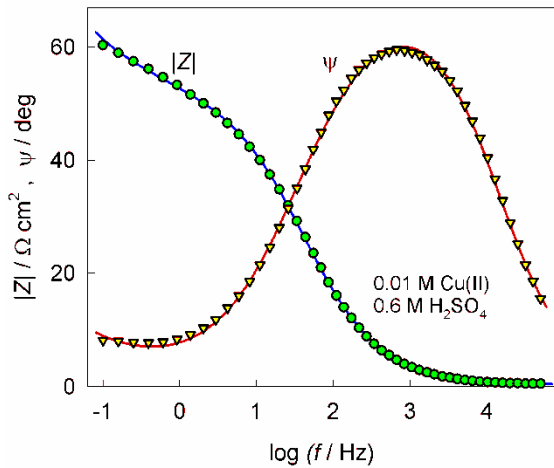


Fig. 3. Experimental (symbols) and simulated (lines) spectra of the impedance modulus, $|Z|$, and the phase shift, ψ

Fitting procedures performed with EC N2 show rather rapid convergences. When containing Warburg elements, this EC describe experimental spectra with error $\sim 2\%$ (Fig. 3). Even better results ($\sim 1\%$ error) are obtained on substitution of Q for W . Non-faradaic elements are given in Fig. 2; the faradaic ones are as follows: $R_3 = 53.6 \Omega \text{ cm}^2$, $R_4 = 20$

$7.22 \Omega \text{ cm}^2$, $Y_{03} = 0.106 \Omega^{-1} \text{ cm}^{-2} \text{ s}^{0.5}$, $Y_{04} = 5.5 \times 10^{-4} \Omega^{-1} \text{ cm}^{-2} \text{ s}^{0.5}$. The same results of simulation are obtained with EC N1 and faradaic elements recalculated with Eqns. (A.4)-(A.8): $R_0 = 6.36 \Omega \text{ cm}^2$, $R_1 = 47.0 \Omega \text{ cm}^2$, $Y_{01} = 7.08 \times 10^{-4} \Omega^{-1} \text{ cm}^{-2} \text{ s}^{0.5}$, $Y_{02} = 0.107 \Omega^{-1} \text{ cm}^{-2} \text{ s}^{0.5}$, $C_2 = 3.55 \text{ mF cm}^{-2}$.

Fitting with EC N1 operated less successful and did not improve the results obtained with EC N2. The main weakness consists in the elevated uncertainty in determination of some elements, especially of C_2 . This supposedly arises from the restriction given by Eq. (2). Besides, the EC N2 is preferable due to more clear physical sense. For instance, in the case of metal deposition, the following relationships are valid under the equilibrium (open circuit) conditions [7,8]:

$$j_{01} + j_{02} = (RT/F) \left(1/R_3 + 1/R_4 \right), \quad (3)$$

$$\frac{1}{j_{01}} + \frac{1}{j_{02}} = \frac{(R_3 + R_4)(1/c_O + 4/c_Y)}{[(\sigma_3 + \sigma_4)F\sqrt{D}]}, \quad (4)$$

where j_{01} and j_{02} are the exchange current densities of charge transfer steps, c_O and c_Y are the equilibrium concentrations of O and Y species (of Cu^{2+} and Cu^+ ions). Warburg coefficients (σ) have their common meaning with $\sigma = 1/\sqrt{2} Y_0$. With $D = 5 \times 10^{-6} \text{ cm}^2 \text{ s}^{-1}$ and $[\text{Cu}^+] = 77 \mu\text{mol dm}^{-3}$ [12], these relationships yield $j_{01} = 0.09 \text{ mA cm}^{-2}$ and $j_{02} = 3.8 \text{ mA cm}^{-2}$. Since Eqns. (3) and (4) are symmetric with respect to R and σ , the established j values may be counterchanged. Therefore, to determine the rate-determining step, extra data should be invoked.

It can be seen from Eqns. (3) and (4) that R_1 and R_2 represent the charge transfer kinetics, whereas W_1 and W_2 is characterized by both the charge transfer and the semi-infinite diffusion. We wish to emphasize particularly that all faradaic elements are interrelated and each of them depends on the characteristics of both steps. Close inspection of mathematics regarding similar but adsorption-complicated processes [13] shows that this conclusion is more general and might be extended to more complex mechanisms. Otherwise, the attempts to construct EC with elements attributed to separate charge transfer steps, as is done in [14], seem to be questionable. The second EC was successfully, to our opinion, employed in the investigation of Cu(II) systems containing such surfactants as oligomers of ethylene glycol [12] and other polyethers [15].

CONCLUSIONS

Two different faradaic equivalent circuits, $R_\infty(R_1W_1)(C_2W_2)$ and $([R_3W_3][R_4W_4])$, can be derived from kinetic equations obtained for consecutive charge transfer with the formation of soluble intermediate. Both circuits follow from Grafov's EC, when the adsorption states are neglected,

The aforementioned circuits are indistinguishable, if and only if a certain interrelation between R_1 , W_1 , W_2 and C_2 is satisfied. Then, upon a proper choice of parameters, both EC display the same impedance spectrum at all frequencies.

All faradaic elements are interrelated and each of them depends on the characteristics of the overall process. Neither of EC elements can be attributed to the separate charge transfer step.

Though the EIS data obtained for the Cu|Cu(II) system can be described by either of the two EC, the second EC is preferred due to its simplicity and more clear physical sense.

REFERENCES

1. D.A. Harrington, P. van den Driessche, *Electrochim. Acta*, **56**, 8005 (2011).
2. J. H. Sluyters, Russ. *J. Electrochem.*, **45**, 25 (2009).
3. B.M. Grafov, E.A. Ukshe. *Elektrokhimicheskiye tsepi peremennogo toka*. Nauka, Moscow, 1973.
4. A.R. Despić, D.R. Jovanović, S.P. Bingulac, *Electrochim. Acta*, **15**, 459 (1970).
5. R.D. Armstrong, R.E. Firman, *J. Electroanal. Chem.*, **45**, 3 (1973).
6. M. Rueda, M. Sluyters-Rehbach, J.H. Sluyters, *J. Electroanal. Chem.*, **222**, 45 (1987).
7. A.A. Survila, A.A. Katkus, *Sov. Electrochem.*, **16**, 1483 (1980).
8. A. Survila, V. Baliukienė, *Chemija (Vilnius)*, **12**, 195 (2001).
9. A. Lasia, in: *Modern Aspects of Electrochemistry*, B. E. Conway, J. Bockris, R.E. White (eds), vol. 32, Kluwer Academic/Plenum Publishers, New York, 1999, p. 143.
10. B.A. Boukamp, *Equivalent circuits (EQUIVCRT.PAS)*, users manual. University of Twente, the Netherlands, 1989.
11. R. de Levie, *Ann. Biomedical Eng.*, **20**, 337 (1992).
12. D. Bražinskienė, A. Survila, Russ. *J. Electrochem.*, **41**, 979 (2005).
13. C. Gabrielli, P. Moçotéguy, H. Perrot, D. Nieto-Sanz, A. Zdunek, *Electrochim. Acta*, **51**, 1462 (2006).

14. W. Wang, Y.B. Li, *J. Electrochem. Soc.*, **155**, D263 (2008).

15. A. Survila, Z. Mockus, S. Kanapeckaitė, D. Bražinskienė, R. Juškėnas, *J. Electrochem. Soc.*, **159**, D296 (2012).

APPENDIX

It follows from Eq. (1) that

$$Z_F = R_\infty + \left(1/R_1 + Y_{01}\sqrt{s}\right)^{-1} + \left(C_2s + Y_{02}\sqrt{s}\right)^{-1}, \quad (\text{A.1})$$

where $R_1 = R_\infty(c-b)/b$, $Y_{01} = 1/R_\infty(c-b)$,

$$C_2 = 1/R_\infty d, \quad Y_{02} = b/R_\infty d.$$

Eq. (A.1) shows that the faradaic circuit should include the resistance R_∞ that is in series with two other subcircuits whose admittances are given by two respective denominators in this equation. The terms $1/R_1$ and $Y_{01}\sqrt{s}$ testify that the first subcircuit contains R_1 and W_1 in parallel. Similarly, another term in the parenthesis suggests the parallel connection of C_2 and W_2 in the second subcircuit.

At the same time, another form of Eq. (1) is possible:

$$Y_F = \left(R_3 + 1/Y_{03}\sqrt{s}\right)^{-1} + \left(R_4 + 1/Y_{04}\sqrt{s}\right)^{-1}. \quad (\text{A.2})$$

It follows from the identity of Eqns. (1) and (A.2) that

$$\begin{aligned} b &= (1/Y_{03} + 1/Y_{04}) / (R_3 + R_4), \\ c &= 1/R_3 Y_{03} + 1/R_4 Y_{04}, \\ d &= 1/R_3 R_4 Y_{03} Y_{04}. \end{aligned} \quad (\text{A.3})$$

Eq. (A.2) shows that alternative faradaic EC, namely $([R_3W_3][R_4W_4])$, is possible. It contains two parallel $[RW]$ subcircuits. Both EC yield the same impedance spectra, when their elements are chosen according to the following equations:

$$R_1 = R_\infty (R_3^2 Y_{03} + R_4^2 Y_{04}) / [R_3 R_4 (Y_{03} + Y_{04})], \quad (\text{A.4})$$

$$Y_{01} = R_3 R_4 (R_3 + R_4) Y_{03} Y_{04} / [(R_3^2 Y_{03} + R_4^2 Y_{04}) R_\infty], \quad (\text{A.5})$$

$$Y_{02} = R_3 R_4 (Y_{03} + Y_{04}) / [(R_3 + R_4) R_\infty], \quad (\text{A.6})$$

$$C_2 = R_3 R_4 Y_{03} Y_{04} / R_\infty, \quad (\text{A.7})$$

$$1/R_3 + 1/R_4 = 1/R_\infty \quad (\text{A.8})$$

The latter relationship also follows from EC structures, as the limiting case when $\omega \rightarrow \infty$.

ЕКВИВАЛЕНТНИ СХЕМИ НА ЕЛЕКТРОХИМИЧНА РЕАКЦИЯ ВКЛЮЧВАЩА ПОСЛЕДОВАТЕЛНИ СТЪПКИ ПРИ ПРЕНОСА НА ЗАРЯД

Арвидас Сурвила

Център за физически науки и технологии, Институт по химия, А. Гостауто 9,

LT 01108 Вилнюс, Литва

Постъпила на 24 април, 2014 г.; коригирана на 4 февруари, 2015 г.

(Резюме)

Две различни еквивалентни схеми могат да бъдат получени от кинетичните уравнения, описващи последователен пренос на зарядуспоредно с образуването на разтворимо междинно съединение. Схемите са описани с кодове: $R_{\infty} (R_1 W_1) (C_2 W_2)$ и $([R_3 W_3] [R_4 W_4])$ (сериините елементиса представени в квадратни скоби, а успоредните елементи са заградени в обикновени скоби). И двете схеми са неразличими, ако и само ако е осъществена определена взаимовръзка между R_1 , W_1 , W_2 и C_2 . След това, при подходящ избор на параметри и двете ЕС показват същия импедансен спектър при всички честоти. Всички „фарадееви“ елементи са взаимно свързани и всеки един от тях зависи от характеристиките на цялостния процес. Нито един от елементите на ЕС не може да бъде приписан на отделната стъпка при преноса на заряд. Въпреки, че данните получени благодарение на еквивалентната импедансна спектроскопия (ЕИС) за системата $Cu | Cu(II)$ могат да бъдат описани от коя да е от двете ЕС. Втората ЕС е предпочетена, поради нейната простота и по-ясен физичен смисъл.

Experimental approach for the study of SOFC cathodes

M.P. Carpanese^{1,2}, A. Giuliano¹, M. Panizza¹, E. Mercadelli³, A. Sanson³, A. Gondolini³,
A. Bertei⁴, A. Barbucci^{1,2,*}

¹Department of Civil, Chemical and Environmental Engineering, University of Genova, P. le J. F. Kennedy 1, 16129 Genova, Italy

²Institute for Energetics and Interphases, CNR, Via De Marini 6, 16149 Genova, Italy

³Institute of Science and Technology for Ceramics, CNR, Via Granarolo 64, 48018 Faenza, Italy

⁴Department of Civil and Industrial Engineering, University of Pisa, Largo L. Lazzarino 2, 56126 Pisa, Italy

Received June 30, 2014; Revised February 4, 2015

The suitability of impedance measurements in Solid Oxide Fuel Cells (SOFCs) is an important concern, especially in case of measuring separately the behaviour of one of the electrode when an overvoltage is applied. In this case a thin electrolyte-supported cell with the RE (Reference Electrode) coplanar with the WE (Working Electrode) is experimentally convenient, but many authors highlighted that incorrect results can be obtained if an inappropriate geometric configuration is used. In this work LSM cathodes ($(La_{0.8}Sr_{0.2})MnO_{3-x}$) were investigated in a Yttria-stabilised Zirconia (YSZ) electrolyte-supported cell, using an electrolyte 3 mm thick. Two types of cells were prepared: the first (Cell1) according to the geometric requirements suggested in literature: little WE (diameter 3 mm) aligned to the CE (Counter Electrode) and with equal R_{pol} (polarisation resistance) and time constant; RE co-planar around the WE and placed at a distance greater than three-electrolyte thicknesses from the WE; the second one (Cell2) equal to Cell1 but with a bigger WE (diameter 8 mm). Impedance measurements were carried out both in two- and three-electrode configuration, at OCV (Open Circuit Voltage) and under applied overpotentials. A preliminary comparison between the results extracted from Cell2 at two- and three- electrodes confirms that a thick electrolyte allows extracting suitable three-electrode impedance results in case of OCV and small overpotentials. On the other side, when an overpotential over 0.2 V is applied, a comparison between Cell1 and Cell2 gives quite different results. The investigation here presented considers also an experimental approach useful for the comprehension of the main phenomena governing the kinetic of the process.

Keywords: Solid oxide fuel cells, impedance spectroscopy, electrode kinetic

INTRODUCTION

DC and AC electrochemical techniques are one of the tools necessary for the study of Solid Oxide Fuel Cells. AC measurements are normally performed on experimental cells and cell stacks, which reflects the real features of the electrochemical system, or are carried out on simplified systems, that allow the separated study of one component of the system. In this case a thin electrolyte-supported cell with the RE coplanar with the WE is experimentally convenient, but many authors highlighted that incorrect AC impedance results can be obtained if an inappropriate geometric configuration is used [1,2,3].

Moreover, the quality of the impedance data is not only related to the geometry of the system, but

also to the procedure applied during the testing stage. It is recommended that before systematic impedance investigation the linearity of the system be checked, in order to choose the perturbation amplitude which vouches for the linearity of the system and at the same time the highest quality of the impedance spectra considering also that the maximum permissible amplitude of a perturbing signal is smaller at low frequencies than at high frequencies. This approach should be applied particularly when low impedance systems like SOFCs are studied. The low impedance of the system is a critical factor and can be improved with small cell geometries. The obtained data gain quality if the inductance of the cell rig is extracted under the same conditions of the cell measurements (temperature, cables looping) and is then subtracted to the cell frequency dispersion. Cell geometry remains anyway a crucial point.

In this paper a simplified cathode made of only a porous LSM layer applied on YSZ dense and

* To whom all correspondence should be sent:
E-mail: barbucci@unige.it

thick electrolyte (3mm) is considered. The choice of such a cathode is due to the fact that: i) this electrocatalyst has a real application on SOFCs, ii) it possesses a negligible ionic conductivity with respect to the electronic conductivity, iii) it is still not yet fully clear the mechanism of oxygen reduction at a SOFC cathode.

Two types of cells were prepared. The first (Cell1), according to the geometric requirements suggested in literature, having little working electrode (WE, diameter 3 mm) aligned to the counter electrode (CE) and with equal R_{pol} and time constant. The reference electrode (RE) co-planar around the WE is placed at a distance greater than three-electrolyte thicknesses from the WE. The second type of cell (Cell2) equal to Cell1 but with a bigger WE (diameter 8 mm).

Impedance measurements were carried out both in two- and three-electrode configuration, at OCV and under different applied overpotentials.

This research has the aim to stress some of the most important criteria to be applied when impedance measurements are performed in order to have reliable experimental data to be used for the interpretation of the electrode kinetic. Furthermore, an attempt to understand the main phenomena governing the kinetic of the oxygen reduction on LSM pure cathodes is presented.

EXPERIMENTAL

The supporting electrolytes were produced by uniaxial pressing the YSZ powders (TZ-8Y Tosoh) and sintering at 1500°C for 1h. The electrolyte dye was carefully designed in order to obtain pellets with a reproducible diameter of 35 mm and 3 mm in thickness after sintering.

For the electrodes deposition a screen printing ink was produced adding to the $(La_{0.8}Sr_{0.2})MnO_{3-x}$ powder (LSM20-P Fuelcellmaterials.com) the proper amount of solvent, deflocculant and binder following the procedure reported by Sanson et al [4].

Thick films were screen printed (squeegee speed = 0.12 m/s, squeegee load = 4.5 kgF, snap off = 0.9 mm; AUR'EL 900, AUR'EL Automation S.p.A., Italy) onto the YSZ pellets and dried at 80°C x 30' into an infrared furnace. Suitable masks were used to print the two types of cells (Cell1 and Cell2), according to the desired geometries (Cell1: WE and CE diameter 3 mm; Cell2: WE and CE diameter 8 mm).

The as-deposited films were finally sintered at temperatures of 1050 °C and 1150 °C for 2h, producing Cell1-type at the two different sintering

conditions and Cell2-type at the only 1050 °C sintering condition.

The cells were placed inside an in-lab constructed test station for the electrochemical investigation. The system was heated at a rate of 0.9 °C min⁻¹ up to testing temperature (700-800°C).

The electrochemical measurements were carried out in a two- and three-probe configuration, using a potentiostat coupled to a frequency response analyser (Autolab PGSTAT302N). During the testing procedure, the cathode was exposed to the ambient atmosphere or fed with pure oxygen. Impedance measurements at open circuit voltage (OCV) in a frequency range of 10⁶ to 10⁻¹ Hz were carried out in potentiostatic mode. Before starting any systematic analysis, the linearity of the system response was checked, ranging the voltage perturbation amplitude from 5 to 50 mV. Short circuit measurements were performed under the same conditions of the systematic analysis and the obtained data were subtracted to the impedance spectra for the inductance correction.

A microstructure investigation of cells both before and after the testing was carried out by SEM (LEO1450 VP Scanning Electron Microscope) and EDS microanalysis (INCA Energy 300, Oxford Instruments Analytical).

RESULTS

The first set of experimental tests was focused on the cell with a typical electrode diameter of 8 mm. This size is quite commonly used in literature and in studies performed in our Lab [5, 6]. The first check to verify the measurement reliability was the comparison of the results extracted at two- and three-electrode configuration. Also in the latter case the cell was symmetric, since the two opposite electrodes were prepared according to the same formulation and shape. As mentioned in the experimental section, a careful preparation of the cell was paid as for the alignment, size, thickness, and structure of the electrodes. Typical inductance corrected Nyquist plots are reported in Fig 1.

The spectra show a depressed capacitive loop, which suggests the presence of at least two different time constants, in line with the complex path for the oxygen process. The spectra allow us to extract, with a good precision, the value of the total resistance of the capacitive loop as the difference between the intercept of the frequency dispersion with the real axis at low and high frequencies (polarization resistance, R_{pol}).

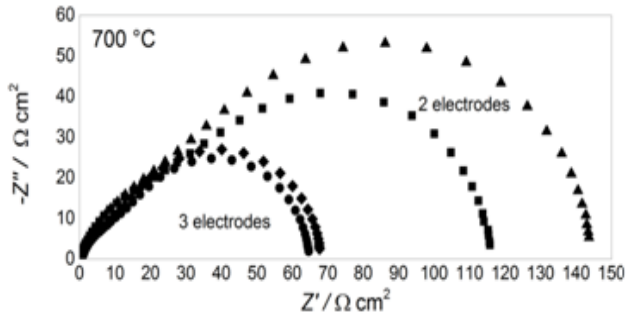


Fig. 1. Impedance spectra of Cell1 at OCV in two- and three-electrode configuration $p(\text{O}_2) = 0.21$ atm (triangle and rhombus), $p(\text{O}_2) = 1$ atm (square and circle). Operating conditions: 700 °C.

This parameter includes all the resistances experienced by the overall process, which takes place at the electrode under investigation, and it is always considered in the studies of the reaction kinetics. In order to ensure the reliability of the results, the same value of the total resistance has to be extracted from the same electrode in both cell configurations. Discrepancies due to different geometry and/or structure of the two opposite electrodes give rise to variations of the single electrode total resistance, which is estimated singularly and totally in the three- and in the two-electrode configuration, respectively [2].

A general view of this aspect is given in Fig 2 through the comparison of the R_{pol} for Cell2 in three-electrode and half of the total resistance in two-electrode configuration, at different operating conditions. The values obtained show a very good symmetry of the system confirming what was already observed through the morphological analysis. In fact both electrodes possess very close polarization resistance. In addition, the results at open circuit voltage and small overpotential (0.1 V) suggest that EIS measurements are reliable in the three-electrode configuration even with a RE placed at a limited distance from the WE.

The comparison of the results obtained from Cell2 ($\Phi_{\text{WE}} = 8$ mm) and Cell1 ($\Phi_{\text{WE}} = 3$ mm), extracted in the 3-electrode configuration, is reported at different overpotentials in Fig. 3. It is highlighted a good agreement of the results obtained at low polarisations (OCV to 0.2 V), while for high polarisations of the electrode (0.3 V and 0.4 V) the two geometries of the same sintering electrode do not match any longer. The increased distance of the RE from the WE is the only difference of Cell1 with respect to Cell2. According to the studies available in literature [7, 8] the reference electrode of Cell2 is polarised when high overpotentials are applied, consequently poor reliability of the measurement data have to be

considered. Measurements on cells with the same apparent geometry but different porosity, which indirectly means different particle size/electrode specific area and TPB length, have been performed, by preparing cells of type 1 with two different sintering process of the LSM electrode. According to previous experiences [9, 10, 11, 12] the electrode sintering at 1050 and 1150°C produces a good variation of the electrode porosity, 50% and 30% respectively, and average particle size, 0.7 μm and 2 μm respectively. Electrode porosity and mean particle size were evaluated by image analysis of SEM micrographies.

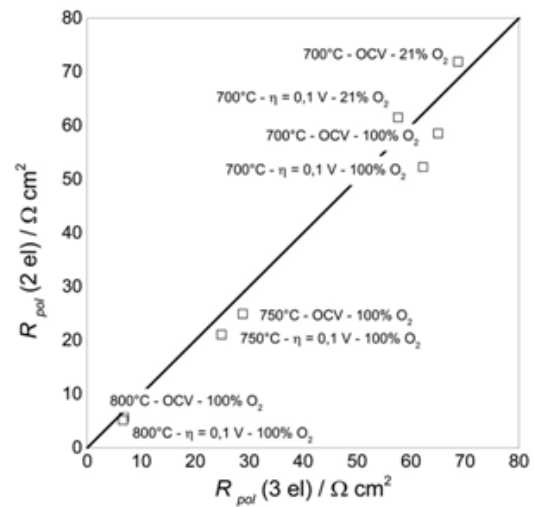


Fig. 2. Comparison between R_{pol} extracted in three-electrode configuration and half of the total R_{pol} resistance in two-electrode configuration, for Cell2. Operating conditions reported on the picture.

The total R_{pol} has been extracted from the impedance measurements on both systems with a three-electrode configuration (Cell1 type) as a function of overpotential and are reported in Fig 4. These results highlight a remarkable difference of the process kinetic in the two samples at OCV. Such difference decreases as the overpotential increases. About the electrode sintering temperature, two main aspects have to be considered and they are: i) a relatively small particle size and high electrode porosity produce a structure with a high LSM active surface per unit volume, useful for adsorption and diffusion phenomena; ii) a relatively small particle size and high sample porosity produce an improved TPB length at the electrolyte interface, which enhances charge transfer.

In order to find a direction between these possibilities that both enhance and control the overall process, the plot of $\ln(R_{\text{pol}})^{-1}$ against the overpotential [13] can be used to check if the

typical Butler-Volmer behaviour for charge transfer controlled reaction hold in this case. A linear trend of the experimental data cannot be considered and a credit to the first hypothesis of adsorption and mass transport of the electroactive species as controlling steps looks more suitable (Fig 5).

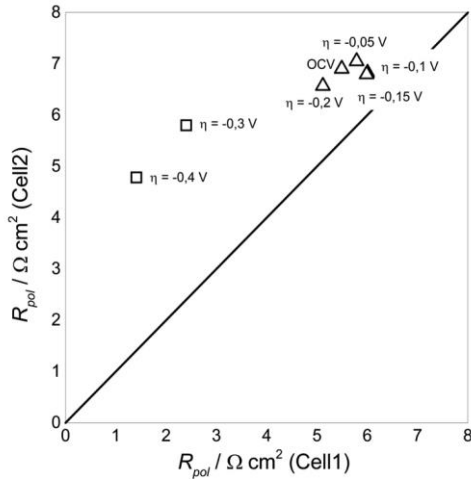


Fig. 3. Comparison of the results obtained from Cell1 and Cell2 in the three-electrode configuration at different overpotentials (triangle OCV \div 0.2 V; square 0.3 V \div 0.4 V) at 800 °C and $p(\text{O}_2) = 1$ atm. Data corrected with the geometric area of the electrodes.

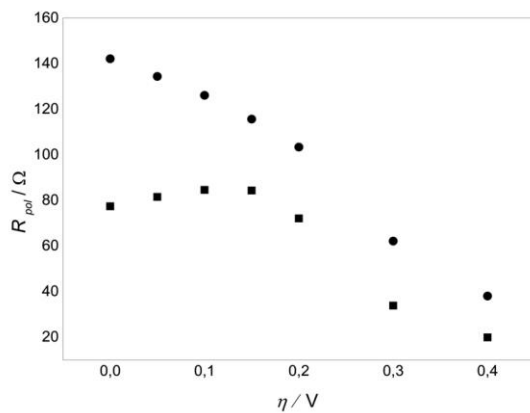


Fig. 4. R_{pol} for Cell1 with LSM electrode sintered at 1050 °C (square) and 1150 °C (circle) at different overpotentials (800°C and $p(\text{O}_2) = 1$ atm).

The role of adsorption and transfer phenomena in the electrode reaction can be faced with the analysis of the impedance spectra. Nyquistplots of Cell1 (Fig. 6) shows that both at OCV and under WE polarisation the high frequency part of the plot contains a component related to linear diffusion in a homogeneous layer with finite thickness [14]. The quantification of this phenomenon can be performed with the aid of data fitting with equivalent circuits models [15] or with other impedance analysis techniques, like Differential

Impedance Analysis [14, 16, 17]. It has to be pointed out that the use of equivalent circuits risks to be speculative if a preliminary basic analysis of the data, which individuate the possible components of the circuit, is not performed.

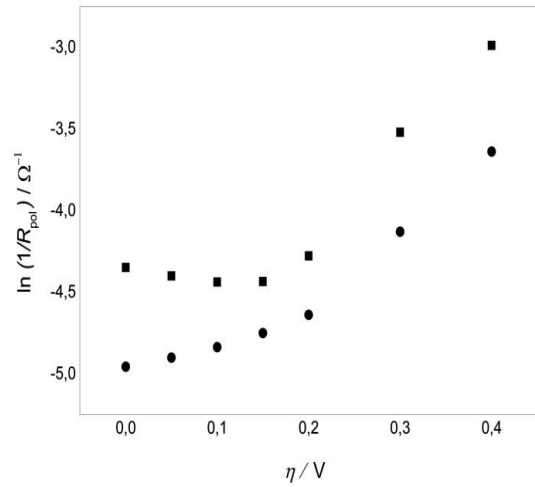


Fig. 5. Trend of $\ln(R_{\text{pol}})^{-1}$ versus overpotential at 800°C and $p(\text{O}_2) = 1$ atm, square sample sintered at 1050 °C, circle sample sintered at 1150 °C.

Good fitting results of the obtained experimental data are already available with a simple typical Voigt model, used in solid-state electrochemical systems. This takes into account of a two time constants equivalent circuit: the low frequency part of the spectra is described with an R/CPE (Resistance-Constant Phase Element, CPE) term and recalls a transport phenomenon, while the high frequency part with an RC (Resistance-Capacitance) in series with the previous term and suitably related to charge transfer. An example of fitting is presented in Fig 7.

The low frequency part of the spectra recalls a transport phenomenon, while the high frequency part is well described by a RC parallel, suitably connected to the charge transfer. The low frequency mesh (R_2Q) ascribed to transport phenomena shows a strong R_2 dependence on the applied overpotential (Fig 8).

At OCV the increasing temperature improves remarkably the kinetic of the process. Considering that at OCV diffusion is the main driving force for mass transport and that the diffusion coefficient in the Fick's law is strongly dependent on temperature [18] the gas diffusion mechanism can be related to the increase of $1/R_2$ with the operating temperature.

At high overpotential $1/R_2$ shows a further improvement with respect OCV. This is especially observed at 700 °C. If the transport mechanism would be controlled only by the gas diffusion the

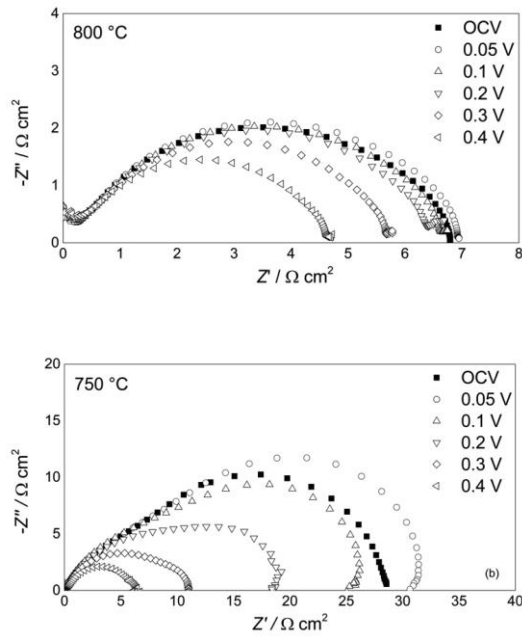


Fig. 6. Nyquist plots of Cell2 at $p(\text{O}_2)=1$ atm, 800°C (a), e 750°C (b), at different cathodic overpotentials.

slope of these curves should not change. Then, when overpotential increases a further transport phenomenon should be considered, which is more important where diffusion is slower (700 °C). Migration of the electroactive species through the subsurface or even inside the bulk of the LSM could be recalled. This supports the mechanisms that foresee the formation of an intermediate charged species (O^{2-} or O^-) adsorbed on the LSM surface, with following incorporation inside the LSM oxygen vacancies, according to literature [19, 20, 21, 22]. This is also in agreement with the values of polarisation resistance at 800°C presented in Fig 4; in fact, at OCV the amount of active site is high in the most porous electrode (sintered at 1050°C), which has available a wide path for surface transport of adsorbed oxygen ions. Under polarisation the transport of oxygen ions is enhanced also into the LSM bulk. Then, the porosity of the electrode does not play a relevant role, providing oxygen gas at the active site for adsorption and first charge transfer, and the total polarisation resistance detected in the differently porous electrodes are getting closer.

CONCLUSIONS

This research has the aim of stressing some of the most important criteria to be applied when impedance measurements are performed, in order to have reliable experimental data to be used for the

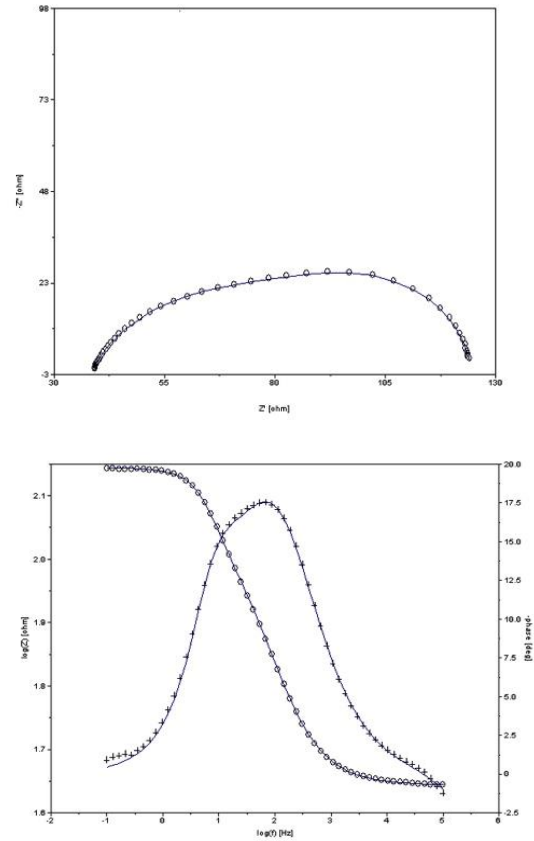


Fig 7. Fitting of the experimental data of Cell2 at 750°C, $p(\text{O}_2) = 1$ atm, two-electrodes configuration, by an $R_1(R_2CPE)(R_3C)$ circuit at OCV ($R_1 = 39.5 \square$, $R_2 = 53.5 \square$, $Y_0 = 0.27 \cdot 10^{-3}$, $n = 0.73$, $R_3 = 46.5 \square$, $C = 0.5$ mF).

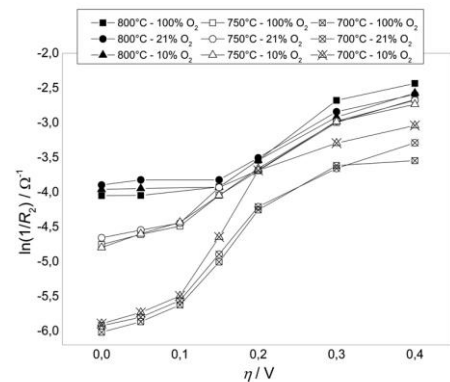


Fig. 8. Low frequency part resistance (R_2) plotted versus overpotential, at different operating temperature and different $p(\text{O}_2)$.

interpretation of the electrode kinetic. The system investigated in this study (pure LSM SOFC cathode) was chosen since it has a real application; moreover, it constitutes a simplified but meaningful configuration with respect to composite electrodes and, finally, because a clear understanding of the electrochemical oxygen reduction is not yet been addressed. The presented approach shows how cell

geometry, cell configuration, electrode porosity and operating conditions (temperature, reactant concentration and overpotential) can be managed to have sensitiveness of the phenomena controlling the overall process. However, the match between the experimental approach, presented in this paper, with a theoretical study, able to simulate the impedance spectra on the basis of a physically consistent model, is the target to achieve a comprehensive analysis of the system [23, 24]. A theoretical approach based on:

- a simplified mathematical reconstruction of the system based on the microscopic observation of the real structure of the electrode and interfaces;
- the quantification of the effective properties (diffusivity, conductivity, tortuosity, TPB length);
- the application of a kinetic model [25, 26] based on the physical processes with related boundary conditions;
- is under study and will be the object of further communications.

REFERENCES

1. Y. Nagata, Y. Itoh, H. Iwahara, *Solid State Ionics*, **67**, 215 (1994).
2. M. Cimenti, V. I. Birss, J. M. Hill, *Fuel Cells*, **7**(5), 377 (2007).
3. J. Rutman, I. Riess, *Solid State Ionics*, **179**, 913 (2008).
4. A. Sanson, E. Mercadelli, E. Roncari, R. Licheri, R. Orrù, G. Cao, E. Merlone-Borla, D. Marzorati, A. Bonavita, G. Micali, G. Neri, *Ceram. Int.*, **36**, 521 (2010).
5. R. G. Toro, D. M. R. Fiorito, M. E. Fragalà, A. Barbucci, M. P. Carpanese, G. Malandrino, *Mater. Chem. Phys.*, **124**(2-3), 1015 (2010).
6. A. Bertei, A. Barbucci, M. P. Carpanese, M. Viviani, C. Nicolella, *Chem. Eng. J.*, **207-208**, 167 (2012).
7. S. B. Adler, *J. Electrochem. Soc.*, **149**(5)E166 (2002).
8. J. Winkler, P. V. Hendriksen, N. Bonanos, M. Mogensen, *J. Electrochem. Soc.*, **145**, 4, 1184 (1998).
9. A. Barbucci, M. P. Carpanese, M. Viviani, N. Vastistas, C. Nicolella, *J. Appl. Electrochem.*, **39**(4), 513 (2009).
10. Bertei, A. Barbucci, M. P. Carpanese, M. Viviani, C. Nicolella, *Chem. Eng. J.*, **207-208**, 167 (2012).
11. Nicolella, A. Bertei, M. Viviani, A. Barbucci, *J. Appl. Electrochem.*, **39**(4), 503 (2009).
12. Barbucci, M. Viviani, M. Panizza, M. Delucchi, G. Cerisola, *J. Appl. Electrochem.*, **35**, 4, 399 (2005).
13. Barbucci, M. Carpanese, A. P. Reverberi, G. Cerisola, M. Blanes, P. L. Cabot, M. Viviani, C. Nicolella, *J. Appl. Electrochem.*, **38**(7), 939 (2008).
14. Z. Stoynov, D. Vladikova, *Differential Impedance Analysis*, Marin Drinov Acad. Publish. House, Sofia, Bulgaria, 2005.
15. B.A. Boukamp, *Solid State Ionics*, **20**, 31 (1986).
16. G. Raikova, D. Vladikova, Z. Stoynov, *Bulg. Chem. Commun.*, **43**, 133 (2011).
17. Vladikova, Z. Stoynov, G. Raikova, A. Thorel, A. Chesnaud, J. Abreu, M. Viviani, A. Barbucci, S. Presto, P. Carpanese, *El. Acta*, **56**(23), 7955 (2011).
18. S. P. Jiang, *J. Mater. Sci.*, **43**, 6799 (2008).
19. Siebert, A. Hammouche, M. Kleitz, *El. Acta*, **40**(11), 1741 (1995).
20. S. B. Adler, *Chem. Rev.*, **104**, 4791 (2004).
21. H.-T. Chen, P. Raghunath, M. C. Lin, *Langmuir*, **27**, 6787 (2011).
22. A. Barbucci, P. Carpanese, G. Cerisola, M. Viviani, *Solid State Ionics*, **176**, 1753 (2005).
23. Bertei, C. Nicolella, *Powder Technol.*, **213**(1-3), 100 (2011).
24. Bertei, A. S. Thorel, W. G. Bessler, C. Nicolella, *Chem. Eng. Sci.*, **68**, 606 (2012).
25. Bertei, B. Nucci and C. Nicolella, *Chem. Eng. Sci.*, **101**, 175 (2013).
26. A. Bertei, A. Barbucci, M.P. Carpanese, M. Viviani, C. Nicolella, Proc. 10th European SOFC Forum, Luzern, , paper B1016 (2012)

ЕКСПЕРИМЕНТАЛЕН ПОДХОД ПРИ ИЗСЛЕДВАНЕ НА КАТОДИ ЗА ТВЪРДООКСИДНИ ГОРИВНИ КЛЕТКИ (SOFC)

М. П. Карпанезе^{1,2}, А. Джулиано¹, М. Паница¹, Е. Меркаделли³, А. Сансон³, А. Гондолини³, А. Бертеи⁴, А. Барбучи^{1,2}

¹*Катедра гражданско химично и екологично инженерство, Университет на Генуа, площ. Д. Ф. Кенеди 1, 16129 Генуа, Италия*

²*Институт по енергетика и интерфази, ЦНИ, ул. Де Марини 6, 16149 Генуа, Италия*

³*Институт за наука и технологии по керамика, ЦНИ, ул. Гранароло 64, 48018 Фаенца, Италия*

⁴*Катедра по гражданско и индустриално инженерство, Университет на Пиза, Ларго Л. Лаззарино 2, 56126 Пиза, Италия*

Постъпила на 30 юни, 2014 г.; коригирана на 4 февруари, 2015 г.

(Резюме)

Пригодността на импедансните измервания на твърдооксидни горивни клетки (SOFC) е основен проблем, особено в случаите на разделно измерване на поведението на един от електродите, когато се прилага свръхнапрежение. В този случай тънка клетка с електролит за опора и СЕ (сравнителен електрод) копланарно с РЕ (работен електрод) е експериментално удобна, но много автори изтъкват, че могат да се получат погрешни резултати, ако се използва неподходяща геометрична конфигурация. В тази работа LSM катода ((La_{0.8}Sr_{0.2})MnO_{3-x}) бяха изследвани в клетка с итриевостабилизиран циркониев (YSZ) електролит за опора, с дебелина 3 мм. Бяха получени два вида клетки: първата (Клетка1) съгласно геометричните изисквания посочени в литературата: малък РЕ (диаметър 3 мм) в права линия спрямо електрода (ПЕ) и с равни R_{pol} (поляризационно съпротивление) и времеконстанта; СЕ се ориентира копланарно около РЕ и се поставя на разстояние по-голямо от три електролитни дебелини от РЕ; втората (Клетка2) е равна на Клетка1, но с по-голям диаметър РЕ (8 мм). Бяха осъществени импедансни измервания при дву- и три- електродни конфигурации, при напрежение на отворена верига (ОВВ) и при прилагани свръхнапрежения. Предварителното сравнение на резултатите, получени за Клетка2 при дву- и три- електродната клетка потвърждава, че един дебел електролит позволява да бъдат получавани подходящи импедансни резултати за трите електрода в случаите при напрежение на отворена верига и малки свръхпотенциали. От друга страна, когато се приложи свръхнапрежение от над 0.2 V, сравнението между Клетка1 и Клетка2 дава трърде различни резултати. Представените тук изследвания разглеждат също така експериментален подход, полезен за разбирането на основните явления които управляват кинетиката на процесите.

Electrochemical impedance investigation of cholesterol enriched supported films of lipids

M.Tanovska, L.Vladimirova-Mihaleva*, K.Bachev, V.Kochev

Sofia University "St. Kliment Ohridski", Faculty of Physics, 5 James Boucher Blvd. 1164 Sofia, Bulgaria

Received September 30, 2014, Revised February 4, 2015

Electrochemical methods of analysis has received a great attention in the enormously large field of Life Sciences at least because of two reasons – first of all, owing to the exclusive role of bioelectrochemical processes at fundamental levels of living matter organization, and second due to specific features of these methods. Some of their advantages as noninvasiveness, sensitivity and inexpensiveness enlarged the reputation of analytical electrochemistry and established its techniques as indispensable tools for research of broad spectrum of problems in Biosciences. Electrochemical Impedance Spectroscopy (EIS) [1-3], on its own, has long been recognized as an extremely informative tool, especially in areas of investigation where contacts between different phases are involved. Biomembranes and their artificial analogs [4, 5] are just such kind of interfaces where the EIS accuracy and sensitivity have already said their heavy word [6]. Most promising results, however, pointing out to a plethora of practical applications, have been obtained with lipid structures deposited on rigid substrates [7, 8]. In the present work we have tried to evaluate the influence of cholesterol on the physicochemical parameters of supported liquid films of lipids, revealed by their specific impedance behavior at different frequencies. The results definitely suggest that cholesterol exert prominent condensing effect on the films, which is demonstrated via the changes in impedance parameters. This is in accordance with commonly accepted role of cholesterol in biological membranes and model systems, which is based on a large body of experimental evidences [9].

Key words: Electrical Impedance Spectroscopy (EIS), lecithin, lipid films, cholesterol.

INTRODUCTION

No doubt, biomembranes, with their morphological diversity, are namely those attributes that give the final shape of the cell and define it as the quant of living matter [10, 11]. Although the native membranes exhibits myriads of forms and functions and their contents comprise thousands of polypeptides, lipids and saccharides, they share a common feature – the canvas of their architecture consists of bimolecular layer of lipid molecules. That cell membranes are arranged over lipid bilayer, became clear after a pioneering work of Gorter and Grendel [12] and in the early 70es Singer and Nicolson introduced their fluid mosaic model explaining how peptides and proteins are attached to it [13]. Furthermore, in the past few decades became evident that lipid bilayer itself is not a passive element of biomembranes, but governs many important cell processes through its physicochemical state [9]. In addition, new concepts for the 3D and 2D (lateral) organization of membranes flourished. Because of their intricate nature biomembranes are often studied via proper

models, mimicking their structures and functions. The most popular of these model systems inevitably contain lipid bilayer and for the aim of our survey they could be divided into two major classes: "free standing" [5, 14] and "supported" [15]. Of course, each of them is characterized with their advantages and drawbacks, which are mainly concerned with the great compromise between stability and fluidity [16].

The great importance of the cholesterol in the life is associated with changes that occur in bilayers during the mixing this more peculiar molecule with other lipids. Its extraordinary realization in the biosphere was considered ever since by Bloch as a consequence of changes in the membranes performance in the synthesis of higher sterols.

As a continuation of these ideas, Meyer Bloom, Ole Mouritsen and their collaborators suggested an answer to the question exactly which features of bilayers depend on the cholesterol content [17-20]. It has been proved that its ability to give the membranes some very specific physical properties is due to their more flexible behavior, leading to an increase of their structural and functional diversity. Adjusting the phase state of bilayers, cholesterol provides strength and elasticity required for

* To whom all correspondence should be sent:
E-mail: vladimirova@phys.uni-sofia.bg

reproduction of more complex forms with greater curvature.

In this work we have studied the main effect of cholesterol as revealed by specific changes in the electrical parameters of the films. In this regard, EIS turned out to be reliable method for investigation of the lipid films behavior. The obtained results undoubtedly suggested the ordering role of cholesterol in the films, which is in agreement with the present viewpoint widely described in the literature [9, 21-23].

EXPERIMENTAL

Experimental Set-Up

The experimental set-up used in the work is described in details in [24]. Briefly, the basic part of the set-up is a measuring head containing two identical electrodes forming the electrochemical cell (Fig.1). They are made of gold coated MOS (Si/SiO₂) structures placed on two different holders. The lower holder is machined from brass and contacts a Peltier element, regulating its temperature. The upper holder is moving up and down and its position is controlled by a micrometer, so the distance between the electrodes can be precisely defined.

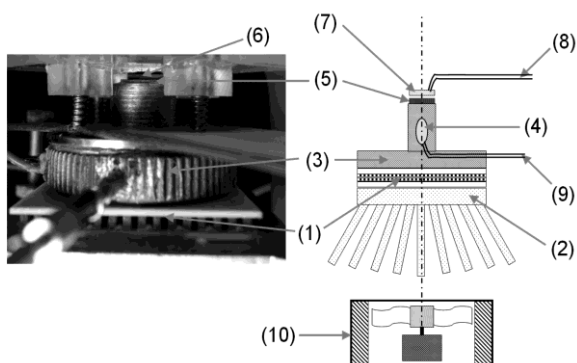


Fig. 1. Overall view (left) and schematic (right) of the experimental set-up: 1) Peltier element; 2) Radiator; 3) Brass holder for the first electrode; 4) Thermoresistor embedded in the brass holder; 5) First electrode - gold (Au); 6) Second Au electrode on Plexiglas holder; 7) Pt thermometer (ceramic substrate with evaporated platinum Pt wire); 8) Leads of Pt thermometer; 9) Leads of thermoresistor; 10) Fan

Materials

Soy-bean lecithin (Walmart, Czech Republic) was used without further purification as lipid material for preparation of the films in this study. Cholesterol (5-cholesten-3 β -ol, C₂₇H₄₅OH, Sigma Chemical Co. USA) analytical grade, also was not purified additionally. Phospholipid dissolved in n-hexane and sterol dissolved in chloroform/methanol

(9/1, vol/vol) were mixed in appropriate quantities to prepare stock solutions with desirable contents.

Gold plated silicon wafers (Microsens SA, Neuchâtel, Switzerland), shown in Fig. 1 were used as solid substrate. The simplest empirical method of preparation of lipid films, known as lipid painting, or paint brush technique, was applied to obtain supported films. Liquid material with different contents of lecithin and cholesterol was deposited directly onto the golden electrode surface, thus so called cast films were realized [25-27]. The lipid solution, pre-prepared at the desired concentration, is applied with a micropipette on to the surface of the substrate for each experiments in equal amounts. After evaporation of the on the dry film remained solvent, electrolyte (0,1 M KCl) is added drop wise and it is waited, until hydration of the layer is succeed.

The two electrodes were then gently pressed one to another by a micrometer screw to a desirable distance between them (Fig.1). In some cases Teflon spacer was used to define the distance. An auxiliary "point" platinum electrode is immersed in the in this way formed electrolytic drop. The impedance between this electrode and the gold coating formed lipid film is measured.

RESULTS AND DISCUSSION

Condensing effect of cholesterol in artificial membranes is a well known and widely investigated phenomenon [28, 29]. For the aim of our survey three types of lecithin films, comprising respectively 49.6, 66.2 and 74.6 mol% cholesterol were studied. First concentration was chosen to represent some higher than normal content of cholesterol in plasmalemma, second one corresponds to saturation limits in phosphatidylcholines and the third is abnormal.

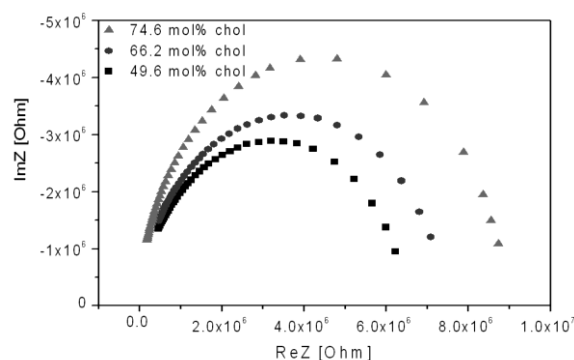


Fig. 2. Nyquist plot for three types of lecithin films with different concentration of cholesterol: 49.6, 66.2 and 74.6 mol%.

The films impedance was measured in the range 130 Hz – 2kHz. Nyquist plots for these frequencies are almost ideal semicircles, revealing increasing modulus of impedance with the increase of the cholesterol concentration(Fig.2). It was useful the impedance to be divided on its components according to the equivalent circuit shown in the inset of Fig. 3.This circuit offered the best fit to the experimental data, obtained with the program ZView. It includes two loops connected in series and represents the closest model, containing minimal number of frequency depending elements (only CPE1).

From the analysis of data, it is clear, that frequency independent parameters R2 and C2 are not very sensitive, while the ARC element, namely R1 and A, varies substantially with cholesterol concentration (Fig. 4).

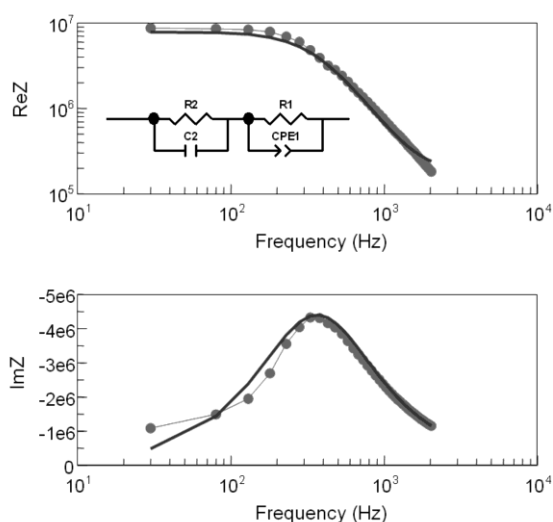


Fig. 3. A fit of the Bode plots with the equivalent circuit used in the work for lipid film with 74,6 mol % cholesterol. A loop of parallel ideal resistor R2 and ideal capacitor C2 is connected in series with so called ARC element consisting of ideal resistor R1 and element with constant phase CPE1. Points are experimental data and line is the fit.

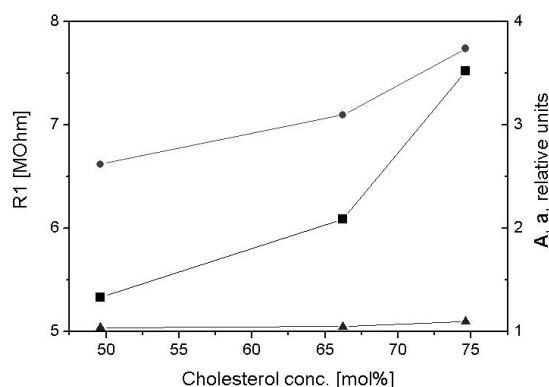


Fig. 4. Depending on the parameters of the equivalent model of the cholesterol content.

Furthermore, the value of ARC parameter a is roughly within the limits of unite, indicating that CPE tends to pure capacitor. However a simplification of the model to plain circuit of frequency independent elements would be not very correct and strongly hampered the fitting procedure. Thus, we can speculate, that the discussed films are made up of two peculiar sub areas depending in different way on the presence of cholesterol. Based on earlier studies, we already have built some ideas about them [30]. The one region (or rather both on two electrodes) is the first monomolecular layer adsorbed on the metal surface, plus, eventually, several adjacent layers oriented according to the first. Orderliness of these layers greatly reduced by closely packed molecules in contact with metal, a fully randomly arranged at the transition to the bulk liquid phase, which in fact may be considered a second characteristic region of the film.

Obviously, the mobility (lateral and rotational diffusion)of the molecules in the layer adhered to the substrate is made difficult by the strong adhesive interactions with the solid phase. Typical of this area with reduced mobility is that its impedance Nyquist format is as lightly curved line running in a semicircle for bulk phase [31].The effect of increasing cholesterol concentration is similar, but unfortunately this is not noticeable in Fig.2 because of not so low frequencies (130Hz) of starting the measurements.

CONCLUSIONS

In this work we have used the method of EIS to study the behavior of cholesterol modified solid supported lecithin films. It was found, that such structures are arranged in two distinguished zones – molecular layers more or less closely attached to the rigid support and bulk phase of initial forming solution. Although this general stratification pattern was previously established by investigation of much thinner lipid layers on different substrates, present results shed new lights on the film architecture. Quite certain is that additional profound investigations of the fine structure of the films and of its rising mechanisms are necessary. Moreover they disclosed the abilities of EIS as a reliable tool for investigation of membrane models.

REFERENCES

1. J. Bard, L. R. Faulkner, Electrochemical methods: Fundamentals and applications. 1st ed., John Wiley & Sons, New York, 1980.
2. E. Barsoukov, J.R. Macdonald, editors, Impedance Spectroscopy. Theory, experiment, and applications.

- 2nd ed. Hoboken, New Jersey: John Wiley & Sons, 2005.
3. M.E.Orazem, B.Tribollet, Electrochemical impedance spectroscopy, John Wiley & Sons, Inc., Hoboken, NJ, 2008.
4. H.T. Tien, Bilayer Lipid Membranes (BLM): Theory and Practice, Marcel Dekker, Inc., New York, 1974.
5. Leitmannova-Liu (ed.), Advances in Planar Lipid Bilayers and Liposomes, Elsevier Inc., Amsterdam, 2006.
6. H.G.L. Coster, Dielectric and electrical properties of lipid bilayers in relation to their structure, In: H.T.Tien, A.Ottova-Leitmannova, (Eds.), Planar lipid bilayers (BLMs) and their applications, Elsevier, Amsterdam, 2003.
7. C. Steinem, A. Janshoff, W.P. Ulrich, M. Sieberand H. L. Galla, *Biophysica Acta*, **169**, 1279 (1996).
8. E.Sackmann, *Science*, **43**, 271 (1996).
9. G. Mouritsen, Life as a Matter of Fat. The Emerging Science of Lipidomics, Springer Verlag, Heidelberg, 2005.
10. B. Alberts, A. Johnson, J. Lewis, M. Raff, K. Roberts, P. Walter, Molecular Biology of the Cell, 4th ed., Garland Publishing, Inc., New York, 2002.
11. H. Lodish, A. Berk, P. Matsudaira, C. A. Kaiser, M. Krieger, M. R. Scott, S. L. Zipursky, J. Darnell, Molecular Cell Biology, 5th ed., W.H.Freeman and Company, New York, 2003.
12. E. Gorter, F. Grendel, *J. Exp. Med.*, **41**, 439 (1925).
13. S. J. Singer, G. L. Nicolson, *Science*, **175**, 720 (1972).
14. H. T. Tien, Bilayer Lipid Membranes (BLM): Theory and Practice, Marcel Dekker, Inc., New York, 1974, p.655.
15. E. Sackmann, *Science*, **271**, 43 (1996).
16. R. Lipowsky, E. Sackmann, (Eds), Structure and Dynamics of Membranes, Elsevier/North Holland, Amsterdam, The Netherlands, 1995
17. M. Bloom, O.G. Mouritsen, *Can.J.Chem.*, **66**, 706 (1988).
18. M. Bloom, O.G. Mouritsen, *Elsevier*, **1**, 65 (1995).
19. Mouritsen, M.J. Zuckermann, *Lipids*, **39**: 1101 (2004).
20. Mouritsen, *Biochim. Biophys. Acta*, **1798**, 1286 (2010).
21. J. H. Ipsen, G. Karlström, H. Wennerström, O. G. Mouritsen, M. J. Zuckermann, *Biochim. Biophys. Acta*, **905**, 162 (1987).
22. G. Mouritsen, M. J. Zuckermann, *Lipids*, **39**, 1101 (2004).
23. G. Mouritsen, *Biochim. Biophys. Acta*, **1798**, 1286 (2010).
24. F. Simeonov, PhD Thesis, Faculty of Physics, Sofia University, 2012.
25. M. Seul, M.J. Sammon, *Thin Solid Films*, **185**, 287 (1990).
26. Ulr. Mennicke, T. Salditt, *Langmuir*, **18**, 8172 (2002).
27. A. Mangiarotti, B. Caruso, N. Wilke, *Biochimica et Biophysica Acta - Biomembranes*, **1838**, 1823 (2014).
28. M. Naumowicz, A.D. Petelska, Z.A. Figaszewski, *Electrochimica Acta*, **50**, 2155 (2005).
29. M. Naumowicz, Z.A. Figaszewski, *Biophysical Journal*, **89**, 3174 (2005).
30. M. Karabaliev, V. Kochev, *Biophys.Chem.*, **103**(2), 157 (2003).
31. M. Karabaliev, V. Kochev, *Material.Sci. Eng.*, **C14**(1-2), 11 (2001).

ЕЛЕКТРОХИМИЧНО ИМПЕДАНСНО ИЗСЛЕДВАНЕ НА ОБОГАТЕНИ С ХОЛЕСТЕРОЛ ПОДДЪРЖАЩИ ЛИПИДНИ ФИЛМИ

М. Тановска, Л. Владимирова-Михалева, К. Бачев, В. Кочев

Физически факултет, Софийския университет "Св. Климент Охридски", бул. Джеймс Баучър №5, 1164 София

Постъпила на 30 септември, 2014; коригирана на 4 февруари, 2015 г.

(Резюме)

Електрохимичните методи за анализ получиха значително внимание в изключително обширната област на природните науки най-малко по две причини – преди всичко, благодарение на изключителната роля на биоелектрохимичните процеси на фундаментално ниво при организацията на живата материя и второ, благодарение на някой черти характерни за тези методи. Някои от предимствата им като неинвазивност, чувствителност и изгодност разширяват репутацията на аналитичната електрохимия и установяват нейните техники като незаменими инструменти при изследване на широк спектър от проблеми в биологичните науки. Електрохимичната импедансна спектроскопия (ЕИС) [1-3], сама по себе си, отдавна е призната като един изключително информативен инструмент, особено в изследователски области, където е налице контакт между различни фази. Биомембраните и техните изкуствени аналози [4, 5] са точно такъв вид интерфейси, където с точността и чувствителността си, ЕИС, вече каза своята тежка дума [6]. Най-обещаващи резултати обаче, посочващи множество практически приложения, са получени с липидни структури, отложени върху твърди подложки [7, 8]. В настоящата работа се опитахме да оценим влиянието на холестерола върху физикохимичните параметри на поддържащи течни липидни филми, разпознати благодарение на поведението на техния специфичен импеданс при различни честоти. Резултатите определено показват, че холестеролът оказва основен кондензиращ ефект върху слоевете, което се вижда от промените в импедансните параметри. Това е в съответствие с общоприетата роля на холестерола в биологичните мембрани и моделни системи, основана на голям обем от експериментални доказателства [9].

Efficient parameter estimation for spectral sensor data by a linear transformation

F. Wendler*, P. Büschel, O. Kanoun

Technische Universität Chemnitz, Reichenhainer Str.70, 09126 Chemnitz, Germany

Received October 15, 2014; Revised March 25, 2015

In this contribution we introduce and evaluate a new approach for solving inverse problems in proximity of a working point with very low computational effort. The non-linear, multi-parametric, complex function will be approximated and inverted by a set of decoupled single parametric, linear equations originating from a sensitivity analysis. The used linear projection condenses the knowledge of the transfer characteristic of the system and provides an alternative to model based and look-up table approaches. The fast estimation of multiple parameters in a limited parameter range is suitable for control applications or investigation of aging and other degeneration processes.

Keywords: Impedance Spectroscopy; Linear Transformation; Parameter Estimation

INTRODUCTION

To increase the amount of information that can be obtained in a single measurement, multi-spectral measurement techniques have been introduced in the recent decades. Multiple influences on a sensor signal can be separated on a frequency scale due to the fact that different effects or mechanisms that sum up to the sensor signal act in different frequency ranges. Common approaches for data analysis of such multispectral data involve a model for regression and a nonlinear optimization process [1]. In many cases the optimization is done by an iterative algorithm [2]. The repeated calculation of the model and the evaluation of some loss functions consume a large amount of computational resources and time. For embedded system solutions, high demands on the dynamics of the measurement and data evaluation speed or models that require high computational effort in the nonlinear regression make the classical approaches unsuitable [3].

The introduced approach is inspired by the Tasseled-Cap-algorithm [4], which is projecting spectral information into a new subspace where quantities of interest are linear independent. The Gram-Schmidt orthogonalization within the Tasseled-Cap-algorithm performs a compensation of independent components in the data set to project the data in subspace. This projection is decoupling the influence by compensation of cross-sensitivities of desired quantities [5]. The orthogonalization uses a pre-defined set of vectors as basis for the new subspace. The possibility to choose these basis vectors based on the sensitivity

of the different quantities of interest, is a useful property in the applications with inverse problems. In the decoupled subspace the desired quantity is then obtained by solving the resulting linear system. The projection formula condenses the knowledge on the systems transfer characteristic in a certain working point and is used to estimate the quantity of interest instead of using models or look up tables. Instead of using the full spectral data the projection uses only two data points selected in a way that they contain maximum information on the quantity of interest. With the presented conditions for these points, they can be chosen in an automated and objective way. The limitation of the measurement to these selected frequency points reduces the measurement time and hardware requirements.

LINEAR PROJECTION

Usually the transfer characteristics of a sensor are described by some model. This model is defined by a set of parameters x . The goal now is to derive the model parameters based only on the measurements performed with the sensor. This is called an inverse problem and usually the calculation of the parameters is challenging as noise in the measurement makes the inversion process ill-posed. With a sensor application in mind one of these parameters is usually of interest and is therefore called a measurement quantity or measurand.

Let us consider that the measurement is performed in some working point (WP) of the sensor. In the proximity of a WP any continuously differentiable function Z characterized by a parameter set x_l to x_m can be expressed as linear approximation \tilde{Z} :

* To whom all correspondence should be sent:
E-mail: frank.wendler@etit.tu-chemnitz.de

$$\tilde{Z} = \sum_{k=1}^m \frac{\partial Z}{\partial x_k} \Delta x_k + Z_{WP}, \quad (1) \quad S_1 = 1, \quad (7)$$

This approximation consists of m products of the sensitivity with respect to the parameters and their corresponding distance from the working point Δx_k and one constant term as working point offset Z_{WP} . In the next step a weighted sum of n of these approximations with weighting factors from a_1 to a_p can be made and rearranged to obtain equation (2). The expression on the right side consists now of m weighted sums of (1). In the case of spectral data each of the p used approximations represents one measurement at a certain frequency:

$$\sum_{n=1}^p a_n \tilde{Z}_n = \sum_{k=1}^m \left(\left[\sum_{n=1}^p \frac{a_n \partial Z_n}{\partial x_k} \right] \Delta x_k \right) + \sum_{n=1}^p a_n Z_{WP,n}, \quad (2)$$

The sensitivity of the entire sum of linear approximations is defined by a suitable set of weighting factors a_n . To obtain the weights a_n we have to introduce a constraint on the sensitivity. In most sensor applications it is useful to set the sensitivity of the wanted parameter x_n (e.g. x_1) to the non-zero value S_1 and all other to zero:

$$\begin{aligned} \sum_{n=1}^p a_n \frac{\partial Z_n}{\partial x_1} &= S_1 \\ \sum_{n=1}^p a_n \frac{\partial Z_n}{\partial x_2} &= 0 \text{ ;} \\ \sum_{n=1}^p a_n \frac{\partial Z_n}{\partial x_m} &= 0. \end{aligned} \quad (3)$$

For the case of spectral data solving the linear system of equations (3) will result in a sum of one quantity at different frequencies, which is now depending on only one parameter:

$$\sum_{n=1}^p a_n Z_n = S_1 (x_1 - x_{WP}) + \sum_{n=1}^p a_n Z_{WP,n}, \quad (4)$$

Rearranging equation (4) and solving for the desired parameter gives:

$$x_{1,est} = \sum_{n=1}^p \frac{a_n Z_n}{S_1} + x_{offset}, \quad (5)$$

The additional constant x_{offset} is calculated with the parameter value at the working point x_{WP} :

$$x_{offset} = x_{WP} - \sum_{n=1}^p \frac{a_n Z_{WP,n}}{S_1}. \quad (6)$$

The defined sensitivity of the weighted sum to the wanted parameter S_1 in equation (3) results in a linear scaling of the weighting factors that are removed by inverting equation (4). For the reason of numerical simplicity it is recommended to choose 1 for the sensitivity.

To successfully perform this procedure, the sensitivity of the desired quantity must be high and the difference to the sensitivity of other system parameters must be maximal. In the simplest case of $p=m$ the parameter vector of all used frequencies needs to be linear independent. This property has to be ensured by the selection of used frequency points like it will be demonstrated. The analyzed transfer characteristic can be any frequency dependent transfer parameter like gain, phase, real or imaginary part. Also a mixed support of those quantities, as two linked real quantities, may be possible if it is required by the application [5]. A generalization for complex transfer functions by the use of complex weighting factors might be a future improvement of the approach. The used quantity as base for the algorithm in the example is the imaginary part of the impedance as real scalar value. For the estimation of other parameters similar formulas like equation (5) can be obtained by adjusting non-zero sensitivity on the right hand side of the system of equations (3).

DEMONSTRATION FOR ONE ESTIMATED PARAMETER

Generic model

In this section, the introduced algorithm is tested and evaluated using generic data to avoid uncertainties of the measurement process. The data is generated from a model for the complex impedance of a solid state electrolyte including electrode effects. The electrodes are represented by the serial resistance R_s , the parallel resistance R_p and the electrode capacitance C_l . The ionic contribution is represented by the Warburg-impedance Z_w with reflecting boundary condition [6]:

$$\underline{Z} = R_s + \frac{1}{j\omega C_l + \frac{1}{R_p} + \frac{1}{Z_w}}, \quad (8)$$

$$\underline{Z}_w = \frac{RT}{l^2 F^2 c_x A \sqrt{2\omega D}} (1 - j) \coth \left(\delta \left(1 + j \sqrt{\frac{\omega}{2D}} \right) \right), \quad (9)$$

The aim of the data analysis is to estimate the concentration c_x while the diffusion coefficient D is unknown. The structure of equation (9) ensures that parts of the impedance spectra have different sensitivity with respect to both unknown parameters. The working point is chosen according table I but it does not refer to a special application. The model represents a general problem in

impedance spectroscopy, when a systematic behavior to the parameters like in figure 1 is observed and a multi parametric interpretation is needed.

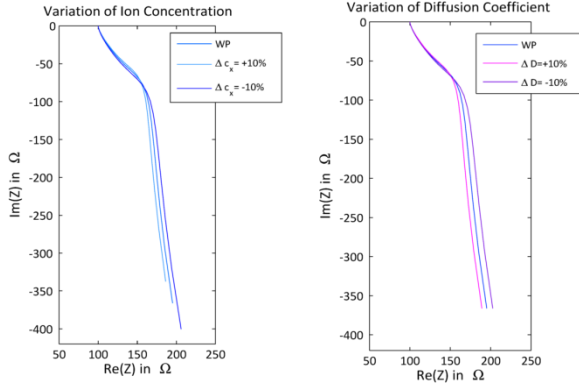


Fig. 1. Transfer characteristic of the generic model due to 10% variation of the two non-constant parameters.

Table 1. Working Point Model Parameters

Name	Symbol	Value
Serial Resistor	R_s	100Ω
Capacitance of the Electrodes	C_1	$500 * 10^{-9}F$
Paralel Resistance	R_p	5 kΩ
Universal Gas Constant	R	$8,31447 \frac{J}{mol K}$
Faraday Constant	F	$96485,34 \frac{C}{mol}$
Distance of Electrodes	δ	$10^{-6}m$
Electrode Area	A	$10^{-4}m^2$
Charge per Ion	I	1
Temperature	T	298 K
Ion Concentration WP	c_x	$10^{-3} \frac{mol}{m^3}$
Diffusion Coefficient WP	D	$10^{-9} \frac{m^2}{s}$

Selection of data support

The first step is the selection of a suitable spectral representation of the system response. Since some representations are more sensitive to certain physical effects this selection is based on the knowledge of the investigated physical system. In this example the targeted effect is the frequency dependent capacitance of the double layer which is represented by the imaginary part of the impedance in equation (8). Due to the reduced influence of the resistive effects caused by the serial and parallel resistance, the entire data analysis focuses exclusively on the imaginary part of the impedance of the entire system.

To estimate the ion concentration in a set of two unknown parameters at least two points in the spectrum of the imaginary part are needed as data support. These points must have a strong sensitivity to the parameter of interest and a linear independent sensitivity vector to solve (3). The presence of a high absolute value of sensitivity is represented by the first criterion K_I for each possible combination of the spectral data at frequencies index d and e :

$$K_I = \left| \frac{\partial Z_d}{\partial x_1} \right| + \left| \frac{\partial Z_e}{\partial x_1} \right|, \quad (10)$$

The independence of the sensitivity information is checked by the second criterion K_{II} in the form of a normalized difference of the sensitivity with respect to the other parameter:

$$K_{II} = \frac{\partial Z_d}{\partial x_2} \frac{\partial x_1}{\partial Z_d} - \frac{\partial Z_e}{\partial x_2} \frac{\partial x_1}{\partial Z_e}, \quad (11)$$

Both criteria have a high absolute value for suitable combinations and tend to zero for unsuited combinations. This numerical property can be used to combine both criteria to one common criterion by multiplication:

$$K_{ges} = K_I K_{II} = \left(\frac{\partial Z_d}{\partial x_2} \frac{\partial x_1}{\partial Z_d} - \frac{\partial Z_e}{\partial x_2} \frac{\partial x_1}{\partial Z_e} \right) \left(\left| \frac{\partial Z_d}{\partial x_1} \right| + \left| \frac{\partial Z_e}{\partial x_1} \right| \right), \quad (12)$$

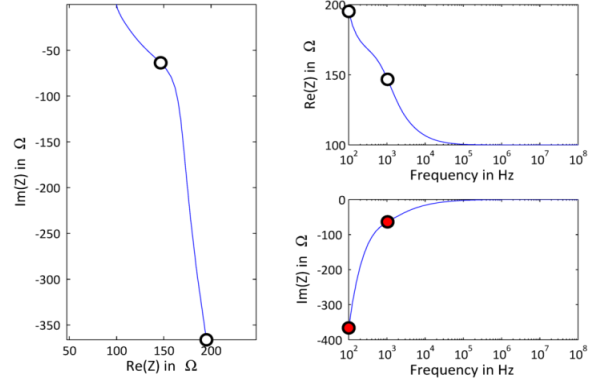


Fig. 2. Selected data support in the spectrum at working point conditions

The common criterion has only a high absolute value for combinations of data from different frequencies that match both criteria. The sensitivities are obtained by numerical derivation with a variation of the parameters of $\pm 1\%$ in equation (13) and (14):

$$\frac{\partial Z_n}{\partial x_1} = \frac{Im\{Z_n(1,01x_1) - Z_n(0,99x_1)\}}{0,02x_1}, \quad (13)$$

$$\frac{\partial Z_n}{\partial x_2} = \frac{Im\{Z_n(1,01x_2) - Z_n(0,99x_2)\}}{0,02x_2}. \quad (14)$$

The analysis of all possible combinations in the spectrum reveals a maximum for the indices 1 and

11 at the frequencies f_1 at 100 Hz and f_2 at 1001 Hz illustrated in figure 2. The imaginary part of the impedance Z_1 and Z_2 at those frequencies is used as data support for the linear transformation to separate and estimate the parameters.

Calculation of the transformation formula

With two parameters to separate the system of equations (3) is reduced to:

$$a_1 \frac{\partial Z_1}{\partial x_1} + a_2 \frac{\partial Z_2}{\partial x_1} = 1 \frac{m^3 \Omega}{mol}, \quad (15)$$

$$a_1 \frac{\partial Z_1}{\partial x_2} + a_2 \frac{\partial Z_2}{\partial x_2} = 0 \frac{s \Omega}{m^2}. \quad (16)$$

Similar to equations (13) and (14) the required numerical derivative at the working point conditions can be obtained as:

$$\frac{\partial Z_1}{\partial x_1} = 3,1298 \cdot 10^5 \frac{m^3 \Omega}{mol}, \quad (17)$$

$$\frac{\partial Z_2}{\partial x_1} = 5,6343 \cdot 10^4 \frac{m^3 \Omega}{mol}, \quad (18)$$

$$\frac{\partial Z_1}{\partial x_2} = -1,0913 \cdot 10^3 \frac{s \Omega}{m^2}, \quad (19)$$

$$\frac{\partial Z_2}{\partial x_2} = 3,4387 \cdot 10^4 \frac{s \Omega}{m^2}, \quad (20)$$

Solving the system of equations (15, 16) results in the weighting factors $a_1 = 3,1769 \cdot 10^{-6}$ and $a_2 = 1,0082 \cdot 10^{-7}$.

To estimate the ion concentration $c_{x,est}$ the weighting factor a_1 has to be multiplied with the imaginary part of the impedance at 100 Hz and added to the imaginary part of the impedance at 1001 Hz multiplied with the weighting factor a_2 . The correct offset value can be calculated with equation 6.

$$\begin{aligned} x_{1,est} = c_{x,est} = & 3,1769 \cdot 10^{-6} \frac{mol}{m^3 \Omega} \cdot Im \{ Z_1 \} \\ & + \dots \\ & 1,0082 \cdot 10^{-7} \frac{mol}{m^3 \Omega} \cdot Im \{ Z_2 \} - 1,6973 \cdot \\ & 10^{-4} \frac{mol}{m^3} \end{aligned} \quad (21)$$

EVALUATION AND DISCUSSION

The evaluation of the procedure is performed by varying the ion concentration as well as diffusion coefficient by $\pm 50\%$ in steps of 1% of the working point value and subsequent calculation of one spectrum for each combination of those two values. Equation 21 was used to estimate the ion concentration out of the resulting 10201 spectra. The result of all 10201 estimations is plotted in 101 graphs in figure 3. The red dashed line represents the perfect estimation of the ion concentration with no systematic error. The strong change in the diffusion coefficient is affecting the estimation in a

very low degree and the 101 graphs nearly overlap each other perfectly. For a high variation of the ion concentrations the estimation error can reach large values due to the nonlinearity of the system and the linear approximation.

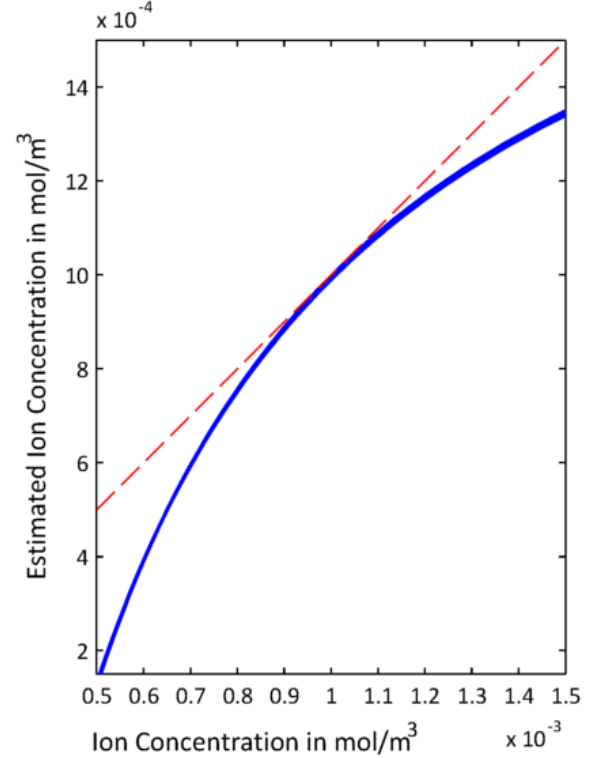


Fig. 3. Estimated ion concentration versus the true value for varying diffusion coefficients (blue graphs). An ideal estimation procedure would produce the red dashed line (red).

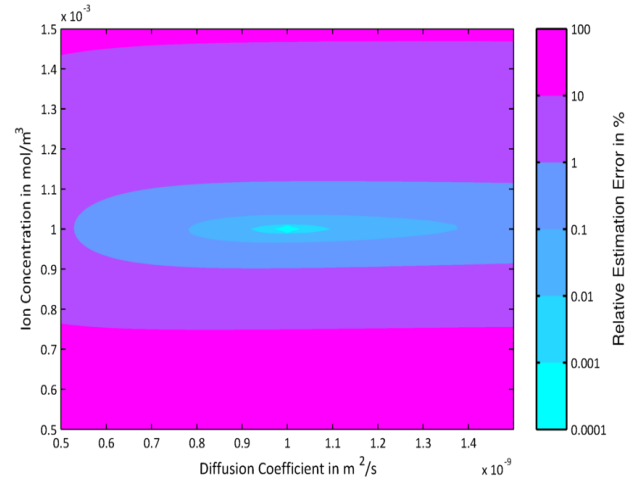


Fig. 4. Estimation error of the ion concentration relative to the actual input value.

Despite of the large error, figure 4 reveals an area with low relative estimation error in the proximity of the working point. In this area an estimation of the parameters can be performed successfully and used in control application or for tracking various aging effects.

REFERENCES

1. O. Kanoun, *Technisches Messen*, **7/8**, 73 (2006).
2. P. Büschel, U. Tröltzsch, O. Kanoun, *Electrochimica Acta*, **56**(23), 8069 (2011).
3. H.-R. Tränkler, O. Kanoun, „Paradigms for Improving Sensory Information using Multi-Sensor and Model-Based Sensor Systems“, IEEE International Conference on Systems, Signals & Devices (SSD'05), Tunisia, 2005.
4. R. J. Kauth, G. S. Thomas “The Tasselled Cap -- A Graphic Description of the Spectral-Temporal Development of Agricultural Crops as Seen by LANDSAT” LARS Symposia, 1976, p. 4B41.
5. J.G Liu, W.J Becker, T. Gerhold, W. Ricken, *Technisches Messen*, **67**(11), 484 (2000).
6. G.H.J Broers, M. Schenke, *Abhandlungen der sächsischen Akademie zu Leipzig*, **49**, 299 (1968).

ОЦЕНКА НА ЕФЕКТИВНИ ПАРАМЕТРИ НА СПЕКТРАЛНИ СЕНЗОРНИ ДАННИ ЧРЕЗ ЛИНЕЙНА ТРАНСФОРМАЦИЯ

Ф. Вендлер, П. Бюшел, О. Каноун

Технически университет Кемниц, 09107 Кемниц, Тюрингер Вег 11, Германия

(Резюме)

В тази публикация ние въвеждаме и оценяваме нов подход за решаване на обратими проблеми в близост до работна точка при твърде занижени изчислителни усилия. Нелинейната, мулти-параметрична, комплексна функция ще се апроксимира и инвертира с помоща на набор от взаимно несвързани монопараметрични линейни уравнения, изведени при анализ на чувствителността. Използваната линейна проекция концентрира знанието за предавателната характеристика на трансфер и осигурява алтернативен модел, основан на подхода; вижте табличните данни. Бързата оценка на множество параметри за ограничен кръг от параметри е подходящ способ при управление на приложения или за изследване на процесите на стареене и други дегенеративни процеси.

Comparative studies of polarizable dielectric fluids in yttrium-doped barium cerate by permittivity spectroscopy

E. Mladenova*, Z. Stoynov, D. Vladikova

Institute of Electrochemistry and Energy Systems, Bulgarian Academy of Sciences, 10, Acad. G. Bonchev St., Sofia 1113, Bulgaria

Received November 1, 2014; Revised April 4, 2015

This paper presents results from studies of processes and phenomena associated with the behavior of polar dielectric liquid (water and alcohol) in the non-polar proton conducting dielectric ceramic material yttrium doped barium cerate $\text{BaCe}_{0.85}\text{Y}_{0.15}\text{O}_{3-\alpha}$ (BCY15). The investigation was performed by Permittivity Spectroscopy which is a branch of the Impedance Spectroscopy especially tuned for measurements and analysis of dielectrics permittivity properties. The measurements were carried out in frequency range 1 MHz down to 0.01 Hz. A gigantic enhancement of the effective capacitance was observed above a certain level of wetting. The influence of the water is stronger than that of the alcohol, which is described with difference in their polarization ability. The results are explained with the formation of absorbed dipole film in the porous ceramic matrix. This phenomenon finds application in proton conducting solid oxide fuel cells.

Key words: permittivity spectroscopy, yttrium-doped barium cerate, impedance spectroscopy, gigantic enhancement of the real part of the complex capacitance, complex permittivity.

INTRODUCTION

Permittivity Spectroscopy is a branch of Impedance Spectroscopy which is tuned for measurement and analysis of dielectrics permittivity properties. In general permittivity is the ability of a space (free or filled with dielectric) to be polarized under external electric field. For some dielectrics this ability is the ground for their property to react on alternative current.

According to the general theory [1,2], dielectrics could be classified in three categories: (i) non-polarizable; (ii) polarizable and (iii) ionic crystals. Non-polarizable dielectrics do not contain dipoles. Polarizable dielectrics contain dipoles (primary or induced) which follow the orientation of an external electric field. When such a field is applied by external electrodes, the dipoles near the electrodes are oriented correspondingly and compensate the external electric field.

The pure capacitive impedance follows the dependence:

$$Z(i\omega) = -i(\omega C)^{-1}, \quad (1)$$

where C is the capacitance. For parallel plate capacitor, it can be expressed as [1-4]:

$$C = \frac{\varepsilon\varepsilon_0 S}{d}, \quad (2)$$

where ε is the relative dielectric permittivity and ε_0

is the permittivity of vacuum, S is the surface area of the capacitor electrodes and d is the distance between them.

Taking into account the polarization losses, when A.C. signal is applied, the relative permittivity can be expressed as a complex number [1,2]:

$$\varepsilon = \varepsilon' - i\varepsilon'', \quad (3)$$

where ε' and ε'' denote the real and the imaginary (loss factor) components of the complex value of ε . Applying equations (2) and (3), the capacitance can be also presented in a complex form:

$$C = C' - iC'' \quad (4)$$

If Eqn. 1 is expressed as admittance $Y(i\omega) = 1/Z(i\omega)$, then

$$Y(i\omega) = i\omega C = i\omega(C' - iC'') = \omega C'' + i\omega C'. \quad (5)$$

The real component $\omega C''$ in Eqn.5 can be regarded as dielectric conductivity [4], which can be expressed also as equivalent resistance $R = 1/\omega C''$ directly monitored by the instrument. It involves the energy dissipative effects as ohmic conductivity, dipole's reorientation losses in electric field and others. C'' is directly related to the dielectric permittivity, i.e. to the polarization ability.

In solid oxide fuel cells (SOFC) water is produced in the porous ceramic matrix of the anode, which has high ionic conductivity at operating temperatures. In several studies on

* To whom all correspondence should be sent:

E-mail: emiliya@bas.bg

yttria-stabilized zirconia (YSZ) based cermet anode a hypothesis for hydroxylation of the active anode surface caused by interaction of YSZ with the produced water is proposed [5-7]. It is expected that this process should improve the conductivity of the ceramic matrix. Thus studies of water behavior as a polarizable fluid in non-polarizable ceramic matrix are important for deeper insight into the mechanisms of SOFC operation. Permittivity spectroscopy can be a useful tool for experiments performed at room temperature where the ceramic matrix will behave as non-polarizable dielectric.

Yttrium-doped barium cerate $\text{BaCe}_{0.85}\text{Y}_{0.15}\text{O}_{3-\alpha}$ (BCY15) is one of the best electrolytes for proton conducting solid oxide fuel cells (PCFC). Recently, it was applied in a new SOFC design known as dual membrane fuel cell (dmFC) [8-10], in which water is produced in a separate compartment. It has mixed ion (proton and oxide ion) conductivity and porous structure, which ensures water formation and evacuation. Due to the discovered mixed ionic conductivity of BCY15 [11] the so called "monolithic" design was developed. It could be also very beneficial for operation in electrolyzer mode due to the separation of the steam from the two electrodes where hydrogen and oxygen are generated and evacuated. For deeper insight into the processes at the interface BCY/water, permittivity studies were performed for a first time on porous composite samples of proton conducting $\text{BaCe}_{0.85}\text{Y}_{0.15}\text{O}_{3-\alpha}$ (BCY15) and oxide ion conducting $\text{Ce}_{0.85}\text{Y}_{0.15}\text{O}_{1.925}$ (YDC15) as well as on BCY15 samples [12,13]. Our experimental results [12,13], registered gigantic enhancement of real component of capacitance C' at a certain level of watering. The effect is stronger for BCY15 samples, which was explained with hemisorption of water species followed by formation and organization of dipole film that covers the pores surface. Very probably the process starts as hydroxylation of the surface [14], preferably the BCY one, for which the dissociative absorption of water is a natural property [15]. This brings to the appearance of a longer-range interaction with volumetric group effect.

The purpose of this work is a deeper insight into the processes and phenomena in the system BCY/polar dielectric liquid combined with further improvements of the complex permittivity analysis. The study stresses on the influence of the polarizable dielectric on the behavior of the system. This investigation is an important step in the

optimization of the "monolithic" dmFC design for operation in reversible mode.

EXPERIMENTAL

The complex permittivity measurements were carried out on porous BCY15 sample with diameter and thickness respectively 2cm and 1,14mm and 33% porosity obtained with graphite as pore former and evaluated by mercury porosimetry and hydrostatic weighing.

BCY15 pellets stability in water has been tested by Differential Thermal Analysis and Thermogravimetry combined with Mass Spectroscopy in the temperature range 20-600°C. A good chemical stability has been observed [16]. The reproducibility and reversibility of the permittivity measurements confirmed the stability of the samples in the selected experimental conditions.

The complex permittivity measurements were performed on Solartron 1260 FRA in frequency range 1 MHz – 0.1 Hz at room temperature with amplitude of the signal 1V and density 5 points/decade. The experimental cell consists of two coaxial brass cylindrical electrodes with coplanar working surface.

The permittivity measurements were carried out first on dry membranes (with humidity equal to that of the ambient atmosphere), followed by a series of measurements with increasing quantity of the liquid introduced in the volume of the samples with a micropipette. Preliminary calibration measurements of pure liquid (water or ethanol) in spacer with the dimensions of the sample showed lack of frequency dependence [12].

The measured data are presented in C'/f or R/f plots, where f is the frequency [12]. The plot is very illustrative for registration of the investigated phenomena. It is used by other authors for studies of permittivity enhancement in ceramic dielectrics [14,17,18].

RESULTS AND DISCUSSION

The results from permittivity measurements of BCY15 sample with 33% porosity at different quantities of ethanol and water are presented in Fig.1. For dry samples a small increase of C' is observed below 1Hz. Having into account the strong affinity of BCY15 towards water, this increase could be caused by the ambient humidity. The effect of water on the enhancement of C' is stronger than that of ethanol – for one and the same sample the sharp increase of C' starts at 20 μ l water with enhancement of 3 orders, while for ethanol it

is observed at 60 μ l and the enhancement is only 10 times. This result is in agreement with the dielectric constant of the two fluids (82 for water and 25,5 for ethanol)[19], which reflects their polarization ability. The additional quantity of the two liquids increases slightly C' (Fig.2).

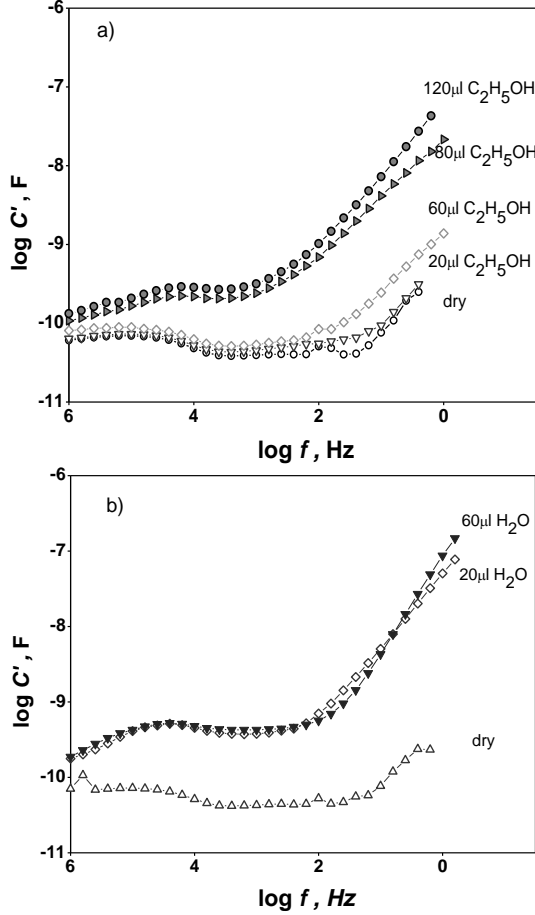


Fig.1. Permittivity measurements of BCY15 sample: a) frequency dependence of C' at different quantities of ethanol; b) frequency dependence of C' at different quantities of water

For elimination of the sample geometry and the influence of the experimental set-up, a dimensionless parameter, named coefficient of enhancement γ_i , was introduced:

$$\gamma_i = \frac{C'_i}{C'_0}, \quad (5)$$

where C'_i is the capacitance at a given frequency ω_i and C'_0 is the capacitance at the highest measured frequency (Fig. 2). Its frequency dependence for the measurements presented in Fig. 1 is given in Fig. 2.

For better presentation of the relation between the enhancement of C' and the microstructure of the ceramic the so called single-frequency analysis was introduced (Fig.3), where the quantity of the liquid is recalculated as percentage of the pores filling in

respect to the measured porosity; the coefficient of the enhancement is calculated at one and the same frequency - the lowest one where reliable results are observed for all the measurements. Results for γ_{4Hz} are presented in Fig.3.

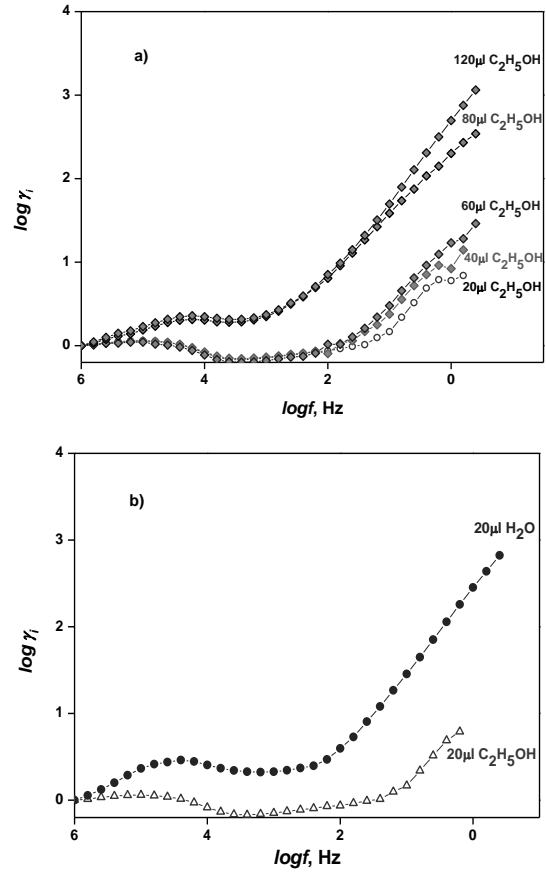


Fig.2. Frequency dependence of the coefficient of enhancement γ_i for BCY15 sample: a) frequency dependence of γ_i at different quantities of ethanol; b) frequency dependence of γ_i for one and the same quantity of water and ethanol

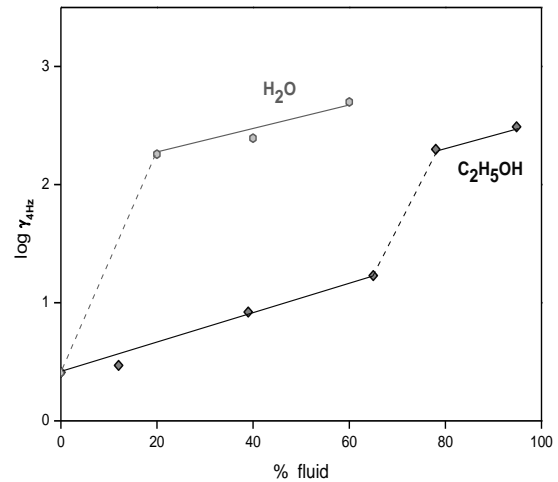


Fig.3. Single-frequency analysis of γ_i at $i = 4Hz$ for water \circ and ethanol \diamond .

CONCLUSIONS

The observed results confirm that the phenomenon gigantic enhancement of C' 's related to the interaction of the well developed hydrophilic ceramic surface with the polar dielectric liquid, which brings to the formation of liquid dipole layer (at elevated temperatures – semiliquid). The effect is stronger for the fluid with higher dielectric constant. This phenomenon should increase the conductivity of the ceramic matrix, which explains the enhanced oxide-ion conductivity of porous BCY15 in wet oxygen registered by impedance spectroscopy. The formation of electrochemically active volumetric hydroxylated layer can be of big importance for operation in electrolyzer mode.

In classical SOFC the water is produced in the porous anode. The developed methodology of complex permittivity could be a new tool for elucidation of water behavior in SOFC anodes. Some experiments on YSZ/Ni cermet are in progress.

REFERENCES

1. R. Coelho, *Physics of Dielectrics for the Engineer*, Elsevier Scientific Publishing Company, 1979.
2. V. Komarov, S. Wangand, J. Tang, in: Kris Parrish (ed.), *Encyclopedia of RF and Microwave Engineering*, John Wiley & Sons, 2005, p.1, DOI: 10.1002/0471654507.eme308
3. A. Cheetham, P. Day (eds), *Solid State Chemistry Techniques*, Clarendon, Oxford, 1988.
4. J. Nowotny, M. Rekas, *Key Eng Mater*, **66-67**, 45 (1992).
5. S. Raz, K. Sasaki, J. Maier, I. Riess, *Solid State Ionics*, **143**, 181 (2001).
6. M. Brown, S. Primdahl, M. Mogensen, *J Electrochem Soc*, **147**, 475 (2000).
7. N. Sakai, K. Yamaji, H. Negishi, T. Horita, H. Yokakawa, Y.P. Xiong, M. Phillips, *Electrochemistry*, **68**, 499 (2000).
8. A. Thorel, *France patent 0550696000* (2005).
9. A. Thorel, J. Abreu, S. Ansar, T. Brylewski, A. Chesnaud, Z. Ilhan, P. Piccardo, J. Prazuch, S. Presto, K. Przybylski, D. Soysal, Z. Stoynov, M. Viviani, D. Vladikova, *J. Electrochem. Soc.*, **160**, F360 (2013).
10. D. Vladikova, Z. Stoynov, G. Raikova, A. Thorel, A. Chesnaud, J. Abreu, M. Viviani, A. Barbucci, S. Presto, P. Carpanese, *Electrochem. Acta*, **56**, 7955 (2011).
11. <http://dx.doi.org/10.1557/opl.2011.1338>
12. Z. Stoynov, D. Vladikova, E. Mladenova, *J. Solid State Electrochem.*, **17**, 555 (2013).
13. Z. Stoynov, E. Mladenova, D. Levi, D. Vladikova, *Acta Chem. Slovenica*, **61**, 255 (2014).
14. C.K. Tan, G.K.L. Goh, W.L. Cheah, *Thin Solid Films*, **515**, 6577 (2007).
15. H. Iwahara, *Solid State Ionics*, **9**, 86 (1996).
16. K. Przybylski, J. Prazuch, T. Brylewski, R. Amendola, S. Presto, M. Viviani, in: D. Vladikova, Z. Stoynov (ed), *Proc. International Workshop Advances and Innovations in SOFCs 2 from Materials to Systems*, Katarino, Bulgaria, 2011 IEES, Sofia, 2011, p. 62.
17. M. Gökçen, O. Köysal, *Mater. Chem. Phys.*, **129**, 1142 (2011).
18. R. Schmidt, D. C. Sinclair, *Chem Mater*, **22**, 6 (2010).
19. D. Lide (ed), *CRC Handbook of Chemistry and Physics*. CRC Press, Boca Raton, 2004.

СРАВНИТЕЛНИ ИЗСЛЕДВАНИЯ НА ДИЕЛЕКТРИЧНИ ПОЛЯРНИ ФЛУИДИ В ИТРИЕВО ДОТИРАН БАРИЕВ ЦЕРАТ ЧРЕЗ ДИЕЛЕКТРИЧНА СПЕКТРОСКОПИЯ

Емилия Младенова*, Здравко Стойнов, Дария Владикова

Институт по електрохимия и енергийни системи "Акад. Е. Бudevски" – БАН, ул. "Акад. Г. Бончев", бл. 10, 1113, София, България

Постъпила на 1 ноември, 2014 г.; коригирана на 4 април, 2015 г.

(Резюме)

Представени са резултати от изследвания на процеси и явления, свързани с поведението на полярни диелектрични течности (вода и алкохол) в неполярен протон провеждащ керамичен материал - итриево – легиран бариев церат $\text{BaCe}_{0.85}\text{Y}_{0.15}\text{O}_{3-\alpha}$ (BCY15). Изследването е извършено с Диелектрична спектроскопия, която е клон на Импедансната спектроскопия, използвана за измервания и анализ на свойствата на диелектричната проникваемост. Измерванията се провеждат в честотен диапазон от 1 MHz до 0.01 Hz. Наблюдавано е гигантско нарастване на ефективния капацитет над определено ниво на омокряне на образците. Влиянието на водата е по-силно от това на алкохола, поради различната им поляризационна способност. Резултатите са обяснени с образуването на диполен абсорбционен филм в пористата керамичната матрица. Това явление намира приложение в протон-проводящи оксиди за твърдооксидни горивни клетки.

Comparative study on the proton conductivity of perfluorosulfonic and polybenzimidazole based polymer electrolyte membranes

S.G. Avramov^{1*}, E. Lefterova¹, H. Penchev², V. Sinigersky², E. Slavcheva¹

¹Acad. Evgeni Budevski Institute of Electrochemistry and Energy Systems, Bulgarian Academy of Sciences

“Acad. G.Bonchev” St. Block10, 1113 Sofia

²Institute of Polymers, Bulgarian Academy of Science, Acad. G.Bonchev St. Block 103A, 1113 Sofia

Received on October 24, 2014; Revised on September 9, 2015

Abstract: The polymer electrolyte membrane (PEM) electrolysis provides a sustainable solution for production of hydrogen with high purity. The most commonly used PEM, the perfluorosulfonic acid membrane (Nafion[®]), successfully works at temperatures up to 80 °C, however above 90-100 °C Nafion[®] it loses both conductivity and mechanical stability. Therefore, there is a need for development of PEM with different chemical structure capable to resist elevated temperatures. This work presents a comparative study on the properties of two commercial and three laboratory prepared PBI membranes applicable for preparation of membrane electrode assemblies for high temperature PEM water electrolysis. The proton conductivity is measured at temperatures up to 170 °C applying the method of impedance spectroscopy. It is found that the conductivity decreases in the order $\sigma_{\text{Celtec}^{\text{®}}\text{-P}} > \sigma_{\text{p-PBI}} > \sigma_{\text{m-PBI}} \geq \sigma_{\text{ABPBI}}$. The differences are discussed in connection with the polymer structure and type of proton transfer mechanism related to the polymer structure and PA doping level.

Key words: PEM, polybenzimidazole membrane (PBI), proton conductivity, high temperature water electrolysis

INTRODUCTION

Polymer electrolyte membrane (PEM) electrolyzers can operate at much higher current densities compared to classical alkaline electrolyzers achieving values above 2 A.cm⁻², while they reduce the operational costs and potentially, the overall cost of electrolysis [1]. The solid electrolyte also allows essential reduction of system dimensions, low gas crossover rate, and wide range of power input (economical aspect). The latter is due to the fact that the proton transport across the membrane responds quickly to the power input, not delayed by inertia as in low molecular liquid electrolytes. In the alkaline electrolyzers the hydrogen permeability through the diaphragm increases at high loads, yielding a larger concentration of hydrogen on the anode (oxygen) side thus, creating hazardous and less efficient conditions. In contrast with the alkaline electrolysis, PEM electrolysis cover practically the full nominal power density range [1,2]. One could speculate that PEM electrolysis could reach 100% of the nominal power density derived from a fixed current density and the corresponding cell voltage. This is due to the low permeability of hydrogen through Nafion (less than 1.25.10⁻⁴ cm³s⁻¹cm² for

Nafion[®] 117 at standard pressure, 80 °C and 2 mA.cm⁻²) [3].

In the recent years the high temperature PEM water electrolysis (HT-PEWE) operating in the temperature range from 100 to 200 °C has been recognized as a promising technology to meet the contemporary technical challenges since the increase in the operational temperature affects favorably the energy demand for the splitting of water to hydrogen and oxygen [4]. The realization of HT-PEWE is a driving force for developing of proton exchange polymer membranes capable to work at such severe conditions [3, 5]. The most critical issues beside the proton conductivity are the thermal, chemical and mechanical stabilities of the polymer materials at these elevated temperatures [6, 7].

Phosphoric acid doped polybenzimidazole (PBI) membranes have been investigated and successfully used in PEM fuel cells at elevated temperatures (HT-PEFC) because of their excellent thermochemical stability, low gas permeability, high mechanical stability and good proton conductivity [7, 8]. Since the chemical processes occurring in hydrogen PEM fuel cells and in water electrolysis are reversible, it is expected that the PBI membranes doped with phosphoric acid could work successfully also in HT-PEWE [9]. The number of commercial HT-PEM is very limited. At the same time there is an intensive research on developing of

* To whom all correspondence should be sent:

E-mail: stephan.avramov@gmail.com

new products with broad variations in their chemical composition [10].

This work presents a comparative study on the conductivity of two commercial products and three laboratory prepared polybenzimidazole based membranes dotted with phosphoric acid at broad range of experimental conditions (temperature, humidity, gaseous atmosphere).

EXPERIMENTAL

Membranes

The commercial products tested are Nafion[®] 117 (perfluorosulfonic acid) and Celtec[®]-P type (para-polybenzimidazole doped with H₃PO₄). It is well known that Nafion[®] 117 optimal working temperature is 80 °C and higher temperatures affect the mechanical stability and conductivity of this membrane [11]. The optimal working temperature of Celtec[®]-P according the literature is 160-170 °C [12]. In this study before measurements the Nafion[®] 117 membrane is activated in 0.05 M sulfuric acid using a standard activation procedure - boiling in 3% H₂O₂, rinsing in boiling water, then boiling in 0.5 M H₂SO₄, and finally rinsing in boiling water (at least 1 h for each step) [13]. The e Celtec[®]-P type membrane is dotted with 70% phosphoric acid and hold in special air free box,

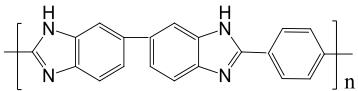
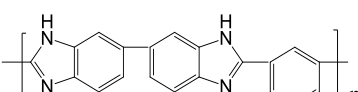
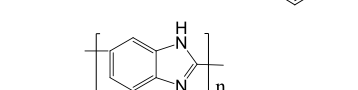
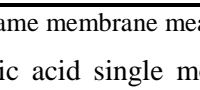
since long exposure in air leads to humidification changes of the phosphoric acid, affecting the membrane conductivity.

Three types of PBI based membranes poly[(2,2-(p-phenylen)-5,5-bisbenzimidazole), poly[2,2-(m-phenylen)-5,5-bisbenzimidazole] and poly(2,5-benzimidazole), denoted as p-PBI, m-PBI and ABPBI respectively were prepared and chemically modified. They differ in chemical structure of the building monomer (Table 1), the method of preparation, and the amount of the doping o-phosphoric acid (PA) inside the polymer electrolyte matrix [8].

The p-PBI membrane is prepared using 2% p-PBI solution from BASF, applying the sol-gel method developed by Xiao [14]. The solution is heated up to 200 °C under stirring and left for 72 hours at open air. The formed dry polymer film is immersed in 70% o-phosphoric acid for conditioning. Thus obtained p-PBI membrane contains 5 wt.% p-PBI and 95 wt.% of 70%PA and has an elastic module of 3.5MPa [15].

The ABPBI membrane is synthesized using a modified Eaton's reagent (8 wt% P₂O₅ in methane sulfonic acid) containing sulfuric acid.

Table 1. Conductivity of Celtec[®]-P and laboratory prepared PBI/PA membranes calculated from the impedance spectra measured at 160°C

Membrane	Structure of the building monomer	Conductivity [S.cm ⁻¹]			Ea [kJ.mol ⁻¹]
		Wet air 20%RH	Air 1st heat	Air 2nd heat	Air 2nd heat
Celtec [®] -P		0.24±0.02	0.22±0.02	0.19±0.01	14.2±0.2
p-PBI/PA		0.21*	0.19±0.01	0.13±0.01	21.1±0.2
m-PBI/PA			0.10±0.005	0.08±0.005	22.8±0.5
ABPBI/PA			0.09±0.006	0.08±0.005	20.6±0.4

*The conductivity of the same membrane measured from [21]

The 3,4- diaminobenzoic acid single monomer precursor is purified by a simple charcoal procedure. Then a thin film is spread using doctor blade technique and left to sol-gel transform in open atmosphere for 48h, washed with water and ammonia solution and dried at room temperature. The obtained dry polymer film is subsequently doped with 85% o-phosphoric acid.

The preparation of the m-PBI membrane is done identically by the described procedure for the ABPBI membranes with two different monomers –

diaminobenzidine and isophthalic acid used for the synthesis of meta-PBI in Eaton's reagent.

Test cell

The experiments are carried out in self-made test cell presented on Fig. 1. It consists of working chamber (Fig.1a) and a Teflon holder (fig. 1b). The temperature in the chamber can be precisely controlled from up to 200°C. The heater is

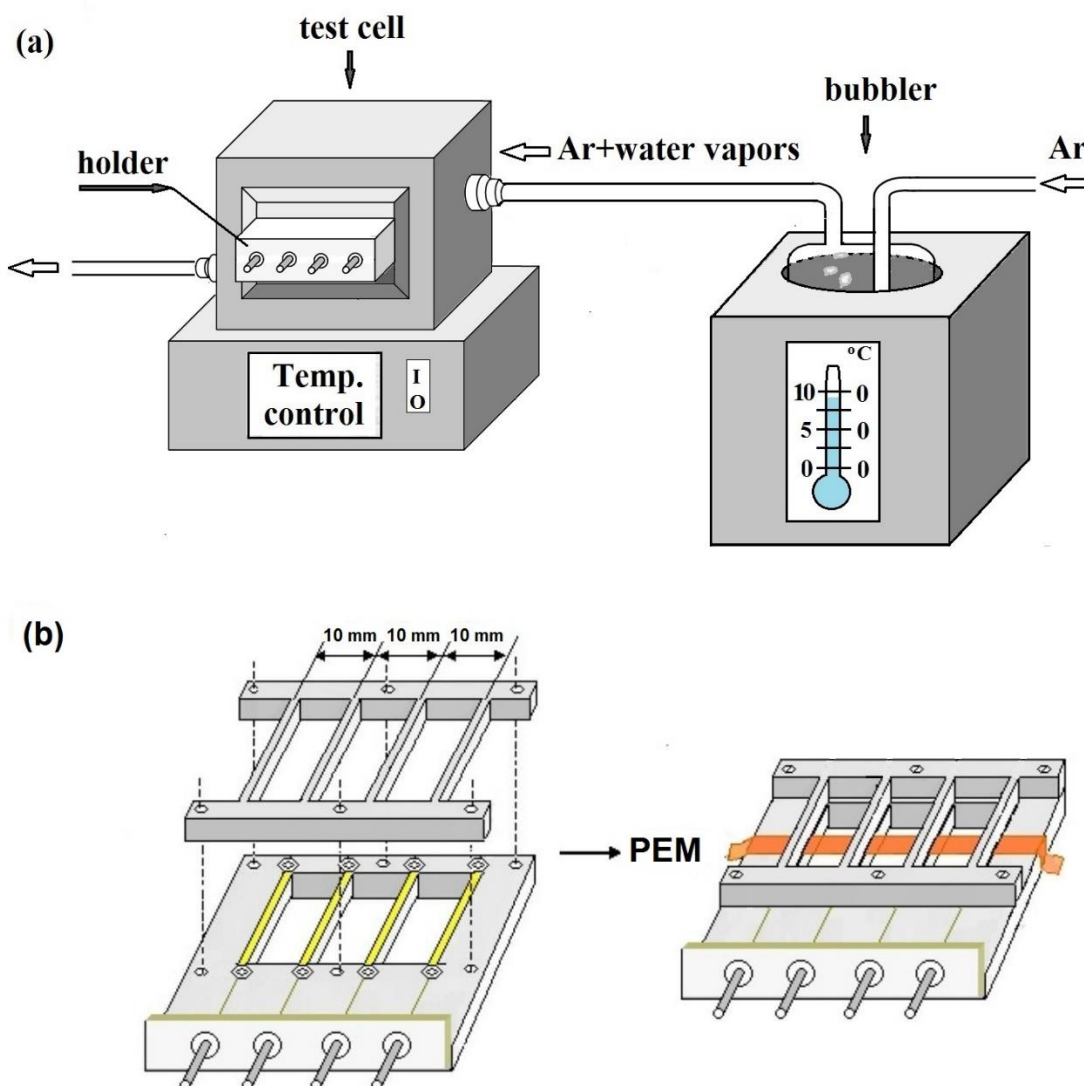


Fig.1. Laboratory test cell for measurement of polymer electrolyte membrane conductivity: a) working chamber with temperature controller; b) membrane holder with sensing contacts/electrodes.

designed as a non-inductive bifilar winding to avoid disturb on impedance measurements. The humidity in the cell is ensured by flow of argon passing through heated water bubbler and controlled by the temperature.

The design of the Teflon holder ensures maximum contact with the gaseous flow, i.e. maximum humidification of the measured membrane. Two, three or four sensing contacts/electrodes are located on the holder, giving a possibility to use 4-probe method or to test different sections of the membrane as well as of samples with different length (1, 2, and 3 cm) by 2-electrode scheme.

Conductivity measurements

The characterization of the membranes is performed by impedance spectroscopy, using Phase

Sensitive Multimeters Newtons4th Ltd. PsimetriQ-PSM1700 equipped with Newtons4th Impedance Analysis Interface (IAI). The measurements are carried out in the frequency range 1MHz-1Hz with sampling rate of 10 points per decade, and ac amplitude ≤ 100 mV. The conductivity is calculated from the determined resistance using the equation:

$$\sigma = \frac{l}{Rdw} \quad (1)$$

where σ is the membrane conductivity, l - the length between the electrodes, R - the membrane resistance, d - the membrane thickness, and w - the membrane width.

RESULTS AND DISCUSSIONS

Commercial membranes

To get consistent results for the newly developed PBI membranes, the reliability of the

developed test cell and the measuring procedure is verified, measuring the proton conductivity of two commercial products with well-known characteristics, namely the Nafion[®] 117 and Celtec[®]-P membranes. Different test procedures are applied. The first one consists of gradual increase of temperature from 25 °C at high levels of humidity (RH=95% at 100°C and RH ≈20% at 160-170 °C) and recording of the impedance spectrum stepwise at different temperatures. Figure 2 presents the Nyquist plot of Nafion[®] 117 and Celtec[®]-P at room temperature. The Nyquist plot consists of part of semicircle in the high frequency range and characteristic spike due to diffusion and polarization in the low frequency range. The resistance of the membranes (R) is determined by the low frequency intersection of the semicircle with Z_{re} axis as pointed (the arrows in fig. 2).

The conductivity is not a monotonic function of the temperature for both type of membranes (fig. 3). Initially the conductivity of Nafion[®] 117 increases with temperature, reaches maximum value 0.13 S.cm⁻¹ around 60°C, and then decreases to 0.11 S.cm⁻¹ at 80 °C. The proton conductivity is a function of both temperature and membrane water content

(water content is defined as the molar ratio of water molecules per SO₃H⁻ group) [16,17]. Reike and Vanderborgh have established that at the decrease in the conductivity at temperatures above 60 °C is not related with the starting drying process since the water content is still high enough. Using FTIR they have showed that at these temperatures fractions of the sulfonic acid groups are no longer ionized and do not participate in the proton transfer which results in decrease of membrane conductivity [16].

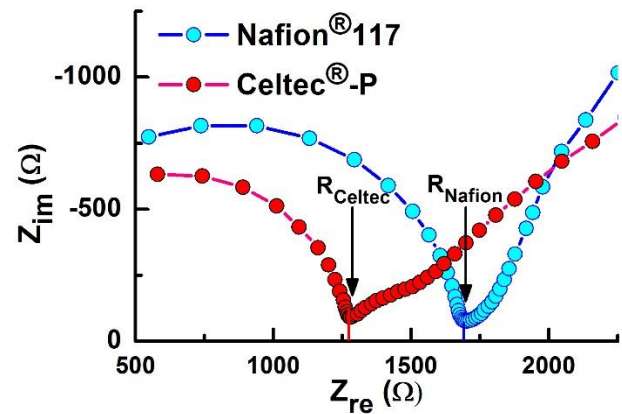


Fig. 2. Impedance Nyquist plot of commercial membranes Nafion[®] and Celtec[®]-P at room temperature

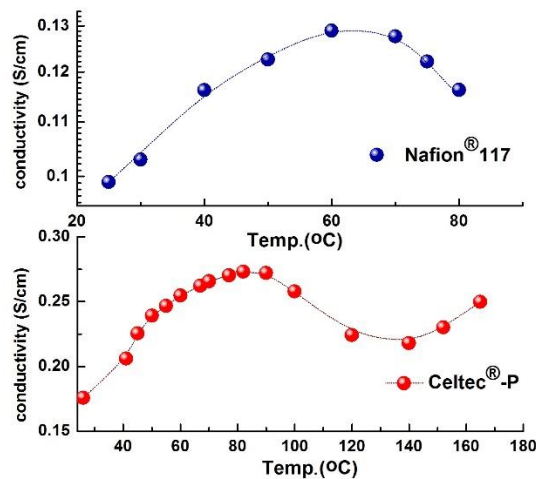


Fig. 3. Temperature dependence of the conductivity of Nafion[®] 117 and Celtec[®]-P.

With the increase of temperature the conductivity of Celtec[®]-P membrane reaches maximum value of 0.27 S.cm⁻¹ around 90°C, then decreases to passes through a minimum ($\sigma=0.22$ S.cm⁻¹ around 140°C, and begins to increase again reaching 0.24 S.cm⁻¹ at 160 °C (Fig 3).

The second series of tests is carried out at constant temperature (80°C and 170 °C for

Nafion[®] 117 and Celtec[®]-P, respectively). Once it is reached, the humidification flow in the chamber is interrupted and a dry Ar flow is introduced in the chamber. The results obtained are compared in fig.4. They show that as soon as the dry argon is delivered in the test chamber, the conductivity of Nafion[®] 117 decreases dramatically. In contrast, after an initial decrease the conductivity of Celtec[®]

P stabilizes at $0.11 \text{ S}\cdot\text{cm}^{-1}$ which is a very good value for dry condition.

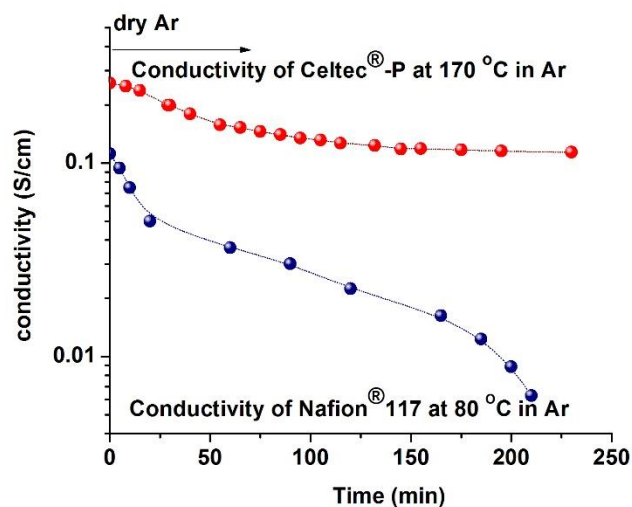


Fig.4. Time dependence membranes conductivity, calculated from the impedance spectra in dry Ar of Nafion® 117 at 80 °C and Celtec®-P at 170 °C.

These results are consistent with the conductivity values for both commercial membranes reported in the literature for Nafion® 117 [16, 19, 20] and Celtec®-P [21]. They are logical and expected since the proton conducting mechanism for both membranes is completely different. In the case of Nafion® 117 the transport of protons requires presence of superacid polymer electrolyte/water clusters in the volume of the membrane. The proton transport occurs by a vehicle mechanism, in which the water molecules forming hydronium ions carry the protons to the adjacent sulfonic sites. In the absence of water, i.e. under dry conditions or above temperatures of 80 °C, the predominant proton transport mechanism is direct hopping between sulfonic sites and Nafion® conductivity decreases significantly. In Celtec®-P the protons move predominantly through the phosphoric acid H-bond intermolecular network (at high PA doping levels) and partially through the PBI N-heterocycles of the polymer chains. The transport in this type of membranes is dominated by the so called proton hopping (Grotthuss) mechanism [18].

Laboratory prepared membranes

It has been verified that while Nafion® 117 is efficient at high humidity, the experiments PBI-based membrane Celtec®-P performs very well at low humidity. Therefore, the the con laboratory prepared p-PBI, m-PBI and ABPBI membranes together with Celtec®-P are further tested in an

open system (i.e. in air) without additional moistening. The experiments are carried out in the temperature range 25÷170°C. The obtained conductivity-temperature dependencies are presented in Fig. 5. The as prepared membranes at room temperature contain some amount of adsorbed water which with heating gradually evaporates. The leakage of that absorbed water in turn, influences the conductivity of the membranes (Fig. 5a). To avoid this inconsistency in the test conditions, a second series of measurements is performed immediately after the first one as the temperature was changed in opposite direction cooling down the system gradually from 160 °C to – form of the test samples measurements. These results are presented in (fig. 5b). For comparison, the values of the proton conductivity calculated from both sets of impedance spectra are summarized in Table 1. As it is seen the conductivity decreases in the order $\sigma_{\text{Celtec}^{\circledR}\text{-P}} > \sigma_{\text{p-PBI}} > \sigma_{\text{m-PBI}} \geq \sigma_{\text{ABPBI}}$. The best result among the laboratory prepared samples is obtained for p-PBI membrane, however its proton conductivity is lower compared to that of the commercial Celtec®-P membrane. The values for m-PBI and ABPBI at 160 °C are close to those obtained by Choi et.al. ($\sigma_{\text{m-PBI}}=0.0951 \text{ S}\cdot\text{cm}^{-1}$ and $\sigma_{\text{ABPBI}}=0.0832 \text{ S}\cdot\text{cm}^{-1}$ [22]).

The mechanism of proton conductivity can be recognized from the temperature dependence [23-25]. Since the PBI membranes possess high glass transition temperature (T_g), the dependence of

conductivity on temperature should obey the Arrhenius equation:

$$\sigma = \frac{\sigma_0}{T} \exp\left(-\frac{E_a}{RT}\right), \quad (2)$$

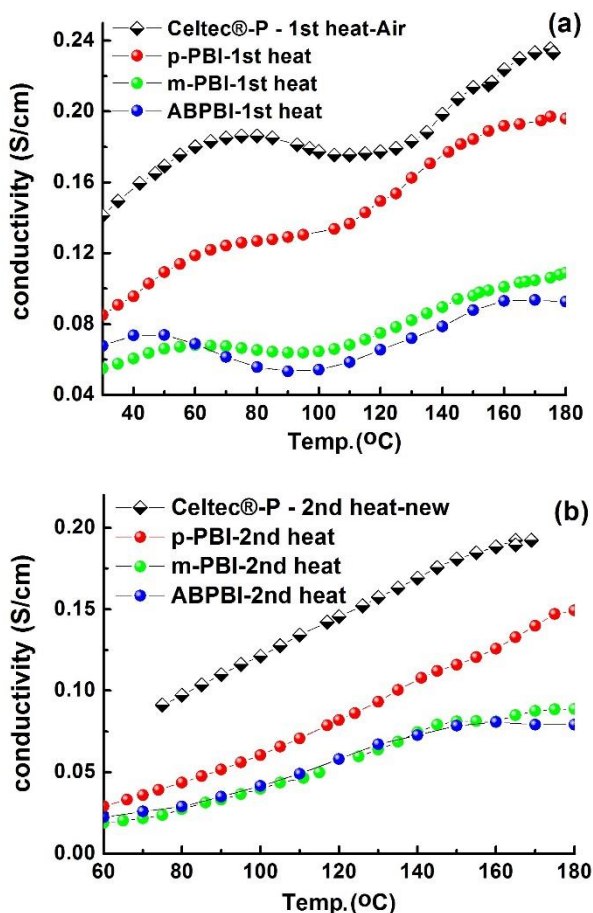


Fig. 5. Temperature dependence of conductivity of Celtec®-P and laboratory prepared PBI-membranes, in air: (a) first heat; (b) second heat.

where σ is the conductivity, σ_0 is a pre-exponential factor, E_a - activation energy, R - the gas constant and T - the absolute temperature.

The results presented in Fig. 6 confirm this assumption. The linearity of the Arrhenius plot $\ln(\sigma T)$ vs T^{-1} sustains in wide temperature range (up 150°C) for the all membranes tested. This means that the proton transport is controlled by the hopping mechanism. Using a linear fit, the activation energies are determined from the slope of PBI-membrane compared to Celtec®-P mean that a higher potential barrier is needed for the proton transfer which in turn, results in lower conductivity of this membrane, despite the almost equal amount of doping PA in both samples. The explanation of this difference should be sought in the structural variation of the membranes. On the other hand, the difference in the calculated activation energies of the three laboratory prepared PBI membranes under study are comparatively low, suggesting that the

mechanism of ion transport is the same. Hence, it can be concluded that the difference in the conductivity is mainly due to the different levels of PA doping. Over 150°C a deviation from Arrhenius dependence is observed. It is connected to dehydration of the phosphoric acid, formation of pyrophosphoric acid ($H_4P_2O_7$), and in result, to drop in the membrane conductivity.

As mentioned before the proton transport in PBI membranes is dominated by the hopping Grotthuss mechanism. According to Ma [26], the conductivity in these type membranes is realized by proton hopping through paths via different hydrogen bonds, depending on different factors such as the doping level, RH, and temperature. At high acid doping

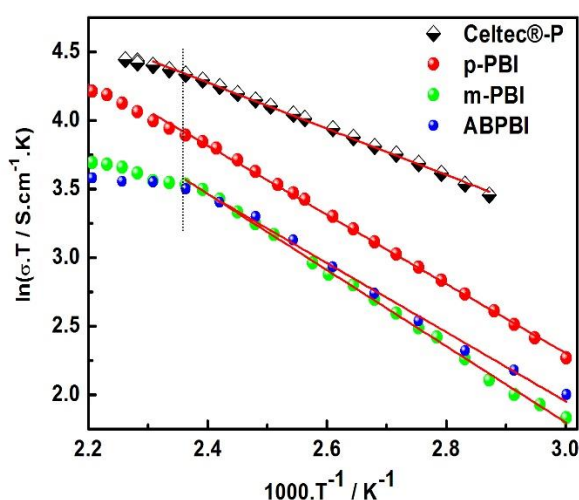


Fig. 6. Arrhenius plot: $\ln(\sigma.T)$ vs. $1/T$ of Celtec®-P and laboratory prepared PBI-membranes.

level and water content and/or at high humidity, the protons are hopping through acid-water path ($H_3PO_4 \dots H-O-H \dots H_2PO_4^-$) and phosphoric acid chains ($H_3PO_4 \dots H_2PO_4^-$) as the former path dominates. This correlates with the measured highest conductivity of Celtec®-P, in wet Argon, as well as with the higher conductivity of the first scan of the impedance with the increasing temperature, where water is still present in the membranes. At low RH or dry conditions, there is deficiency of hydrogen bonds, i.e. of donor/acceptor pairs and the main proton transport is carried out through the phosphoric acid chains i.e. path ($H_3PO_4 \dots H_2PO_4^-$) with small contribution of the ($N-H^+ \dots H_2PO_4^-$) path, which results in decrease of conductivity. The calculated value of E_a for Celtec®-P is close to that of the pure H_3PO_4 [25], suggesting that the protons hop through the long phosphoric acid chains ($H_3PO_4 \dots H_2PO_4^-$). The higher activation energies of the laboratory prepared PBI/PA membranes could be explained with the shorter phosphoric chains, interrupted from $N-H^+ \dots H_2PO_4^-$ and $N-H^+ \dots N-$

H⁺... bonds. Thus, the observed differences in the conductivity of the polymer electrolyte membranes under investigation can be explained with the type of the ion transport determined by the polymer structure as well as the acid doping level.

CONCLUSIONS

The performed comparative study on proton-conductivity of polymer electrolyte membranes (perfluorosulfonic acid Nafion[®] and a polybenzimidazole based membrane dotted with phosphoric acid Celtec[®]-P) and three laboratory prepared PBI based samples (p-PBI, m-PBI, and ABPBI) demonstrated that the applied testing procedure based on electrochemical impedance measurements is a reliable approach for screening and preselection of various type of polymer. The results obtained showed that the conductivity of the home prepared p-PBI, m-PBI and ABPBI membranes are comparable with the best commercial product of that type available on the market and could be used for preparation of membrane electrode assemblies.

The best performance of 0.19 S.cm⁻¹ at 160 °C and very good stability at elevated temperatures without degradation showed the p-PBI membrane, which is considered as the most perspective for practical applications in HT- PEM water electrolysis.

Acknowledgements. The work is partly supported by Bulgarian Ministry of Education and Science, NSF, Contr. No. E02/2.

REFERENCES

1. J. Lobato, P. Cañizares, M. A. Rodrigo, J. J. Linares, *Electrochimica Acta*, **52**, 3910 (2007).
2. M. Boaventura, A. Mendes, *Int. J. Hydrogen Energy*, **35**, 11649 (2010).
3. M. Carmo, D.L. Fritz, J. Mergel, D. Stolten, *Int. J. Hydrogen Energy*, **38**, 4901 (2013).
4. Y. Zhai, H. Zhang, D. Xing, Z. Shao, *J. Power Sources*, **164**, 126, (2007).
5. Q. Li, J. O. Jensen, R. F. Savinell, N. J. Bjerrum, *Prog. Polymer Sci.*, **34**, 449 (2009).
6. A.V. Nikiforov, A.L. Toma's Garcı'a, I.M. Petrushina, E. Christensen, N.J. Bjerrum, *Int. J. Hydrogen Energy*, **36**, 5797 (2011).
7. S. Bose, T.Kuila, T.Nguyen, N. Kimc,K. Lau, J. Lee, *Prog. Polymer Sci.*, **36**, 813 (2011).
8. S. Subianto, *Polym. Int.*, **63**, 1134 (2014).
9. D. Aili, M.K. Hansen, C. Pan, Q. Li, E. Christensen, J. Jensen, N. Bjerrum, *Int. J. Hydrogen Energy*, **36**, 6985 (2011).
10. M. K. Hansen, D. Aili, E. Christensen, C. Pan, S. Eriksen, J. Oluf Jensen, J.H. von Barner, Q. Li, N.J. Bjerrum, *Int. J. Hydrogen Energy*, **37**, 10992 (2012).
11. V. Antonucci, A. Di Blasi, V. Baglio, R. Ornelas, F. Matteucci, J. Ledesma-Garcia, L.G. Arriaga, A.S. Aricò, *Electrochimica Acta*, **53**, 7350 (2008).
12. G. Alberti, M. Casciola, L. Massinelli, B. Bauer, *J. Membr. Sci.*, **185**, 73 (2001)
13. Z. Lu, G. Polizos, D. D. Macdonald, E. Manias, *J. Electrochem. Soc.*, **155**, 163 (2008).
14. L.X. Xiao, H.F. Zhang, E. Scanlon, L.S. Ramanathan, E.W. Choe, D. Rogers, B.C. Benicewicz, *Chem. Mater.*, **17**, 5328 (2005).
15. M. Staneva, D. Budurova, F. Ublekov, I. Radev, H. Penchev, V. Sinigersky, *J. Chem. Eng. Chem. Res.*, **1**, 15 (2014).
16. P. C.Reike, N. E. Vanderborgh, *J. Membr. Sci.*, **32**, 313 (1987)
17. T. A. Zawodzinski Jr., T. E. Springer, F. Urlbe and S. Gottesfeld, *Solid State Ionics*, **60**, 199 (1993).
18. N. Agmon, The Grotthuss mechanism, *Chem. Phys. Lett.* **244**, 456 (1995).
19. V. Neburchilov, J. Martin, H. Wang, J. Zhang, *J. Power Sources*, **169**, 221, (2007)
20. S. Slade, S.A. Campbell, T.R. Ralph, F.C. Walsh, *J. Electrochem. Soc.*, **149**, A1556-(2002).
21. F. Ublekov, H. Penchev, V. Georgiev, I. Radev, V. Sinigersky, *Materials Letters* **135**, 5 (2014)
22. S.-W. Choi, J. Park, C. Pak, K.Choi, J.-C. Lee, H. Chang, *Polymers*, **5**, 77 (2013)
23. H. Pu, W.H. Meyer, G. Wegner, *J. Polymer Sci.: Part B: Polymer Physics*, **40**, 663 (2002)
24. J. Zhang, Y. Tang, C. Song, J. Zhang, *J. Power Sources*, **172**, 163 (2007)
25. R. He, Q.Li, G. Xiao, N.J. Bjerrum, *J. Membr. Sci.*, **226**, 169 (2003).
26. Y.-L. Ma, J. S: Winright, M.H. Litt, R.F. Savinell, *J. Electrochem. Soc.*, **A8**, 151 (2004).

СРАВНИТЕЛНО ИЗСЛЕДВАНЕ НА ПРОТОННАТА ПРОВОДИМОСТ НА
ПЕРФЛУОРОСУЛФОНИРАНИ И ПОЛИБЕНЗИМИДАЗОЛ БАЗИРАНИ ПОЛИМЕРНИ
ЕЛЕКТРОЛИТНИ МЕМБРАНИ

С.Г. Аврамов¹, Е. Лефтерова¹, Х. Пенчев², В. Синигерски², Е. Славчева¹

¹Институт по електрохимия и енергийни системи "Акад. Е. Будевски" (ИЕЕС) - БАН, ул. "Акад. Г. Бончев" 10, 1113, София, България

²Институт по полимери - БАН, ул. "Акад. Г. Бончев" 103А, 1113, София, България

Постъпила на 10 октомври 2014 г.; Коригирана на 9 септември 2015 г.

(Резюме)

Електролизата на вода в клетки с полимерна електролитна мембрана (ПЕМ) осигурява производство на водород с висока чистота. Най-често използваната ПЕМ, перфлуоросулфонова мембрана (Nafion®), успешно работи при температури до 80 °С. Над 90-100 °С тя губи както проводимостта, така и механичната си стабилност. Следователно, съществува необходимост от разработването на ПЕМ с различна химична структура, устойчива на по-високи температури. Тази статия представя сравнително изследване на протонната проводимост на две търговски и три лабораторно подготвени полибензимидазол (ПБИ) базирани мембрани, приложими за високотемпературна ПЕМ електролиза на вода. Проводимостта е измервана при температури до 170°C с импедансна спектроскопия и е установено, че намалява в реда Celtec®-P>p-PBI>m-PBI≥ABPBI. Разликите са обсъдени в контекста на механизма на протонния трансфер, свързан със структурата на полимера и степента на дотиране с фосфорна киселина.

Proceedings of the Sofia Electrochemistry Days

Pravetz, Bulgaria, June 10, 2015

Visiting editor:

A.Stoyanova

Surface morphology and corrosion behavior of zinc and zinc composite coatings with Cr(III) based conversion films

N.D. Boshkova¹, P.D. Petrov², V. Chukova³, L.Lutov³, S.D. Vitkova¹, N.S. Boshkov^{1*}

¹*Institute of Physical Chemistry, Bulgarian Academy of Sciences, Sofia, Bulgaria*

²*Institute of Polymers, Bulgarian Academy of Sciences, Sofia, Bulgaria*

³*University of Sofia, Department of Chemistry and Pharmacy, Blvd J. Boucher No.1, Sofia, Bulgaria*

Received October 14, 2015; Revised February 2, 2016

The results concerning the obtaining of protective conversion films (CF) on zinc and zinc composite coatings from environmentally friendly solutions are demonstrated and commented. The newly obtained CF are based on the application of ammonium-Cr(III) salt with oxalic acid - ammonium tris (oxalato) chromate [III] –(ATOC). Depending on its concentration as well on the immersion time three types of CF can be obtained – transparent, light-green and gray-black colored which differ in their corrosion resistance and protective properties. The latter are estimated in a neutral corrosion medium of 3% NaCl containing chloride ions as corrosion activators and leading in general to appearance of local corrosion. The protective ability of CF is investigated by using of polarization resistance measurements and neutral salt spray chamber test. Their surface morphology is characterized with SEM.

The composite zinc coatings contain embedded core-shell type stabilized polymeric micelles (SPMs, based on poly-propylene oxide and poly-ethylene oxide). The influence of the SPMs incorporated in the metal matrix on the surface morphology and on the corrosion behavior of the obtained CF is commented on and discussed.

Key words: composite coatings, conversion films, corrosion, zinc, stabilized polymeric micelles

INTRODUCTION

Zinc is a metal that is not widespread in the earth crust and its content is about 0,007 wt.%. However, the electrogalvanized zinc coatings find significant application on an industrial scale for corrosion protection of different parts, components and structures of steel. Zinc coatings are relative stable at atmospheric conditions and their corrosion rate is the lowest in the pH range 7 – 12. Under the influence of environment and in the presence of moisture this metal is covered with a layer of the so called “white rust” the latter consisting of different corrosion products depending on the medium – for example zinc hydroxide chloride, zinc oxide, zinc hydroxide, zinc hydroxide sulfates. This layer has in general barrier properties and impedes the penetration of the corrosion agents deeply inside.

The electrodeposition of Zn coatings on steel substrates is applied since the zinc is a sacrificial coating due to its more negative potential compared to the iron or steel substrate. However, its safe exploitation is relative limited due to the aggressive nature of environment containing industrial pollutants which demonstrates the need of additional efforts to improve its protective properties[1-14].

One possible way is to electrodeposite zinc composite coatings the latter containing incorporated metallic, non-metallic, polymeric particles etc., which method is often applied in the last decades in many industrial sectors[15-17]. In general, such coatings exhibit high corrosion resistance [15-19]. Another method is the alloying of Zn with metals like Mn, Co, Ni etc., but the protective characteristics of these galvanic alloys also need additional improvement especially in aggressive media.

The lifetime of the galvanized steel is significantly prolonged by application of different post-treatment, for example, short-time immersion in special developed chemical solutions for obtaining of conversion films (CF) like chromite (Cr³⁺) ones[20-22]. They show lower susceptibility against aggressive corrosion solutions and can be a basis for further treatment with organic paints. Their color and thickness can be altered by variation of the solution composition, pH value, temperature, immersion time.

The aim of the present work is to obtain appropriate solutions for conversion films on zinc and composite Zn coatings, to characterize and evaluate their protective parameters in selected model corrosion medium and to estimate the surface peculiarities of these layers.

To whom all correspondence should be sent:
E-mail: NBoshkov@ipc.bas.bg

EXPERIMENTAL

Sample preparation

The investigated samples are electrodeposited on a low carbon steel substrate with sizes 20 x 10 x 1 mm, whole surface area of 4 cm² and coating thickness of approximately 12 μm. Deposition conditions: current density of 2 A/dm²; room temperature – 22 °C; metallurgical zinc anodes.

Galvanic coatings

Zinc coatings are electrodeposited from electrolyte with a composition 150 g/l ZnSO₄·7H₂O, 30 g/l NH₄Cl, 30 g/l H₃BO₃, additives AZ-1 (wetting agent) - 50 ml/l and AZ-2 (brightener) - 10 ml/l, pH value 4,5–5,0.

Composite zinc coatings

These coatings are electrodeposited from the same electrolytes and at the same electrodeposition conditions described above with an addition of 1g/l of powdered stabilized nano-sized polymeric micelles (SPMs) based on PEO₇₅PPO₃₀PEO₇₅ (polyethylene oxide – poly-propylene oxide – polyethylene oxide) tri-block copolymer. PPO is the hydrophobic core and the PEO is the hydrophilic shell of the SPMs.

Stabilized polymeric micelles (SPMs)

The procedure for preparation of the SPMs includes the formation of core-shell type micelles in aqueous media at 60 °C followed by UV-induced polymerization leading to the formation of a semi-interpenetrating polymer network [23].

Solutions for chemical treatment/passivating

The additional surface treatment of Zn and composite coatings is carried out by usage of three solutions with different chemical composition based on the application of ammonium-Cr(III) salt with oxalic acid - ammonium tris (oxalato) chromate [III] – (ATOC) presented in Table 1.

The surface layer of the chromite films appeared on the metal surface after a short-time immersion of the sample is transparent-, gray-black- or light green-colored dependent on the ATOC concentration, pH value and immersion time. The latter varies from 30 seconds up to about 1 minute and the obtained CF has a thickness of about 200–300 nm. The concentration of the main components demonstrated in Table 1 is given in definite limits since the quality of the obtained films varies depending on some functional parameters like color, adhesion etc.

The obtained CF-s are ready for corrosion treatment after 24 h stay – the so called “time for ripening of the films”. During this period the latter become more hard, hydrophobic and wear-resistant.

Table 1. Composition of the passivating solutions for obtaining of CF-s

Chromite film	Components	Amounts
Transparent CF	ATOC	5,0– 15,0 g/l 0 -1,2 g/l up to pH 1,6 – 2,0
	Co ²⁺	
	HNO ₃ (50%)	
Gray-black CF	ATOC	10,0– 20,0 g/l 1,0 - 2 ,0 g/l 0 –10,0 ml/l up to pH 1,6 - 1,7
	AgNO ₃	
	H ₃ PO ₄	
	HNO ₃ (50%)	
Light-green CF	ATOC	10,0– 20,0 g/l 50,0 – 65,0g/l up to pH 1,7 – 2,0
	Na ₂ S ₂ O ₅	
	HNO ₃ (50%)	

In all cases the pH value of the solutions is corrected by using of different HNO₃ amounts in order to improve the adhesion of the conversion films to the zinc. The samples are also prior immersed for several seconds in a 0,2% HNO₃ solution for “activating” of the surface and thereafter rinsed with distilled water.

Corrosion medium and reproducibility

A model corrosion medium of 3% NaCl solution with pH 6.7 at ambient temperature of about 25°C is used. The results from the electrochemical investigations are in average of 5 samples per type i.e. for each measurement 5 replicates of Zn or its composites. Aiming at receiving of better reproducibility prior to the polarization resistance test all samples are temporized for a definite period in the model medium at conditions of open circuit potential (OCP).

Sample characterization

The sample characterization is realized by using of the following methods:

- Polarization resistance (Rp) – the measurements are carried out for a test period of about 300 hours with “Corrovit” equipment in the range of ±25 mV relative the corrosion potential. From the Stern–Geary equation [24] it is known that higher Rp value (in Ω·cm²) corresponds to higher corrosion resistance and to lower corrosion rate;

- Neutral salt spray (NSS) chamber – the investigations are conducted in compliance with the requirements of BDS EN ISO 9227: 2012 and ASTM B-117-03 by application of “Heraeus-Vötsch” corrosion chamber, Germany. Corrosion medium was pulverized NaCl solution at pH 6,5 – 7,2 and temperature of 35 ± 2 °C. During the testing the time for appearance of the so called “white rust” (corrosion of the coating – Zn or composite zinc with CF) or “red rust” (corrosion of the steel substrate and diffusion of iron ions as a result of the degradation process) as well as the change of the surface area damaged by the corrosion can be registered.

The evaluation of the conversion coatings is presented in estimation marks according to BDS 15258-81, method C (for cathodic coatings) in the case when the “white rust” is estimated. The degree of the surface damages (in %) is brought into relevant estimation mark. For example, mark 10 means that the coating is without damages; 8 means that the damaged surface area is between 0,25 - 0,5%; 6 – between 1 and 2%; 1 – between 32 and 64%; 0 - the coating does not fulfill its protective functions any more.

The “red rust” is estimated according to BDS 15258-81, method B (for anodic coatings) and also in estimation marks: mark 10 means without damages; 9 – damaged surface (red spots) occupy up to 1% from the sample surface; 8 – damaged surface is between 1 and 2,5% from the whole surface; 6 – between 5 and 10%; 4 – over 30%. It is assumed that below estimation mark 4 the substrate is so heavily damaged from the corrosion that it is practically unusable.

- Scanning electron microscopy – the surface morphology of the samples is investigated by using of INCA Energy 350 unit.

All electrochemical measurements are performed in a common three-electrode cell (volume of 250 ml). The ohmic resistance of the corrosion medium is minimized by application of a Luggin-capillary. Platinum plate is taken for a counter electrode and the potentials are measured with respect to the saturated calomelectrode (SCE).

RESULTS AND DISCUSSION

Obtaining of ammonium oxalate chromium (III) complex

The crystals of ammonium tris (oxalato) chromate are thin elongated prisms and have a monoclinic structure. Their color varies. The three oxalate groups of the complex ion are planar while the three inner oxygen atoms form octahedral

surrounding with a central Cr atom – Figure 1. The crystals lose water in a dry atmosphere and absorb water in a humid air.

For obtaining of ATOC initially definite amounts of $\text{H}_2\text{C}_2\text{O}_4 \cdot 2\text{H}_2\text{O}$ are mixed with $(\text{NH}_4)_2\text{C}_2\text{O}_4 \cdot \text{H}_2\text{O}$ in a minimal water amount. The appearing suspension is slowly stirred with saturated solution of ammonium dichromate leading to the final product – violet crystals. The latter are dried at room temperature.

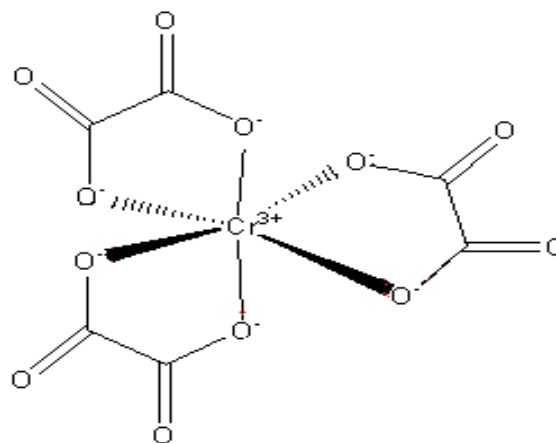
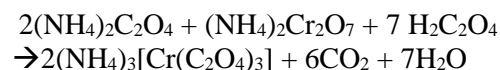


Fig. 1. Structure of ammonium tris (oxalato) chromate [III] anion.

The formal equation of the reaction can be presented as follows:



The preparation procedure must be realized very carefully in order to avoid in the possible appearance of Cr^{6+} -ions in the final product.

Polarization resistance (Rp) measurements

The data obtained from the polarization resistance measurements for zinc coatings with different CF after 300 hours of corrosion treatment in the model medium are demonstrated in Figure 2. At the beginning of the testing the samples with the transparent (TCF) and light-green CF (LGCF) show very high R_p values – curves 1 and 3, respectively. Thereafter the result for the transparent film decreases readily and it becomes the lowest one at the end of the experiment. The zinc coating with the light-green CF has relative close R_p values during the whole period. The sample with gray-black CF (GBCF) presents the lowest polarization resistance in the first 50 hours but thereafter its protective ability increases and at the end of the test period its R_p data is comparable with that of the sample with light-green CF – about $2700\text{-}2800 \Omega \cdot \text{cm}^2$.

The results for galvanic and composite zinc coatings (from bath containing 0,1wt% SPMs) with and without light-green CF are shown in Figure 3.

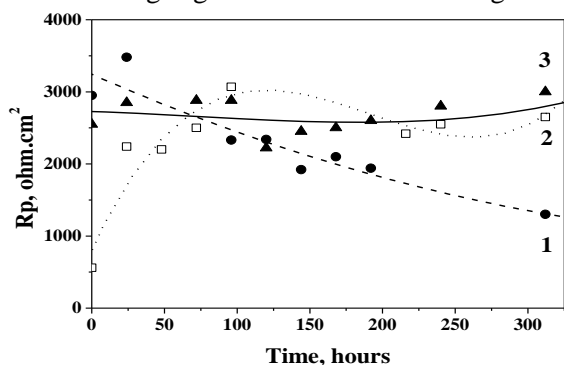


Fig. 2. Polarization resistance of zinc with different CF-s: 1 – transparent; 2 – grey-black; 3 – light-green

The polarization resistance of the zinc is the lowest one with Rp values of about 1000-1500 $\Omega.cm^2$. Contrary to this the Rp values of the composite zinc are greater and show an increasing tendency at the end of the period. These results qualitatively correlate to the data obtained for the same coating types in 5% NaCl solution although the Rp values in the latter are to a certain extent lower.

At the end of the testing both coatings with light-green CF do not have remarkable damages on the surface but the Rp values of the composite one are with about 500 $\Omega.cm^2$ greater than that of the non-composite zinc sample (curves 4 and 3, respectively). The reason for this can be explained with the formation of a mixed surface layer which consists of newly formed corrosion product – zinc hydroxide chloride (ZHC), registered previously by us with XRD method from one side - and of SPMs from another. As well known ZHC characterizes with a low product of solubility value ($\sim 10^{-14}$) which has a barrier effect. In that case the hydrophobic part of the SPMs leaving in the mixed layer additionally increases the inhibiting of the penetration of the corrosion medium deeply inside.

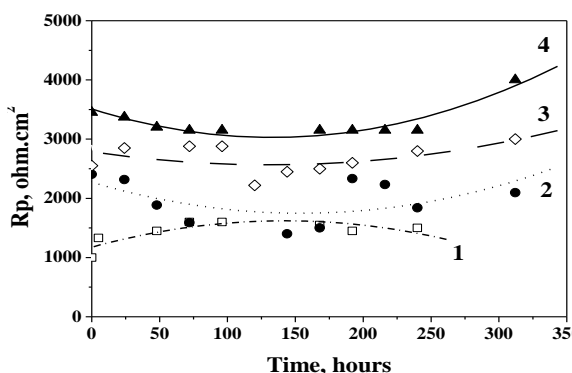


Fig. 3. Polarization resistance of zinc and composite zinc with different CF-s: 1 – Zn; 2 – composite Zn; 3 – Zn

with light-green CF; 4 – composite Zn with light-green CF.

NSS method

The results obtained from the NSS method concerning electrodeposited non-composite zinc coatings with three different CF (transparent, gray-black and light-green) are demonstrated in Figure 4. The experimental data registered show best protective ability of the light-green CF which does not have any damaged surface areas during the first 3 cycles. Thereafter the newly appeared zinc corrosion products begin to cover the coating and at the 4-th cycle the “white rust” occupies between 4 and 8 % of its surface. At the 9-th cycle the damaged surface of this sample is between 32 and 64%.

The other two CF-s demonstrate in general close tendencies of decreasing which is more strongly expressed for the transparent one the latter been almost totally covered by “white rust” after the 5-th cycle. Contrary to this, the gray-black CF lasts relative longer time – up to the 8-th cycle.

The results obtained about the appearance of “red rust” of zinc and composite zinc samples are presented in Figure 5.

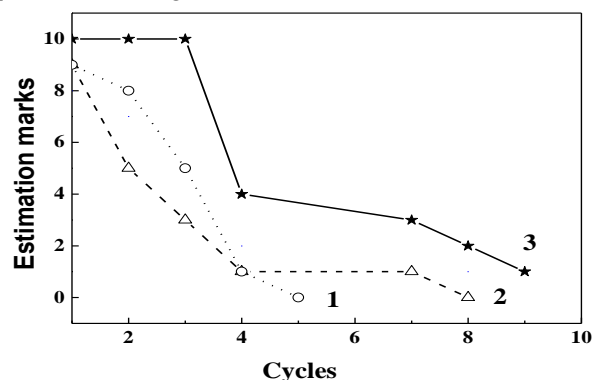


Fig. 4. NSS data about “white rust” registered on Zn with different CF-s:

1 – transparent (TCF); 2 – grey-black (GBCF); 3 – light-green (LGCF).

After 8 cycles the best results (without any damages) show both Zn (1) and composite Zn (2) with light-green CF as well as the composite zinc with transparent (4) and with gray-black CF (6). At the 15-th cycle the zinc and its composite with light-green CF are still without damages (1,2), both coatings with transparent CF (3,4) have “red rust” on about 1% of the surface and the Zn coating with gray-black CF (5) has between 10 and 30% damages on the surface. At the 22 cycle only the composite zinc with light-green CF (2) is without “red rust” on the surface which means this CF protects successfully the substrate. The galvanic Zn with LGCF (1) and the composite one with TCF (4) demonstrate estimation mark 9.

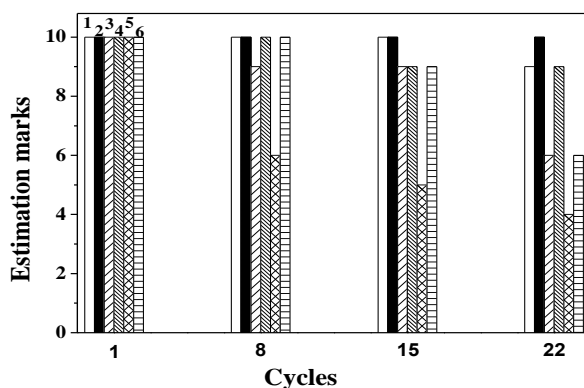


Fig. 5. NSS data about “red rust” registered on Zn and composite Zn with CF-s: 1 –Zn with LGCF; 2 – composite Zn with LGCF; 3 – Zn with TCF; 4 – composite Zn with TCF; 5 – Zn with GBCF; 6 – composite Zn with GBCF.

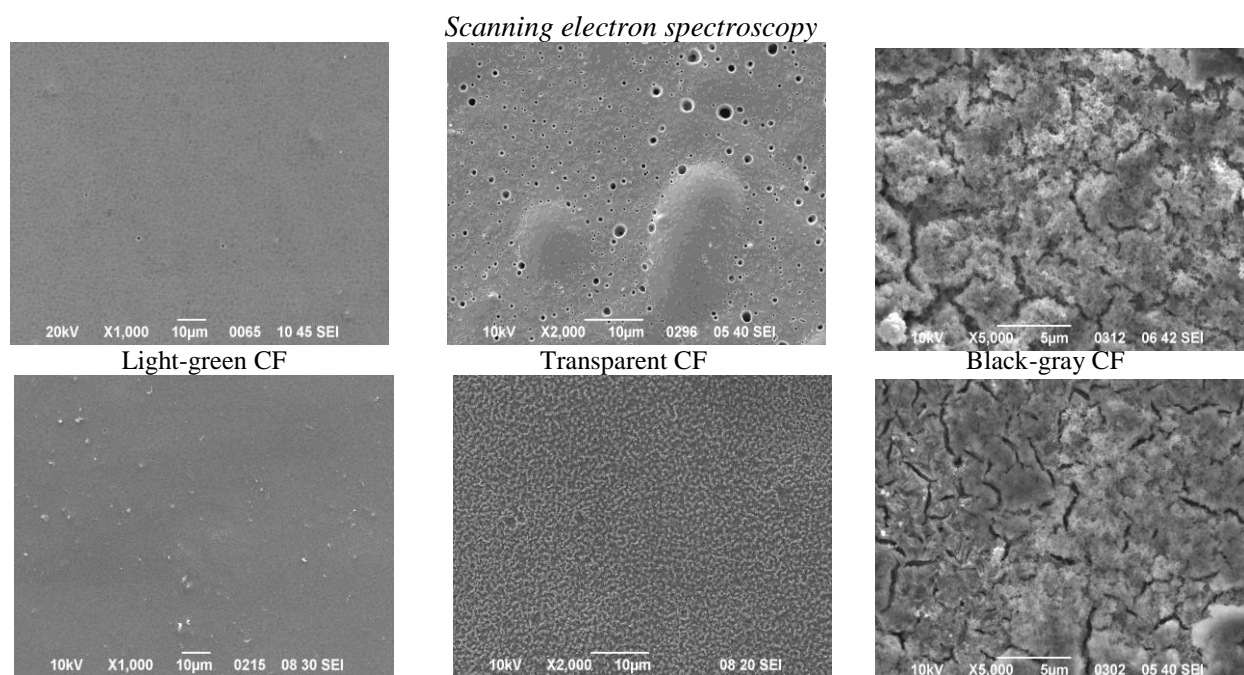


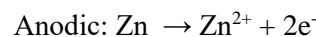
Fig. 6. SEM images of Zn(up) and composite Zn(down) with different CF

Typical surface morphology of non-composite and composite zinc coatings are presented in Fig. 6. It is seen that the sample surfaces of the presented coatings exhibit marked differences. The surface of the non-composite with CF is more uneven and in some places also some holes or other inhomogeneity appear. Contrary to this the surface morphology of the composite zinc looks in general more even especially when light-green CF is applied.

DISCUSSION

As well known the corrosion resistance of the zinc depends on the formation of a protective layer of corrosion products with low product of solubility which distinguishes with barrier properties. When the electrodeposited coating (composite or non-

composite) is chemically treated at low pH value in solutions containing for example Cr(III) based salts two parallel processes are appear - dissolution of zinc and evolution of hydrogen with following reactions presented below:



The reduction of hydrogen ions leads to an increase of pH value in the vicinity of the Zn surface, which results in the precipitation of chromium hydroxide and zinc hydroxide from Cr(III) and Zn(II) ions and formation of additional thin surface layer.

Finally, the simultaneously presence of conversion film, corrosion products as a result of the dissolution process and incorporated in the

metal matrix SPMs (practically insoluble in the model corrosion medium) lead to better corrosion resistance of the chromited composites compared to the chromited non-composite zinc deposits.

CONCLUSIONS

The presented results demonstrated clearly the possible application of environmentally Cr(III) based solution for chemical treatment of composite and non-composite zinc coatings in order to increase their protective properties. Depending on the composition and on the content of the ATOC the protective action of the chromite layer can change providing protection to different extent. The presence of SPMs in the zinc matrix leads to increase of the corrosion resistance compared to the pure non-composite zinc.

It can be finally summarized that the presented coatings demonstrate high protective ability in the selected corrosion medium which could be viewed and comparable with some of the "smart" composite coatings with embedded nano-containers with inhibitor [25,26].

REFERENCES

1. P.C. Tulio, S.E.B. Rodrigues, I.A. Carlos, *Surf. Coat. Technol.*, **202**, 91 (2007).
2. T. Ohgai, K. Ogushi, K. Takao, *J. of Physics: Conference Series*, **417**, 012006 (2013).
3. A. Brenner, *Electrodeposition of Alloys. Principles and Practice*, Academic Press, New York, 1963, p. 123.
4. Z.I. Ortiz, P. Diaz-Arista, Y. Meas, R. Ortega-Borges G. Trejo, *Corr. Sci.*, **51**(11), 2703 (2009).
5. A. Vlasa, S. Varvara, A. Pop, C. Bulea, L.M. Mureshan, *J. of Appl. Electrochem*, **40**(8), 1519 (2010).
6. A. Shamsolhodaie, H. Rahmani, S. Rastegari, *Surf. Eng.*, **29**(9), 695 (2013).
7. O.S.I. Fayomi, A.P.I. Popoola, C.A. Loto, *Int. J. of Electrochem. Sci.*, **9**(7), 3885 (2014).
8. O. Hammami, L. Dhouibi, P. Bertzot, E. M. Rezaei, *J. of Appl Electrochem*, **44**(1), 115 (2014).
9. K. Wykpiś, J. Niedba, M. Popczyk, A. Budniok, E. Bagiewka, *Russ. J. of Electrochem*, **48**(11), 1123 (2012).
10. S. Pouladi, M.H. Shariat, M.E. Bahrololoom, *Surf. Coat. Technol.*, **213**, 33 (2012).
11. M. Sajjadnejad, H. Omidvar, M. Javanbakht, R. Pooladi, A. Mozafari, *Trans. Inst. Met. Finish.*, **92**(4), 227 (2014).
12. K. Vathsala, T. V. Venkatesha, *Appl. Surf Sci*, **257**(21), 8929 (2011).
13. P.I. Nemets, M. Zaharescu, L.M. Muresan, *J. Solid State Electrochem.*, **17**(2), 511 (2013).
14. P.I. Nemets, M. Lekka, L. Fedrizzi, L.M. Muresan, *Surf. Coat. Technol.*, **252**, 102 (2014).
15. N. Boshkov, N. Tsvetkova, P. Petrov, D. Koleva, K. Petrov, G. Avdeev, Ch. Tsvetanov, G. Raichevsky, R. Raicheff, *Appl. Surf. Sci.*, **254**(17), 5618 (2008).
16. D. Koleva, N. Boshkov, V. Bachvarov, H. Zhan, J.H.W. de Wit, K. van Breugel, *Surf. Coat. Technol.*, **204**, 3760 (2010).
17. D.A. Koleva, P. Taheri, N. Tsvetkova, N. Boshkov, K. van Breugel, J. H. W. de Wit, J.M.C. Mol, *ECS Transactions*, **33**(35), 85 (2011).
18. N. Boshkov, K. Petrov, S. Vitkova, S. Nemska, G. Raichevski, *Surf. Coat. Technol.*, **157**, 171 (2002).
19. N. Boshkov, K. Petrov, D. Kovacheva, S. Vitkova, S. Nemska, *Electrochem. Acta.*, **51**, 77 (2005).
20. C.R. Tomachuk, C.I. Elsner, A.R. Di Sarli, O.B. Ferraz, *Math. Chem. Phys.*, **119**, 19 (2010).
21. C.R. Tomachuk, A.R. Di Sarli, C.I. Elsner, *Port. Electrochim. Acta*, **30**(3), 145-162 (2012).
22. R. Berger, U. Bexell, T.M. Grekh, S.E. Hornstrom, *Surf. Coat. Technol.*, **202**, 391 (2007).
23. P. Petrov, M. Bozukov, Ch.B. Tsvetanov, *J. Mater. Chem.*, **15**, 1481 (2005).
24. M. Stern, A.L. Geary, *J. Electrochem. Soc.*, **104**, 56 (1957).
25. M.I. Zheludkevich, D.G. Shchukin, K.A. Yasakau, H. Mohwald, M.G.S. Ferreira, *Chem. Mater.* **19**, 402 (2007).
26. M.I. Zheludkevich, J. Tedim, M.G.S. Ferreira, *Electrochim. Acta*, **82**, 314 (2012).

ПОВЪРХНОСТНА МОРФОЛОГИЯ И КОРОЗИОННО ПОВЕДЕНИЕ НА ЦИНКОВИ И ЦИНКОВИ КОМПОЗИТНИ ПОКРИТИЯ С КОНВЕРСИОННИ ЗАЩИТНИ ФИЛМИ НА БАЗА ТРИВАЛЕНТЕН ХРОМ

Н.Д. Божкова¹, П.Д. Петров², В. Чукова³, Л. Лютов³, С.Д. Виткова¹, Н.С. Божков^{1*}

¹*Институт по физикохимия, БАН, София 1113*

²*Институт по полимери, БАН, София 1113*

³*Софийски университет, Факултет по химия и фармация, бул. "Дж. Баучер" 1, София*

Постъпила на 14 октомври, 2015 г.; коригирана на 2 февруари, 2016 г.

(Резюме)

Представени и коментирани са резултатите по получаване на защитни конверсионни филми върху цинкови и цинкови композитни покрития от екологични разтвори. Новоразработените конверсионни филми съдържат амониево-хромена сол на тривалентния хром с оксалова киселина – амониево-три-оксалат-хроматен комплекс. В зависимост от неговата концентрация и от времето на потапяне са получени три типа конверсионни филми върху цинкови и цинкови композитни покрития – прозрачен, светлозелен и сиво-черен – които се различават по своята корозионна устойчивост и защитни свойства. Последните са оценени в неутрална корозионна среда на 3% NaCl с хлорни йони като корозионни активатори, които предизвикват локална корозия. Защитната способност на конверсионните филми е изследвана с методите на поляризационното съпротивление и камера „Солена мъгла“. Повърхностната морфология е оценена със сканираща електронна микроскопия. Композитните цинкови покрития съдържат вградени стабилизирани полимерни мицели тип „ядро-обвивка“ на база полипропилен оксид и полиетилен оксид. Дискутирано е влиянието на тези стабилизирани мицели върху повърхностната морфология и върху корозионното поведение на покритията.

Effect of quartz plate roughness on ZnO/QCM response to NO₂

H. Nichev¹, B. Georgieva^{1,2}, M. Petrov¹, K. Lovchinov¹, V. Georgieva³, L. Vergov³, G. Alexieva⁴,
D. Dimova-Malinovska¹

¹Central Lab. of Solar Energy and New Energy Sources – Bulgarian Academy of Sciences, 72, Tzarigradsko Chaussee, 1784 Sofia, Bulgaria

²University of Chemical Technology and Metallurgy, blvd. “St. Kliment Ohridki” 8, Sofia 1756, Bulgaria

³Institute of Solid State Physics – Bulgarian Academy of Sciences, blvd. “Tsarigradsko chaussee” 72, 1784 Sofia, Bulgaria

⁴Department of Solid State Physics and Microelectronics, Sofia University, 1164 Sofia, Bulgaria

Received October 16, 2015; Revised November 17, 2015

The influence of the quartz roughness on the ZnO sorption properties is investigated. AT-cut quartz plates with differently treated surface - flat polished and unpolished ones are used. The nanostructured ZnO layers are deposited by electrochemical method on the Au electrodes of the quartz crystal micro-balances resonators (QCM). Thin ZnO nanostructured films are deposited by an electrochemical process from slightly acid aqueous solution of ZnCl₂ (5 · 10⁻³ M) and KCl (0.5 M) with pH 4.0 at 80°C and -1000mV (vs SCE) using a three-electrode electrochemical cell. The structure of the ZnO layers deposited on the polished and unpolished QCM surface is studied by SEM, AFM and the optical spectroscopy - by the spectra of specular and diffused reflection. The results are compared to the corresponding data obtained for the QCM before ZnO growing. The sorption ability of the ZnO thin layers is defined by measuring the resonant frequency shift (Δf) of the QCM-ZnO structure in the presence of different NO₂ concentration (50 - 5000 ppm). The correlation between the sorption ability of the ZnO and the different state of the quartz surface is obtained from the QCM response. The QCM with ZnO deposited on the polished quartz demonstrate better sorption ability compared to QCM fabricated on unpolished quartz surface.

Key words: ZnO, nanostructure, electrochemical deposition, quartz microbalance resonator, gas sensors.

INTRODUCTION

The quartz crystal microbalance (QCM) is one of the extremely sensitive mass detection devices. It is widely used such as gas sensors, biosensors, etc. The QCM sensor properties such as sensitivity, selectivity, and time response are strongly influenced by the properties of the sensing films. These sensors are highly sensitive to mass changes in the presence of a coating, which interacts with the test gas. The characteristics of QCM gas sensors depend on the kind and structure of sensing films coated on their electrodes. A number of materials have been successfully employed in the coating of QCM sensors and one of them is ZnO, II–VI semiconductor. This material possesses high chemical stability, low dielectric constant and high luminous transmittance. As gas sensing material, it is one of the earliest discovered and most widely applied oxide gases sensing material because of its optical, electronic, and chemical properties [1, 2-5].

In this paper results from investigation of the optical and the structural properties of nanostructured ZnO thin films formed by

electrochemical deposition on two Quartz Crystal Microbalance (QCM) resonators with differently treated surface – polished and unpolished are presented. The sensitivity of both QCMs to NO₂ is compared and the influence of the roughness of the quartz substrate on ZnO sorption properties of two QCM is investigated.

Electrodeposition has some advantages as a method of deposition because it is a low cost industrially up-scalable process, relevant to different substrates for preparation of well defined nanostructures with reasonable physical parameters [2, 3, 6].

EXPERIMENTAL

The nanostructured ZnO layers are deposited by electrochemical method on the Au electrodes of the QCM resonators. Thin ZnO nanostructured films are deposited from slightly acid aqueous solution of ZnCl₂ (5 · 10⁻³ M) and KCl (0.5 M) with pH 4.0 at 80°C and -1000mV (vs SCE) using a three-electrode electrochemical cell [7,8]. The electrolyte is agitated by magnetic stirrer. The Au electrode of the QCM is used as a cathode. Spectrally pure graphite plate electrode is used as an anode. The deposition is carried out controlling the redox potential of the system WENKING HP 96. The total

To whom all correspondence should be sent:
E-mail: dmalinovska@yahoo.co.uk

oxygen content in solution is controlled by a DO&T meter Hanna Instruments 9146. Duration of the ZnO deposition is 60 min. The thicknesses of the prepared ZnO films are in the range of 0.5-0.7 μm .

The morphology of the obtained ZnO layers is characterized by Scanned Electron Microscopy (SEM) (microscope Lyra (Tescan) with Secondary Electron and Back Scattering Electron detector and EDX detector Quantax 200 (Bruker) and AFM (Multimode V -Veeco) in tapping mode and height, amplitude and phase images are recorded. The optical properties - spectra of specular reflectance, diffuse reflection and haze ratio in reflection are measured by a spectrophotometer Shimadzu UV-3600 in the range 330 -1200 nm employing a 60 mm integrating sphere. The sorption ability of the ZnO thin layers is defined by measuring the resonant frequency shift (Δf) of the QCM-ZnO structure in the presence of different NO_2 concentrations (50 - 5000 ppm). The experimental setup works in a dynamic regime in continuous flow of testing and carrying gases. The QCM is installed on a special holder inside the test chamber. The flow rates of the used gases are measured inside the test chamber by a Pt-thermo-sensor placed next to it and is kept constant $24 \pm 0.2^\circ\text{C}$ during the kept constant by two mass flow controllers (FC-260 and FC-280). Mixing camera provides the homogeneity of the gas mixtures. The ratio of the flows of the test and diluting gases defines NO_2 gas concentration. In the experiments a dry synthetic air

– high purity and 10 000 ppm NO_2 diluted in synthetic air are used. The measurement process consists of three basic stages: purging the camera with air flow until the frequency of the QCM-ZnO reaches a constant value; switching NO_2 and reaching the saturation frequency value; purging the camera with dry air until approaching the initial frequency of the investigated structure. The measurements have been carried out continuously at two seconds interval. A frequency counter Hameg 8123 is connected to the QCM and to the computer for data recording QCM frequency. In this way the frequency change of the QCM-ZnO structure as a function of time is registered for different NO_2 concentrations.

RESULTS AND DISCUSSION

The surface morphology of the polished and unpolished quartz substrates studied by SEM and AFM before ZnO layers coating are shown in figure 1 and 2, respectively. The surface of polished QCM with deposited Au electrode is very flat (figure 1 a) and the value of the average surface roughness is $R_{\text{avr}} = 7.45 \text{ nm}$ and of the maximal roughness $R_{\text{max}} = 34.9 \text{ nm}$ (figure 1 b and c).

The surface of the unpolished QCM is very rough – the plates and pyramidal like structures with size of several μm and different high (between about 2 and $8 \mu\text{m}$) are seen in the SEM image (figure 2a). The surface roughness is 246 nm and the maximal roughness is 461 nm (figures 2 b and c).

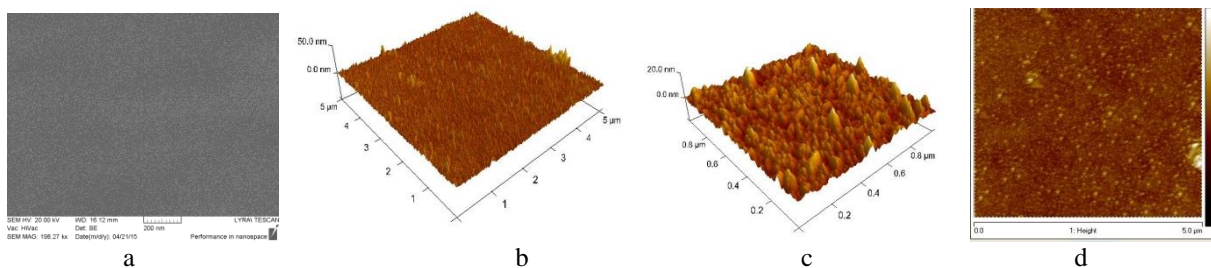


Fig. 1. SEM micrographs (a) and AFM pictures (b,c,d) of the polished quartz substrate with $R_{\text{avr}} = 7,45 \text{ nm}$ and $R_{\text{max}} = 34,9 \text{ nm}$ (d). The marker in (a) corresponds to 200 nm.

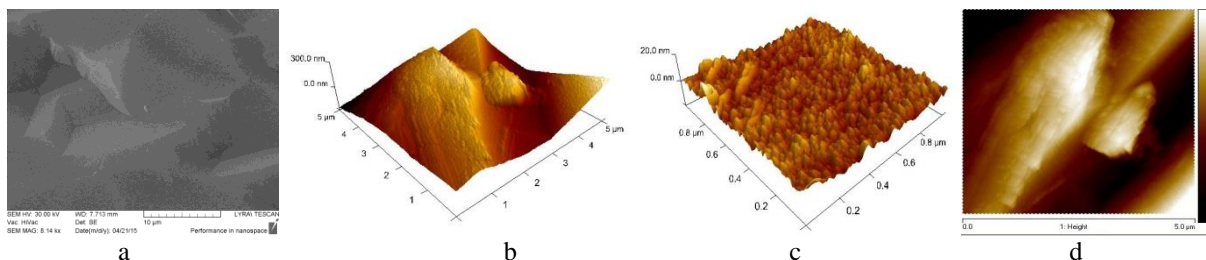


Fig. 2. SEM micrographs (a) and AFM pictures (b,c,d) of unpolished quartz substrate with $R_{\text{avr}} = 246 \text{ nm}$ and $R_{\text{max}} = 461 \text{ nm}$ (d). The marker in (a) corresponds to 10 μm .

The SEM pictures of the deposited ZnO layers on the polished surface of QCM are shown in figure 3 a and b. The ZnO layer consists of hexagonal nanowires about 700-800 nm thick grown with different orientation to the surface.

In the case of growing on unpolished QCM surface (SEM are shown in figures 4 a and b) the ZnO nanowires with different size – diameter (from 200 nm to 1,5µm) and height have grown perpendicular to the substrate surface. The difference in the height of the ZnO nanowires probably is due to the growing on electrode deposited on the quartz plates with different height. The substrate with higher surface roughness induces the ZnO nanowire growing with higher inhomogeneity in the surface morphology.

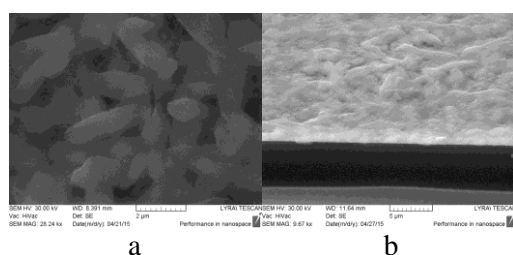


Fig. 3. SEM of ZnO nanostructured layer deposited by electrochemical method on polished quartz substrate of QCM resonator (G 111): (a) – surface view and (b) - cross section view. The markers correspond to 1 µm.

Figure 5 shows spectra of specular reflection, diffuse reflection and haze ratio in reflection of ZnO layers deposited on polished and unpolished QCM substrate. For comparison the corresponding spectra of the QCM before ZnO growing are presented as well. The polished substrate has high values of reflection, low value of diffused reflection and of haze ratio in reflectance. In opposite, the unpolished QCM surface demonstrated low specular reflection, high diffused reflection, and haze in reflectance. After ZnO deposition on polished QCM surface, the reflectance decreases, the diffuse reflection and haze in reflectance increase. In the case of growing on unpolished QCM surface the presence of ZnO nanowires (NW) leads to slight decreasing of the specular reflection, decreasing of diffused reflection and slightly increasing in haze of reflection. It has to be noticed that values of the specular reflection decrease from 70% to 20% after ZnO layer deposition on QCM with polished substrate while these values after ZnO growing on the rough quartz surface of QCM decrease slightly - from 20% to 10% (figure 5a). The changes in the values of reflection are due to the increased surface inhomogeneity after ZnO NW growing, more pronounced in the case of growing on polished QCM surface.

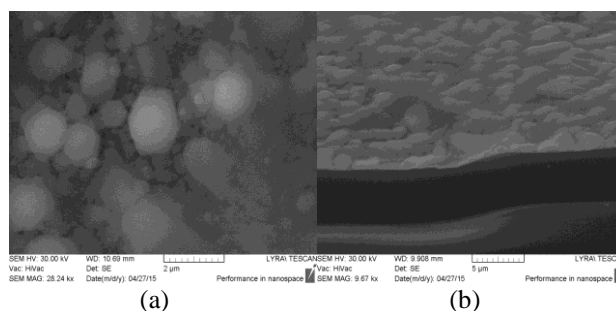


Fig. 4. SEM of ZnO nanostructured layer deposited by electrochemical method on unpolished quartz substrate of QCM resonator (G 121): (a) – surface view and (b) - cross section view. The markers correspond to 1 µm.

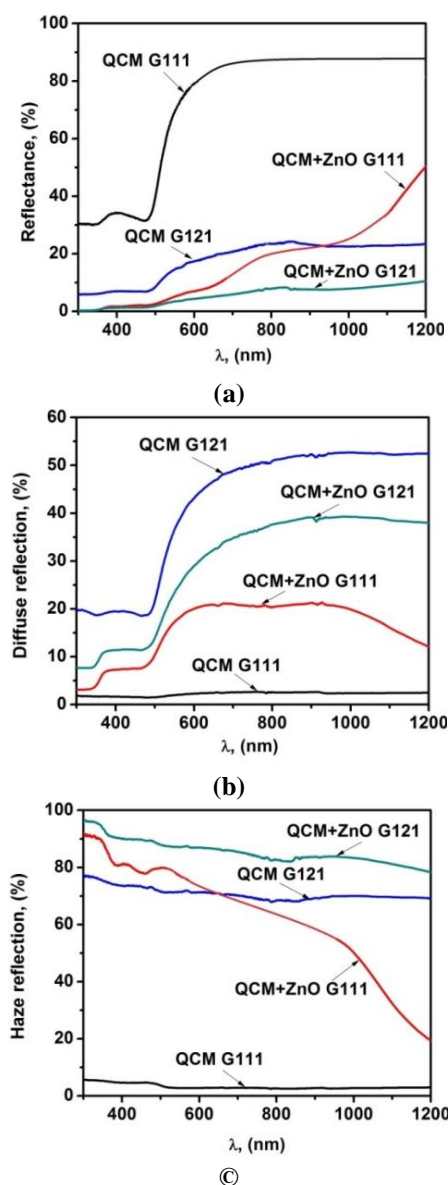


Fig. 5. Spectra of specular reflectance (a), diffused reflection (b) and haze ratio in reflection (c) from the ZnO deposited on polished QCM (G 111) and unpolished surface of QCM (G 121).

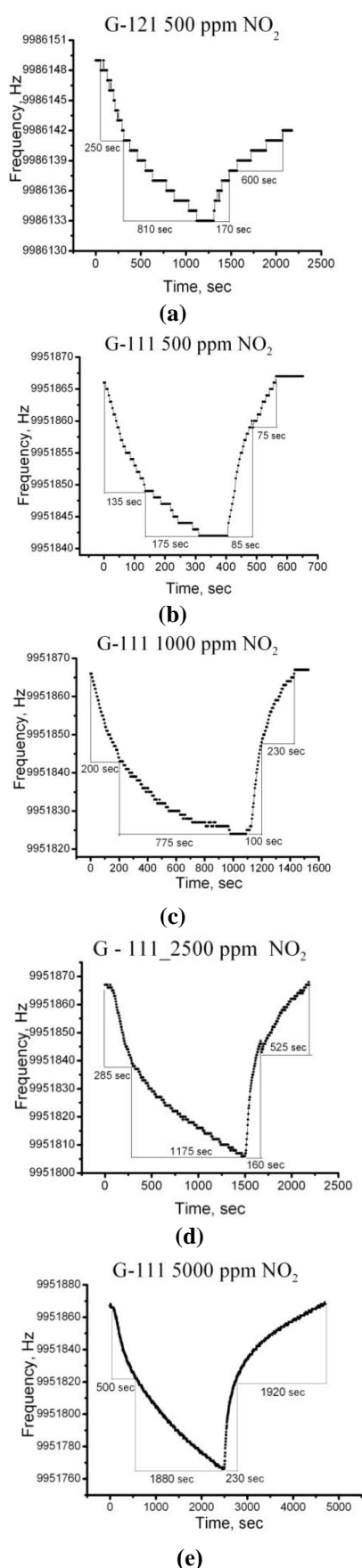


Fig. 6. Frequency – time characteristics of QCM with NS ZnO layer at different NO₂ concentrations: (a) QCM G-121 (unpolished) and (b) QCM G-111 (polished) - 500 ppm; c) 1000 ppm; d) 2500 ppm; e) 5000 ppm.

The process of sorption of NO₂ is compared for two kinds of QCM layers fabricated on different differently treated quartz surface – polished and unpolished at NO₂ concentration for 500 ppm (figures 6 a and 6 b). The QCM with ZnO nanostructured formed on polished quartz surface demonstrates that the process of sorption is reversible in the time of 150 sec. However in the case of the QCM formed on the unpolished quartz surface the value of half of initial frequency is notreached for the time as long as 770 sec. Thedifference in the behavior of two types of QCMs under investigation could be explained by the differences in the structure and morphology of ZnO layers formed on different surfaces. The Zn layer on polished quartz has hexagonal nano-rods with size of 500 nm grown in different angles to the substrate. The ZnO layer grown on the rough quartz surface (QCM G-121) has hexagonal rods with larger size - 2 μm with perpendicular orientation to the substrate.

The higher gas sensitivity of the QCM G-111 compared to QCM G-121 can be explained by the lower size of the grown ZnO rods which results in larger effective surface area. Additionally, it is possible to suppose that the difference in the crystalline orientation of the ZnO rods is a reason for the different sensitivity of QCM. The different crystalline planes of ZnO have different surface defects which are responsible for the gas absorption and this could reflect in different sensibility of the sensors.

The frequency-time characteristics at different NO₂ concentrations are measured for the QCM-111 which demonstrates reversible process of NO₂ sorption. The frequency-time characteristics (figure 6) show that both, the process of sorption and desorption of the NO₂ consist of twosteps: quick and slow ones.

The time of both processes is determined for each value of NO₂ concentration applied. The values of the time of sorption and desorption are shown in figure 6 and summarized in table 1. The results demonstrate that time of the process of quick sorption (t_{s1}) rises about 4 times and the time of the slow sorption (t_{s2}) – about 11 times with increasing the NO₂ concentration from 500 ppm to 5000 ppm. The total time for reaching the dynamic equilibrium of the process of absorption rises about 8 times. Similar tendency is observed for the process of desorption – the time of the process of initial desorption (t_{d1}) increases about 3 times and that of final step of desorption (t_{d2}) - about 25 times. It is measured that the total desorption time increases about 13 times with increasing of the NO₂ concentration.

The comparison of the frequency shifts of both QCMs (G-111 and G-121) obtained as a function of NO₂ concentration is shown in figure 8. It is seen that the QCM G-111 with ZnO grown on polished quartz substrate demonstrates higher sensitivity for all values of NO₂ concentrations under investigation.

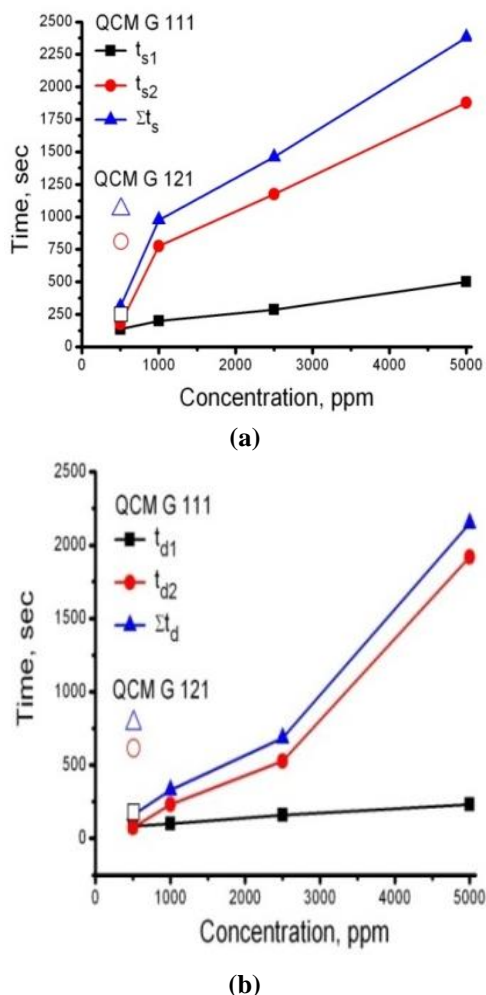


Fig. 7. Dependence of the QCM-ZnO time of sorption, t_s , (a) and desorption, t_d , (b) vs. NO₂ concentration.

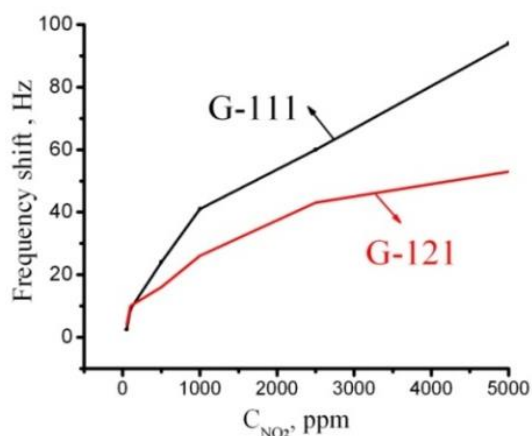


Fig. 8. Dependence of QCM-ZnO frequency shift vs NO₂ concentration.

Table 1. The values of the times of the processes of the quick and slow sorption and desorption by QCMs and the corresponding total times.

Sample	C _{NO₂} ppm	Time, sec					
		t _{s1}	t _{s2}	Σ t _s	t _{d1}	t _{d2}	Σ t _d
QCM G 111	500	135	175	310	85	75	160
	1000	200	775	975	100	230	330
	2500	285	1175	1460	160	525	685
QCM G 121	5000	500	1880	2380	230	1920	2150
QCM G 121	500	250	810	1060	170	600	770

CONCLUSIONS

The ZnO nanostructured layers with developed surface morphology are electrochemically deposited on Au electrodes of QCM on polished and unpolished quartz plate. The surface morphology on the grown ZnO depends on the roughness of the quartz substrate of QCM. The values of reflectance decrease more pronounced after deposition of ZnO on polished quartz surface. The response, maximal frequency shift and recovery times of the processes of sorption and desorption at different NO₂ concentrations between 500 and 5000 ppm of QCMs are measured at room temperature. The QCM formed on polished quartz surface shows good response to NO₂, higher sensitivity that QCM on the rough quartz substrate and the process of sorption is reversible. The electrochemically deposited nanostructured ZnO layer grown on QCM on polished quartz surface can be used for detection of NO₂.

REFERENCES

1. S.C. Navale, V. Ravi, I. S. Mulla, S.W. Gosavi, S. K. Kulkarni, *Sensors and Actuators B*, **126**, 382 (2007).
2. M. S. Wagh, G.H. Jain, D. R. Patil, S. A. Patil, L. A. Patil, *Sensors and Actuators B*, **115**, 128 (2006).
3. W. H. King, *Anal. Chem.*, **36**, 1735 (1964).
4. L.-H. Sun, T. Okada, *Anal. Chim. Acta*, **421**, 83 (2000).
5. K. Nakamura, T. Nakamoto, T. Moriizumi *Mater. Sci. Eng. C*, **12**, 3 (2000).
6. J. Zhang, J. Q. Hu, F. R. Zhu, H. Gong S. O'Shea, *Sens. Actuators B*, **87**, 159 (2002).
7. D. Dimova-Malnovska, P. Andreev, M. Sendova-Vassileva, H. Nichev, V. Mikli, 24th EPVSEC, Hambourg, Germany, 2009, p.391.
8. M. Petrov, K. Lovchinov, H. Nichev, D. Karashanova, D. Dimova-Malinovska, *NATO Science for Peace and Security Series A: Chemistry and Biology*, **39**, 151 (2015).

ВЛИЯНИЕ НА ПОВЪРХНОСТНАТА ГРАПАВОСТ НА КВАРЦОВИ ПОДЛОЖКИ ВЪРХУ СОРБЦИОННИТЕ СВОЙСТВА НА ZnO/QCM КЪМ NO₂

Хр. Ничев¹, Б. Георгиева^{1,2}, М. Петров¹, К. Ловчинов¹, В. Георгиева³, Л. Вергов³,
Г. Алексиева⁴, Д. Димова-Малиновска¹

¹Централна лаборатория по слънчева енергия и нови енергийни източници – БАН, бул. Цариградско шосе 72,
1784 София, България

²Химикотехнологичен и металургичен университет, бул. Кл. Охридски 8, 1756 София, България

³Институт по физика на твърдото тяло- БАН, бул. Цариградско шосе 72, 1784 София, България

⁴Катедра физика на твърдото тяло и микроелектроника., СУ, 1164 София, България

Постъпила на 16 октомври, 2015 г.; коригирана на 17 ноември, 2015 г.

(Резюме)

В настоящата работа са представени резултати от изследване на влиянието на повърхностната грапавост на кварцови подложки, използвани в кварцови микро-резонатори (QCM), върху сорбционните свойства на отложени върху тях слоеве от ZnO. Използвани са кварцови пластини с АТ-срез с различна повърхостна морфология – с полирана и неполирана повърхност. ZnO слоеве с наноструктура са отложени чрез електрохимичен процес върху Au електрод на QCM в слабокисел разтвор на ZnCl₂ ($5 \cdot 10^{-3}$ M) и KCl (0.5 M) с рН=4.0 при 80°C и 1000 mV (vs SCE), използвайки три-електродна система. Структурата на отложените ZnO слоеве върху двата вида повърхности на QCM е изследвана чрез SEM и AFM, а оптичните свойства – от спектрите на директно и дифузно отражение. Резултатите са сравнени със съответните данни, получени за QCM преди отлагането на ZnO. Сорбционните свойства на ZnO слоевете са охарактеризирани чрез измерване на промяната на резонансната честота (Δf) на QCM-ZnO при различни концентрации NO₂ (50 - 5000 ppm) в газовия поток. Показана е корелация между сорбционна способност на ZnO, отложен върху кварцовите подложки с различна повърхостна морфология. Кварцовият микро-резонатор с ZnO, отложен върху полирана кварцова повърхност, показва по-добра сорбционна способност в сравнение с QCM с ZnO, отложен върху неполирана повърхостна кварцовата подложка.

Corrosion behavior of nitrogen stainless steel in Ringer's solution

G.P. Ilieva¹, M.H. Loukaycheva^{2*}, B.R. Tzaneva², L.T. Gekova³ and L.B. Fachikov¹

¹University of Chemical Technology and Metallurgy, 8 Kliment Ohridski Blvd, 1756 Sofia, Bulgaria

²Technical University- Sofia, 8 Kliment Ohridski Blvd, 1756 Sofia, Bulgaria

³Institute of Metal Science, Equipment and Technologies "Acad. A.Balevski" with Hydro-aerodynamics Centre - BAS, 67 Shipchenski prohod Str., 1574 Sofia, Bulgaria

Received October 13, 2015; Revised November 30, 2015

The implant materials used in medicine are made from different materials and the principle requirement to each material used is its biocompatibility. This work reports preliminary results regarding assessment of high nitrogen stainless steel (HNS) Cr18Mn12N as an implant material replacing of the common Ni containing stainless steels which are toxic. Short - time (for 1 h) and long - time (for up to 220 h) open circuit potential measurements were performed as well as potentiodynamic and potentiostatic studies in Ringer's solution at 37°C. The effect of the preliminary treatment was also considered. After the potentiostatic tests optical and scanning electron microscopies were used to determine the character of the corrosion attack. The surface of the samples was examined and by EDX analysis in order to find out the corrosion products content. Based on the obtained results it can be concluded that the HNS steel exhibits better corrosion resistance in Ringer's solution.

Key words: stainless steel, HNS, nitrogen, Ringer solution, potentiodynamic polarization, potentiostatic polarization

INTRODUCTION

Orthopedic implants use various biocompatible materials [1, 2] which have to be corrosion resistant to body fluids since the release of metallic ions could provoke their degradation and undesired reactions in the human body. Stainless steels, Co, Ti, Ta, Mg and its alloys, for instance, are widely used [3, 4] as materials of implants in surgical operations. Therefore, electrochemical tests of new materials suggested as implants should be performed in controlled media simulating human body fluids prior to final implementations.

The use of austenitic stainless steels as surgical implants is due to its relatively low value in comparison with the other biocompatible materials. The classic austenitic stainless steels exhibit good mechanical and corrosion properties but its Ni content provokes toxicity in the human body [5]. To avoid this problem high nitrogen stainless steels (HNS) such as 314L [6] have been developed to replace Ni-containing materials for implants. The interest about the corrosion resistance of HNS as implant material is provoked by the fact that stems

made of Orthinox (high nitrogen stainless steel but still containing nickel), for instance, occupies 70 % of the hip prostheses market in the UK [7], and it is necessary to be replaced by non-toxic materials.

This work reports preliminary results regarding assessment of high nitrogen nickel free stainless steel Cr18Mn12N as an implant material for replacing the common Ni containing stainless steel Cr18Ni9.

EXPERIMENTAL

Two austenitic stainless steels: the conventional Cr18Ni9 and the new HNS Cr18Mn12N (for chemical content see Table 1) were investigated in Ringer's solution containing (in g/l): 6.8 NaCl, 0.2 CaCl₂, 0.4 KCl, 0.2048 MgSO₄·7H₂O, 0.143 NaH₂PO₄·H₂O, 2.2 NaHCO₃ and 1.0 C₆H₁₂O₆, with pH 7.25 [8]. All tests were carried out in a conventional three electrodes cell in open air conditions at 37°C with a platinum counter electrode and a saturated calomel electrode (SCE) as a reference electrode. All potentials were reported with respect to the SCE. Three electrochemical methods were used: (i) Cyclic potentiodynamic polarization method (scan rates 0.16, 1.0 and 5.0 mV s⁻¹), (ii) Open circuit potential (OCP) - time measurement (up to 1 or 240 hours) and (iii) Potentiostatic method.

To whom all correspondence should be sent:
E-mail: loukaycheva@tu-sofia.bg

The electrochemical results were obtained with a Galvanostat/potentiostat (Princeton Applied Research Model 263) and computer software Power Suite.

After the anodic polarization for 20 minutes at potential 100 mV more positive than the pitting potential obtained potentiodynamically, the topography and chemical content of the surface layers were studied by optical microscope, SEM and EDX analysis. Bruker GmbH, primary energy 30 keV and detector type XFlash 5010 were used.

RESULTS AND DISCUSSION

OCP - time measurements: Two types of OCP - time measurements were performed: *short-time* (for 1 h) and *long-time* (for up to 220 h) tests. During the short-time measurements the OCP - time dependencies indicate that both steels are in passive state since the potentials shift in positive direction. The initial potential values are in range of -0.35 V and after 1 hour reach about -0.2 V (SCE) for both steels. The small difference between the open circuit potentials of both steels specimens could be attributed to dissimilarities in their surface states, i.e. presence of non-metallic inclusions, scratches, crevices, etc., associated with the steel surface morphology and content. However, the measured potentials for both steels are quite close and correspond to the steels surface passivation.

After 1 hour stay of samples in the experimental solution the potentials of both steels do not reach constant values. For this reason the tests were extended up to 220 h. The obtained results provide information about the steel surface state in conditions close to the real encountered in practice.

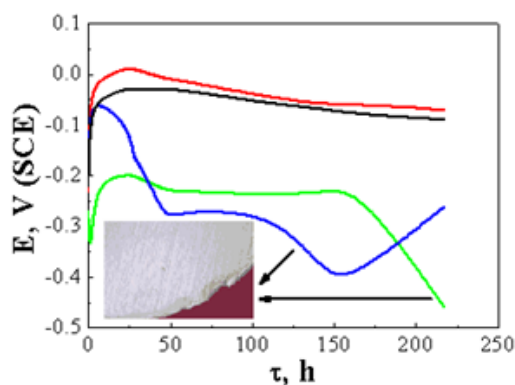


Fig. 1. Long OCP - time measurements for Cr18Mn12N steel in Ringer's solution, for 220h, 37°C

During the long-time experiments performed only for the HNS (Fig. 1) two types of behaviors were observed. The first ones show that the potential slightly shifts in negative direction after one initial ennoblement and attains almost stable value of about -0.05 V(SCE). This slight potential

shift in negative direction could be associated with partial dissolution of non-metallic inclusions or of the metallic surface around them.

The second type dependencies are characterized by sharp decrease in the potential due to crevice corrosion development (between the steel sample and the insulation) which was proved by optical microscopy after the experiments.

Potentiodynamic studies: Regarding the European [9] and American [10] standards for local corrosion investigations it is accepted the experiments to be carried out with scan rate 0.16 mV s⁻¹. However, in the corrosion investigations it is common to use significantly higher scan rate and to perform a large number of repetitions because of the random nature of the pits nucleation. Thus, in the most of the scientific works the potentiodynamic investigations were performed with scan rate 1.0 mV s⁻¹ and even with 5 to 10 mV s⁻¹ [11].

In order to check if the scan rate effects on the corrosion parameters of investigated steels in Ringer's solution tree different scan rates were chosen: 0.16, 1.0 and 5.0 mV s⁻¹. In addition, the effect of different preliminary treatments of the steel surface was considered, too. The potentiodynamic studies revealed that both, the scan rates and the preliminary treatment of the samples affect significantly the obtained electrochemical parameters such as: corrosion potential (E_{corr}), pitting potential (E_{pit}), repassivation potential (E_{rp}), passive current density (j_{pass}), etc.

Influence of the scan rate: The increase of the scan rate (Fig. 2) induces increase in corrosion (j_{corr}) and passive (j_{pass}) current density for both steels. The corrosion current densities of Cr18Mn12N and Cr18Ni9 steels change from 0.32 to 6.36 $\mu\text{A cm}^{-2}$ and 0.29 to 4.26 $\mu\text{A cm}^{-2}$ respectively with the scan rate increase. The obtained values for passive current densities are 0.50 to 16.18 $\mu\text{A cm}^{-2}$ for nitrogen steel and 0.69 to 19.00 $\mu\text{A cm}^{-2}$ for the nickel bearing steel. The effect of the scan rate on the E_{corr} , E_{pit} and E_{rp} is not so considerable for both steels.

The scan rate effects on the electrochemical parameters of both steels revealing that the passive film formation and recovery if it is broken take place slowly. For the investigated steels the passive film formation and its quality are in a great importance. The hold of the steels at potentials in the passive area at scan rate 0.16 mV s⁻¹ allows formation of thick passive film. The increase in the film thickness results in reduced current densities when the scan rate is decreased. Moreover, at slow

scan rates the pits on the surface of both steels try to repassivate and this is more pronounced for the Cr18Mn12N steel samples.

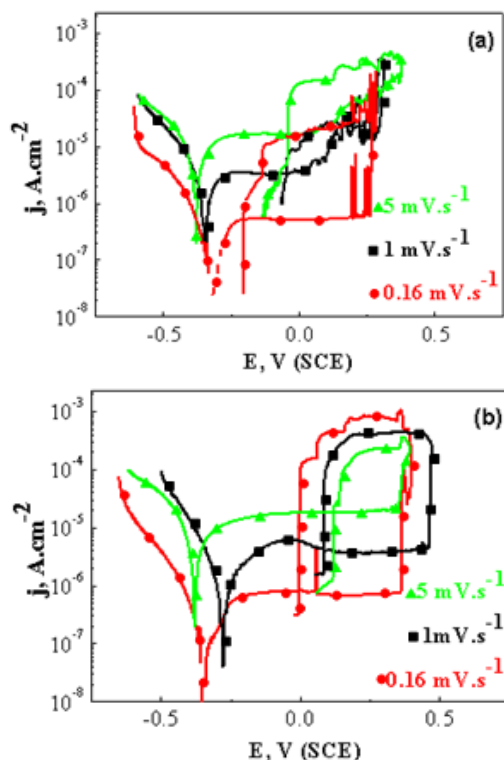


Fig. 2. Potentiodynamic dependencies for (a) Cr18Mn12N and (b) Cr18Ni9 steels obtained with 0.16, 1.0 and 5.0 mV s^{-1} , 37°C.

Effect of the preliminary treatment: With a view to investigate the effect of the initial surface state on the electrochemical parameters of the investigated steels, four different type of dependencies according to preliminary treatments were obtained (Fig. 3): (i) dependencies obtained immediately after the grinding and degreasing of specimens starting from potential by 0.25 V more negative than the OCP, (ii) after grinding, degreasing and cathodic treatment for 5 min at -0.7 V (SCE), (iii) after grinding, degreasing and 1 hour stay in solution and (iv) after grinding, degreasing and 120 hours stay in Ringer's solution.

Contrary, of the scan rate, the preliminary treatment affects mainly the E_{corr} , E_{pit} and E_{rp} , but does not change significantly j_{corr} and j_{pass} .

The preliminary cathodic treatment at negative potential (-0.7 V (SCE)) leads to dissolution of the passive film formed on the steel surface (at air) prior to the immersion in the corrosive solution. Alternatively, the preliminary stay of steels in corrosive media leads to natural formations of passive layers and this is manifested by lower corrosion current densities and ennoblement of the corrosion potential.

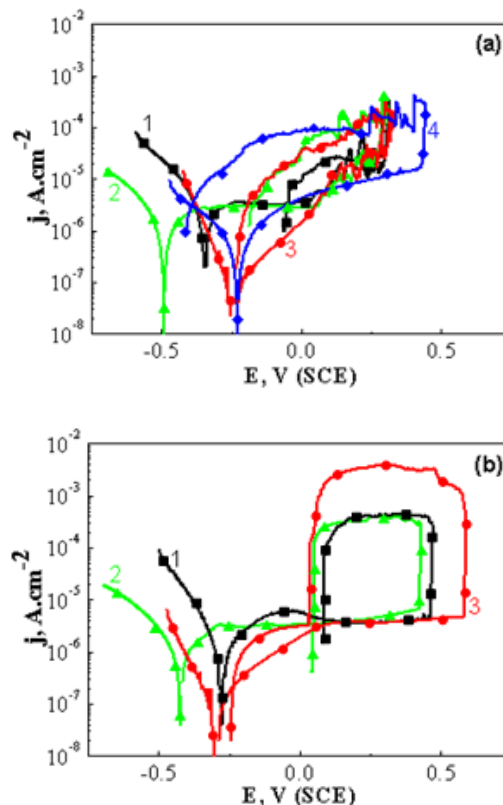


Fig. 3. Potentiodynamic dependencies for (a) Cr18Mn12N and (b) Cr18Ni9 steels obtained after different preliminary treatment, 1.0 mV s^{-1} , 37°C.

(1) ■ scan in positive direction from -0.25 V in regards to OCP (2) ● cathodic treatment for 5 min. at -0.7 V(SCE) and subsequent scan in positive direction (3) ▲ after 1 hour in solution and scan in positive direction from -0.25 V in regards to OCP (4) ◆ after 120 hours in solution (only for HNS steel) and scan in positive direction from -0.25 V in regards to OCP.

The preliminary stay of nitrogen bearing steel in the work solution, irrespective how long it is (1 or even 200 hours), leads to steady increase in j_{pass} , without clearly expressed plateau. This behavior could be result of the difference in the structure of naturally formed passive layer compared to the structure of the layer formed under polarization. The longer stay in the Ringer's solution prior the potentiodynamic study shifts E_{corr} and E_{pit} in positive direction and wide the passive area, but on the other hand the re-passivation of appeared pits during the scan in opposite direction is impossible.

For the nickel containing steel the passive area also expands for longer preliminary stays in the corrosive solutions. In this case, the appeared pits repassivate during the scan in negative direction and E_{rp} is not affected by the time of preliminary stay.

Potentiostatic studies: The potentiodynamic studies described above showed significant effect

of scan rate on the values of the characteristic potentials. The last could be avoided by obtaining dependencies current vs. time at applied potential. In this way the series of dependencies at applied potentials from 0.05 to 0.4 V (SCE) were developed. This range of potentials was determined from potentiodynamic tests and it includes potentials lower and greater than E_{pitt} obtained potentiodynamically. The potentiostatic curves (Fig. 4) allow both E_{pitt} and the incubation time (t_i) to be determined. At the beginning of each experiment the current goes down reaching a minimum value. If it remains stable in time at this value this indicates that the steel surface is in passive state. If, in opposite the current suddenly grows up this is an indication of pits nucleation. The incubation time is defined by range between the experiment start-up and the onset of the abrupt current rise, which physically corresponds to the time necessary for passive film to be destroyed at the applied potential.

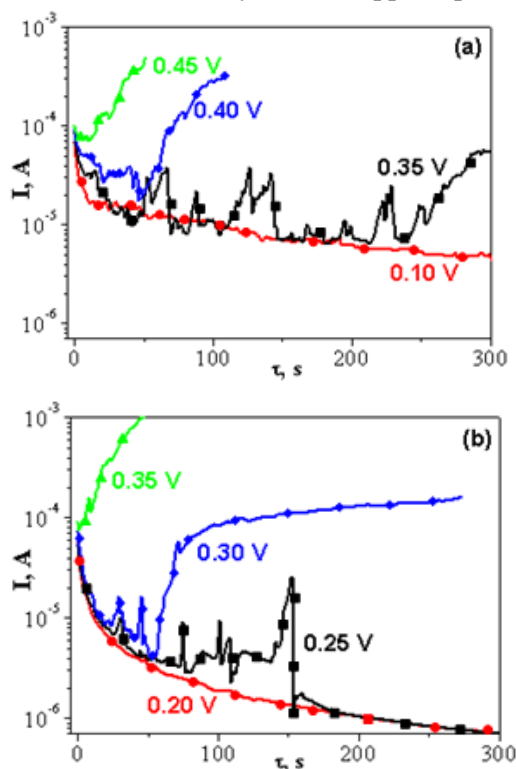


Fig. 4. Potentiostatic dependencies (the applied potentials are presented against SCE) for (a) Cr18Mn12N and (b) Cr18Ni9 steels, 37°C.

The plots in Fig. 5 show that for the Cr18Mn12N steel the pitting potential is $E_{\text{pitt}} = 0.35$ V (SCE) (Fig. 4a) while for the Cr18Ni9 sample it is $E_{\text{pitt}} = 0.30$ V (SCE) (Fig. 4b). These values vary from the values obtained potentiodynamically, as the E_{pitt} of Ni-bearing steel is significantly more negative than the same obtained by potentiodynamic method. The numerous fluctuations in the current vs. time dependence of

nitrogen steel at 0.35 V(SCE) correspond to the formation of metastable pits, which completely re-passivate and stop to develop.

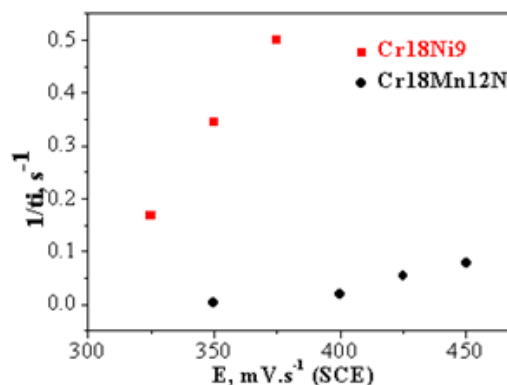


Fig. 5. Pits nucleation rate as a function of the applied potential.

For the applied potentials at which the pits do not appear, the established stationary current for nickel bearing steel is lower than those of nitrogen steel at the same applied potential. This lower value, to some extent, indicates denser and thicker as well as more stable protective layers [12, 13].

Alternatively, the incubation time required for the destruction of Cr18Mn12N steel passive layer is ten times longer than the same for Ni containing steel. For example, at applied potential of 0.35 V (SCE) the incubation time for the nickel steel is about 2.91 s, while for the nitrogen steel it is about 255 s. Therefore, it could be decided that the value of the established stationary current is not adequate for evaluation of the passive layer stability.

The inverse of the incubation time ($1/t_i$) known as *the pit nucleation rate* [13] exhibits almost linear behavior (see Fig. 5) as a function of applied potential. It is obvious that the pits on the high nitrogen steel occur with a lesser speed, which increases slightly with the rise of applied potential. The pits nucleation rate for the chromium-nickel steel is significantly higher and increases linearly with the shift of applied potential in positive direction by step of 25 mV.

Optical microscopy and SEM: In order to establish the type, size and shape of the pits appeared on the surfaces of both investigated steels after the potentiostatic experiments at applied potential by 100 mV more positive than E_{pitt} , the samples were observed by optical and scanning electron microscopy. The images for both steels are presented on Fig. 6.

The optical microscopy after the potentiostatic experiments indicate numerous pits on Cr18Ni9 steel surfaces which are larger in contrast to these on the surface of the Cr18Mn12N samples. These observations confirm the results from potentiostatic

method where the Cr18Ni9 steel has higher pits nucleation rate and shorter incubation time. The pits on nickel bearing steel are in bigger size, more numerous and deeper.

The pits at the nitrogen steel surface are with fine lace cover into which residues of salt products can be observed. The pits are in spherical shape and could be divided formally in two groups: small pits with diameters in the rage 50-60 μm and large pits with diameters of about 200-250 μm .

The pits on the nickel steel surface are also in spherical shape, but in contrast to the nitrogen steel

ones they are larger (with 200-1000 μm in diameter), the pit covers are partially dissolved and with greater degree of cracking.

EDX analysis: EDX analyses of the steels surfaces were performed for surface after 20 minutes stay in Ringer's solution at applied potential more positive than the E_{pitt} . The value of the potential chosen in order to ensure development of the pits at about 10^{-4} A cm^{-2} anodic current density.

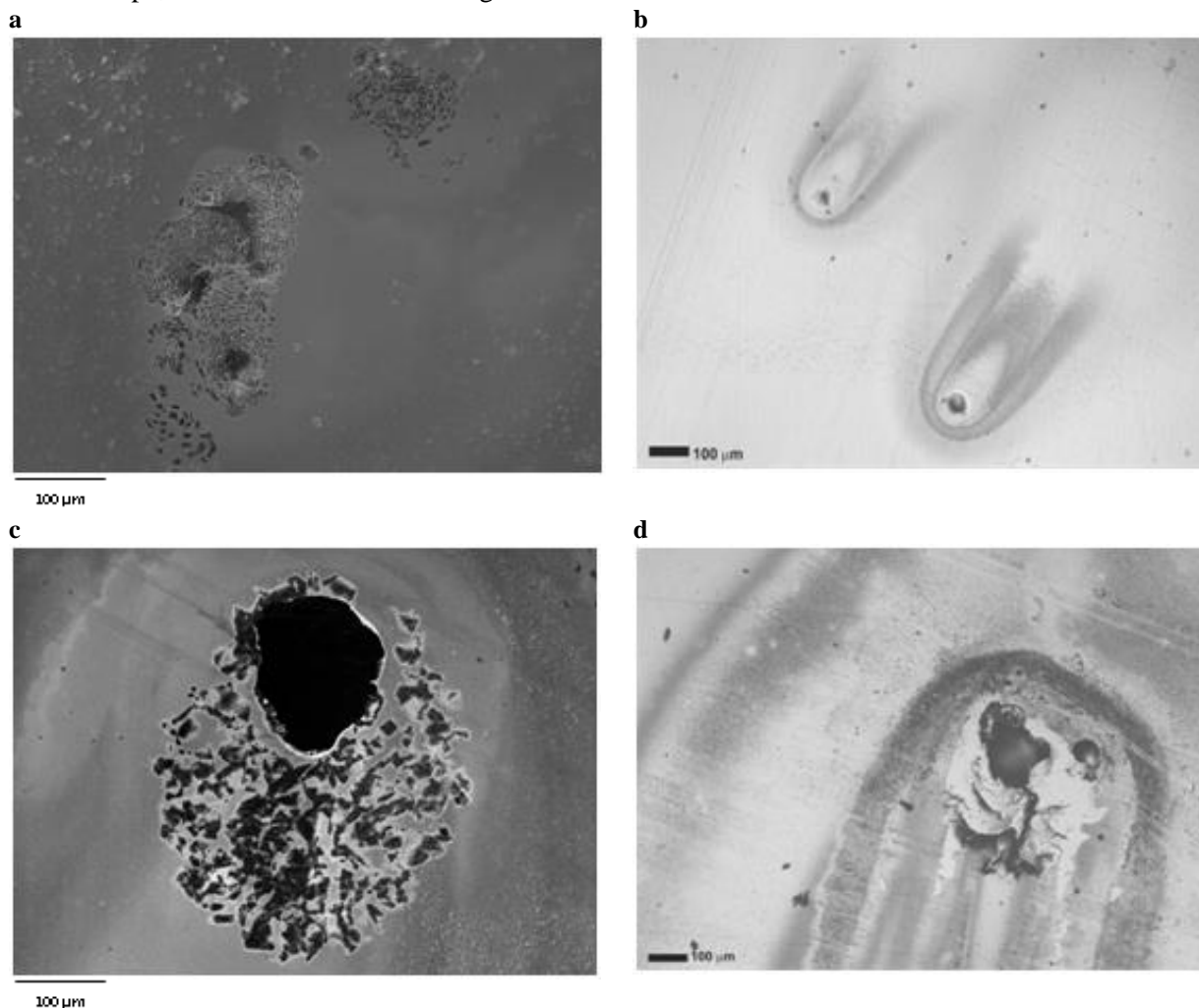


Fig. 6. SEM and optical images of (a, b) Cr18Mn12N and (c, d) Cr18Ni9 steels after potentiostatic polarization

Table 1. The chemical composition (wt.-% and at. %) of the tested stainless steels.

Steel		Cr	Ni	Mn	C	N	Si	P	S
Cr18Mn12N	wt.%	16.50	0.05	12.00	0.04	0.61	0.36	0.011	0.023
	at.%	17.07	0.05	11.74	0.16	2.37	0.70	0.02	0.005
Cr18Ni9	wt.%	17.49	9.37	1.29	0.05	-	0.52	0.022	0.009
	at.%	18.74	8.85	1.23	0.23	-	1.03	0.04	0.016

Table 2. Chemical content of the surface after the potentiostatic corrosion tests, at. %

Elements	Fe	Cr	Mn	Ni	O	C	Si	P	S	Cl	Ca
Cr18Mn12N	24.20	9.08	3.53	-	56.14	4.21	0.63	1.46	0.47	0.17	0.13
Cr18Ni9	37.49	10.24	-	5.24	37.50	6.16	1.00	1.13	0.63	0.30	0.13

The results reveal that in the passive layer of Cr18Mn12N steel the following elements are included (in descending content): Fe, O, Cr, N, Mn and C. For the Cr18Ni9 steel the passive layer consist from Fe, O, Cr and Ni. Therefore, it can be assumed that the passive films on both steels are built mainly from iron and chromium oxides. The high nitrogen content in Cr18Mn12N steel could be result of N enrichment under the passive layer as it is previously described in the literature [14].

The analysis of the surface after the potentiostatic corrosion tests (Table 2) shows that the surface layers consist of oxides of the main alloying elements. Besides, small quantities of C, P, Cl, and Ca are registered. These are result of corrosion solution salts inclusion in the passive layer. It worth noting that the Cl content in Cr18Mn12N corrosion products is relatively low which can be related to formations of nitrates form complexes with iron chlorides and hydroxychlorides which finally hinder the pitting processes [6]. This explanation was proved by Fu et al. [15] and Misawa and Tanabe [16] who demonstrated that the iron dissolution can be reduced by increase in the nitrogen content which actually facilitates the passivation process. The Raman spectroscopy studies [16] revealed that the nitrogen and the oxygen ions in the passive layer form nitrate ions which are incorporated into the oxide layer and suppress the action of the hydrated chloride ions resulting in increased pitting corrosion resistance.

CONCLUSIONS

The corrosion behavior of the high nitrogen steel Cr18Mn12N compared to the nickel steel Cr18Ni9 in Ringer's solution was studied by electrochemical and physical methods in order to evaluate preliminarily the possibility of using Cr18Mn12N for implants in the human body. The study allows to claim the following results, among them:

1. The open circuit potentials of both examined steels in the corrosive media are in the passive states and very close as values.

2. The extended in time stay of the samples in the corrosive solution prior to the electrochemical tests improves the passive films formation.

3. The potentiodynamic and potentiostatic results reveal that the nitrogen steel passes through the stage of metastable pits formation which need more time to pass into active dissolution state. For the nickel steel the pits nucleate faster in shorter incubation time and are larger in size.

Finally, it could be outlined that the HNS steel exhibits better corrosion resistance in Ringer's solution, but additional studies in various media stimulating human body fluids should be carried out.

REFERENCES

1. A.C. Fraker, in ASM Handbook, vol.13, ASM International, USA, 1987, p. 3313.
2. M.Li, T. Yin, Y. Wang, F. Du, X. Zou, H. Gregersen, G. Wang, *Mater. Sci. Eng.*, **C 43**, 641 (2014).
3. S. Virtanen, I. Milosev, E. Gomez-Barrena, R. Trebse, J. Salo, Y.T. Konttinen, *ActaBiomater.*, **4**, 468 (2008).
4. G.E. Novikova, *Prot. Met. Phys. Chem. Surf.*, **47**, 372 (2011).
5. M. Sumita, T. Hanawa, S. H. Teoh, *Mater. Sci. Eng.*, **C 24**, 753 (2004).
6. M. Talha, C.K. Behera, O.P. Sinha, *Mater. Sci. Eng.*, **C 40**, 455 (2014).
7. Q. Chen, G.A. Thouas, *Mater. Sci. Eng.*, **R87**, 1 (2015).
8. M.V. Popa, I. Demetrescu, E. Vasilescu, P. Drob, D. Ionita, C. Vasilescu, M.F. Popa, Proc. 16th Int. Corr. Congr., Beijing, China, 2005.
9. ISO/FDIS 17475 (2005).
10. ASTM G61-86 (2003).
11. I. Milosev, *J. Appl. Electrochem.*, **32**, 311 (2002).
12. M. Kumagai, S.T. Myung, S. Kuwata, R. Asaishi, Y. Katada, H. Yashiro, *Electrochim. Acta*, **54**, 1127 (2009).
13. M.A. Amin, S.S. Abd El Rehim, E.E.F. El Sherbini, *Electrochim. Acta*, **51**, 4754 (2006)
14. H.J. Grabke, *ISIJ Int.*, **36**, 777(1996)
15. Y. Fu, X. Wu, E. Han, W. Ke, K. Yang, Z. Jiang, *Electrochim. Acta.*, **54**, 4005 (2009).
16. T. Misawa, H. Tanabe, *ISIJ Int.*, **36**, 87 (1996).

КОРОЗИОННО ПОВЕДЕНИЕ НА N-СЪДЪРЖАЩИ НЕРЪЖДАЕМИ СТОМАНИ В РАЗТВОР Ringer

Г. П. Илиева¹, М. Х. Лукайчева^{2*}, Б. Р. Цанева², Л. Ц. Жекова³ и Л. Б. Фачиков¹

¹*Химикотехнологичен и металургичен университет, бул. Кл. Охридски 8, 1756 София, България*

²*Технически университет- София, бул. Кл. Охридски 8, 1756 София, България*

³*Институт по металознание, съоръжения и технологии "Акад. А. Балевски" с Център по хидроаеродинамика при БАН, ул. Шипченски проход 67, 1574 София, България*

Постъпила на 13 октомври, 2015 г.; коригирана на 30 ноември, 2015 г.

(Резюме)

Материалите за изработване на импланти използвани в медицината са изработени от различни метали и сплави като основното изискване към всеки от тях е биосъвместимостта. Настоящата работа представя предварителни резултати касаещи приложимостта на високоазотната стомана Cr18Mn12N като материал за изработване на импланти заместващ Ni-съдържащите стомани, които са токсични. За целта са проведени краткосрочни (в продължение на 1 час) и дългосрочни (до 220 часа) измервания на потенциала на отворена верига, както и потенциодинамични и потенциостатични изследвания в разтвор Ringer при 37°C. Разгледано е и влиянието на предварителната подготовка на повърхността. След потенциостатичните измервания с цел определяне на характера на корозионната атака са използвани оптична и сканираща електронна микроскопия. Повърхността на образците е изследвана и посредством Енергийно-дисперсивна спектроскопия с цел определяне на състава на корозионните продукти. На базата на получените резултати може да се заключи, че високоазотната стомана показва по-добра корозионна устойчивост в разтвор Ringer.

Hydrogenation and cracking of nickel coatings electrodeposited in the presence of brighteners

M. Monev

Institute of Physical Chemistry, Bulgarian Academy of Sciences, Acad. G. Bonchev Str., Bl.11, Sofia 1113, Bulgaria

Received October 9, 2015; Revised November 3, 2015

During cathodic polarization in an acidic media containing hydrogenation-enhancing additives, nickel absorbs large quantities of hydrogen and a new crystal phase, nickel hydride is formed. The investigation of the phase transformation of electrodeposited nickel into nickel hydride under cathodic charging showed that the organic compounds 1,4-butyne-2,3-diol and saccharine, both being typical representatives of two classes of additives for nickel electrolytes, which are usually added in order to improve the properties of the layers such as their appearance, internal stresses, *etc.*, contribute to a more complete phase transformation of nickel into nickel hydride. This is assisted by the fine structure of the nickel deposits with a higher density of defects as well as the incorporated compounds containing sulphur as a product of electrochemical transformation of the saccharine. The type of the additives influences both the tendency of the nickel layers to form cracks and the shape of the cracks.

Key words: electrodeposition; nickel coatings; cathodic hydrogenation; nickel hydride; X-ray diffraction; crack formation.

INTRODUCTION

During cathodic polarization in acidic media containing hydrogenation-enhancing additives, nickel absorbs large quantities of hydrogen [1]. A new crystal phase, nickel hydride (β -NiH_x, where $0.7 \leq x \leq 0.8$) with a f.c.c. lattice is formed, the lattice parameter being approximately 6% larger than that of nickel [2]. For a very short time strongly stressed layers are formed [3] that lead to lasting structural alterations - broadening of the grain boundaries [4], crushing of the crystallites [5], formation of cracks [6].

In a previous X-ray analysis it has been established that the conversion of nickel into nickel hydride in bright nickel electrodeposits is more complete than that of matt ones obtained from an additive-free electrolyte [7]. The hydride phase is unstable and disintegrates under normal conditions. In contrast to matt coatings where the disintegration follows an equation inherent to first-order reactions [8], the disintegration of the hydride phase in the bright coatings is not so a fast process and it begins after a certain period of time after the end of hydrogenation [7]. When the hydrogenation is over above a certain degree, a process of crack formation in the bright nickel deposits starts [9]. The cracking process proceeds at a rate which offers a possibility for a direct observation of the initiation and

propagation of the cracks by using a metallographic microscope. A part of the cracks shows a shape close to that of the Archimedes spiral [10].

However, bright coatings can be obtained in the presence of at least two organic additives – each one of the two classes of additives for nickel electrodeposition [11]. In the present work the effect of saccharine and 1,4-butyne-2,3-diol - typical representatives of the two classes of additives on the process of phase transformation, as well as on the subsequent cracking of the nickel coatings after the end of cathodic hydrogenation was investigated.

The study of the process of phase transformation and hydrogen induced cracking can be also of interest for the water electrolysis. Nickel electrodes are widely used in the electrochemical technologies for hydrogen production [12]. With long-term electrolysis in alkaline solution, energy efficiency losses at the nickel cathodes are established, which is manifested in increase in the hydrogen overvoltage at constant cell current [13]. According to one of the hypotheses, such a behavior is associated with the formation of hydride at the nickel cathode surface [14]. In order to reduce the energy consumption, a large number of studies are focused on electrodeposition of new electrode materials on the base of nickel for alkaline as well as for acidic medium (Proton exchange membrane (PEM) hydrogen generators work at very low pH values) [15]. Lowering of the hydrogen overvoltage is reached by increase of the catalytic activity (modification of nickel by incorporation of

To whom all correspondence should be sent:
E-mail: monev@ipc.bas.bg

metallic/non-metallic compounds, including such, containing sulfur [16-18]) and/or by increase of the active surface area of the electrodes. However, the modification of the elemental composition and/or the structure changes the susceptibility of the electrode to hydrogenation, as well. Consequently, the question about the stability of the electrodes in acidic media arises also in the case, where inorganic materials like solid acids or a composite material based on them, containing S, Se, P, As (hydrogenation-enhancing compounds) are used in order to extend the working window of PEM [19].

EXPERIMENTAL

Nickel coatings of thickness approximately 20 μm were deposited onto mechanically polished copper substrates from electrolyte containing: $\text{NiSO}_4 \cdot 7\text{H}_2\text{O}$ - 280 g l^{-1} , $\text{NiCl}_2 \cdot 6\text{H}_2\text{O}$ - 50 g l^{-1} and H_3BO_3 - 30 g l^{-1} . Current density of 5 A dm^{-2} , pH 4.0-5.0, deposition temperature of 55 $^\circ\text{C}$ and air agitation of the bath were used. Saccharine up to concentration of 1.0 g l^{-1} and 1,4-butynediol up to concentration of 0.2 g l^{-1} were added to this electrolyte either separately or in a combination. Immediately after deposition and rinsing, the samples were subjected to hydrogenation in a 1N H_2SO_4 solution containing selenious acid (H_2SeO_3). The conditions of each hydrogenation procedure are given in the figure captions.

After rinsing with distilled water and ethyl alcohol the hydrogenated samples were studied by X-ray analysis with Co K_α X-rays. The volume fraction of the hydride phase (M_{NiH}) was calculated by means of the formula proposed in [7]:

$$M_{\text{NiH}} = \frac{(I_{hkl})_{\text{NiH}}}{(I_{hkl})_{\text{NiH}} + (I_{hkl})_{\text{Ni}}}$$

The integral intensities of the Ni line 111 ($(I_{hkl})_{\text{Ni}}$) and Ni-H line 111 ($(I_{hkl})_{\text{NiH}}$) were measured by oscillating the goniometer of the X-ray diffractometer within the range of $47^\circ \leq \theta \leq 55^\circ$.

The samples were examined for cracking by a metallographic microscope using a magnification of 120 x.

RESULTS

Formation and disintegration of nickel hydride

The X-ray analysis of samples, deposited from electrolytes containing individual brighteners shows that in both cases the tendency towards hydrogenation increases with increase of their concentration the effect being more expressed in the presence of 1,4-butynediol in the electrolyte

(Fig. 1). The successive addition of both brighteners leads to an increase in their activity, and almost a total transformation of the nickel coating into a hydride phase is achieved for a short time (Fig. 2). According to the previous investigations, the saccharine activity could be related to deposition of fine-grained coatings [20] and to incorporation of disintegrated products containing sulphur [21]. The addition of 1,4-butynediol also causes a decrease of the crystallites size [20, 22] as well as an increase of the value of microdeformations [20]. Moreover, the 1,4-butynediol stimulates the incorporation of sulphur when both saccharine and 1,4-butynediol are added in the electrolyte [11].

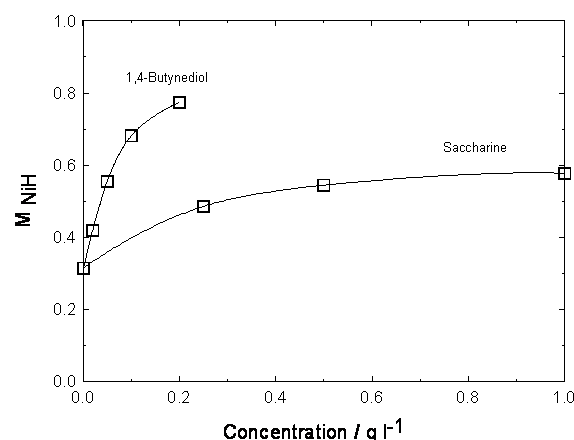


Fig. 1. Volume fraction of hydride phase as a function of brighteners' concentration at separate addition to the nickel electrolyte. Hydrogenation conditions: 1n H_2SO_4 + 10 mg l^{-1} H_2SeO_3 , 15 mA cm^{-2} (1.5 A dm^{-2} cathodic current density), 30 min.

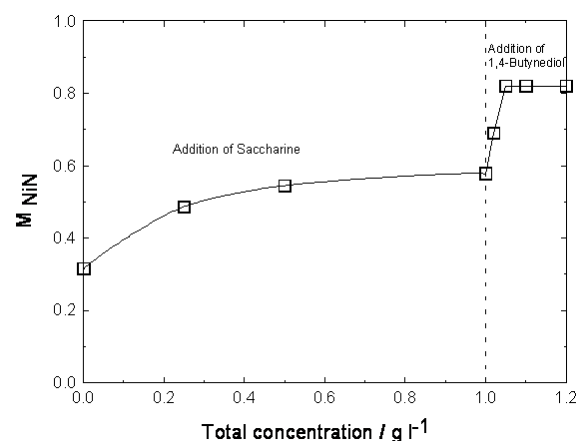


Fig. 2. Volume fraction of hydride phase as a function of brighteners' concentration at successive addition to the nickel electrolyte. Hydrogenation conditions: 1n H_2SO_4 + 10 mg l^{-1} H_2SeO_3 , 15 mA cm^{-2} , 30 min.

Under normal conditions, the nickel hydride phase is unstable (Fig. 3). Coatings, deposited from electrolyte containing only saccharine disintegrate

immediately when the hydrogenation is over. Obviously, the incorporation of sulphur in the coatings as a product of electrochemical transformation of the saccharine facilitates not only the hydrogenation of nickel layers but also the desorption of the hydrogen after the end of hydrogenation. Coatings, deposited from electrolyte containing both brighteners exhibit a retarded disintegration and the time of delay increases with increasing butyndiol concentration (Fig. 4).

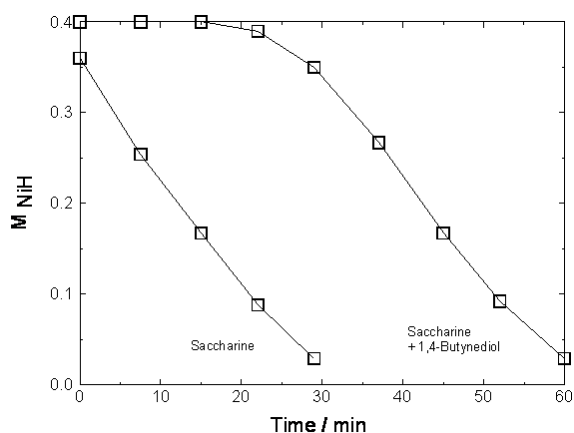


Fig. 3. Disintegration of hydride phase at a room temperature as a function of the type of the nickel coating. Hydrogenation conditions: 1n H₂SO₄ + 1 mg l⁻¹ H₂SeO₃, 2.5 mA cm⁻², 40 min.

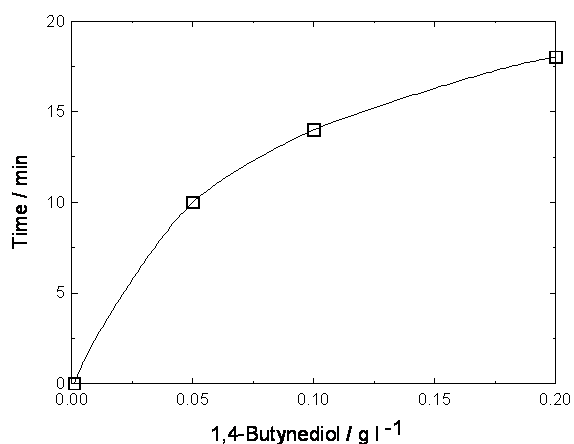


Fig. 4. Time of delay of hydride phase disintegration as a function of 1,4-butynediol concentration in electrolyte containing 1 g l⁻¹ saccharine. Hydrogenation conditions: 1n H₂SO₄ + 1 mg l⁻¹ H₂SeO₃, 15 mA cm⁻², 30 min.

A smaller delay of hydride phase disintegration is observed in coatings obtained from an electrolyte containing only butyndiol. The influence of 1,4-butynediol on the disintegration of the hydride phase could be seen in several directions. The addition of 1,4-butynediol leads to deposition of coatings with a fine structure, showing a higher density of defects [20] and by this way, favourable conditions are created for stronger absorption of the

hydrogen into the nickel matrix. It is known that the defects and grain boundaries are sites which could act as H traps [23, 24]. Moreover, a largest quantity hydrogen is absorbed in the coatings obtained from an electrolyte containing both brighteners. The bright nickel coatings occlude hydrogen in amounts exceeding those needed for hydride phase formation [21, 25], and this phase visibly begins to disintegrate only after desorption of a portion of the occluded hydrogen.

Cracking of the hydrogenated nickel coatings

The metallographic study of samples subjected to cathodic hydrogenation indicates that cracking of the coatings is not observed when they are produced in an additive-free electrolyte. The hydrogenation degree of such coatings is considerably low [7, 21] and obviously, the internal stresses are not so high in order to cause cracks. The coatings produced in electrolyte containing only saccharine didn't show a tendency for cracking. These coatings are strongly hydrogenated and this effect is confirmed by the great alteration of the internal stresses during the cathodic hydrogenation [21]. However, cracks are not formed and this is probably due to the internal stresses which after the end of cathodic hydrogenation (followed by the hydrogen desorption) remain in the range of compressive stresses as are the own stresses of these coatings after deposition [21]. Cracks of an irregular shape are formed after hydrogenation of coatings, deposited from electrolyte containing only 1,4-butynediol. The spiral type of cracking begins to appear when the deposits are obtained from an electrolyte containing both brighteners (Fig. 5a). This occurs under "mild" hydrogenation. Ununiform cracking after "mild" hydrogenation shows that the hydrogenation doesn't run uniformly, both on the surface and in the bulk of the bright coatings. A regular net of cracks is formed after a strong hydrogenation of the coatings obtained from electrolyte containing both brightening additives [9, 10].

In some cases, probably due to improper preliminary processing of the substrate, the cathodic hydrogenation doesn't cause crack formation but blistering. Formation of bubbles is observed after cathodic hydrogenation of the coatings, deposited in the presence of saccharine (Fig. 5b). In coatings, deposited from electrolyte containing both brighteners, circle peelings are removed from their surface because these coatings are more brittle (Fig. 5c). The same circle peelings were also observed on the surface of zinc coatings,

obtained from zincate electrolytes in the presence of certain brighteners [26]. This effect could be connected with a hydrogenation of the iron substrate in the initial stages of the process when the rate of hydrogen reaction is much higher than that of the zinc electroreduction. The formation of bubbles as well as the removal of circle peelings from the surface of the coatings were observed after a certain period of time after the end of hydrogenation of nickel as well as after the deposition of zinc. The form and the time for appearance of blistering indicate that centres of internal stresses are created because of the ununiform hydrogenation and/or of the redistribution of the hydrogen after ending up the hydrogenation.

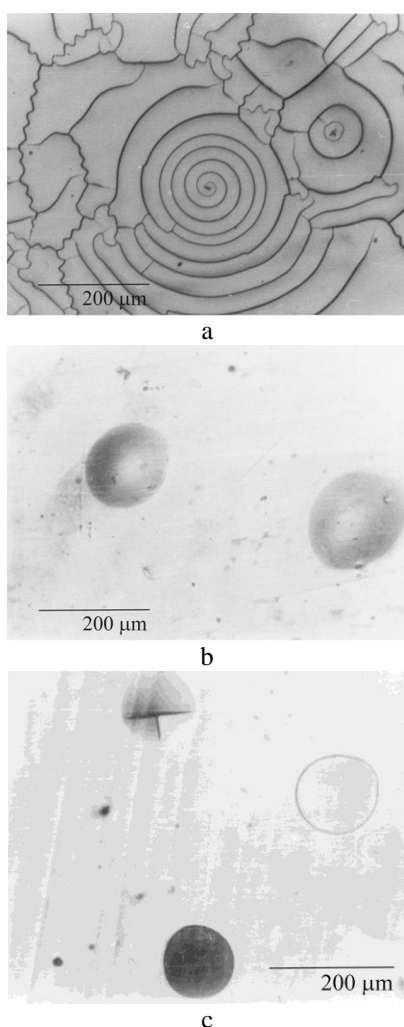


Fig. 5. Hydrogen induced structural alterations in nickel coatings: a - cracking after cathodic hydrogenation of coatings deposited from electrolyte containing both brighteners; b - blisters, formed after cathodic hydrogenation of a coating deposited from electrolyte containing saccharine; c - circles, peeled after cathodic hydrogenation of a coating deposited in the presence of both brighteners.

CONCLUSION

Both additives in the nickel electrolyte - 1,4-butynediol and saccharine contribute to a more complete phase transformation of nickel into nickel hydride. This is assisted by the fine structure of the nickel deposits with a higher density of defects as well as the incorporated compounds containing sulphur as a product of electrochemical transformation of the saccharine.

The delay of the hydride phase disintegration is related to the influence of 1,4-butynediol on the coating structure, the effect being more enhanced in combination with saccharine.

Cracking of the coatings, as a result of cathodic hydrogenation, is not observed when they are produced in an additive-free electrolyte or in an electrolyte containing saccharine. Concentric and spiral cracks are formed only in coatings, deposited from an electrolyte containing both brightening additives. It could be suggested, that this is related to the influence of three factors: formation of strain regions in the nickel deposits, as a result of irregular hydrogenation; various mechanical properties of the layers due to the influence of the additives and adhesion of the layers to the substrate.

Acknowledgement: The present studies were performed with the kind support of Fund "Scientific Research" (Research Project X-484) and Deutsche Forschungsgemeinschaft (Research Project 436 BUL 113/97).

REFERENCES

1. B. Baranowski, M. Smialowski, *Bull. Acad. Pol. Sci., Ser. Sci. Chim., Geol. Geogr.*, **7**, 663 (1959).
2. A. Janko, *Bull. Acad. Pol. Sci., Ser. Sci. Chim.*, **8**, 131 (1960).
3. Z. Szklarska-Smialowska, M. Smialowski, *Bull. Acad. Pol. Sci., Ser. Sci. Chim.*, **6**, 427 (1958).
4. A. Janko, P. Michel, *C.R. Acad. Sci.*, **251**, 131 (1960).
5. A. T. Sanzharowski, O. S. Popova, *Zh. Prikl. Khim.*, **34**, 2120 (1961).
6. A. Janko, A. Szummer, *Bull. Acad. Pol. Sci., Ser. Sci. Chim.*, **14**, 885 (1966).
7. St. Rashkov, M. Monev, I. Tomov, *Surface Technology*, **16**, 203 (1982).
8. A. Janko, *Bull. Acad. Pol. Sci., Ser. Sci. Chim.*, **10**, 617 (1962).
9. St. Rashkov, M. Monev, N. Atanassov, *Surface Technology*, **17**, 309 (1982).
10. M. Monev, St. Rashkov, R. Kaishev, *Surface Technology*, **17**, 315 (1982).
11. Yu. Yu. Matulis, *Blestjashtie elektroliticheskie pokritija*, Vilnius, Mintis, 1969.
12. K. Zeng, D. Zhang, *Prog. Energy Combust. Sci.*, **36**, 307 (2010).

13. H. E. G. Rommal, P. J. Moran, *J. Electrochem. Soc.*, **132**, 325 (1985).
14. D. M. Soares, O. Teschke, I. Torriani, *J. Electrochem. Soc.*, **139**, 98 (1992).
15. E. Navarro-Flores, Zh. Chong, S. Omanovic, *J. Mol. Catal. A: Chem.*, **226**, 179 (2005).
16. J. I. Krjukov, S. F. Chernishov, A. G. Pshenichnikov, L. I. Altentaller, I. P. Naumov, J. S. Lapin, N. P. Kuznecov, *Elektrochimija*, **29**, 504 (1993).
17. N. A. Assuncao, M. J. Giz, G. Tremiliosi-Filho, E. R. Gonzalez, *J. Electrochem. Soc.*, **144**, 2794 (1997).
18. Y. Tie-chui, L. Rui-di, Zh. Ke-chao, *Trans. Nonferrous Met. Soc. China*, **17**, 762 (2007).
19. A. Goñi-Urtiaga, D. Presvytes, K. Scott, *Int. J. Hydrogen Energy*, **37**, 3358 (2012).
20. N. Atanassov, Hr. Bozhkov, St. Rashkov, *Surface Technology*, **17**, 291 (1982).
21. M. Monev, M. E. Baumgärtner, O. Loebich, Ch. J. Raub, *Metalloberfläche*, **45**, 2 (1991).
22. I. Tomov, M. Monev, *J. Appl. Electrochem.*, **22**, 262 (1992).
23. A. Atrens, D. Mezzanote, N. F. Fiore, A. Genshaw, *Corros. Sci.*, **20**, 673 (1980).
24. R. M. Latanision, M. Kurkela, *Corrosion-Nice*, **39**, 174 (1983).
25. P. Ch. Borbe, F. Erdmann-Jesnitzer, W. Schoebel, *Z. Metallkd.*, **71**, 227 (1980).
26. M. Monev, L. Mirkova, I. Krastev, Hr. Tsvetkova, St. Rashkov, W. Richtering, *J. Appl. Electrochem.*, **28**, 1107 (1998).

НАВОДОРОДЯВАНЕ И НАПУКВАНЕ НА НИКЕЛОВИ ПОКРИТИЯ ЕЛЕКТРООТЛОЖЕНИ В ПРИСЪСТВИЕ НА БЛЯСЪКООБРАЗОВАТЕЛИ

М. Монеv

Институт по физикохимия, Българска академия на науките, ул. Акад. Г. Бончев, Бл. 11, 1113 София

Постъпила на 9 октомври, 2015 г.; коригирана на 3 ноември, 2015 г.

(Резюме)

При катодна поляризация в кисела среда, съдържаща стимулиращи наводородяването добавки, никелът абсорбира значителни количества водород и се образува нова кристална фаза, никелов хидрид. Изследването на фазовото превръщане на електроотложен никел в никелов хидрид при катодно наводородяване показва, че органичните съединения 1,4-бутиндиол и захарин, типични представители на два класа добавки за никелови електролити, които обичайно се използват за подобряване на свойствата на покритията като външен вид, вътрешни напрежения и др., допринасят за по-пълното превръщане на никела в никелов хидрид. Това се дължи на по-фината структура на никеловите отложения с по-висока плътност на дефекти, както и на включенията, съдържащи сяра като продукт от електрохимичното превръщане на захарина. Добавките оказват влияние както върху склонността на никеловите слоеве към напукване, така също и върху вида на пукнатините.

Influence of glycine on the electrochemical deposition of Sn-Co alloy from gluconate electrolyte

T. Valkova*, I. Krastev

Institute of Physical Chemistry, Bulgarian Academy of Sciences, 1113 Sofia, Bulgaria

Received November 11, 2015; Revised January 5, 2016

The influence of glycine on the electrochemical processes of deposition and dissolution of tin, cobalt and tin-cobalt alloy from a gluconate/sulfate electrolytes are studied by means of cyclic voltammetry.

The addition of glycine to the weak acid electrolyte for deposition of Sn-Co alloy has no significant influence on the deposition of tin and relatively strong influence on the deposition of cobalt, as well as a strong effect on the deposition of Sn-Co alloy. The addition of glycine and the increase of its concentration lead to increase in the cobalt percentage in the coatings.

Dull coatings with high cobalt content can be deposited from the investigated electrolyte. Depending on the pH and glycine addition the deposition of coatings with cobalt content in the range from 0 up to 65 wt. % is possible.

Key words: electrodeposition, tin-cobalt alloys, glycine

INTRODUCTION

Tin-cobalt electrodeposited alloy coatings are extensively applied as a convenient and economic way to achieve an attractive finish on lock and door hardware, plumbing fixtures, tubular furniture, and automobile interior trim and fittings. In addition, bright tin-cobalt alloy coatings have mechanical and electrochemical properties similar to those of chromium coatings. However, chromium plating is hazard. In view of that, electrolytic tin-cobalt alloy coatings can be considered to effectively replace chromium coatings [1, 2].

Tin-cobalt alloys plating could also be a substitute for cadmium in electronic application since the alloy resist oxidation and has a low contact resistance [3]. The Co-Sn electrolytes used are environmentally friendly, non-toxic, non-corrosive, and the electrodeposition process takes place at high energy efficiency. Tin-cobalt coatings can be used as a substitute of precious-metal coatings, avoiding the use of highly toxic cyanide electrolytes [4].

Much attention has been recently paid in the field of lithium batteries for the synthesis of new negative materials as alternatives to graphite materials. Among them, tin-based compounds have reached a particular attention. Tin-cobalt alloys find extensive application in this field, because it has been shown that the addition of Co gives the highest specific capacity [5], avoiding mechanical stress due to the Li-intercalation process [6].

Electrodeposited lead-based alloys have been used as overlays for plain bearing for many years. The toxicity of lead requires searching for lead-free alternatives. Tin-cobalt alloys [7] and compositionally modulated Sn-Co alloy multilayer coatings can be used as alternatives [8].

According to the phase diagram Sn-Co alloy may be composed of various intermetallic compounds depending on its metal content [9]. The preparation of heterogeneous coatings offers possibilities for investigation of the self-organization phenomena as observed during the deposition of other cobalt alloys – i.e. those with indium and antimony [10].

The deposition of the Sn-Co alloys is performed from sulfate/gluconate, citrate, fluoride and pyrophosphate electrolytes [11-13]. The sulfate/gluconate bath is highly prone to oxidation.

Glycine is known to stabilize both alkaline and acidic plating baths, it exhibits high buffering properties, which is important for stabilizing of pH on the electrode surface during electrodeposition [14]. Electrolytes containing glycine were used for electrodeposition of Co [15, 16] and some Co alloys [17-19].

The aim of this work is to study the influence of glycine on the electrochemical deposition of Sn-Co alloys.

EXPERIMENTAL

The composition of the electrolyte for deposition of Sn-Co alloy coatings is given in Table 1.

To whom all correspondence should be sent:

E-mail: tvalkova@ipc.bas.bg

Distilled water and *p.a.* grade reagents were used. The experiments were performed in a glass cell of 100 cm³ at room temperature without stirring of the electrolyte. The working electrode (1 cm²) and the two counter electrodes were made of platinum. A reference electrode Ag/AgCl with $E_{\text{Ag/AgCl}} = + 0.197$ V against the hydrogen electrode was used. All potentials in the present study are given against this reference electrode. The sweep rate of the potential was 0.020 V s⁻¹.

Table 1. Electrolyte composition

Composition	Concentration, g dm ⁻³
Sn as (CH ₃ SO ₃) ₂ Sn	0-5
Co as CoSO ₄ ·7H ₂ O	0-5
Na ₂ SO ₄	0-50
C ₆ H ₁₁ NaO ₇	0-50
C ₂ H ₅ NO ₂	0-50
KOH	0-5

The cyclic voltammetric investigations were performed by means of a computerized potentiostat/galvanostat PAR 273A (Princeton Applied Research) using the PowerCorr software for electrochemical corrosion studies.

The alloy coatings, *ca.* 5 μm thick, were deposited on 0.3 mm thick copper substrates, 2 x 1 cm in an electrolysis cell of 100 cm³. The cobalt content in the coatings as well as their thickness was determined using a Fischerscope XRAY-XDAL apparatus for X-ray fluorescence.

RESULTS AND DISCUSSION

Tin deposition

Figure 1 shows the effect of the complex forming agent for tin (C₆H₁₁O₇Na in this case) on the electrode processes. The main function of sodium gluconate is to inhibit the hydrolysis of Sn(II) ions. Gluconate form soluble complexes in both slightly acidic and alkaline baths. Molar ratio of Na-gluconate to Sn should be at least 1.5 : 1 [8]. The presence of C₆H₁₁O₇Na in the electrolyte leads to a slight polarization and inhibition of the cathodic reaction. Gluconate is designated as GH₄⁻, and the corresponding acid is gluconic acid, i.e. HGH₄, where the first H refers to the carboxylic acid hydrogen and H₄ refers to the four hydrogen

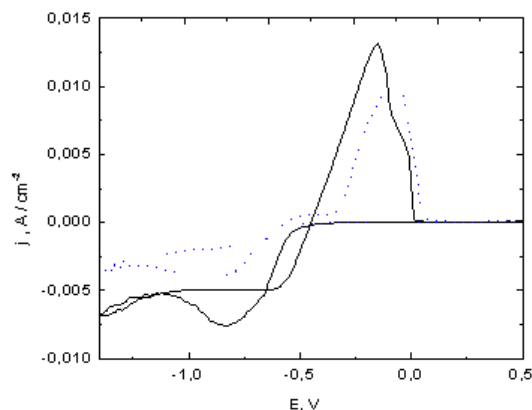


Fig.1. Influence of gluconate on the electrode processes during electrodeposition of tin from *sulphate electrolyte* at pH=3.5. $C_{\text{Sn}}=5$ g dm⁻³; $C_{\text{Na}_2\text{SO}_4}=40$ g dm⁻³ — $C_{\text{C}_6\text{H}_{11}\text{NaO}_7}=0$ g dm⁻³; ---- $C_{\text{C}_6\text{H}_{11}\text{NaO}_7}=50$ g dm⁻³; $v= 20$ mV s⁻¹

atoms on the secondary alcohol. Gluconic acid forms two kinds of complexes [20]. In acid media, the metal ion is bound into a complex via a carboxyl group ligand. The stability constants have relatively small values. Marksin et al. [21] reported that tin forms Sn(GH₄)⁺ and Sn(GH₄)₂ complexes with stability constants logK = 3.01 and logK = 2.28. In presence of gluconate the tin reduction starts at more negative values, due to the formation of tin-gluconate complexes.

Two anodic reactions are detected at case of dissolution of tin in presence of gluconate ions instead of one observed in the absence of gluconate. The first oxidation peak is small and is related to the complexing action of gluconate ions on tin ions produced during oxidation process [22].

Figure 2 shows the cyclic voltammetric curves obtained for tin electrodeposition from sulphate/gluconate electrolyte with addition of 50 g dm⁻³ glycine. The presence of glycine in the gluconate containing electrolyte at pH=3.5 has very slight effect on deposition of tin (Fig. 2a).

At pH=5 (Fig 2b) during the deposition of tin two cathodic reactions are detected corresponding to deposition from different complexes. According to Survila [23] three complex species can be present in comparable amounts in such electrolyte. Sulphate complexes prevail in more acidic media and, as pH increase, they are replaced by Sn(GH₄)₂. Also Sn(OH)⁺ and Sn(OH)₂ products of Sn(II) hydrolysis, can be formed at pH > 4, but this process is kinetically impeded [23]. The addition of glycine in the electrolyte has negligible effect on the first cathodic process but leads to some depolarization of the second cathodic reaction which correspond to the tin gluconate complexes in the presence of glycine (Fig. 2b).

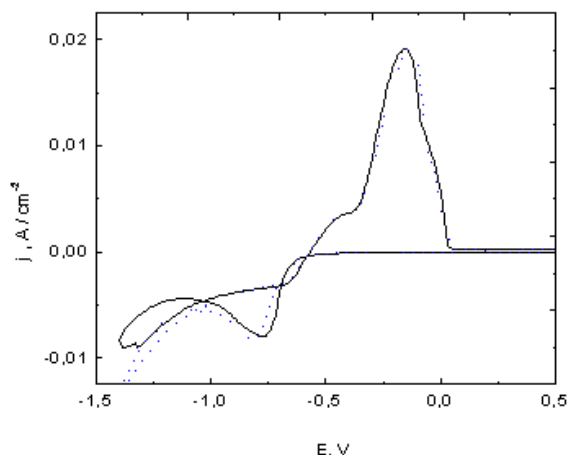


Fig. 2a. Influence of glycine on the electrode processes during electrodeposition of tin from sulphate/gluconate electrolyte at pH=3.5. $C_{Sn}=5 \text{ g dm}^{-3}$; $C_{Na_2SO_4}=40 \text{ g dm}^{-3}$; $C_{C_6H_{11}NaO_7}=50 \text{ g dm}^{-3}$; — $C_{C_2H_5NO_2}=0 \text{ g dm}^{-3}$; ---- $C_{C_2H_5NO_2}=50 \text{ g dm}^{-3}$; $v=20 \text{ mV s}^{-1}$

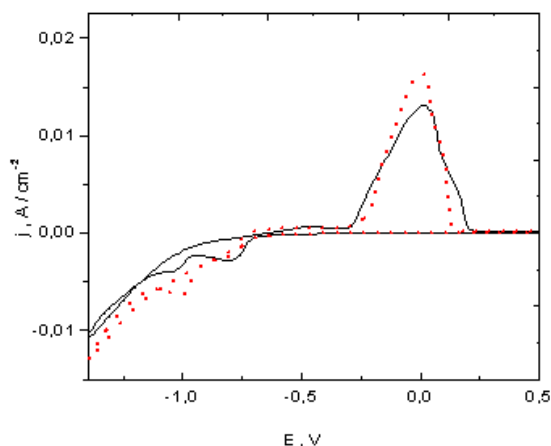


Fig. 2b. Influence of glycine on the electrode processes during electrodeposition of tin from sulphate/gluconate electrolyte at pH=5. $C_{Sn}=5 \text{ g dm}^{-3}$; $C_{Na_2SO_4}=40 \text{ g dm}^{-3}$; $C_{C_6H_{11}NaO_7}=50 \text{ g dm}^{-3}$; — $C_{C_2H_5NO_2}=0 \text{ g dm}^{-3}$; ---- $C_{C_2H_5NO_2}=50 \text{ g dm}^{-3}$; $v=20 \text{ mV s}^{-1}$

In the anodic processes, there is no polarization effect of the glycine ions on tin dissolution at both pH.

Cobalt deposition

The effect of the complex forming agent ($C_6H_{11}O_7Na$) on the deposition of cobalt from sulfate electrolyte is shown on Fig.3. Strong polarization of the cathodic process in the presence of $C_6H_{11}O_7Na$ is observed due to the formation of $[Co(C_6H_{11}O_7)]^+$ complex (Fig.3 dashed line). Gluconate complex of cobalt have been found to be $[Co(C_6H_{11}O_7)]^+$ in solution of pH < 7.5 with stability constant $\lg K=0.57$ [24]. It has been suggested that the gluconate ion is attached to Co, by coordination through carboxyl group and one of

the adjacent hydroxyl groups [25]. The cobalt electrodeposition is accompanied with simultaneous hydrogen evolution as a side reaction. Decreased overall rate of the electrochemical reaction in presence of gluconate is registered.

In the anodic processes, the effect of the gluconate ions on cobalt dissolution is ambiguous. The anodic peak potential of the dissolution of cobalt in presence of gluconate is observed in the same potential range compared with the gluconate free electrolyte.

Glycine is a simple amino acid usually presented with the chemical formula NH_2CH_2COOH . Depending of the pH of the solution, glycine exists as a cation in acidic solution, as neutrally charged zwitterion at intermediate pH values, and as anion in basic media. It is known from basic chemistry that glycine form complexes with Co^{2+} ions in aqueous solution [26]. Formation of three complexes is possible depending on the pH of the

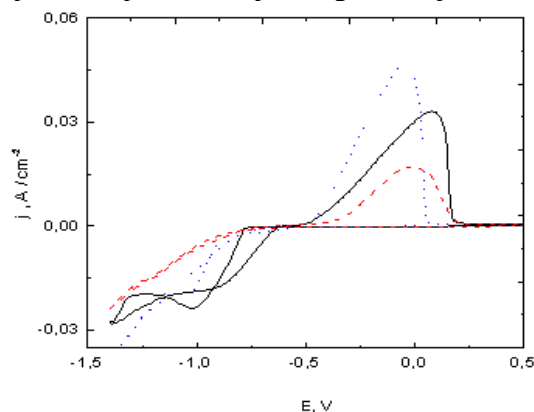


Fig. 3. Influence of glycine and gluconate on the electrode processes during electrodeposition of cobalt from sulphate electrolyte at pH=5. $C_{Co}=5 \text{ g dm}^{-3}$; $C_{Na_2SO_4}=40 \text{ g dm}^{-3}$; $v=20 \text{ mV s}^{-1}$; — $C_{Na_2SO_4}=40 \text{ g dm}^{-3}$; ... $C_{C_2H_5NO_2}=50 \text{ g dm}^{-3}$; ---- $C_{C_6H_{11}NaO_7}=50 \text{ g dm}^{-3}$

solution $Co(NH_2CH_2COOH)^+$, $Co(NH_2CH_2COOH)_2$ and $Co(NH_2CH_2COOH)_3^-$ with stability constant $\lg K=4.6$, $\lg K=8.4$ and $\lg K=10.8$ respectively. The formation of Co-glycine complexes is favored at high pH in the cobalt electrolyte.

The effect of the glycine addition on the deposition of cobalt from sulfate electrolyte is shown also on Fig.3. Strong polarization of the cathodic process in the presence of NH_2CH_2COOH is observed due to the formation of $Co(NH_2CH_2COOH)_3^-$ complex (Fig.3 dot line).

In the anodic processes, the effect of the glycine ions on cobalt dissolution is registered. The anodic peak potential of the dissolution of cobalt in presence of glycine increased and is shifted to more negative values compared with the glycine free electrolyte.

Figure 4 shows the cyclic voltammetric curves obtained for cobalt electrodeposition from sulphate/gluconate electrolyte with addition of 50 g dm⁻³ glycine. The presence of glycine in this

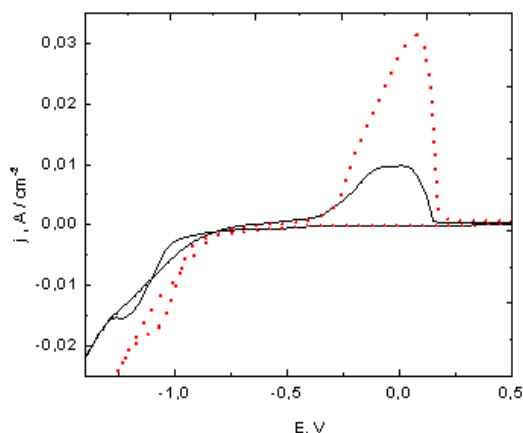


Fig. 4. Influence of glycine on the electrode processes during electrodeposition of cobalt from sulphate/gluconate electrolyte at pH=5. $C_{Co}=5 \text{ g dm}^{-3}$; $C_{Na_2SO_4} = 40 \text{ g dm}^{-3}$; $C_{C_6H_{11}NaO_7} = 50 \text{ g dm}^{-3}$; — $C_{C_2H_5NO_2} = 0 \text{ g dm}^{-3}$; --- $C_{C_2H_5NO_2} = 50 \text{ g dm}^{-3}$; $v = 20 \text{ mV s}^{-1}$

electrolyte has very strong depolarizing effect. Glycine acts as accelerator for cobalt reduction and does not block the active sites on the electrode surface for cobalt deposition.

The higher anodic maximum corresponds to the dissolution of increased co-amount, deposited in the cathodic period.

Tin-Cobalt alloy deposition

Figure 5 shows the cyclic voltammetric curves recorded at pH=5 in sulphate/gluconate electrolytes containing ions of both metals separately and together. During the deposition of tin two cathodic reactions are registered. During investigation of cobalt deposition from the same electrolyte in the absence of tin the occurrence of one cathodic reaction is observed. In this case, tin is the more positive component (both deposition peaks of tin, respectively the firsts peak recorded at -800 mV and the second peak recorded at -1050 mV are less cathodic (less negative) compared with the deposition peak of pure cobalt registered at -1200 mV). When cobalt is added to the solution of tin two cathodic maxima are observed. The first cathodic maximum recorded on cyclic voltammetric curve of the alloy, which corresponds to the deposition of pure tin is polarised compared with those of pure tin and the second cathodic maximum is depolarized compared to pure cobalt. The differences between the size and the position of the peaks in the case of the alloy deposition and the deposition of the separate metals are due to the

reformation of the complexes in the alloy electrolyte, because the experiments are carried out using the same concentration of free complexing agents in all electrolytes.

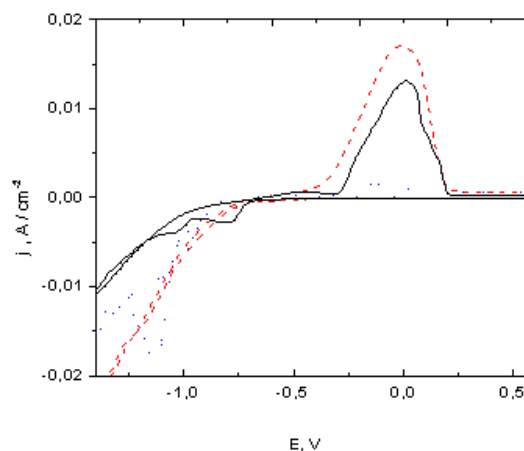


Fig. 5. CVA curves of tin, cobalt and alloy deposition from sulphate/gluconate electrolytes at pH=5 $C_{Na_2SO_4} = 40 \text{ g dm}^{-3}$; $C_{C_6H_{11}NaO_7} = 50 \text{ g dm}^{-3}$; $v = 20 \text{ mV s}^{-1}$ — $C_{Sn} = 5 \text{ g dm}^{-3}$; --- $C_{Co} = 5 \text{ g dm}^{-3}$; $C_{Sn} = 5 \text{ g dm}^{-3}$; $C_{Co} = 5 \text{ g dm}^{-3}$

Co-deposition of tin and cobalt from sulfate/gluconate electrolyte solution was mainly reported as a normal system [11]. The more positive metal, tin, was deposited preferentially.

Two anodic reactions are detected at case of dissolution of tin and one during dissolution of cobalt and the alloy. The main oxidation peak of the reaction of the alloy is in the potential range where dissolution of tin and cobalt takes place.

Figure 6 shows the cyclic voltammetric curves in sulphate/gluconate electrolytes recorded at different pH. The fresh prepared solution has pH of about 3.5. Adjusting the pH to 5 by addition of KOH results in a strong polarization effect on the first cathodic maximum during the deposition of the alloy. This maximum is connected with deposition of pure tin. It is known that the pH is the main factor that governs the rate of Sn(II) reduction. In gluconate solution the electroreduction of tin is accompanied by inhibitive adsorption that grows with pH [27]. The potential of the second cathodic reaction remains unchanged and a strong decrease of the reaction rate is registered.

Figure 7 shows the cyclic voltammetric curves at different glycine concentrations in the alloy deposition electrolyte recorded at pH=5. The increase of the glycine concentration leads to increase of reaction rate of the first cathodic reaction, and depolarization of the second cathodic reaction. During anodic scan easier dissolution of

the coating depending on the glycine concentration is observed. At pH=3.5 the same effect of glycine concentration on the deposition of the alloy is observed (not shown in the paper).

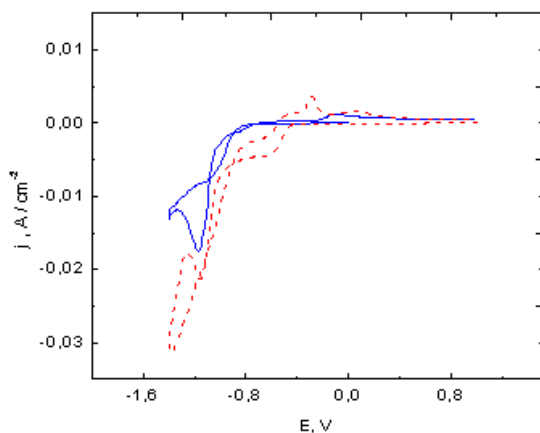


Fig. 6. Influence of the pH on the electrode processes during electrodeposition of the alloy from sulphate/gluconate electrolytes. $C_{Na_2SO_4} = 40 \text{ g dm}^{-3}$; $C_{C_6H_{11}NaO_7} = 50 \text{ g dm}^{-3}$; $C_{Sn} = 5 \text{ g dm}^{-3}$; $C_{Co} = 5 \text{ g dm}^{-3}$ $v = 20 \text{ mV s}^{-1}$ — pH = 5 ; ---- pH = 3.5

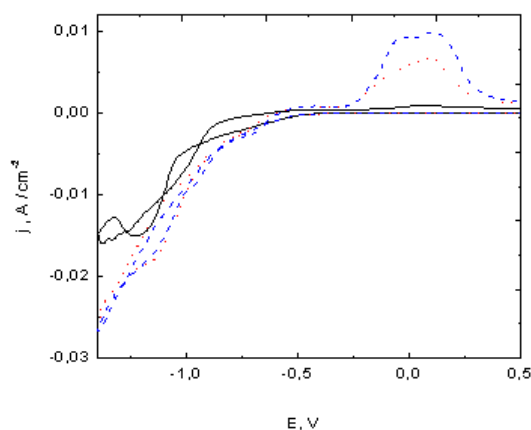


Fig. 7. Influence of glycine on the electrode processes during electrodeposition of the alloy from sulphate/gluconate electrolyte pH=5. $C_{Na_2SO_4} = 40 \text{ g dm}^{-3}$; $C_{C_6H_{11}NaO_7} = 50 \text{ g dm}^{-3}$; $C_{Sn} = 5 \text{ g dm}^{-3}$; $C_{Co} = 5 \text{ g dm}^{-3}$ $v = 20 \text{ mV s}^{-1}$ — $C_{C_2H_5NO_2} = 0 \text{ g dm}^{-3}$; $C_{C_2H_5NO_2} = 15 \text{ g dm}^{-3}$; ---- $C_{C_2H_5NO_2} = 30 \text{ g dm}^{-3}$

Figure 8 shows the effect of both pH of the electrolyte and the addition of glycine in the electrolyte on the composition of the alloy. In the absence of glycine in the electrolyte at pH=3.5, pure tin coatings are deposited at low current densities. With the rise of the current density, the cobalt content in the coating increases up to about 50 wt.%. At the low pH (around 3.5) the effect of addition of glycine is more obvious, the cobalt content in the coatings rise with about 10 % compared to the cobalt content in the coating obtained from glycine free electrolyte.

Figure 9 shows SEM images of coatings deposited from glycine free electrolyte at current density 6 mA cm^{-2} and pH = 3.5 (Fig.9 a) and pH = 5.0 (Fig.9 b) respectively. The increase of pH results in more compact morphology and globular structures formed by agglomeration of fine grains. At low pH=3.5 X-ray fluorescence analysis gives up to 40 wt. % cobalt content in the coatings. At pH=5 at the same conditions, the coatings contain 54% cobalt.

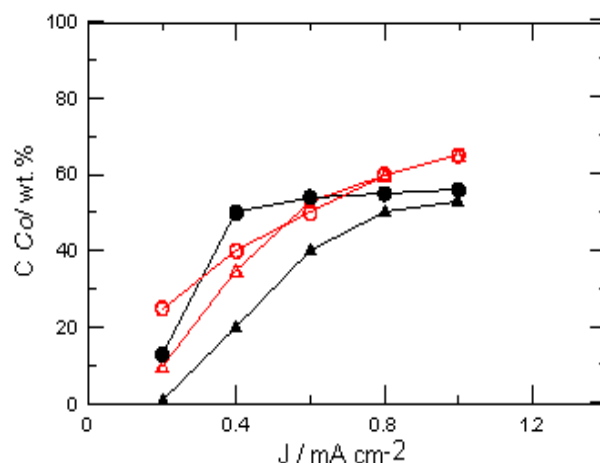


Fig. 8. Influence of the current density on the cobalt content in the alloy at different pH in presence and absence of glycine. $C_{Na_2SO_4} = 40 \text{ g dm}^{-3}$; $C_{C_6H_{11}NaO_7} = 50 \text{ g dm}^{-3}$; $C_{Sn} = 5 \text{ g dm}^{-3}$; $C_{Co} = 5 \text{ g dm}^{-3}$ $v = 20 \text{ mV s}^{-1}$; ● $C_{C_2H_5NO_2} = 0 \text{ g dm}^{-3}$; pH=5.0; ○ $C_{C_2H_5NO_2} = 50 \text{ g dm}^{-3}$; pH=5.0; ▲ $C_{C_2H_5NO_2} = 0 \text{ g dm}^{-3}$; pH=3.5; △ $C_{C_2H_5NO_2} = 50 \text{ g dm}^{-3}$; pH=3.5.

Figure 10 shows SEM images of coatings deposited at current density 10 mA cm^{-2} and pH = 5 in absence (Fig.10 a) and in presence (Fig.10 b) of glycine. The addition of glycine in the electrolyte results in more compact morphology and very smooth surface. In absence of glycine in the electrolyte, the cobalt content in the coatings was 55%. The presence of glycine in the electrolyte results in increased cobalt content 60 wt. % cobalt.

CONCLUSIONS

Addition of glycine to the sulfate/gluconate electrolyte for electrodeposition of SnCo alloys leads to:

- Deposition of more homogeneous compact alloy coatings with better appearance.
- Glycine favors the cobalt deposition, accelerates the Co^{2+} ions reduction as confirmed by CV curves.
- Cobalt content in the alloy increases in the presence of glycine.
- Coatings with up to 65 wt. % Co can be deposited from investigated electrolyte.

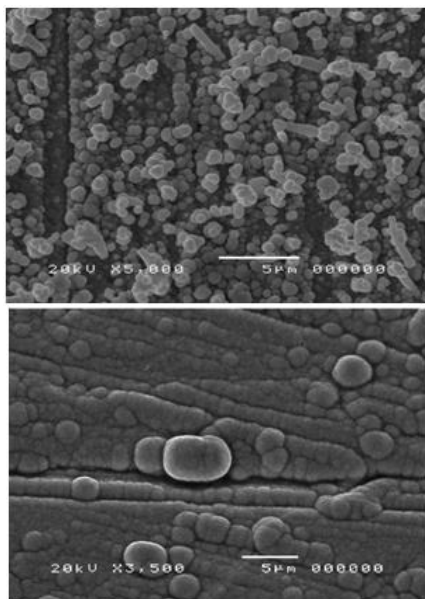


Fig. 9. Surface of tin-cobalt alloy coatings $C_{Sn}= 5 \text{ g dm}^{-3}$; $C_{Co}= 5 \text{ g dm}^{-3}$; $C_{Na_2SO_4}= 40 \text{ g dm}^{-3}$; $C_{C_6H_{11}NaO_7}= 50 \text{ g dm}^{-3}$ $C_{C_2H_5NO_2} = 0 \text{ g dm}^{-3}$; 6 mA cm^{-2} (a) pH=3.5, 40 wt. % Co;(b)pH=5.0, 54 wt. % Co;

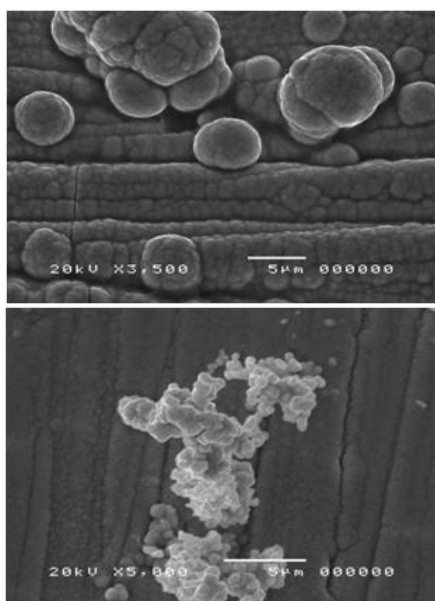


Fig. 10. Surface of tin-cobalt alloy coatings at pH=5 $C_{Sn}=5 \text{ g dm}^{-3}$; $C_{Co}=5 \text{ g dm}^{-3}$; $C_{Na_2SO_4}=40 \text{ g dm}^{-3}$; $C_{C_6H_{11}NaO_7}=50 \text{ g dm}^{-3}$; 10 mA cm^{-2} (a) $C_{C_2H_5NO_2}=0 \text{ g dm}^{-3}$, 55wt. % Co; (b) $C_{C_2H_5NO_2}=50 \text{ g dm}^{-3}$,65wt. % Co.

Acknowledgements. The authors express their gratitude to National Science Fund (Project T02/27) „Multifunctional innovative layers for construction metals and alloys”.

REFERENCES

1.P.K. Datta, ‘Coatings and Surface Treatment for Corrosion and Wear Resistance’, (K.N. Strafford, P.K. Datta and G.C. Gookan (Ed.) Chichester: Ellis Horwood, 1984, p. 74.

2.R. Sabitha, MalathyPushpavanam, M. Mahesh Sugatha, T. Vasudevan, *Trans. Met. Fin. Ass. of India*, **5**, 267 (1996).

3.M. Degrez, R. Winand, Second Congress on ‘Cobalt Metallurgy and Uses’, (Cobalt Development Institute, Bruxelles, 1986, p. 432.

4.V.N. Kudryavtsev, K.M. Tyutina, A.N. Popov, S.A. Maksimenko and V.A. Zonin, *Plat. Surf. Finish.*, **79**, 57 (1992).

5.A.D. W. Todd, R. E. Mar, J.R. Dahn, *J. Electrochem. Soc.*, **153**, A1998 (2006).

6.H. Guo, H. Zhao, X. Jia, X. Li, W. Qiu, *Electrochim. Acta*, **52**, 4853 (2007).

7.I.Vitina, V.Belmane, A. Krumina, V. Rubene, *Surface and Coatings Tech.*, **205**, 2893 (2011).

8.K. Chen, Thesis, Loughborough University, Electrodeposition of compositionally modulated tin-cobalt alloy multilayer coatings as plain bearing overlays, 2004.

9.T. Nishizawa and K. Ishida, *Bull. Alloy Phase Diagrams*, **4**(4), 387 (1983).

10.S.Nineva, Ts. Dobrovolska, I. Krastev, *Zastita Materilala*, **52**, 80 (2011).

11.S. Rehim, S. Refaey, G. Schwitzgebel, F. Tara, M. Saleh, *J. of Appl. Electrochem*, **26** (4), 413 (1996).

12.E. Gómez, E. Gaus, J. Torrent, X. Alcobe, E. Vallés, *J. of Appl. Electrochem*, **31**(3), 349 (2001).

13.E. G. Vinokurov, *Russian J. of Appl. Chem.*, **83**(2), 258 (2010).

14.N.V. Sotskaya, O.V. Dolgikh, *Prot. Met.*, **44**, 479 (2008).

15.S.I. Berezina, R.M. Sageeva, L.G. Sharapova, *Prot. Met.*, **86**, 228 (1986).

16.R. Critelli and P.Sumodjo, *ECs Trans.*, **50**(52), 75 (2013).

17.J.C. Wei, M. Schwartz, K. Nobe J. *Electrochem. Soc.*, **155**, D660 (2008).

18.F.M. Takata, P.T.A. Sumodjo, *Electrochim. Acta*, **52**, 6089 (2007).

19.O. Ergeneman, K.M. Sivaraman, S. Pané, E. Pellicer, A. Teleki, A.M. Hirt, M.D. Baró, B.J. Nelson, *Electrochim. Acta*, **56** (3), 1399 (2011).

20.D. Sawyer, *Chem. Rev.*, **64**(6), 633 (1964).

21.T.N. Maksin, B.Z. Zmbova and D.S. Veselinovic, *J. Serb. Chem. Soc.*, **56**, 337 (1991).

22.J. Torrent-Burgués, E. Gaus, F. Sanz, *J. of Appl. Electrochem.*, **32**(2), 225 (2002).

23.A. Survila, Z. Mockus, S. Kanapeckaitė, G. Stalnionis, *J. of Electroanal. Chem.*, **667**, 59 (2012).

24.J. Ashton, W. Pickering, *Aust. J. of Chem.*, **23**(7) 1367 (1970).

25.L. Joyce and W. Pickering, *Aust. J. of Chem.*, **18**, 783. (1965).

26.A. Survila, Z. Mockus, S. Kanapeckaitė, Remigijus Juškėnas, *T. of the Inst. of M. Finish.*, **91**(4), 197 (2013).

27.Cotton, F. Albert and Geoffrey Wilkinson, *Advanced Inorganic Chemistry*, 3 ed. Interscience Publishers, 1972..

ВЛИЯНИЕ НА ГЛИЦИН ВЪРХУ ЕЛЕКТРОХИМИЧНОТО ПОЛУЧАВАНЕ НА СПЛАВ Sn-Co ОТ ГЛЮКОНАТЕН ЕЛЕКТРОЛИТ

Т.Вълкова* и И.Кръстев

Институт по физикохимия, Българска академия на науките, ул. „Акад. Г. Бончев“, бл. 11, 1113 София, България

Постъпила на 11 ноември, 2015 г.; коригирана на 5 януари, 2016 г.

(Резюме)

Изследвано е влиянието на глицин върху електродните процеси на отлагане и разтваряне на калай, кобалт и сплав калай-кобалт от глюконатно-сулфатен електролит посредством метода на циклична волтамперометрия.

Установено е, че добавянето на глицин към слабо кисел електролит за получаване на покрития от сплав калай-кобалт не оказва съществено влияние върху отлагането на калай, но има силен ефект, като при отлагането на чист кобалт, така и при отлагане на сплавта калай-кобалт. Добавянето на глицин и повишаването на концентрацията му в електролита води до нарастване на процентното съдържание на кобалт в покритията. От изследвания електролит могат да бъдат получени качествени покрития с високо съдържание на кобалт. Промяната рН на електролита и добавянето на глицин дава възможност за получаване на покрития със съдържание на кобалт от 0 до 65 тегл. %.

Influence of metal loading on morphology and performance of oxide supported cobalt electrocatalysts

K. Maksimova – Dimitrova^{1*}, E. Lefterova¹, S. Atanasova – Vladimirova², E. Slavcheva¹

¹“Acad. Evgeni Budevski Institute of Electrochemistry and Energy Systems Bulgarian Academy of Sciences, Acad. G. Bonchev bl. 10, Sofia – 1113, Bulgaria

²“Rostislav Kaishev” Institute of Physical Chemistry, Bulgarian Academy of Sciences, Acad. G. Bonchev bl.11, Sofia – 1113, Bulgaria

Received October 29, 2015; Revised November 20, 2015

This work presents a research on the synthesis of composite nanosized Co-based materials deposited by sol-gel method on Magnelli phase titanium oxide (MPT) and their investigation as anode catalysts for alkaline water electrolysis. The chemical composition, surface structure and morphology are characterized by EDX, SEM, and XRD analysis. The activity toward the partial electrode reaction of oxygen evolution (OER) is assessed in aqueous alkaline media at room temperature. Cyclic voltammetry and steady state polarization curves are used to obtain information about the reactions proceeding on the catalysts surface, to determine the potentials of oxygen offset and the corresponding current densities and thus, to assess the OER catalytic efficiency. The results obtained showed that the Co-based MPT-supported catalysts are stable at the aggressive conditions of the alkaline water electrolysis. The metal content influences the structure and morphology. Among the tested samples the one with 30 wt.% metal content (Co30) demonstrates superior performance and best catalyst utilization. The OER starts at 0,64V (vs. Ag/AgCl) and reaches current density of about 55 mA cm⁻² already at 0,75V. This is explained with size effects (smallest Co particles) ensuring largest electrochemically active surface area.

Keywords: hydrogen generation, alkaline water electrolysis, non-precious catalysts, oxide support

INTRODUCTION

Since the first observation of water electrolysis by van Trostwijk and Deiman in 1789 [1,2] this method for hydrogen generation has been investigated in depth by many authors [3-7]. It is characterized with flexibility, almost zero detrimental emissions, and high purity of the produced gases. However, in order to become an economically attractive, the technology still needs to be improved in terms of efficiency and durability. The main classification of water electrolysis is based on the type of the used electrolyte (aqueous solution or solid polymer membrane) and the operating temperature. The classical water electrolysis which is a well-established technological process for decades is carried out in aqueous alkaline electrolytes. This type of electrolysis has the advantage of using cheap non-noble metal catalysts, while the main drawbacks are the decrease of process efficiency at high loads and potential risk of environment pollution due to leakage of the aggressive electrolyte. The electrolysis of water in cells with a

solid polymer electrolyte is a relatively new technology. In advanced stage of development are the electrolyzers using proton exchange membranes (PEMWE). Such systems with capacity of up to 10 Nm³/h are already available on the market. They offer number of advantages compared to the classical alkaline electrolysis: efficiency reaching 95% at current density of 1-2 A cm⁻², very high purity of the produced gases, compatibility with renewable energy sources, environmentally friendly [8-10]. The main problem in regard to this technology is the fact that hydrogen produced in PEMWE is still rather expensive due to the high price of the used polymer membranes and the rare noble metal catalysts [11,12]. Recently there is an increasing interest in development of electrolyte membranes with anion (OH⁻) conductivity. The usage of anion exchange membrane (AEM) would prevent the deposition of solid carbonaceous residue on the electrode / electrolyte interface, which in the conventional aqueous alkaline electrolyzers often leads to problems during the start-ups of the system. Another major advantage of this type of hydrogen generators is the possibility to use inexpensive and broadly available catalysts (mainly non-precious transition metals from the

To whom all correspondence should be sent:

E-mail: katerina.maksimova87@iees.bas.bg

iron group and their alloys). In summary, AEMWE are supposed to combine the advantages of the classical aqueous alkaline and the acidic PEM systems - cheaper base metal catalysts, high efficiency, none risk for environment pollution.

Common to both PEMWE and AEMWE is the significant overpotential at the anode side where the oxygen evolution reaction (OER) takes place [13]. The OER is studied intensively for decades in order to elucidate the reaction mechanism. Various anode catalysts are employed in effort to minimize the energy loss during water electrolysis. The investigations are aimed to development of catalysts combining high efficiency with corrosion stability and performance durability. The establishment and elucidation of the correlation between catalyst activity and catalyst corrosion mechanisms is another important objective. Such an analysis allows for better understanding of the advanced catalysts design principles and definition of best trade-off between activity and stability.

One way to reduce the cost of the catalysts is to disperse the active component on catalytic support with high surface area and thus, to increase the catalyst utilization [14,15]. Thus obtained composite catalysts often show higher activity compared to the non-supported metals due to realization of electronic interactions with the support. The effect is known as strong metal-support interaction (SMSI-effect) [16]. It is related to redistribution of the electron density of the active surface sites which influences the adsorption strength of the intermediates and facilitates the mechanism of the electrode reactions. As a result, the catalytic loading can be drastically reduced preserving the efficiency of the electrolysis. The main advantage of the most broadly used carbon supports is their high surface area (over $200 \text{ m}^2 \text{ g}^{-1}$) combined with excellent electro-conductivity. Unfortunately, the carbon is not suitable for electrolysis applications since the high operative potentials cause its oxidation, followed by gradual electrode degradation and consequent failure of the system. Therefore, recently there is an increased interest in application of non-carbon supporting materials such as carbides, nitrides, and oxides which in addition to the required high surface area and good electrical conductivity offer increased chemical and electrochemical stability.

It is known that the metals from the iron group (Fe, Ni, Co, etc.) have high catalytic activity and corrosion stability in alkaline solutions, and that some of their composite and alloy systems demonstrate even superior performance compared to the pure metals [17-19]. This is due to increased

surface roughness as well as to changes in the electronic structure of the mixed catalysts leading to synergism. The catalytic activity of these systems can be further enhanced if they are dispersed on properly chosen catalytic support ensuring SMSI-effect. Such approach is applied and proven to be favourable in PEMWE [20], while in alkaline electrolysis there is a lack of systematic research and publications on the topic.

The main objective of this work is the preparation of advanced corrosion resistant composite catalysts based on cobalt nano-particles deposited on Magnelli phase titanium oxide and investigation of the influence of embedded metal content on the catalysts structure, morphology, and OER efficiency in alkaline water electrolysis. Another important aspect of the research is to elucidate the expected metal/support interactions and the resulting effects on electrode performance and durability.

EXPERIMENTAL

The catalysts under study are prepared by sol-gel method using acetylacetonate precursor $\text{Co}[\text{C}_5\text{H}_7\text{O}_2]_2$ (Alfa Acer). The cobalt nanoparticles are supported on Magnelli phases titanium oxide with general formula $\text{Ti}_n\text{O}_{2n-1}$ (MPT, Ti-dynamics Co. Ltd). The metal content is varied in the range 20-40 wt.% and the test samples are denoted accordingly (Co20, Co30, and Co40). The preparation procedure includes two steps: i) pretreatment of the support and the metal precursor using magnetic stirrer and ultrasonic bath, their mixing, and heating at 60°C under constant stirring until a fine gel is obtained; ii) thermal treatment of the obtained mixture at 240°C in reducing H_2 -atmosphere for 2 hours and gradual cooling to room temperature. The obtained powder is homogenized in a mortar and stored in dry oxygen-free atmosphere. To prepare the test electrodes the catalysts are mixed with propanol, spread as a thin film on the top of commercial gas diffusion layer (Freudenberg, Germany), and left to dry at room temperature.

The surface area of the support is measured by BET analysis. The composition, surface structure and morphology of the synthesized composite catalysts are studied by energy dispersion elemental analysis (EDX), scanning electron microscopy (SEM), and X-Ray diffraction (XRD) methods. SEM and EDX analysis are obtained by JEOL JSM 6390 electron microscope (images in secondary and back-scattered electrons), equipped with INCA Oxford elemental detector. XRD analysis is

performed by X-ray diffractometer Philips APD15. The diffraction data were collected at a constant rate of $0.02^\circ \text{ s}^{-1}$ over an angle range of $2\theta = 10\text{--}90^\circ$. The size of Co crystallites is determined by Scherrer equation [21].

The electrochemical performance and catalytic activity toward the oxygen evolution reaction are investigated applying the common experimental techniques of cyclic voltammetry and steady state polarization. The experiments are carried out in aqueous alkaline media (25% KOH) at room temperature using a standard three-electrode electrochemical cell with Ag/AgCl reference electrode and Pt wire as a counter electrode. The working electrode has geometric area of 0.5 cm^2 and contains $0.5 \text{ mg}_{\text{Co}}\text{cm}^{-2}$. All electrochemical measurements are carried out with a commercial Galvanostat/Potentiostat POS 2 (Bank Elektronik, Germany).

RESULTS AND DISCUSSION

According the technical specification of the producer the chosen support, MPT, has surface area of $7\text{--}8 \text{ m}^2\text{g}^{-1}$, very good electrical conductivity and corrosion stability both in acidic and in alkaline media. The performed BET analysis verified a surface area of $8 \text{ m}^2\text{g}^{-1}$.

The MPT electrochemical performance in aqueous alkaline electrolyte is shown in figure 1. As expected the support is very stable at high anodic potentials where the oxygen evolution takes place. The measured low current is of pseudo-capacitive nature and does not change with time indicating lack of catalytic activity.

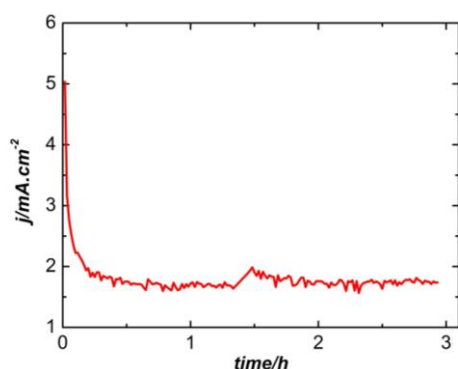


Fig. 1. Potentiostatic polarisation curve of MPT in 25% KOH at 1.8V.

To investigate the morphology and surface structure, XRD and SEM analysis were performed. The results obtained (figure 2 a,b) show that MPT consists of two well recognized crystalline phases -

(Ti_4O_7 and $\text{K}_x\text{Ti}_8\text{O}_{16}$) having homogeneously distributed particles with size in the range $100\text{--}150 \text{ nm}$.

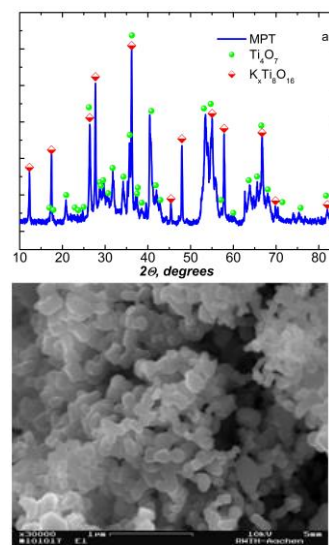


Fig. 2. X-ray diffraction patterns (a) and SEM image (b) of the MPT support.

Samples of the synthesized composite Co/MPT catalysts with target Co content 20, 30, and 40 wt.% (Co20, Co30, and Co40, respectively) are studied by energy dispersive X-ray diffraction to determine the exact metal content. The results obtained are presented in **Table 1**. They show that the amount of the detected cobalt correlates well with that introduced by the acetylacetonate precursor during the synthesis, except for Co20 in which case the deviation is relatively high.

Table 1. Cobalt content in the test samples determined by EDX analysis.

Sample	Co wt. %	
	target	obtained
Co20	20	15
Co30	30	29
Co40	40	40

According the SEM images (figure 3) the metal particles (white spots) of all three samples are homogeneously dispersed on the substrate, forming cauliflower-type aggregates.

The XRD spectra of the catalysts under study (figure 4) show the presence of metallic cobalt in all test samples. In Co20 the metal exists only in a hexagonal crystallographic state, while in Co30 and Co40 both hexagonal and cubic forms are detected. The values of the crystallite size determined by Sherrer equation using the half width of the full maximum (HWFMM) of the peaks for all registered crystallographic planes are summarized in **Table 2**. They show that the synthesized catalysts have

relatively large cobalt crystallites with size varying in the range 30-50 nm. The smallest are the crystallites of the test sample having moderate cobalt content, Co30.

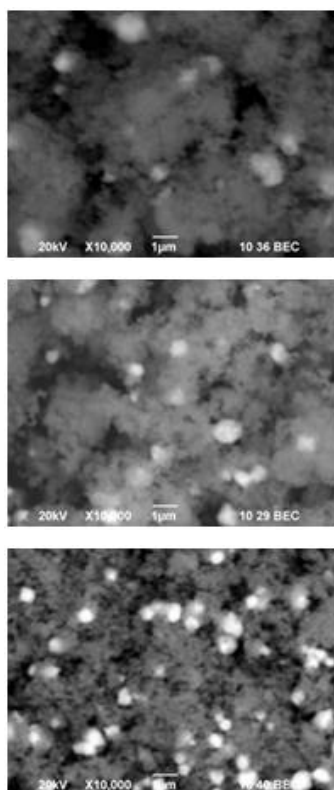


Fig. 3. SEM images (in back-scattered electrons) of the synthesized Co/MPT catalysts; a) Co20; b) Co30; c) Co40

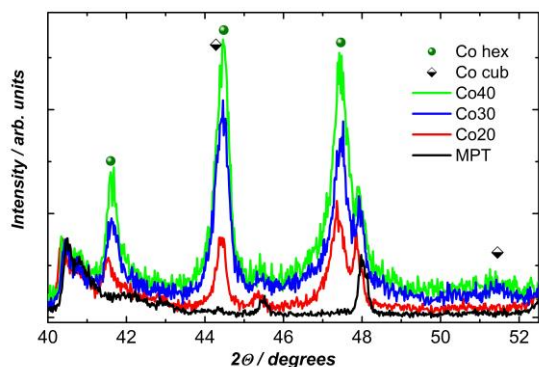


Fig. 4. X-ray diffraction patterns of the synthesized Co/MPT catalysts

The cyclic voltammograms in figure 5 show two well defined anodic current peaks related to changes in the oxidation state of Co (Co to Co^{2+} and Co^{2+} to Co^{3+}), followed by intensive oxygen evolution above 0,65V. The process starts earlier and is most intensive for the catalyst with 30 wt.% metal content. During the cathodic scan reduction current peaks can be seen on the curves of Co30 and Co40, while for the sample with lowest metal

content the cathodic branch of the curve is rather shapeless. The CVs do not change at long term cycling, demonstrating durability of the catalyst performance.

Table 2. Crystallite size of Co/MPT catalysts

Sample	hcp			fcc	
	41.6	44.5	47.7	44.5	51.5
	(100)	(001)	(101)	(111)	(200)
	nm	nm	nm	nm	nm
Co20	40	35	26	-	
Co30	26	30	20	20-	<10*
Co40	38	33	20	14	<10*

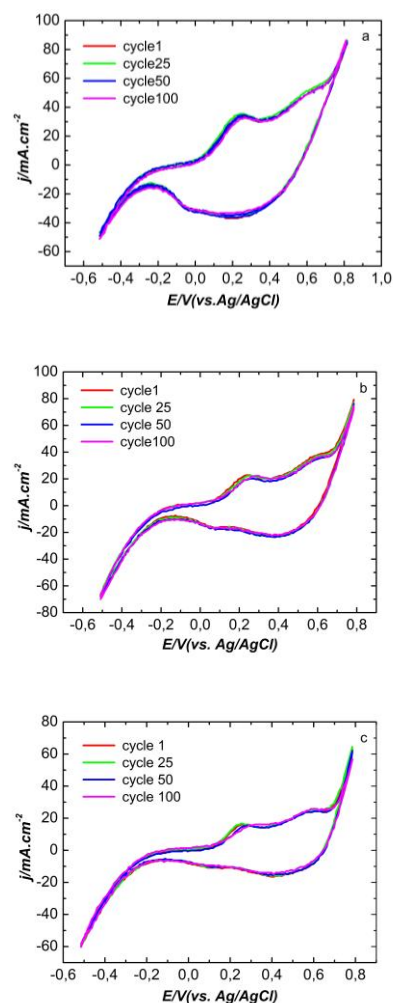


Fig. 5. Cyclic voltammograms of Co/MPT catalysts in 25% KOH at room temperature; a) Co20; b) Co30; c) Co40; potential scan rate 100 mV s^{-1}

The anodic polarisation curves are presented in figure 6. The intensity of the oxygen evolution reaction is nearly equal for Co30 and Co40, while the reaction proceeds slower on Co20.

In order to obtain information about the catalyst utilization, the morphology factor, f , is determined following the method of Da Silva [22]. The procedure is illustrated in figure 7.

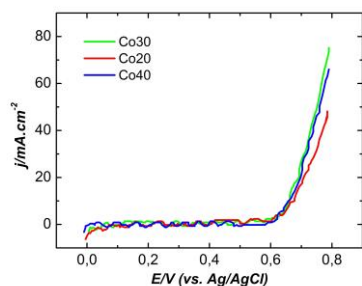


Fig. 6. Anodic polarisation curves of the Co/MPT in 25% KOH; room temperature; potential scan rate 1 mV s⁻¹

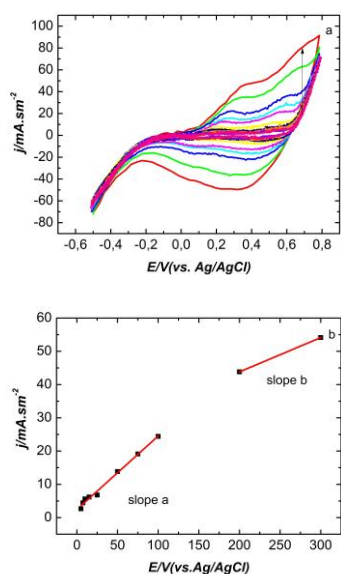


Fig. 7. Graphical illustration of DaSilva method for evaluation of catalyst utilization in OER porous electrodes

It includes recording of cyclic voltammograms at different scan rates and plotting the current at defined potential where the OER starts as a function of the scan rate. The slope of the obtained linear part of the curve at low scan rates (*slope a*) is a measure for the total capacity of the electrode surface C_T . The slope at high scanning rates (*slope b*) represents the capacity of the "external" easily accessible electrode surface, C_{EXT} . The difference $C_{INT} = C_T - C_{EXT}$ gives the capacity of the "internal" difficult to access surface. The ratio $f = C_{INT} / C_T$ gives the value of the morphology factor, which is a measure for the unused part of the catalyst. The calculated values of the morphology factor and the corresponding catalyst utilization are presented in Table 3. It is seen that for the catalysts under study the lowest f value is obtained for the sample Co30, meaning that for this catalyst the utilization is superior. The result correlates well with the data in Table 2 according which this sample has smallest

particles size which in turn, ensures the highest surface area available for the proceeding electrode reaction.

Table 3. Morphology factor and utilization of the Co/MPT catalysts

Sample	Co 20% wt	Co 30% wt	Co 40% wt
f	0.55	0.43	0.55

Finally, the stability of catalytic performance at long service was investigated, recording potentiostatic polarisation curves at high anodic potential of 1,8 V where an intensive oxygen evolution takes place. Figure 8 presents the results obtained in 48-hour experiment on the best performing electrode containing 0.5 mg cm⁻² Co30. It is seen that the intensity of the OER sustains for the whole duration of the experiment without any indications for decrease in catalyst performance and degradation of the electrode.

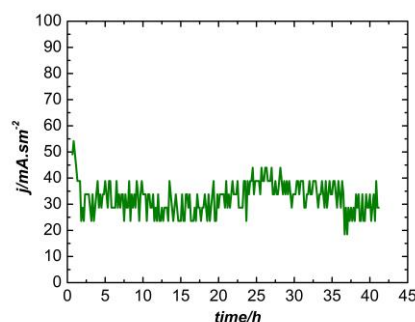


Fig. 8. Potentiostatic polarisation curve of Co30/MPT in 25% KOH.

CONCLUSION

The research performed verified that Magnelli phases titanium oxide is a promising catalytic support for application in alkaline water electrolysis. The synthesized Co/MPT catalysts possess high efficiency toward OER combined with good durability and corrosion resistance. The optimal metal loading of 30 wt. % Co ensures superior performance combined with best catalyst utilization, resulting from the most developed active surface of this sample. Further research is in progress focused on the influence of the electronic metal-support interactions on catalysts performance.

Acknowledgments: This research has been carried out with the financial support of NSF, Bulgarian Ministry of Education and Science, Contract No. ДФНН E-02/9.

REFERENCES

1. S. Trasatti, *J. Electroanal. Chem.*, **476**, 90 (1999).
2. R. de Levie, *J. Electroanal. Chem.*, **476**, 92 (1999).
3. N. Ramaswamy, S. Mukerjee, *Adv. Phys. Chem.*, **2012** 17 (2012).
4. K. Zeng, D. Zhang, *Prog. Energy Combust. Sci.*, **36**, 307 (2010).
5. K. B. Oldham, J. C. Myland, *Fundamentals of electrochemical science*. 1st ed., San Diego: Academic Press, 1993.
6. S. Trasatti, *Electrochim. Acta*, **29**, 1503 (1984).
7. H. Ibrahim, A. Ilinca, J. Perron, *Renewable Sustainable Energy Rev.*, **12**, 1221 (2008).
8. K. E. Ayers, E. B. Anderson, C. Capuano, B. Carter, L. Dalton, G. Hanlon, J. Mancoand M. Niedzwiecki, *ECS Trans.*, **33**, 3 (2010).
9. P. Millet, R. Ngameni, S. A. Grigoriev, N. Mbemba, F. Brisset, A. Ranjbari, C. Etievant, *Int. J. Hydrogen Energy*, **35**, 5043 (2010).
10. S. Stucki, G. G. Scherer, S. Schlagowski, E. Fisher, *J. Appl. Electrochem.*, **28**, 1041 (1998).
11. M. H. Miles, E. A. Klaus, B. P. Gunn, J. R. Locker, W. E. Serafin, S. Srinivasan, *Electrochim. Acta*, **26**, 521 (1978).
12. Damjanovic, A. Dcy. And J. M. Bockris, *J. Electrochem. Soc.*, **113**, 739 (1966).
13. Y. Matsumoto and E. Sato, *Mater. Chem. Phys.*, **14**, 397 (1986).
14. E. Slavcheva, V. Nikolova, T. Petkova, E. Lefterova, I. Dragieva, T. Vitanov, E. Budevski, *Electrochim. Acta*, **50**, 5444 (2005).
15. M.S. Kim, S.H. Chung, C.J. Yoo, M. S. Lee, II-H. Cho, D.W. Lee, K.Y. Lee, *Applied Catalysis B: Environmental*, **142–143**, 354 (2013).
16. M. Jaksic M, *Int. J. Hyd. Energy*, **26**, 657 (2001).
17. R. Rashkov, M. Arnaudova, G. Avdeev, A. Zielonka, P. Jannakoudakis, A. Jannakoudakis, E. Theodoridou, *Int. J. Hyd. Energy*, **34**, 2095 (2009).
18. E. Daftsis, N. Pagalos, A. Jannakoudakis, P. Jannakoudakis, E. Theodoridou, R. Rashkov, M. Loukaytsheva and N. Atanassov, *J. Electrochem. Soc.*, **150**, C787 (2003).
19. R. Rashkov, N. Atanassov, A. Jannakoudakis, P. Jannakoudakis, E. Theodoridou, *J. Electrochem. Soc.*, **153**, C152 (2006).
20. A. Stoyanova, G. Borisov, E. Lefterova, E. Slavcheva, *Int. J. Hyd. Energy*, **37**, 16515 (2012).
21. J. Lanford, A.A. Wilson, *J. Appl. Crystallogr.*, **11**, 102 (1978).
22. L.M. Da Silva, D.V. Franco, L.A. De Faria, J.F.C. Boodts, *Electrochim. Acta*, **49**, 3977 (2004).

ВЛИЯНИЕ НА КАТАЛИТИЧНОТО НАТОВАРВАНЕ ВЪРХУ МОРФОЛОГИЯТА И РАБОТНИТЕ ХАРАКТЕРИСТИКИ НА КОБАЛТОВИ ЕЛЕКТРОКАТАЛИЗАТОРИ, ОТЛОЖЕНИ ВЪРХУ ОКСИДЕН НОСИТЕЛ

К. Максимова – Димитрова¹, Е. Лэфтерова¹, С. Атанасова – Владимирова², Е. Славчева¹

¹Институт по електрохимия и енергийни системи „Акад. Евгени Бudevски“, Българска академия на науките, Акад. Г. Бончев бл.10, София – 1113, България

²Институт по физикохимия „Акад. Ростислав Каишев“, Българска академия на науките, Акад. Г. Бончев бл.11, София – 1113, България

Постъпила на 29 октомври, 2015 г.; коригирана на 20 ноември, 2015 г.

(Резюме)

Статията представя изследване върху синтеза на композитни наноразмерни материали на базата на кобалт, отложени по зол-гел метод върху Магнели фази титанов оксид и тяхното приложение като анодни катализатори за алкална електролиза на вода. Химичният състав, структурата на повърхността и морфологията са охарактеризирани с методите на сканираща електронна микроскопия (SEM), рентгеноструктурен анализ (XRD) и дисперсен елементарен анализ (EDX). Активността по отношение на реакцията на отделяне на кислород (OER) е определена във водна алкална среда при стайна температура. Методите на циклична волтаметрия и поляризационни криви са използвани за получаване на информация относно реакциите, които протичат на повърхността на катализаторите, за определяне на потенциалите, при които протича реакцията на отделяне на кислород при съответните токови плътности и на каталитичната активност. Получените резултати показват, че катализаторите на базата на кобалт, отложени върху оксиден носител са стабилни при агресивните условия на алкална електролиза на вода. Съдържанието на метал в катализаторите оказва влияние върху морфологията и структурата. От изследваните проби, тази с 30 тегловни процента съдържание на кобалт, показва отлична възпроизводимост и най-висока каталитична използваемост. Реакцията на отделяне на кислород (OER) започва при 0,64 V спрямо сравнителен електрод сребро/сребърен хлорид (Ag/AgCl), а при 0,75 V достига токова плътност от 55 mA.cm⁻². Това се обяснява с ефекта на размера на каталитичните частици - катализаторът с най-малки кобалтови частици, осигурява най-голяма активна повърхност.

Electrochemical investigation of cementation process

B. Tzaneva^{1*}, T. Petrova², J. Hristov³ and L. Fachikov³

¹Technical University of Sofia, 8 Kliment Ohridsky blvd., 1756 Sofia, Bulgaria

²Institute of Catalysis, Bulgarian Academy of Sciences, Sofia 1113, Acad. G. Bonchev str., bl.11, Bulgaria

³University of Chemical Technology and Metallurgy, Kliment Ohridsky blvd., 1756 Sofia, Bulgaria

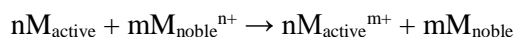
Received October 3, 2015; Revised November 24, 2015

Cementation of metals is a spontaneous electrochemical reaction at the interface of an active metal and the electrolyte containing ions of more noble metal. In this work the electrochemical behaviour of the redox couples was studied experimentally with a special emphasis the mixed cementation potential compared to the potentials of the individual couples at open circuit state. This approach allows determining the values of both the anodic and cathodic polarisations but not the reaction kinetics. The potentiodynamic method separately applied to the iron and the copper electrodes was used to elucidate the nature of the kinetics of the half-reactions of the electrodes. The intersection of the anodic branch of the polarisation curve of the iron electrode with the cathodic one of the copper electrode corresponds to the rate of copper deposition at the iron surface, represented indirectly by the deposition current density. The determined corrosion potentials, however, are more positive with respect to the open circuit potentials when direct copper cementation by iron takes place. More accurate results about the reaction rate were obtained by plotting of the values of the open circuit potentials of a real cementation process onto the polarisation curves of a copper electrode. The intersection is located in the area corresponding to an active iron dissolution and copper deposition under a transport control. These results correspond adequately to those obtained by inductively coupled plasma spectroscopy applicable to kinetic measurements.

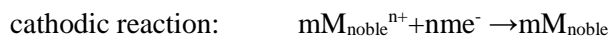
Key words: copper cementation, mixed potential, potentiodynamic,

INTRODUCTION

Cementation of metals is spontaneous electrochemical oxidation-reduction reaction taking place at the interface active *metal/solution containing ions of more noble metal* ($M_{\text{active}}/M_{\text{noble}}^{n+}$), [1-4] namely:



The ratio of the electrode potentials (E) of the oxidation-reduction couples is $E(M_{\text{active}}^{m+}/M_{\text{active}}) < E(M_{\text{noble}}^{n+}/M_{\text{noble}})$. The cementation process can be considered as a work of short circuit galvanic element where two half-reactions of oxidations and reduction take place simultaneously on one and the same surface [5]:



The common approach in the cementation kinetics is the use of physical methods analyzing the solution [6-9]. The electrochemical dynamic methods cannot be applied directly for the analysis

of the cementation processes. The high reaction rate results in rapid changes in the interface (i.e. contact areas, structures of the anodic and cathodic sites, etc) and the chemical content of the electrolyte.

A real analysis of the electrochemistry of the sub-processes involved in the cementation reaction can be done on the basis of the mixed potential of the system $M_{\text{active}}/M_{\text{noble}}^{n+}$ [10] and of the potentials of the separate couples $M_{\text{active}}^{m+}/M_{\text{active}}$ and $M_{\text{noble}}^{n+}/M_{\text{noble}}$ at the open circuit conditions. The determination of the potentials of the separate couples allows to assess the values of the anodic and cathodic polarisations. When the volume of the solution is quite enough and the contact area ($M_{\text{active}}/M_{\text{noble}}^{n+}$), enough small, then the measured values of OCP are independent of the area of contact. This is an advantage, because the cementation is commonly performed by using particles (iron spheres, scrap, iron wool, etc) which surface area taking place in the solid/fluid contacts is hard to be defined.

This paper demonstrates the possibility to apply two electrochemical methods in investigation of copper cementation by iron in solutions containing different anions: the open circuit potential measurements (OCP) and potentiodynamic method. The results contributed to the development of a

To whom all correspondence should be sent:

E-mail: borianatz@tu-sofia.bg

kinetic model of the cementation of the couple Cu^{2+}/Fe and to determine the rate of the process.

EXPERIMENTAL

The electrochemical experiments used copper and iron electrodes with a surface of about 2 cm^2 . At the beginning of each experiment the metal surface was grinded mechanically by SiC paper № 600 and degreased in ethanol-ether mixture. The electrolytes are based on bivalence salts of copper and iron with SO_4^{2-} , SeO_4^{2-} , TeO_4^{2-} , PO_4^{3-} , NO_3^- , Cl^- и IO_3^- and concentration of 0,08M (or 5 g /L M^{2+}). Due to the instability and the low solubility of some compounds of Fe^{2+} , the equilibrium potential of the iron electrode were determined in solutions of FeSO_4 , FeCl_2 и $\text{Fe}(\text{NO}_3)_2$ only.

The electrochemical tests were carried out in a classical three-electrode cell with a platinum counter electrode and a reference saturated calomel electrode. The time variation of OCP was registered up to its almost stationary level, but for a time not less 30 min. The potentiodynamic relationships were obtained at a potential scan rate 10 mVs^{-1} by a potentiostatic-galvanostatic device PAR 273 and treated by a software package PowerSuit. The potentials reported in this paper are presented with respect to normal hydrogen electrode (NHE). All the experiments were carried out at ambient temperature of about $25 \text{ }^\circ\text{C}$ without initial de-aeration of the electrolyte solutions.

The elemental analysis of the solutions before and after the cementation process was performed by inductively coupled plasma (ICP) device (model High dispersion ICP-OES "Prodigy" of Teledune Leeman Labs).

RESULTS AND DISCUSSION

Open circuit potential - time measurements

The difference in the equilibrium potentials at 0.08 mol/L M^{2+} of the more-noble metal, i.e. the copper (0.308 V) and the iron electrode (-0.472 V) is the theoretical value of the electromotive force ($\Delta E^0 = 0.78 \text{ V}$) of the cementation reaction $\text{Cu}^{2+} + \text{Fe} \rightarrow \text{Cu} + \text{Fe}^{2+}$. This value can be used only as a theoretical benchmark referring to the

Table 1. The OCP and polarization values (vs. NHE) of the copper and the iron electrodes in 0.08 mol/L solutions containing different anions.

	SO_4^{2-}	SeO_4^{2-}	TeO_4^{2-}	Cl^-	IO_3^-	NO_3^-	PO_4^{3-}
$E(\text{Cu}^{2+}/\text{Cu}), \text{V}$	0.317	0.300	0.190	0.203	0.344	0.296	0.300
$E(\text{Fe}^{2+}/\text{Fe}), \text{V}$	-0.430	---	---	-0.360	---	-0.120	---
$E(\text{Cu}^{2+}/\text{Fe}), \text{V}$	-0.340	0.270	0.070	-0.300	0.830	-0.110	-0.240
$E(\text{Cu}^{2+}/\text{Fe}) - E(\text{Cu}^{2+}/\text{Cu}), \text{V}$	-0.657	-0.030	-0.183	-0.503	0.486	-0.406	-0.540

cementation reaction under standard conditions. The measured values of OCP in electrolytes with 0.08 mol/L M^{2+} containing different anions are summarized in Table 1.

The data summarized in Table 1 indicate that the nature of the anions affects strongly the values of the potentials. Generally, the measured potentials in the sulphate environments are too close to the theoretical values. The values corresponding to the iron electrode are more positive than the theoretical ones which can be attributed to the aerated neutral solutions.

The time evolution of the open circuit potentials in the case of the iron electrode when the solutions containing of various salts of Cu^{2+} with a concentration of 0.08 mol/L (or 5 g/L Cu) is shown in Fig. 1. In almost all cases the OCP values was established for 5-10 minutes and the stationary levels are strongly affected by the anion contents of the solutions.

Depending on the direction of the OCP change in time it is possible to detect two typical cases:

- a sharp shift of the potential in the negative direction and a gradual change to the equilibrium level (in solutions of SO_4^{2-} , for instance) and
- slow and almost smooth shifts of the potential in the positive direction.

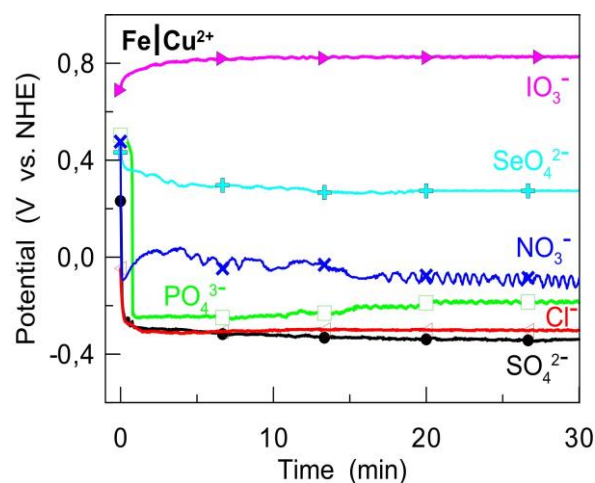


Fig. 1. Time evolution of the Open Circuit Potential (OCP) in case Cu^{2+} cementation by Fe in various solutions with concentration of 0.08 mol/L.

The first case can be considered a typical one for the cementation processes taking place under the diffusion control of the cathodic process when the mixed potential is established to levels close to that of the anodic half-reaction (dissolution of Fe) due to the high cathodic polarization. In accordance with this standpoint, the initial shift in the potential in the negative direction is caused by the depletion of copper ions at the vicinity of the iron surface and consequently the demand copper ions to be transported from the bulk of the solutions. Moreover, if it is supposed that the movement of the OCP in a negative direction is totally due to the depletion Cu^{2+} , the initially shift of the potential may be used as an indicator of the cementation rate. In addition, in sulphate electrolytes, for instance, the copper cementation occurs with highest rate because the slope of the initial linear section is the highest (27 mV/s) while in the selenate solution it is only (4.5 mV/s).

The second case characterizes the behaviour in the iodate solution. The high value of OCP in this case does not indicate the dominating role of the cathodic half-reaction in the process of metal deposition but the hindered anodic reaction of Fe dissolution. The observations of the iron surfaces in copper iodate solutions for the period of the experiments do not indicate any changes which may be attributed to surface passivation and missing cementation processes.

The cathodic polarization can be adequately represented by the difference in potentials of cementation in $\text{Fe} | \text{Cu}^{2+}$ and the equilibrium values at the electrodes $\text{Cu} | \text{Cu}^{2+}$. The calculated values of the cathodic polarization are summarized in last row of Table 1. In all the case all values are negative with only exception related to the case of the iodate solution. In contrast to the OCP, the values of the polarization can be used to establish the electromotive force of the cementation reactions. This suggestion can be easily explained by the results obtained from the cementation of Cu from solutions of SO_4^{2-} , Cl^- , NO_3^- , PO_4^{3-} . However, when positive cathodic polarizations take place the cementation processes cannot be performed.

The experimental results allow elucidating the strong effect of the anion nature in the electrolyte on the cementation process. The change in the OCP during a real cementation process and the comparison of the stationary level with the equilibrium potentials of the two half-reactions provide only qualitative information of the ability of a cementation process of a particular system but are not informative about its kinetics.

Potentiodynamic tests

The kinetics of the cathodic reaction of the cementation process was investigated by recording potentiodynamic relationships of copper electrodes $\text{Cu} | \text{Cu}^{2+}$ (0,08 mol/L) with various anionic contents of the electrolyte. The electrodes were cathodic polarized with an initial potential of 0.25 V, more positive than OCP up to -1.0 V. The anodic reaction of iron dissolution was investigated through anodic polarization of iron electrodes with concentration 0.08 mol/L Fe^{2+} of the solution, starting from OCP and a shift in the positive direction up to 0.4 V. The concentration of the iron ions was taken equal to that of the deposited metal (0.08 mol/L) with the assumption that the entire quantity of the noble metal from the solution (Cu^{2+}) is replaced by iron ions.

The polarization curves of copper sulphate and chloride electrodes are shown in Fig. 2.

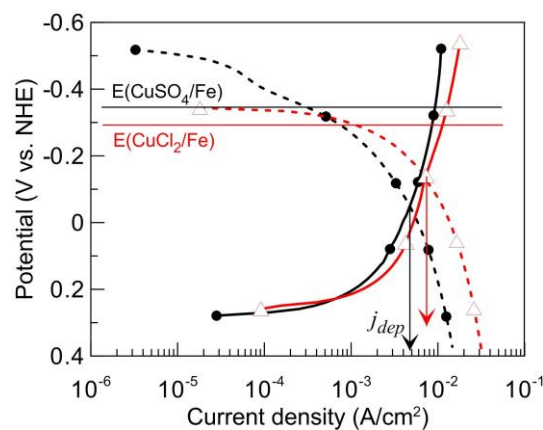


Fig.2. Potentiodynamic relationships of copper (solid lines) and iron (dashed lines) electrodes in sulphate (●) and chloride (Δ) solutions with a concentration of 0.08 mol/L copper salts.

Table 2. Current density and rate (electrochemical and through ICP) of contact deposition of copper on iron electrode from solutions of various copper salts with concentrations 0.08 mol/L.

	SO_4^{2-}	SeO_4^{2-}	TeO_4^{2-}	Cl^-	NO_3^-	PO_4^{3-}	IO_3^-
j_{dep} , A/cm ²	$4,8 \cdot 10^{-3}$	$6,8 \cdot 10^{-4}$	$1,8 \cdot 10^{-5}$	$7,3 \cdot 10^{-3}$	$1,6 \cdot 10^{-2}$	$1,9 \cdot 10^{-2}$	-
ν_{Cu} , (el.chem.) mg/h cm ²	5,69	0,81	$2,13 \cdot 10^{-2}$	8,64	18,9	22,5	-
ν_{Cu} , (ICP) mg/h cm ²	93.2	27.4	1.3	n.a.	49.4	87.2	-

The intersection of the anodic curve of the iron electrode with the cathodic section of copper electrode theoretically should coincides with the rate of copper deposition on the iron surface represented as a current density, j_{dep} [5]. The current densities by the these points of intersection in the case of sulphate and chloride solutions are $4.8 \cdot 10^{-3}$ и $7.3 \cdot 10^{-3}$ A/cm², respectively with corresponding potentials of -0.05 V and -0.13V. These potentials, however, are more positive than the experimentally determined OCP in the case of copper cementation by iron in sulphate (-0.34 V) and chloride (-0.30 V) electrolytes. The difference in the mixed potential of the real cementation process (OCP) and the value determined potentiodynamically separately with iron and copper electrodes indicates that the real anodic polarization is too low and this can be attributed to some reasons, among them:

- The Fe²⁺ concentration in the electrolyte during the real cementation process varies, while in the model iron electrode it is constant. At the onset of the real cementation process, iron ions in the electrolyte are missing but after that their concentration rises in time and at the vicinity of the electrode surface it probably exceeds the value of 0.08 mol/L. Such a difference in the concentration most likely affects the potential and shifts the potentiodynamic plot along the ordinate.

- The ratio of the areas of the anodic and cathodic sites of the real cementation process varies in time, while in the model the polarization relationships corresponds to constant ratio of 1:1. The differences in the area of the anodic and cathodic sites could results in shifts of both relationships with different extents along the abscissa that finally results in different current densities determined by the potentiodynamic method used.

As a consequence of these experiments and the analysis performed it may be decided that the use of a separate iron electrode for the study of copper cementation is not the adequate approach.

However, when the OCP values for the systems Fe | CuSO₄ and Fe | CuCl₂ are plotted over the polarization plots of the copper electrodes Cu | CuSO₄ и Cu | CuCl₂ they corresponds to the sections of active iron dissolution and copper deposition under diffusion control (see Fig. 2). This result corresponds adequately to the initial suggestion about the process control based on the OCP measurements.

The polarization relationships of copper electrodes with various anionic contents are shown in Fig. 3. In accordance with these plots, the lowest rate of metal deposition was observed in the

solution of copper tellurate. In iodate solution the OCP line crosses the anodic curve of the copper electrode which indicates that the deposition of the copper does not take place, but the value of the mixed potential is dues to occurrence of auxiliary reactions at the iron surface such as the release of iodine.

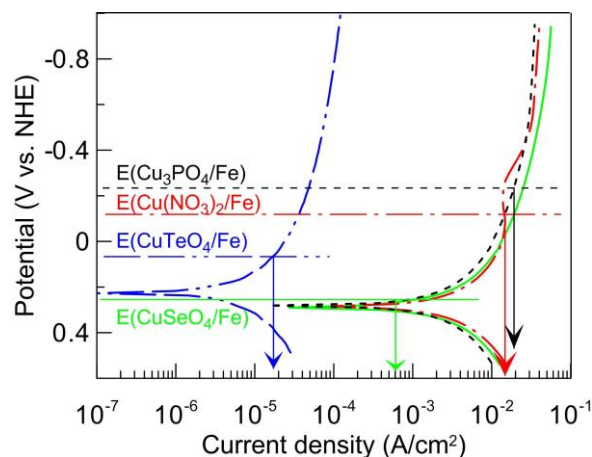


Fig.3. Potentiodynamic relationships of copper electrodes in solutions with a concentration of 0.08 mol/L copper salts.

The intersection of OCP corresponding to Fe | Cu²⁺ and the cathodic section of the polarization relationship of the copper electrode Cu | Cu²⁺ can be used for an experimental determination of the rate of the cementation process, represented as the density of the current of copper deposition onto iron (j_{dep}).

The rate of a heterogenic cementation reaction (v) is generally expressed by the relationship:

$v = dm/S \cdot dt$ where dm is the mass of copper deposited on unit surface S per time dt . The mass of copper deposition can be calculated by the current density (j_{dep}) through the Faraday law. As a result the cementation rate assumes the form:

$$v = m_{\text{Cu}}/t \cdot S = I \cdot A M_{\text{Cu}} / 2 \cdot S \cdot F = j_{\text{dep}} \cdot A M_{\text{Cu}} / 2 \cdot F$$

where $A M_{\text{Cu}}$ is the atomic mass of copper in g/mol; $F = 96495$ C/mol is the Faraday constant and j_{dep} is the cathodic density of current of copper deposition. The rates of copper depositions calculated by this methodology are summarized in Table 2.

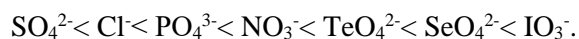
Results from ICP spectroscopy

The ICP results about the copper content in 50 mL of the solutions before and 1 h after the cementation (on 1.14 cm² iron surface) under intensive mixing are presented in the last row of Table 2 as a cementation rate. They are calculated on the basis of the reduction of the concentration of Cu²⁺ in the solution. The cementation rates determined by both methods are different that is an

expected result due to the differences in the experimental conditions. In addition, the cementation times are different: the electrochemical method requires several minutes and a clean surface of the cementer, while the ICP results correspond to the situation after 1h after the end of the cementing process carried out under intensive mixing; the intensive mixing allows permanently creating fresh contacting sites on the cementer surface. As a confirmation of the prescreening comments, it is obvious that the lowest rate of cementations are observed in solutions of selenate and telluride, while in the iodate solution the copper cementation does not take place.

CONCLUSIONS

The paper reports the effect of the nature of anions in the electrolyte on the copper cementation by iron. It was established that the stationary values of OCP strongly depend on the anionic content of the solution and can be arranged in the following order:



In the first five solutions, the OCP shifts sharply in negative direction which indicate diffusional control of the cathodic process (diffusion control of Cu^{2+} transport from the bulk of the solution towards the cementer surface). The only exception was

observed in the iodate solutions where a positive polarization was determined.

It is assumed as possible that the rate of the cementation process can be determined by the superposition of the OCP values and the potentiodynamic relationships in case of copper electrodes $\text{Cu} | \text{Cu}^{2+}$. The fast recovery of copper by cementation was observed in the sulphate electrolyte, while in the iodate solutions the process does not take place.

REFERENCES

1. P.H. Strickland, F. Lawson, *Proc. Australas. Inst. Min. Metall.*, **237**, 71 (1971).
2. M. Jaskuła, *Jordan Journal of Earth and Environmental Sciences*, **2**, 84 (2009).
3. S. Aktas, *Hydrometallurgy*, **104**, 106 (2010).
4. I. Yahiaoui, F. Aissani-Benissad, *Arabian Journal of Chemistry*, **3**, 187 (2010).
5. C. Alemany, M. Aurousseau, F. Lapicque, P. Ozil, *J. Appl. Electrochem.*, **32**, 1269 (2002).
6. G. Viramontes Gamboa, M. Medina Noyola, A. López Valdivieso, *J. Colloid Interface Sci.*, **282**, 408 (2005).
7. G.D. Sulka, M. Jaskuła, *Electrochim. Acta*, **51**, 6111 (2006).
8. W. Djoudi, F. Aissani-Benissad, S. Bourouina-Bacha, *Chem. Eng. J.*, **133**, 1 (2007).
9. N. Naseri Joda, F. Rashchi, *Separation and Purification Technology*, **92**, 36 (2012).
10. O. Aaboubi, J. Douglade, *J. Electroanalytical Chem.*, **693**, 42 (2013).

ЕЛЕКТРОХИМИЧНО ИЗСЛЕДВАНЕ НА ЦЕМЕНТАЦИОННИ ПРОЦЕСИ

Б. Цанева¹, Т. Петрова², Й. Христов³ и Л. Фачиков³

¹ Технически университет - София, бул. "Климент Охридски" 8, София 1756, България

² Институт по катализ, БАН, ул. "Акад. Г. Бончев", бл. 11, София 1113, България

³ Химикотехнологичен и металургичен университет, бул. "Климент Охридски" 8, София 1756, България

Постъпила на 3 октомври, 2015 г.; коригирана на 24 ноември, 2015 г.

(Резюме)

Цементацията на метали е спонтанна електрохимична реакция, протичаща на границата на активен метал и електролит, съдържащ йони на по-благороден метал. В тази работа е изследвано електрохимичното поведение на окислително-редукционни двойки като са сравнявани смесените потенциали при цементация със съответните, експериментално получени потенциали на отделните двойки. Този подход позволява да се определят стойностите на анодната и на катодната поляризация, но не и кинетиката на цементационната реакция. За изследване на кинетиката на електродните полуреакции са снети потенциодинамични зависимости на железни и медни електроди. Скоростта на отлагане на мед върху желязна повърхност е представена чрез плътност на тока, получена при наслагване на анодната поляризационна зависимост на железен електрод с катодната на меден електрод. Корозионните потенциали, определени в пресечната точка на двете зависимости, са значително по-положителни от съответните потенциали на отворена верига при директна цементация на мед върху желязо. По-точни резултати за скоростта на цементационната реакция се получават чрез нанасяна на стойността на смесения потенциал на реален цементационен процес върху поляризационната зависимост на меден електрод. Така получената пресечна точка попада в областта от потенциали, съответстващи на активно разтваряне на желязо и на отлагане на мед при дифузионен контрол. Тези резултати съответстват в достатъчна степен на получените чрез ICP спектроскопия.

Corrosion behavior of anodically formed oxide films on aluminum, sealed in cerium-ions containing solutions

R.A. Andreeva¹, E.A. Stoyanova¹, A.S.Tsanev², D.S. Stoychev^{1*}

¹*“Rostislav Kaischew” Institute of Physical Chemistry, Bulgarian Academy of Sciences, “Acad. G. Bonchev” Str., bl. 11, Sofia 1113, Bulgaria*

²*Institute of General and Inorganic Chemistry, Bulgarian Academy of Sciences, “Acad. G. Bonchev” Str., bl. 11, Sofia 1113, Bulgaria*

Received October 30, 2015; Revised January 24, 2016

The corrosion behavior of anodically deposited oxide films on Al-1050 has been studied in 0.1M NaCl solution. The Al₂O₃ films have been formed in an electrolyte containing H₃PO₄ – 40 g/l under voltastatic conditions of anodization. The sealing has been carried out in 0.5M CeCl₃ solutions at temperatures 25°C and 60°C. The thickness of the coatings was 3-5µm.

The surface morphology and the composition of the sealed nano-porous anodic films have been studied by means of scanning electron microscopy (SEM) and energy dispersive analysis (EDS). It has been established that depending on the conditions of sealing the concentration of cerium inside the pores of the oxide films is growing up from 5.3 up to 10.4 wt.%. On the basis of the XPS spectra of the studied systems the chemical state of cerium in the nano-pores of the oxide film has been defined.

Potentiodynamic investigations have been carried out and the corrosion currents from polarization (E-i) curves have been determined for non-sealed and sealed in solutions containing Ce³⁺ ions anodic oxide coatings on aluminum. It has been shown that the filling up of the nano-pores of the formed Al₂O₃ anodic film with Ce(OH)₃/Ce₂O₃ is promoting its corrosion protection ability.

Key words: anodizing, aluminum oxide, sealing, corrosion.

INTRODUCTION

Anodizing is among the most widely applied methods for anti-corrosion surface treatment of aluminum and its alloys. It is known that the anodized oxide films consist of two layers: internal - barrier layer, and external - porous layer. An important step, aimed at improving of the protective ability of the porous oxide films, is the so called sealing process [1-4]. Taking into account the porosity of alumina films, the sealing step is indispensable [5,6] to enhance corrosion resistance. Sealing concepts involving various combinations of temperature and sealing bath chemical composition all promote the corrosion resistance to a certain degree [6]. Sealing traditionally is being done through immersion in boiling water – the so called “hot water sealing” method [7-9]. The need of high temperature and slow kinetics, however, mean considerable energy consumption [10]. As a result the hot water process has been gradually replaced since 1980s by cold sealing [8]. Dichromate and nickel acetate sealing are well established to be the most effective sealing methods for corrosion prevention [6]. However, it is proved that Cr⁶⁺ ions

have toxic effect [9, 11-13]. A number of sealants have been put forward for sealing applications and some new sealing processes are developed [14].

Nowadays studies on new types of sealants and sealing processes involve cold nickel acetate sealing [9], sodium silicate sealing [14], nickel fluoride sealing [6,14], Cr₂O₃ sealing [15], sodium acetate sealing [8, 10], cerium acetate sealing [13, 16], cerium nitrate and yttrium sulfate sealing [5], sol-gel sealing [12], and even an expensive sealing process using polytetrafluoroethylene [15]. However these efforts to improve the performance seem to be insufficient. Therefore more convenient and effective processes are still needed [15].

The aim of the present work was to investigate and compare the influence of the composition of the sealing solution (aqueous solutions of CeCl₃, containing Ce³⁺ ions or boiling distilled water) and the conditions of sealing on the anodic oxide films, being formed in phosphoric acid on Al-1050 upon their corrosion-protection ability.

EXPERIMENTAL

In the present work we have applied a conventional procedure of anodization of Al in aqueous solution of H₃PO₄ [17]. High purity aluminium Al-1050 was used for anodization. The

To whom all correspondence should be sent:
E-mail: stoychev@ipc.bas.bg

aluminium substrates (10x2x0.2 cm) were degreased in aqueous solution of NaOH at 60°C followed by etching and surface activation in aqueous solution of HNO₃ (50 wt. %) for 30s at room temperature. Anodization was conducted under constant cell potential in 4 wt.% H₃PO₄ aqueous solution. The temperature in each case was kept constant at 25°C. The DC voltage in each case was 40 V. The current density was varied from 2 to 0.2 mA/cm². The aluminium sample was anodized from 60 to 120 min. After anodizing the samples were rinsed with distilled water and sealed.

Two different sealing techniques were applied to the anodic films after anodizing:

1. Boiling distilled water sealing (pH 6–7.5) for 60 min.
2. CeCl₃ sealing: The specimens were dipped in 0.5M CeCl₃ solution (at 25°C or 60°C) for 60 and 120 min.

All the samples were rinsed by cold (25° C) water after sealing and air dried.

The morphology, structure and elemental composition of the aluminum oxide films, as well as the distribution of the elements on the aluminum surface, prior to and after the deposition and sealing of the protective layers, were observed by the electronmicroscope JEOL JSM 6390 (under the conditions of secondary electron image - SEI, back-scattered electrons -BEC and characteristic energy dispersive X-rays EDS, the applied voltage was 20 kV, $I \sim 100 \mu\text{A}$) and XPS studies. The XPS measurements were carried out on AXIS Supra electron- spectrometer (KratosAnalytical Ltd.) using monochromatic AlK_α radiation with a photon energy of 1486.6 eV. The energy calibration was performing by normalizing the C1s line of adsorbed adventitious hydrocarbons to 285.0 eV. The binding energies (BE) were surrounding in the depth of the films were determined monitoring the areas and binding energies of C1s, O1s, Al2p, Na1s and N1s photoelectron peaks. Using the commercial data-processing software of Kratos Analytical Ltd. the concentrations of the different chemical elements (in atomic %) were calculated by normalizing the areas of the photoelectron peaks to their relative sensitivity factors.

The corrosion behavior of the samples was tested in 0.1 M NaCl (“p.a.” Merck) model medium at 25°C. Platinum electrode was used as the counter electrode having dimensions 10x10x0.6 mm, while the reference electrode was saturated calomel electrode (SCE), ($E_{\text{SCE}}=+0.240 \text{ V vs. SHE}$). All the potentials in this study are compared to SCE. The anodic and cathodic polarization curves were obtained by means of a potentiostat/galvanostat

Gamry Interface 1000, whereupon the obtained results were processed with the help of specialized software. The curves were recorded at a sweeping rate of the potential 1.0 mV s⁻¹ in the range of potentials from –2500 up to + 2500 mV.

RESULTS AND DISCUSSION

The polarization curves of the anodized aluminum samples, sealed by applying various sealing techniques, in the chosen corrosion medium (0.1M NaCl), are represented in Fig. 1 and Fig. 2. In the model solution of 0.1M NaCl the potentiodynamic studies prove that the sealing of the anodic films in 0.5M solution of CeCl₃ for 2 hours at room temperature leads to insignificant reduction of the corrosion currents in the system - Fig. 1, while upon increasing the time interval of sealing from 2 hours to 48 hours, the corrosion current of the system with about one order of magnitude (Table 1).

Table 1. Electrochemical parameters obtained from the potentiodynamic curves.

Anodic film	Corrosion potential, E_{corr} , V	Corrosion current, i_{corr} , A.cm ⁻²
Unsealed	-0.710	1.75×10^{-6}
Sealed by boiling water	-0.701	1.65×10^{-6}
Sealed by cold CeCl ₃ (2h)	-0.671	1.24×10^{-6}
Sealed by cold CeCl ₃ (48h)	-0.674	2.27×10^{-7}
Sealed by hot CeCl ₃ (1h)	-0.718	7.97×10^{-7}
Sealed by hot CeCl ₃ (2h)	-0.702	3.16×10^{-7}

The sealing of the anodic oxide films in 0.5M solution of CeCl₃ at 60°C (Fig. 2) results in a more substantial decrease in the corrosion current of the system Al/Al₂O₃ under the conditions of steady state (Table 1). The juxtaposition of the cathodic polarization curves, characterizing the depolarization reaction of oxygen reduction shows that the filling up of the pores of the anodic oxide film with Ce(OH)₃ and Ce₂O₃ is inhibiting the reaction of oxygen reduction, which is most strongly expressed in the case of time interval of the treatment 48 hours (at room temperature, Fig. 1)

and respectively 2 hours (at 60°C, Fig. 2). Similar effect is observed also with the respective anodic potentiodynamic curves, but it is more slightly expressed.

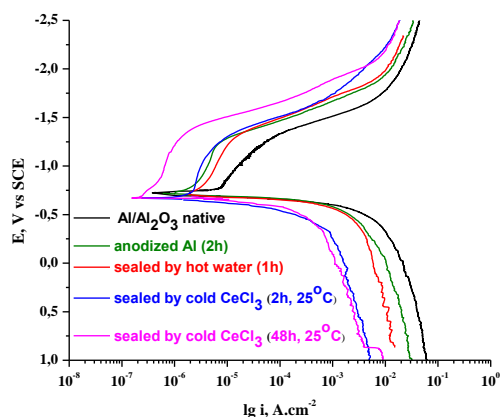


Fig.1. Polarization curves of systems tested in 0.1M NaCl at 25°C.

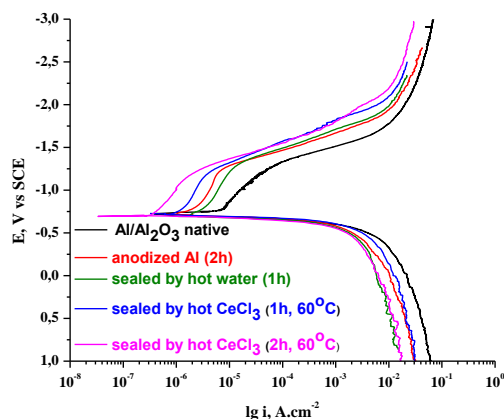


Fig. 2. Polarization curves of systems tested in 0.1M NaCl at 25°C.

For comparison Figures 1 and 2 represent the anodic and the cathodic potentiodynamic curves for anodized samples, sealed in boiling distilled water for 60 min. In contrast to the sealing in solutions of 0.5M CeCl₃, the standard sealing in boiling distilled water consists in filling up of the pores by hydrated aluminum oxide-boehmite (Al₂O₃ + H₂O → 2AlO(OH)), whose influence is expressed in a barrier effect and this leads to insignificant change in the kinetics of the corrosion process (Fig. 2) [1].

Fig. 3a illustrates the morphology of a non-sealed oxide film, formed by anodizing. It is seen that the film is strongly porous, with average diameter of the pores ~ 75 nm. Fig. 3b shows cross-section of the same film. The hexagonal (cellular)

structure of the porous film is observable, formed in the electrolyte containing phosphoric acid. This result is in correspondence with the literature data on similar oxide films [17]. It should be noted, however, that in comparison with the anodic films, prepared by other researchers, the alumina obtained by us has some non-uniformity in the arrangement of the cells (Fig. 3b). One of the reasons for this non-uniformity is the fact that we used technically pure aluminum for our purposes. Another possible reason is that the higher degree of ordering is achieved by means of two consecutive oxidation steps – after dissolving the oxide film, obtained in the first step, during the second oxidation one obtains considerably more uniformly structure layer [18].

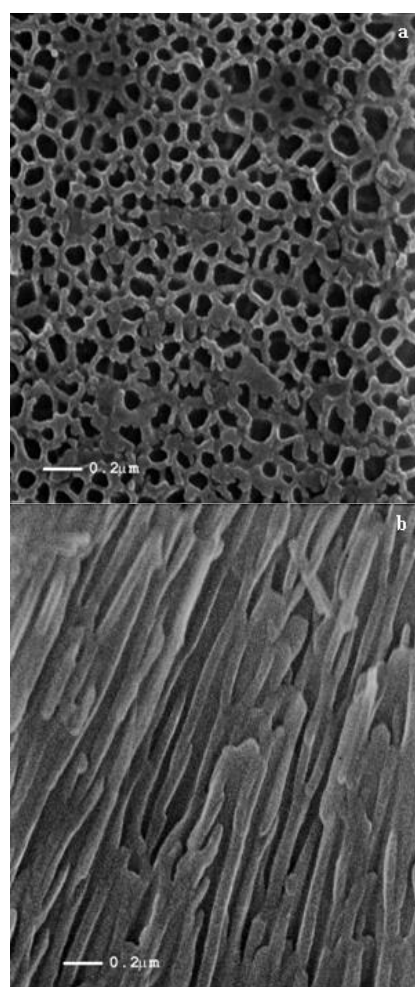


Fig. 3. SEM micrographs of the surface (a) and cross-section image (b) of unsealed Al₂O₃ film formed at 40V, for 2 hours (x50000).

Fig. 4a illustrates the morphology of the aluminum surface after anodic oxidation and sealing of the anodic layer in solution, containing Ce³⁺ at room temperature for 48 hours. In this case the influence of porosity of the oxide film is expressed by increase in the contact surface, interacting with the cerium ions, which is a

prerequisite for promoting the rate of spontaneous formation of the cerium oxide film. Thereupon the film formed inside the pores has a complex nature. It consists of two layers, the internal one represents a mixture of alumina/hydroxides Ce_2O_3 , and an external one, containing cerium oxides/hydroxides, which covers the cracks of the anodic film (Fig. 4a and b).

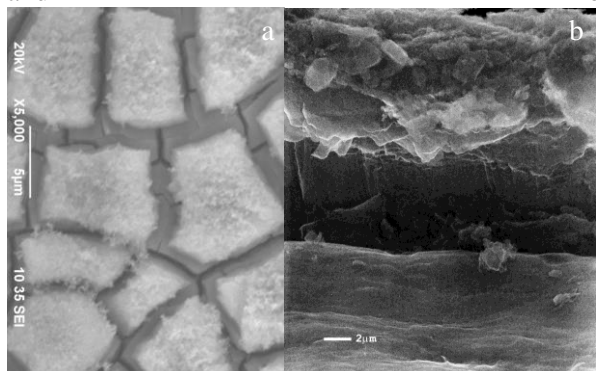


Fig. 4. SEM micrograph (a) and cross-section image (b) of the Al_2O_3 film sealed in cold solution of CeCl_3 , for 48h (x5000).

For comparison Fig. 5a shows analogous surface of aluminum sample after anodic treatment upon changing the conditions of sealing. In this case the sealing has been carried out at 60°C in the course of 2 hours in solution of 0.5M CeCl_3 . Fig. 5b illustrates cross-section of the same sample and it follows thereof, that upon increasing the temperature of the solution for sealing exerts substantial effect on the rate of precipitation of the cerium oxides, whereupon during the time interval of sealing (2 hours) the formed protective layer on the aluminum sample is similar in its thickness to the one formed at room temperature for 48 hours.

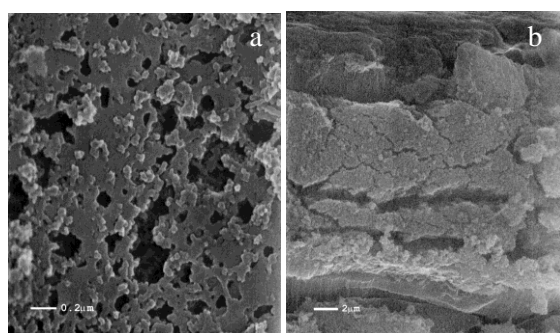


Fig. 5. SEM micrographs (a) and cross-section images (b) of the Al_2O_3 film sealed in hot CeCl_3 solution, for 2h (x50000, x5000).

By means of EDS analyses it was established that depending on the conditions of sealing the concentration of cerium on the anodized aluminum support grows up from 2.69 up to 6.18 wt.% upon increasing the time interval of sealing from 1 to 2 hours in hot solution (60°C) of 0.5M CeCl_3 , while

in the case of sealing at room temperature the concentration of cerium reaches 10.4 wt.% for immersion time interval of 48 hours. This result is in accordance with the data from the potentiodynamic investigations, showing lower corrosion currents, respectively better protective ability, at time intervals of sealing 2 hours in hot solution of CeCl_3 .

Fig. 6 demonstrates the surface morphology after corrosion test through anodic polarization (at potential +2.5 V) of samples subjected only to anodizing (Fig. 6a) and after consecutive sealing in solution of 0.5M CeCl_3 (Fig. 6b). It is known that the region of potentials more positive than 2.0V (vs. SCE) is the area, where the potential of pitting formation, characteristic of aluminum, has been surpassed [19]. It follows from Fig. 6a and b that the sealing changes the corrosion behavior of the system $\text{Al}/\text{Al}_2\text{O}_3/\text{Ce}_2\text{O}_3$ whereupon the type of corrosion passes over from pitting corrosion (Fig. 6a) into total corrosion (Fig. 6b). After the anodic polarization the external layer of the cerium oxide film loses its anti-corrosion properties, but the internal complex oxide layer has not been corroded, as a consequence of which there is no observation of any appearance of pitting corrosion damages on the surface of the sample.

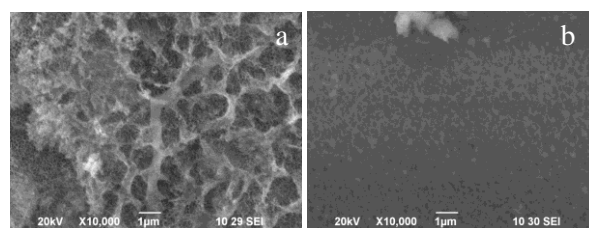


Fig.6. Surface morphology of the Al_2O_3 films unsealed (a) and sealed (in hot solution of CeCl_3) after anodic polarization to the zone of pitting formation (b) ($\sim +2.5$ V).

Some additional light is shed upon the results, commented on above, by the data from the X-ray photoelectron spectroscopy study on the composition and chemical state of the elements comprising the formed protective films. Figures 7, 8 and 9 illustrate part of the results, obtained with the studied samples. Figure 7 a, b represents the typical $\text{Al}2p$ and $\text{O}1s$ - spectra for anodized and sealed in boiling distilled water sample. They characterize in a unique way the changes on the surface of the aluminum sample, which occur as a result of anodizing. The spectrum of $\text{Al}2p$ (Fig. 7a) is characterized by a wide peak, consisting of several peaks. Its de-convolution leads to identification of four peaks, located at 74.6, 76.4, 78.0 and 80.7 eV. The presence of these peaks could be connected with the different in magnitude

charging of the particles on the surface of the sample, determined by the presence of two separate phases [20]. On the basis of the values for the binding energy of the respective peaks and their integral peak area, and the comparison with the values of the oxygen peaks for the same sample, we can identify the valence state of the chemical elements, building up the separate phases on the surface. It follows from this juxtaposition that the peak, positioned at 74.6 eV, corresponds to Al^{3+} in Al_2O_3 [21]. Due to the above-mentioned charging a shoulder of this peak is formed, remotely positioned from it at about 3 eV, at 78.0 eV. Its corresponding peak in the spectrum of O1s (Fig. 7b) is located at 531.4 eV. The ratio between these two peaks indicates a certain deficit of oxygen in the formed compound.

having coordination number 6. A confirmation of this statement is the fact, that the ratio between the sum of total integrated areas of the two peaks and the area of the corresponding oxygen peak at 533.0 eV is 1:6. It is possible that the O1s peak at 533.0 eV is overlapped with the oxygen peak, corresponding to oxygen bonded in the carbonate groups. We can state that the ratio oxide/hydroxide is approximately 2:1. The remaining two peaks at 535.5 and 538.1 eV in the spectrum of oxygen possibly correspond to bonded oxygen in water molecules adsorbed on the surface as well as in phosphate groups.

The spectra of Al2p and O1s for the sample, sealed in solution of cerium ions (Fig. 8 a, b), are characteristic of all the prepared and studied samples of anodized aluminum, treated in solution

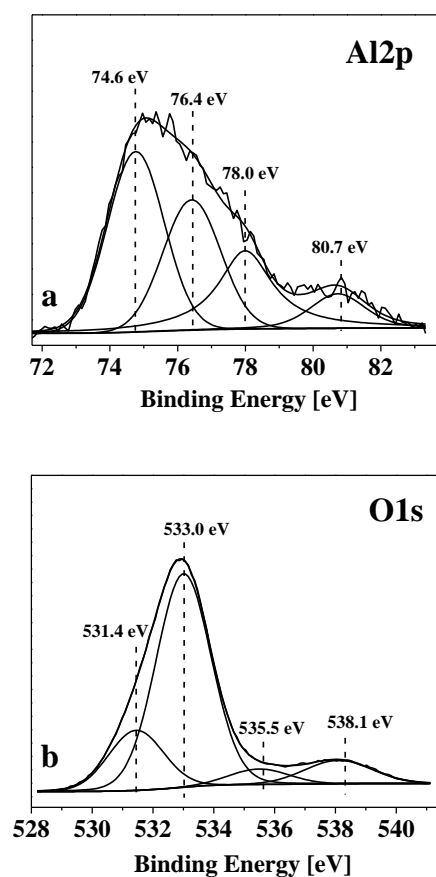


Fig. 7. Deconvoluted XPS – Al2p (a) and O1s (b) spectra of a film, obtained by anodization (after hot water sealing).

The peak, positioned at 76.4 eV, corresponds to Al^{3+} , connected with OH^- or H_2O ligands [22]. This peak has also a shoulder, which is located at 80.7 eV, whereupon the distance between the two peaks is 4 eV. An additional shifting of the peak at 76.4 eV towards higher energies could be attributed to formation of hydroxides and aqua-complexes

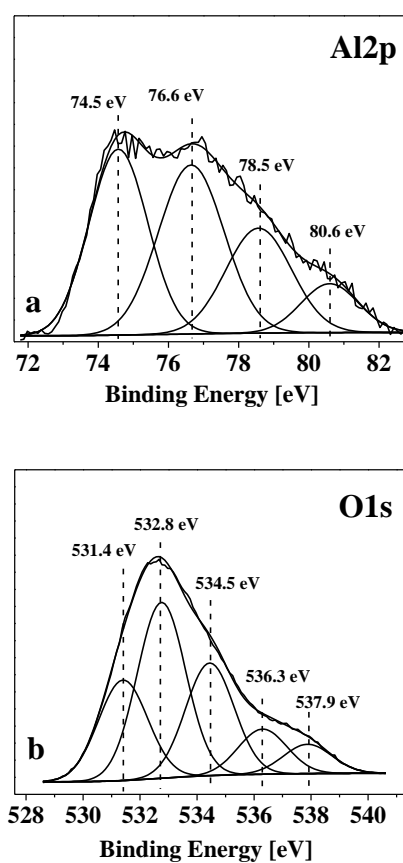


Fig. 8. Deconvoluted XPS – Al2p (a) and O1s (b) spectra of a film, obtained by anodization after hot CeCl_3 solution sealing.

of CeCl_3 . They are also distinguished by complex structure, owing to the presence of different phases on the surface. The spectrum of Al2p (Fig. 8a) is similar to that of the sample, non-coated with cerium oxide. Here again there are four peaks present – at 74.5, 76.6, 78.5 and 80.6 eV, corresponding to Al^{3+} in the composition of Al_2O_3

and $\text{Al}(\text{OH})_3$, whereupon again there are probably two different phases of these compounds present. The spectrum of O1s is more interesting (Fig. 8b). It is composed of five peaks. The first peak, located at 531.4 eV, is wider, due to its overlapping with the peak of the lattice oxygen in the composition of cerium oxide [23]. It is characteristic of Al_2O_3 . Again due to the difference in charging of the

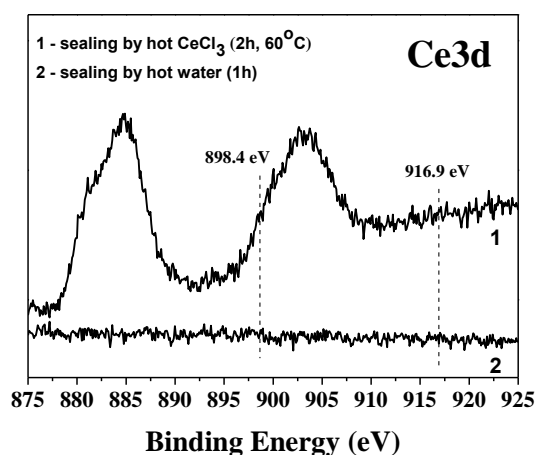


Fig.9. Ce3d - XPS spectra of a film, obtained by anodization after hot CeCl_3 solution sealing.

separate phases, a shoulder of this peak is observable, shifted away from it with 3 eV at 534.5 eV. The second peak at 532.8 eV, corresponds to $\text{Al}(\text{OH})_3$. The peak at 537.9 eV can be associated with the presence of phosphate groups [24, 25].

The spectrum of the cerium oxide formed (as a result of the sealing process) on the anodized surface layer, represented in Fig. 9, is characterized by complex structure, due to hybridization of cerium ion with the ligands of oxygen and partial occupation of the valence 4f orbital [26]. As a result of this spin orbital splitting occurs with the formation of doublets, whereupon each doublet has an additional structure, owing to the effect of the final state. The peaks at 916.9 eV and at 898.4 eV are characteristic of CeO_2 and they result from a $3d^{10}4f^1$ final state. The spectrum shows that as a result of the sealing process, a layer of Ce_2O_3 is being formed.

The results, obtained in the course of the studies carried out, show that the sealing of the anodic oxide films in solutions of CeCl_3 leads to formation of cerium oxide layers on the surface of the treated samples. These layers contribute to the formation of an efficient barrier against the occurrence of corrosion process influencing substantially the kinetics of the partial electrode reactions, determining its occurrence.

CONCLUSIONS

In this study, the effects of sealing process on the corrosion resistance of anodized aluminum (Al-1050) were investigated. We found out that the reaction products of cold and hot CeCl_3 solutions sealing contain $\text{Al}(\text{OH})_3$, $\text{Ce}(\text{OH})_3$ and Ce_2O_3 . These products co-precipitate inside the micropores of the anodic films and they block the pores, so the anodic films have higher corrosion resistance compared to the films sealed by boiling water. Moreover the CeCl_3 sealing makes the surface structure and morphology of anodic films more uniform and compact.

Acknowledgement: The financial support of the Bulgarian National Science Fund under grant T02/22 is gratefully acknowledged.

REFERENCES

1. S. Wernick, R. Pinner, P. Sheasby, The surface treatments of aluminium and its alloys, 5th Edition, ASM International and Finishing Publications Ltd. Metals Park, Ohio, 1987.
2. X.Yu, Ch. Yan, Ch. Cao, *J. Mat. Sci. Technol.*, **19**, 51 (2003).
3. M. Bartolome, V. Lopez, M. Escudero, G. Garuana, A.J. Gonzalez, *Surf. Coat. Technol.*, **200**, 4530 (2013)
4. M.R. Kalantary, D.R. Gabe, D.H. Ross, *Journal of Applied Electrochemistry*, **22**, 268 (1992).
5. F. Mansfeld, C. Chen, C. Breslin, D. Dull, *J. Electrochem. Soc.*, **145**, 2792 (1998).
6. Y. Zuo, P. Zhao, J. Zhao, *Surf. Coat. Technol.*, **166**, 237 (2003).
7. M.C. Garcia-Alonso, M. Escudero, J. Gonzalez-Carrasco, *Materials and Corrosion-Werkstoffe Und Korrosion*, **52**, 524 (2001).
8. J.A. Gonzalez, V. Lopez, E. Otero, A. Bautista, R. Lizarbe, C. Barba, J. Baldonado, *Corros. Sci.*, **39**, 1109 (1997).
9. H. Herrera-Hernandez, J. R. Vargas- Garcia, J.M. Hallen- Lopez, F.Mansfeld, *Materials and Corrosion-Werkstoffe Und Korrosion*, **58**, 825 (2007).
10. V. Lopez, J. Gonzalez, A. Bautista, E. Otero, R. Lizarbe, *Corros. Sci.*, **40**, 693 (1998).
11. M. Whelan, K. Barton, J. Cassidy, J. Colreavy, B. Duffy, *Surf. Coat. Technol.*, **227**, 75 (2013).
12. M. Whelan, J.Cassidy, B. Duffy, *Surf. Coat. Technol.*, **235**, 86 (2013).
13. J.M. Zhao, S.L. Chen, P. Huo, *Corros. Eng. Sci. Techn.*, **47**, 203 (2012).
14. L. Hao, B.R. Cheng, *Metal Finishing*, **98**, 8 (2000).
15. J. Lee, Y. Kim, H. Jang, U. Jung, W. Chung, *Procedia Engineering*, **10**, 2803 (2011).
16. M. Whelan, J. Cassidy, B.Duffy, *Surf. Coat. Technol.*, **235**, 86(2013).
17. J. Rasmussen, Tin / zinc alloys and anodizing of aluminium, Ph. D. thesis, Technical University of Denmark, p. 167,1994.

18. L. Bouchama, N. Azzouz, N. Boukmouche, J.P. Chopart, A.L. Daltin, Y. Bouznit., *Surf. Coat. Technol.*, **235**, 676 (2013).
19. [19]. Lian-peng Tian, Yu Zuo, Xu-hui Zhao, Jing-mao Zhao, Jin-ping Xiong, *Surf. Coat. Technol.*, **201**, 3246 (2006).
20. D. Stoychev, I. Valov, P. Stefanov, G. Atanasova, M. Stoycheva, Ts. Marinova, *Materials Science and Engineering*, **C 23**, 123 (2003).
21. A. Lippitz, E. Kemnitz, O. Bose, W.E.S. Unger, *Fresenius J Anal. Chem.*, **358**, 175 (1997).
22. A. Nylund, I. Olefjord, *Surface and Interface Analysis*, **21**, 283 (1994).
23. J.M. Sánchez-Amaya, G. Blanco, F.J. Garcia-Garcia, M. Bethencourt, F.J. Botana, *Surf. Coat. Technol.*, **213** 105 (2012).
24. I. V. Gordovskaya, T. Hashimoto, J. Walton, M. Curioni, G. E. Thompson, P. Skeldon, *Journal of The Electrochemical Society*, **161** (14) C601-C606 (2014).
25. H. Goretzki, H.-U. Chun, M. Sammet, R. Bruckner, *Journal of non-crystalline solids*, **42**, 499 (1980).
26. X. Yu, G. Li, *Journal of Alloys and Compounds* **364**, 193 (2004).

КОРОЗИОННО ПОВЕДЕНИЕ НА АНОДНО ФОРМИРАНИ ОКСИДНИ ФИЛМИ ВЪРХУ АЛУМИНИЙ, УПЛЪТНЕНИ В РАЗТВОРИ, СЪДЪРЖАЩИ ЦЕРИЕВИ ЙОНИ

Р. А. Андреева¹, Е. А. Стоянова¹, А. С. Цанев², Д. С. Стойчев^{1*}

¹ *Институт по физикохимия „Академик Ростислав Каишев“, Българска академия на науките, ул. „Акад. Г. Бончев“ бл. 11, София 1113, България.*

² *Институт по обща и неорганична химия, Българска академия на науките, ул. „Акад. Г. Бончев“ бл. 11, София 1113, България.*

Постъпила на 30 октомври, 2015 г.; коригирана на 24 януари, 2016 г.

(Резюме)

Изучено е корозионното поведение на анодно получени оксидни филми върху Al-1050 в разтвор на 0.1M NaCl. Оксидните филми са формирани в електролит, съдържащ H₃PO₄ – 40g/l, при волтастатични условия на анодиране. Уплътняването е осъществено в разтвори на 0.5M CeCl₃ при температури 25° и 60°C. Дебелината на филмите е 3-5µm.

Морфологията и съставът на формираните порьозни анодни филми са изследвани с помощта на сканираща електронна микроскопия (SEM) и енергийно дисперсионен анализ (EDS). Установено е, че в зависимост от условията на уплътняване, концентрацията на церий в порите на оксидните филми нараства от 5.3 до 10.4 тегл.%. Въз основа на проведени XPS изследвания на изучените системи е дефинирано химичното състояние на церия в порите на оксидния филм. Проведени са потенциодинамични изследвания и са определени корозионните токове на неуплътнените и уплътнените анодни оксидни покрития. Показано е, че запълването/уплътняването на порите на формирания Al₂O₃ аноден филм с Ce(OH)₃/Ce₂O₃ повишава неговата корозионно-защитна способност.

Electrodeposition and structure of binary alloys of silver, tin and antimony

A. Gyzova¹, I. Krastev², L. Petkov¹ and Ts. Dobrovolska^{2*}

¹University of Chemical and Metallurgical University, 8, Kl. Ohridski blvd, Sofia 1756, Bulgaria

²Institute of Physical Chemistry, Bulgarian Academy of Sciences, Acad. G. Bonchev str. Bl. 11, Sofia 1113, Bulgaria

Received November 20, 2015; Revised February 2, 2016

Is it possible to obtain periodic spatio-temporal structures during electrodeposition of Ag-Sb and Ag-Sn alloys from non-cyanide electrolytes? To find out suitable electrolytes for the deposition of the antimony-tin alloy in order to obtain coatings in a wide range of compositions as well as the conditions for obtaining of heterogeneous coatings – these are the questions to be answered in the present study. It was established, that spiral structures formed by different alloy phases are observed during electrodeposition of silver-tin alloys from thiocyanate-pyrophosphate electrolytes. The phase analysis shows that the structures are formed by the phases Ag₃Sn and Sn.

Depending on the electrolysis conditions during deposition of Ag-Sb alloys it is possible to obtain structures with different level of spatio-temporal organization from thiocyanate electrolyte. The pyrophosphate-tartrate electrolytes for the deposition of Sb-Sn alloys is developed for deposition of alloy coatings appropriate for investigation of their phase heterogeneity and properties.

Keywords: alloys, antimony, electrodeposition, silver, tin, self-organization

INTRODUCTION

Finding out the proper electrolytes for obtaining of silver-antimony, silver-tin and antimony-tin alloys is an actual problem, regardless of fact, that these are not exotic alloys [1]. The main problems are connected with the necessity to avoid well-worked but toxic, containing free-cyanide ions electrolytes for deposition of the mentioned alloys. Our intensive investigations in the last years led to the challenge to obtain spatio-temporal structures onto the cathode surface during electrodeposition of alloys of silver with antimony and tin[2-4]. Some unsolved tasks during electrodeposition of binary alloys of silver, tin and antimony from aqueous solutions could be formulated:

Silver-tin alloy is a very important material for solders, especially after the strict regulations of EU on the use of lead. Despite the intensive efforts of the scientific community stable electrolytes for deposition of this alloy are still not formulated [5-7]. The main reason is the reduction of tetravalent tin ions to a two valent ones, wherein the silver ion is reduced immediately in the solution. One of the few electrolyte options for the deposition of silver-tin alloys is the cyanide-pyrophosphate electrolyte [4]. From this electrolyte deposited structures, especially waves, composed from different phases of the alloy could be observed onto the cathode

surface.

It is well-known that antimony, as an alloying metal to silver (up to 5 wt. %) provides lustre of the precious metal [1]. By increasing the composition of the antimony in the coatings a wide variety of structures could be observed and this electrodeposited system is one deeply investigated system, but the procedure of electrolyte preparation is awkward due to the difficulties of the preparation of the silver complex [8-12].

Is it possible to obtain periodic spatio-temporal structures during electrodeposition of Ag-Sb and Ag-Sn alloys from non-cyanide electrolytes?

Tin-antimony alloy, electrodeposited from aqueous electrolytes practically is not investigated. However, it has been found, that bright coatings of alloys based on tin provide good solderability with non-acid flux [13, 14]. The electrodeposited alloy containing 5-10 wt. % antimony prevents the transformation of the lead from white to grey modification and in this way provides the ability for soldering for long storage time of the parts. Furthermore, this alloy has shown anti-friction properties and higher corrosion resistance as compared to pure tin [15].

The phase diagram indicates the presence of intermetallic compounds, which suggests the possibility of deposition of heterogeneous coatings [16].

The next goal of the present study is to find out suitable electrolytes for the deposition of the antimony-tin alloy in order to obtain coatings in a

To whom all correspondence should be sent:
E-mail: tsvetina@ipc.bas.bg

wide range of compositions as well as the conditions for obtaining of heterogeneous coatings.

EXPERIMENTAL

The composition of the used electrolytes presented in Table 1.

Table. 1. Composition of the electrolytes

Components	Quantity, g dm ⁻³
Sn as Sn ₂ P ₂ O ₇ /Umicore/	0-30
Ag as KAg(CN) ₂ /Umicore/	0-16
Sb as K(SbO)C ₄ H ₄ O ₆ /Merck/	0-30
C ₄ H ₄ O ₆ KNa*4H ₂ O	0-60
K ₄ P ₂ O ₇ /Umicore/	0-280
KSCN _{Merck/}	0-60

Chemical substances of *pro analisi* purity and distilled water were used.

The experiments were performed in a 100 cm³ tri-electrode glass cell at room temperature. The vertical working electrode (area 2 cm²), and the two counter electrodes were made from platinum. Prior to each experiment, the platinum working electrode was electrochemically etched in a solution of 0.1 M H₂SO₄ using platinum as a counter electrode till obtaining a clear surface. An Ag/AgCl reference electrode ($E_{\text{Ag}/\text{AgCl}} = 0.197$ V vs NHE) was used. The experiments were carried out at room temperature by means of a computerized potentiostat/galvanostat PAR 273 using the software Suite Corr. The polarization curves were recorded at the sweep rate of 20 mV s⁻¹.

The coatings were deposited under galvanostatic conditions at room temperature onto copper and brass substrates (4 cm²).

The surface morphology of the coatings was studied by scanning electron microscopes (SEM) – JEOL 6390 and Hitachi S-4000.

The content of antimony (respectively silver and tin) in the coatings depending on the electrolysis conditions was determined by X-ray fluorescence analysis (Fischerscope X-RAY XDAL) in 9 points (three points in the bottom, middle and top of the sample, respectively).

The phase composition was characterized by X-ray diffraction (XRD) using a PANalytical Empyrean device equipped with a multichannel detector (Pixel 3D) using (Cu-K α 45 kV-40mA) radiation in the 2 θ range 20–115°, with a scan step of 0.01° for 20 s.

RESULTS AND DISCUSSION

Silver-tin alloy

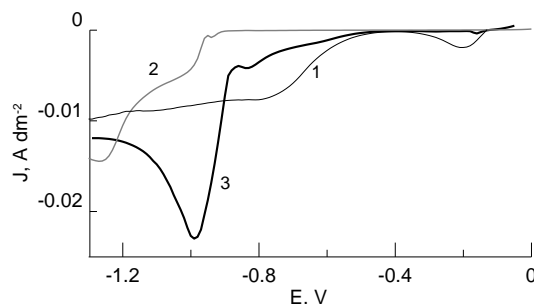


Fig.1. Polarization curves of an electrolyte, containing Ag and Sn separately or together, registered at $v=20$ mV s⁻¹, in g dm⁻³: Curve 1: Ag-5; K₄P₂O₇-280, KSCN-60; Curve 2: Sn-50; K₄P₂O₇-280, KSCN-60; Curve 3: Ag-5; Sn-50; K₄P₂O₇-280, KSCN-60.

Figure 1 shows cathodic part of the polarisation curves of electrolytes, containing silver and tin separately and together. Electrodeposition of silver (curve 1) is characterized by the cathodic maxima at a potential -0.2 V and this peak results from the silver reduction from the silver cyanide complex, which confirms the previous results of silver deposition from water solutions of potassium dicyanoargentate onto different substrates [17]. This means that despite of the quantity, the pyrophosphate does not influence the polarization of the cathodic peak of the silver from potassium dicyanoargentate complex in the silver electrolyte. The electrode processes in the pyrophosphate electrolyte for the silver deposition are presented in details by S. Nineva et al. [18, 19]. It is worthy to note, that the instability constant of the pyrophosphate complex of silver has a value of about $K_{\text{inst}}=10^{-4}$. This is a weak complex of silver, compared with the silver-cyanide complex, which constant is about $K_{\text{inst}}=10^{-22}$ [20].

Curve 2 presents the behaviour of tin ions in the alloy electrolytes, without silver. Two well-visible waves with some indication of peak are situated at potentials at -1.0 V and -1.25 V. The first small cathodic maximum (at -0.8 V) in the alloy electrolyte (curve 3) corresponds to the deposition of silver. Some small shift of the peak in comparison with those in electrolyte without tin could be explained with a different amount of ligands around the silver ion. The second cathodic maximum, appearing at the potential of tin deposition from a pure tin electrolyte, corresponds to the tin and most probably some silver-tin phase formation

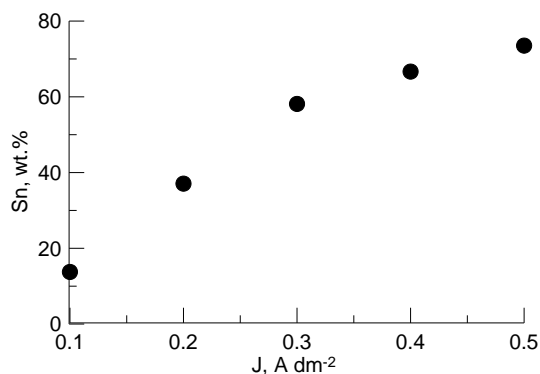


Fig. 2. Content of tin in the Ag-Sn coatings depending on the current density (The composition of the electrolyte is described in the caption of Figure 1).

Figure 2 shows the dependence on the composition of the silver-tin coatings from the current density. It could be clearly seen that with increasing current density the content of tin in the coatings increases, which is consistent with the results from polarization curves, presented in Figure 1. At low current densities the coatings are bright, silver-like. With the increasing of the current density the coatings become visibly heterogeneous. In the upper part of the electrode the coatings are richer in tin, and in the bottom - of silver. Upon reaching up to about 42-50 wt. % tin on the surface of the electrode spirals with more than 10 runs could be seen even with naked eyes – Figure 3. It should be noted that similar structures were not observed when the electrodeposition is performed incyanide-pyrophosphate electrolytes[4]. In these electrolytes the spatio-temporal structures are only in the form of waves. In the present studies well-defined spiral structures together with waves could be seen.

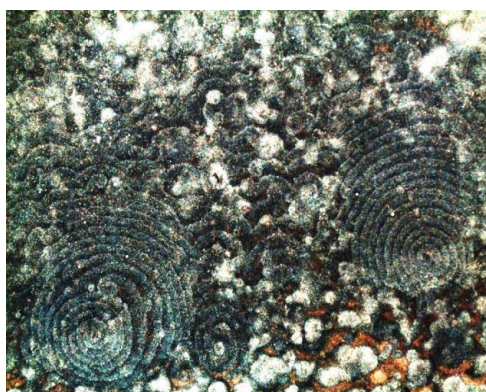


Fig. 3. Optical image of the spiral structures (Composition of the electrolyte is described in the caption of Figure 1), width of the image is 2 mm.

The Sn content of the structures is 41-43 wt. %. Scanning-electron images are pale, due to the approximately identical composition in the dark and light areas as well as the similar surface morphology in them (Figure 4). The image

presented was obtained at low energy of the accelerating voltage – 5 keV. Standard voltages for handling such images - about 20 keV good resolution of the structures cannot be observed. The difference in the composition in various areas of the well visible optical structures is minimal – the difference of the tin content is less than 1 wt. % in both zones. Some porosity is observed in the region, richer of tin.

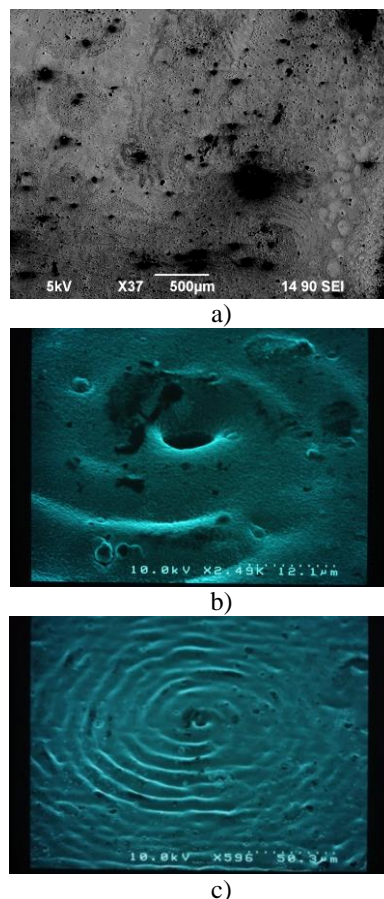


Fig.4. Scanning-electron images of the part of coatings, shown in Figure 3. Obtained in the SEM JEOL at 20 keV; b,c) at different magnifications, obtained in the SEM Hitachi at 10 keV.

Considering that the same structures are optically well visible and with good contrast, a conclusion could be drawn that the wave fronts move at a sufficiently high speed so that the thickness of the formed dark and light layers during deposition is substantially smaller than the penetration depth of the electron-beam during EDAX analysis. As a result the beam penetrates through several light and dark layers, and the estimated average content of tin in both zones is almost the same.

That is the reason for the observation of the both dark and light zones with high quality only at low accelerating voltages (5keV) of the electron beam.

Figure 4 b, c shows the morphology of the center of the spiral in the Belousov–Zhabotinsky reaction the rotating spiral waves with many turns could be created by breaking of a circular wave. In the case of silver-tin electrodeposited coatings some “initial” defect is observed in the core of the rotating spiral waves. It could be possibly formed by adsorption of some impurities or hydrogen evolution on this position of the surface.

Figure 5 presents the phase composition of the coatings with different tin content. When the tin content in the coating about 44-56 wt.% Sn (coatings with spatio-temporal structures) the reflexes of 2 different phases appear - these of Ag_3Sn and Sn. Further increasing the tin content (up to 56 wt.%) in the coating leads only to the changes of the intensity of reflexes.

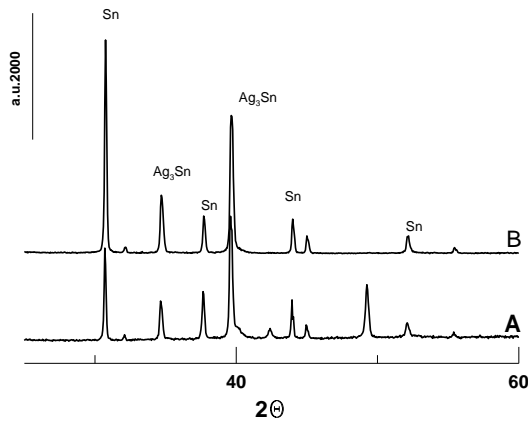


Fig. 5. XRD patterns of the samples, obtained from the electrolyte, described in Figure 1 (curve 3) ²A-sample with 44 wt. % Sn (0.2 A dm⁻²); B- sample with 56 wt. % Sn (0.3 A dm⁻²).

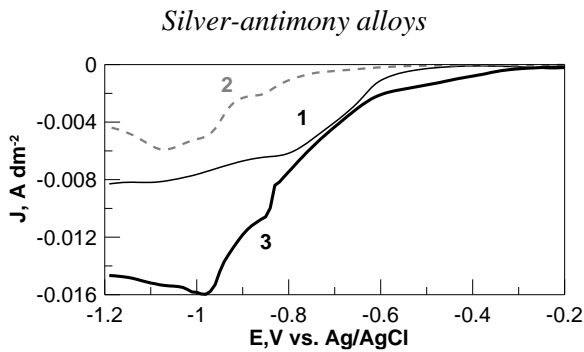


Fig. 6. Polarization curves of an electrolyte, containing Ag and Sb separately or together, registered at $v=20 \text{ mV s}^{-1}$, in $g \text{ dm}^{-3}$: Curve 1: Ag- 16; $C_4H_4O_6KNa \cdot 4H_2O - 60$; KSCN-150; Curve 2: Sb-7.5; $C_4H_4O_6KNa \cdot 4H_2O - 60$; KSCN-150; Curve 3: Ag- 16; Sb-7.5; $C_4H_4O_6KNa \cdot 4H_2O - 60$; KSCN-150.

Figure 6 shows the polarization curves obtained in the electrolytes for deposition of an alloy of silver-antimony in the presence of the metal ions separately or together. Silver in this system is the

more positive metal and its deposition starts at potentials around -0.5V (Curve 1). Antimony in this composition of the electrolyte is reduced at potentials of about -0.9V. The alloy curve shows regular type of according to the classification of Brenner [1].

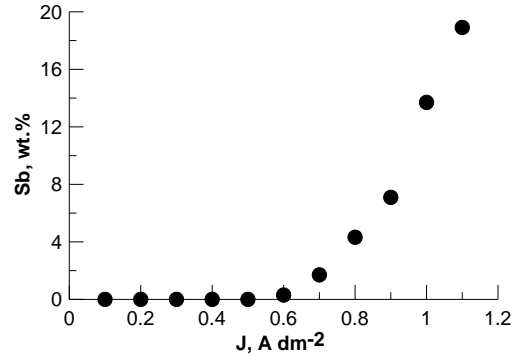


Fig. 7. Content of antimony in the Ag–Sb coatings depending on the current density (Composition of the electrolyte is described in the caption of Figure 6).

At low current densities up to 0.5 A dm^{-2} the coatings are silver-like in appearance and practically free of antimony (Figure 7). After 0.5 A dm^{-2} the content of antimony in the coatings increases and reaches 20 wt. % at 1.1 A dm^{-2} .

Coatings, containing between 7 wt. % and 13 wt. % of antimony show optical heterogeneity.

A similar phenomenon was observed by Krastev in a slightly different composition of the electrolyte, also in the simplified procedure of the preparation of electrolyte [3].

Figure 8a-c presents optical images depending on the current density. When the content of Sb is about 7 wt. % some spots could be seen (Figure 8a), and at higher current density these spots are formed into a more organized conglomerates (Figure 8b) where the content of Sb is 9 wt. % and afterward, at content of antimony about 11 wt. % a spiral formation could be clearly seen (Figure 8c).

The phase composition of the coatings with different content of antimony is shown in Figure 9. At the content of 2 wt. % Sb (curve A) only reflexes of the α -phase of silver are detected. According to the phase diagram of the alloy [16] the solubility of the antimony in the silver is about 6-7wt. %.

By increasing the antimony content in the coatings (curve B, coating with 7 wt. % Sb and curve C, coating with 11 wt. % Sb, respectively) the reflexes of two phases appear – $Ag_{3.84}Sb_{0.16}$ and $Ag_{0.63}O_{6.1}Sb_{2.5}$. These results clearly confirm that the structure formation, i.e. formation of spatio-temporal structures appears at elemental and phase composition similar to those, presented in another investigations [21].

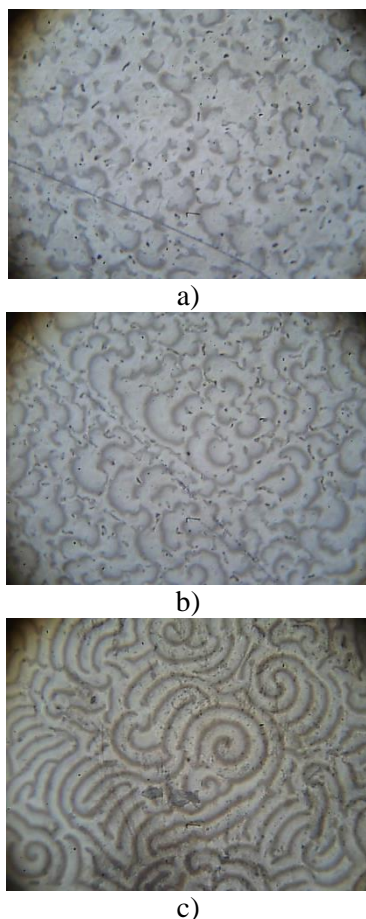


Fig.8. Optical images of the heterogeneous structures (The composition of the electrolyte is described in the caption of Figure 7), width of the image is 2 mm: a) 0.8 A dm⁻² (7 wt. % Sb); b) 1.0 A dm⁻² (9 wt. % Sb); c) 1.1 A dm⁻² (11 wt. % Sb);

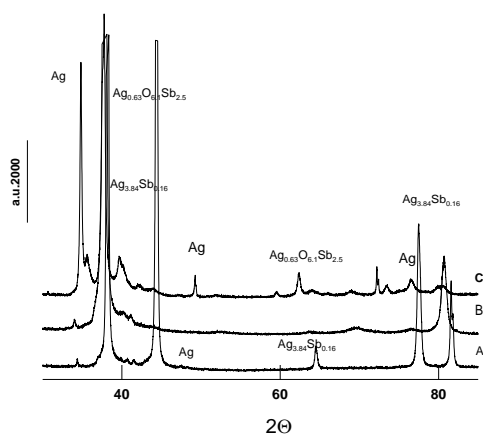


Fig. 9. XRD patterns of the samples, obtained from the electrolyte, described in Figure 6 (curve 3) A - 2 wt. % Sb-(0.6 A dm⁻²); B - 7 wt. % Sb (0.8 A dm⁻²); C- 11wt. % Sb (1.1 A dm⁻²).

Antimony-tin alloy

The electrodeposition of antimony-tin alloys was investigated in 3 electrolytes, where the concentrations of the metal ions have been varied. Figure 10 shows the polarization curves obtained in

electrolytes with the same metal ions concentrations - 5 g dm⁻³ Sn and 5 g dm⁻³ Sb.

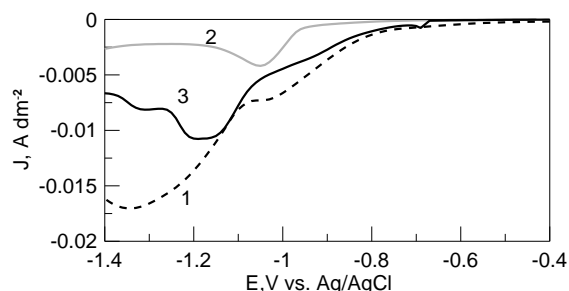


Fig. 10. Content of antimony in the Sn-Sb coatings depending on the current densities. Concentrations in g.dm⁻³. Curve 1: Sb- 5; C₄H₄O₆KNa*4H₂O - 60; K₄P₂O₇-150; Curve 2: Sn-5; C₄H₄O₆KNa*4H₂O - 60; K₄P₂O₇-150; Curve 3: Sb - 5; Sn-5; C₄H₄O₆KNa*4H₂O - 60; K₄P₂O₇-150.

The reduction of antimony (curve 1) starts at about -0.75 V and two peaks are observed and the first one coincides with the reduction peak of the two-valenced tin ions in the investigated electrolyte (curve 2). The polarization curve of the alloy electrolyte repeats the runs between the curves of the separate metals.

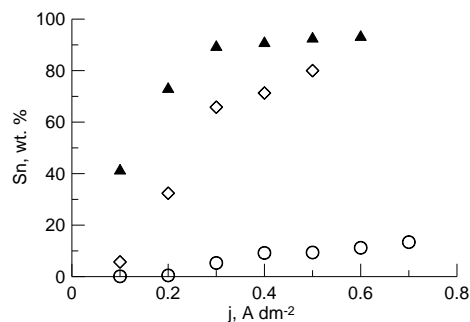


Fig.11. Content of tin in the Sn-Sb coatings depending on the current density. Composition of the electrolytes: ▲ Sn - 30; Sb - 5; C₄H₄O₆KNa*4H₂O - 60; K₄P₂O₇-150; ◊ Sn - 5; Sb - 5; C₄H₄O₆KNa*4H₂O - 60; K₄P₂O₇-150; ○ Sn - 5; Sb - 30; C₄H₄O₆KNa*4H₂O - 60; K₄P₂O₇-150

The dependence of the content of the coatings on the current densities is presented in Figure 11. The obtained results confirm the fact, that the antimony is the more positive element in this alloying system and with the increasing of the current density its content in the coatings decreases. The electrolytes are stable and at concentrations of 5 g dm⁻³ Sn and 5 g dm⁻³ Sb ensure wide range of the percentage of Sn (from 0 to 80 wt. % of Sn). The optical heterogeneity onto the coatings with 50-70 wt. % of Sn could be detected, but without any indications of the structures similar to those, observed in the Ag-Sn and Ag-Sb alloys.

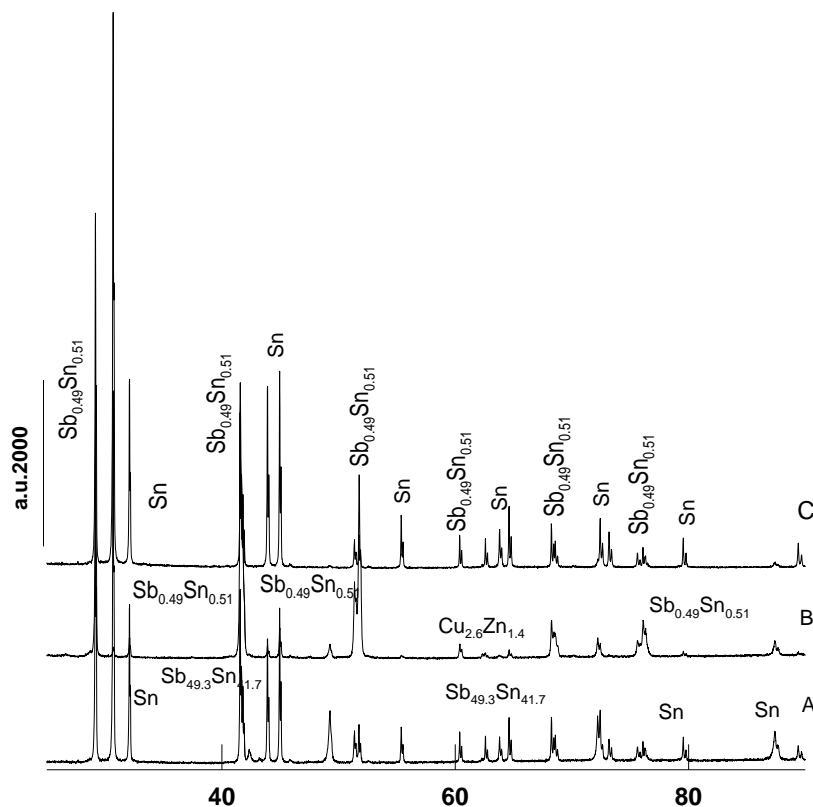


Fig. 12. XRD patterns of the samples, obtained from the electrolyte, described in Figure 10 (curve 3); A - 41 wt. % Sn; (0.2 A dm⁻²); B - 66 wt. % Sn (0.3 A dm⁻²); C- 77 wt. % Sn (0.4 A dm⁻²).

Figure 12 shows the phase composition of the coatings with a content of Sn between 41 and 77 wt. %.

The diffractogram A corresponds to the coating with 41 wt. % Sn and the reflexes of the phases Sb_{49.3}Sn_{41.7} and Sn could be detected. At higher content of Sn in the coatings (curves B and C) reflexes of the phases Sb_{0.49}Sn_{0.51} and Sn are observed.

The obtained results could be a basis for future investigations on the formation of ordered structures in the heterogeneous Sb-Sn alloys.

CONCLUSIONS

1. Spiral structures formed by different alloy phases are observed during electrodeposition of silver-tin alloys from thiocyanate-pyrophosphate electrolytes. The phase analysis shows that the structures are formed by the phases Ag₃Sn and Sn.
2. Depending on the electrolysis conditions during deposition of Ag-Sb alloys it is possible to obtain structures with different level of spatio-temporal organization.
3. The pyrophosphate-tartrate electrolytes for the deposition of Sb-Sn alloys is developed for deposition of alloy coatings appropriate for investigation of their phase heterogeneity and properties.

Acknowledgements: The authors express their gratitude to Bulgarian National Science Fund for the financial support of project T02-27/2014.

REFERENCES

1. Brenner, Electrodeposition of alloys, *Principles and Practice*, New York, vol. 2, (1963)
2. I. Krstev and M. Nikolova, *J. Appl. Electrochem.*, **16**, 875 (1986).
3. I. Krstev, M. Nikolova, I. Nakada, *Electrochim. Acta* **34**, 1219 (1989).
4. A. Hrussanova, I. Krstev, *J. Appl. Electrochem.*, **39**, 989 (2009).
5. P. Zhang, Y. Wang, J. Wang, D. Zhang, X. Ren, Q. Yuan, *Electrochim. Acta*, **137**, 121 (2014).
6. M. Mouas, J. G. Gasser, S. Hellal, B. Grosdidier, *Elsevier*, **44**, 102 (2014).
7. A.F. Abd El-Rehim, H.Y. Zahran, *Materials Sci. Technol.*, **30**, 434 (2014).
8. S. Nakabayashi, K. Inokuma, A. Nakao, I. Krstev, *Chem. Lett.*, 88-89 (2000).
9. S. Nakabayashi, I. Krstev, R. Aogaki, K. Inokuma, *Chem. Phys. Lett.*, **294**, 204 (1998).
10. I. Krstev, M. T. M. Koper, *Phys. A Stat. Mech. Appl.*, **L213**, 199 (1995).
11. Y. Nagamine, M. Hara, *Phys. A Stat. Mech. Appl.*, **327**, 249 (2003).
12. Y. Nagamine, N. Kuroono, M. Hara, *Thin Solid Films*, **460**, 87 (2004).
13. T. Gancarz, *J. Electron. Mater.*, **43**, 4374 (2014).

14. A. Wang, Y. Li, B. Yang, B. Xu, L. Kong D. Liu, *Elsevier*, **109**, 127 (2014).
15. S. A. El Rehim, A. Awad, A. El Sayed, *J. Appl. Electrochem.*, **17**, 156 (1987).
16. F. A. Shunk, M. Hansen, K. Anderko, *Constitution Of Binary Alloys*, McGraw-Hill, 1969.
17. Ts. Dobrovolska. *Electrodeposition, Structure And Properties Of Silver-Indium Alloys*, Phd Thesis, Ipc-Sofia, 2006.
18. S.L. Nineva, T.V. Dobrovolska, I.N. Krastev, *Bulg. Chem. Commun.*, **43**, 96 (2011).
19. S. Nineva, T. Dobrovolska, I. Krastev, *J. Appl. Electrochem.*, **41**, 1397 (2011).
20. L.G. Sillián, A.E. Martell, J. Bjerrum, *Stability Constants Of Metal-Ion Complexes*, Chemical Society London, 1964.
21. I. Krastev, M. Nikolova, *J. Appl. Electrochem*, **16**, 867 (1986).

ЕЛЕКТРООТЛАГАНЕ И СТРУКТУРА НА БИНАРНИ СПЛАВИ ОТ СРЕБРО, КАЛАЙ И АНТИМОН

А. Гъзова¹, Ив. Кръстев², Л. Петков¹ и Цв. Доброволска^{2*}

¹ Химико-технологичен и металургичен университет, бул. Кл. Охридски, 8, София 1756

² Институт по физикохимия, Българска академия на науките, ул. Акад. Г. Бончев, бл. 11, София 1113

Постъпила на 20 ноември, 2015 г.; коригирана на 2 февруари, 2016 г.

(Резюме)

Възможно ли е да се получат периодични пространствено-времени структури при отлагане на сплавите Ag-Sb и Ag-Sn от нецианидни електролити? Да се намерят подходящите електролити, при които да се получат сплавни покрития от Sb-Sn в широк диапазон от състав на компонентите – това са въпросите, на които е необходимо да се отговори в настоящето изследване. Установено е, че спиралните структури, получени от различни фази на сплавта се наблюдават при електроотлагане на сплав Ag-Sn от тиоцианатно-пирофосфатни електролити. Фазовият анализ показва, че структурите са съставени от фазите Ag₃Sn и Sn.

В зависимост от условията на електроотлагане на сплавта Ag-Sn от тиоцианатни е възможно получаването на структури с различно ниво на самоорганизация. Определени са състави на пирофосфатно-тартаратни електролити за отлагане на сплави Sb-Sn, при които е възможно получаването на хетерогенни покрития за последващо изследване на техният фазов състав

Structure-conductivity correlation in $(\text{TiO}_2)_5(\text{V}_2\text{O}_5)_{70}(\text{P}_2\text{O}_5)_{25}$ glass for low-temperature SOFCs

O. Koleva^{1*}, D. Kochnitcharova^{1,2}, E. Mladenova¹, E. Lefterova¹, T. Petkova¹, D. Vladikova¹

¹*Institute of Electrochemistry and Energy Systems Acad. Evgeni Budevsky, Bulgarian Academy of Sciences, Acad G. Bonchev Str., bl 10, 1113 Sofia, Bulgaria*

²*University of Chemical Technology and Metallurgy, Department of Electrochemistry, Sofia 1756, Bulgaria*

Received February 3, 2016; Revised February 18, 2016

This article focuses at searching of a direct relationship between composition and structure, on one hand and electrochemical behavior (conductivity), on the other hand of transition metal oxide system. Bulk sample with composition $(\text{TiO}_2)_5(\text{V}_2\text{O}_5)_{70}(\text{P}_2\text{O}_5)_{25}$ has been synthesized by means of melt quenching method. The XRD diffraction study has defined the amorphous nature of the sample; the structure determined by IR technique displays presence of VO_5 groups and isolated PO_4^{3-} (Q^0) structural units. The sample possesses both proton and oxide ion conductivities registered by electrochemical impedance spectroscopy. The observed change in the impedance behavior at 350 °C in hydrogen atmosphere is related to the intrinsic transformation from glass to crystalline state.

Keywords: solid electrolytes, SOFCs, electrochemical impedance analysis

INTRODUCTION

Economically competitive solid oxide fuel cells (SOFC) appear suited for commercialization but widespread market penetration requires continuous innovation of materials and fabrication processes to enhance system lifetime and reduce costs. An effective approach to cost reduction is the lowering of the operating temperature without inferring performance losses and improvement in the cell architecture and technology [1]. This can be achieved through several ways. One approach is decrease of the active layers thickness. For electrolyte 5 μm is already a realistic dimension in respect to technological realization [1]. Another pathway is the introduction of new architectures, such as composite cathodes based on a mixture of electrode and electrolyte material [1] or new designs. An important achievement is the development of the proton conducting fuel cell (PCFC), where the more mobile protons are transported through the electrolyte, which reduces the operating temperature. Recently an innovative concept, called dual membrane fuel cell (dmFC) was introduced [2-3]. It combines the advantages and bypasses the disadvantages of both SOFC and PCFC in respect to the effect of the water, introducing a separate chamber for its formation and evacuation. This design is connected to the application of materials with mixed ionic (protonic

and oxide ion) conductivity. The most promising approach in SOFC optimization is the development of new materials with high conductivity at lower operating temperatures. The current target is 600-500 °C.

The traditional electrolytic material in SOFCs - Yttrium-stabilized zirconium oxide YSZ which has high oxide conductivity and high stability in both oxygen and in reduction atmosphere [4] is replaced most often with (i) Cerium oxide CeO_2 doped with CaO , Y_2O_3 and rare earth oxides such as Gd_2O_3 [5], (ii) SrO- and MgO-doped Lanthanum galalate LaGaO_3 [6].

However, the challenge is to decrease additionally the operating temperature, filling the gap between SOFC and PCFC with polymeric membrane which is the range between 200-400 °C. In this direction a good strategy for development of new proton conducting materials with high proton conductivity is the introduction of cation-off stoichiometric materials. The charge imbalance caused by the cation non-stoichiometry is compensated by protons. Phosphates are among the materials that receive much attention due to the high thermal conductivity [6]. Depolymerization of the phosphate network and incorporation of transition metal ions, such as vanadium, produces new pathways for proton mobility by modification and deformation of the crystal structure. Furthermore, transition metals, when combined with other elements, can form compounds with various chemical bonding: ionic (oxides), covalent (sulfides, arsenide), metallic (carbides, nitrides).

To whom all correspondence should be sent:
E-mail: ofeliya.kostadinova@gmail.com

Vanadate glasses contain V^{4+} and V^{5+} ions where the electrical conduction is facilitated to the hopping of $3d_1$ unpaired electron from V^{4+} to V^{5+} sites. Vanadate glasses have been considered as a new branch in semiconducting glasses because of their wider glass-forming region and possible technological applications [1].

The Electrochemical Impedance spectroscopy is a powerful technique to reveal underlying chemical processes as a response of the applied small perturbation signal. The strength of EIS originates from its capability to differentiate the steps comprising the overall electrochemical process and to supply detailed information about the surface and the bulk properties of various electrochemical systems [7].

This article focuses at searching of a direct relationship between composition and structure, on one hand and electrochemical behavior (conductivity), on the other hand of transition metal oxide system. Having into account the observed mixed ionic conductivity obtained in some proton conducting ceramic electrolytes for PCFC [8], in addition to the proton conductivity studies, investigation for oxide ion conductivity were also performed.

This work presents study of relationship between structure of the materials and conductivity of mixed $(\text{TiO}_2)_5(\text{V}_2\text{O}_5)_{70}(\text{P}_2\text{O}_5)_{25}$ glass in view of their potential use as electrolytes in SOFCs.

EXPERIMENTAL

A bulk glass with composition $(\text{TiO}_2)_5(\text{V}_2\text{O}_5)_{70}(\text{P}_2\text{O}_5)_{25}$ was synthesized by means of melt quenching method. The homogenized mixture of initial materials: TiO_2 and V_2O_5 powders and orthophosphoric acid H_3PO_4 , were loaded in a quartz crucible. The heating process was carried out in a furnace gradually increasing the temperature upto 1000°C . The glass was obtained by quenching between two pre-cooled copper plates.

The phase formation of the sample was investigated by X-ray diffraction (XRD) method by means of X-ray diffractometer Philips APD-15. The data were collected with a constant rate of 0.02 deg.s^{-1} over an angle range $2\theta = 20^\circ\text{--}70^\circ$ using $\text{CuK}\alpha$ radiation ($\lambda = 1.54178 \text{ \AA}$) at ambient temperature.

Fourier Transformed Infrared (FTIR) spectrum was recorded with a FTIR spectrometer model VARIAN 660-IR in the frequency range $400 - 1300 \text{ cm}^{-1}$. The data were collected with a resolution of 2 cm^{-1} at room temperature.

The impedance measurements were performed on polished sample with Ag electrodes in hydrogen

and air atmosphere. The experiments were carried out on Solartron 1260 FRA in temperature interval $25^\circ\text{C} - 350^\circ\text{C}$, frequency range from 1 MHz down to 0.1 Hz, density of 5 points/decade.

The differential thermal analysis (DTA) and the thermogravimetric analysis (TGA) analyses were performed on Seteram DTA/TGlab Sysevo 1600 technique in temperature range between 25°C and 800°C in air at heating rate of $10^\circ\text{C}/\text{min}$ in platinum crucible.

RESULTS AND DISCUSSION

X-ray Diffraction investigation

The investigated sample is considered as roentgenographically amorphous. The spectrum is characterized by a broad halo and absence of crystalline peaks as seen from the XRD analysis (Fig. 1).

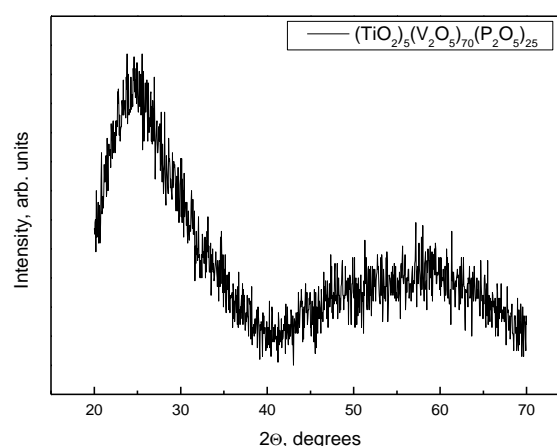


Fig. 1. XR-diffractogram of $(\text{TiO}_2)_5(\text{V}_2\text{O}_5)_{70}(\text{P}_2\text{O}_5)_{25}$ glass.

Infrared spectroscopy study.

The infrared spectrum presented in fig. 2 is analyzed by using the Tatre and Condrate empirical method. According to this approach, one can compare the glass spectra with their crystalline counterparts. Similarity of the spectra in the two solid states is considered as confirmation for existence of resemblance in the type and the symmetry of the building structural units. The interpretation is based on the following observations: (1) the glasses have a local symmetry of the separate molecular groups; (2) the intermolecular vibrations are less intensive than those between the groups due to the absence of long range order.

Phosphate glasses might be analyzed as a polymeric network of tetrahedra composed of $[\text{PO}_4]$ groups. The structure is usually described by Q^n , where n stands for the number of bridged oxygen atoms in a tetrahedron and different structures can

be formed depending on the [O]/[P] ratio: the Q^3 tetrahedra form network, while Q^2 tetrahedra are arranged in polymeric metaphosphoric chains with (PO_2) -bond. "Inverted" glasses are based on pyro (Q^1) with a structural unit of $(\text{PO}_3)^{2-}$ groups [9-11].

The absorption band at 1020 cm^{-1} most probably is a superposition of overlapping peaks. It is due to VO_5 deformed trigonal bipyramids with vanadium ion in the center and short $\text{V}=\text{O}$ (vanadyl) bond. The addition of modifier (phosphorus) introduces non-bridged oxygen atoms in the glass and leads to depolymerization of the phosphate network. The oxygen atoms destroy the P-O-P bridge structure [10-12] forming isolated phosphate groups (short chains and pyrophosphate groups). The absorption at 1020 cm^{-1} indicates the presence of these groups.

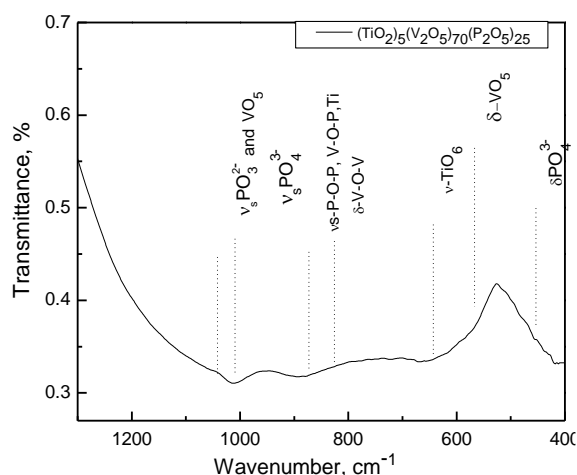


Fig. 2. Infrared spectra of $(\text{TiO}_2)_x(\text{V}_2\text{O}_5)_y(\text{P}_2\text{O}_5)_{100-x-y}$ glassy system.

The 900 cm^{-1} mode is assigned to the mixed V-O-P bonds. The band suited between $838 - 820 \text{ cm}^{-1}$ arises from V-O-V bending, while bending vibrations of VO_5 -groups are found below 600 cm^{-1} . The characteristic absorptions of VO_4 bands are located in the $980 - 820 \text{ cm}^{-1}$ range. The vibrational modes located at around 640 cm^{-1} belong to TiO_6 octahedral structures that define the structure of titanium oxides [13].

Conductivity studies by Electrochemical Impedance Spectroscopy.

Two impedance spectra of the sample measured in both oxygen and hydrogen atmosphere at $250 \text{ }^\circ\text{C}$ are represented in fig. 3.

The low-frequency semicircles are well-defined and describe the behavior of the electrode reaction. There is a strong deformation in air, i.e. strong frequency distribution arising from the changes that are commented below (fig. 5). The high frequency part corresponds to the electrolyte reaction with a

resistance that can be easily evaluated: 350Ω in hydrogen atmosphere and 290Ω in air. Since the sample is amorphous, the electrolyte resistance should be related only to the bulk material. The results show that at $250 \text{ }^\circ\text{C}$ the sample possesses mixed oxide and proton conductivity and the oxide one is higher.

A possible explanation of this phenomenon is the existence of oxygen vacancies which are needed for the activation of the proton conductivity [14]. Obviously, their concentration, according to eq. 1 [14], is high enough to introduce good oxide ion conductivity.

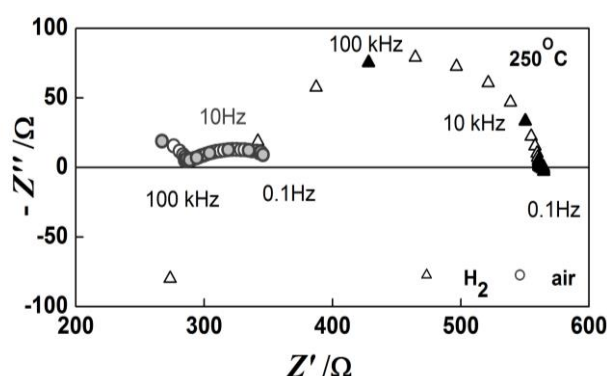
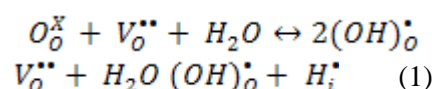


Fig. 3. Impedance diagram of $(\text{TiO}_2)_5(\text{V}_2\text{O}_5)_{70}(\text{P}_2\text{O}_5)_{25}$ composition in both air (at 178 min) and hydrogen atmospheres at $250 \text{ }^\circ\text{C}$.

Additional phenomenon is observed in air atmosphere at $250 \text{ }^\circ\text{C}$ where the sample resistance decreases from 430Ω to 260Ω (fig. 5). As a consequence of this decrease, the resistance values of the material in air and hydrogen atmospheres become similar in the temperature range $250 - 350 \text{ }^\circ\text{C}$. This is evident from the Arrhenius plots in air and hydrogen atmospheres, displayed in fig. 6.

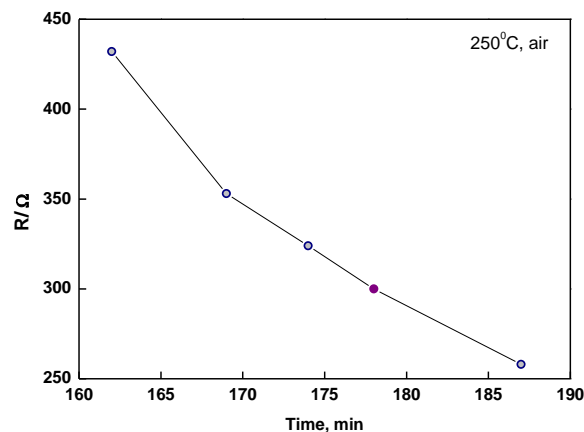


Fig. 5. Resistance change of $(\text{TiO}_2)_5(\text{V}_2\text{O}_5)_{70}(\text{P}_2\text{O}_5)_{25}$ sample with time in air.

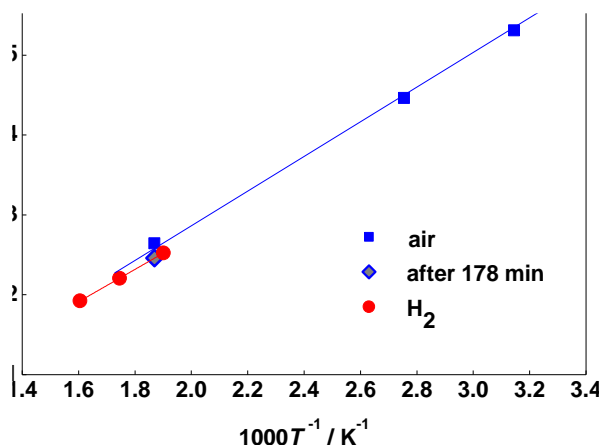


Fig. 6. Bulk Arrhenius plots of $(\text{TiO}_2)_5(\text{V}_2\text{O}_5)_{70}(\text{P}_2\text{O}_5)_{25}$ in air and hydrogen.

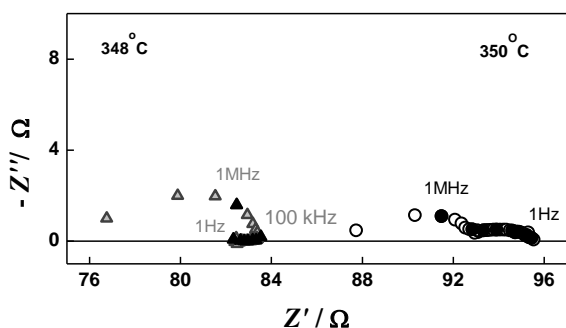


Fig. 7. Impedance spectrum of $(\text{TiO}_2)_5(\text{V}_2\text{O}_5)_{70}(\text{P}_2\text{O}_5)_{25}$ glass at 350 °C (measured first) and at 348 °C measured 2 min after the first one.

In hydrogen the sample follows the temperature trend shown in fig. 6. At 350 °C an abrupt change in the impedance behavior (including the value of the resistance) is clearly seen in fig. 7.

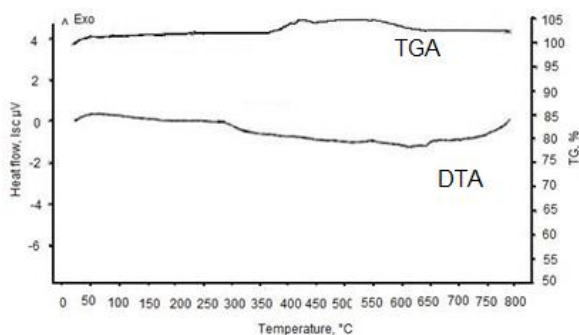


Fig. 8. DTA/TG analysis of $(\text{TiO}_2)_5(\text{V}_2\text{O}_5)_{70}(\text{P}_2\text{O}_5)_{25}$ glass.

The performed DTA/TG analysis (Fig. 8) shows that 350 °C marks exactly the beginning of glass transition temperature, i.e. the temperature region where transformation of the intrinsic nature of the material occurs and therefore, where a change in the electrochemical impedance behavior has been

detected. Obviously, the impedance diagram shown in fig. 7 at 348 °C registers exactly the transformation in the state.

CONCLUSIONS

The bulk material with composition $(\text{TiO}_2)_5(\text{V}_2\text{O}_5)_{70}(\text{P}_2\text{O}_5)_{25}$ synthesized and characterized by means of XRD diffraction and IR techniques has been found roentgenographically amorphous. The structure of the glass studied by IR analysis indicated presence of VO_5 groups and isolated $\text{PO}_4^{3-}(\text{Q}^0)$. EIS investigation shows that the material possesses proton and oxide ion conductivities. We observed a change in the impedance spectrum at intermediate temperatures which is due to intrinsic transformation during the heating of the material of the $(\text{TiO}_2)_5(\text{V}_2\text{O}_5)_{70}(\text{P}_2\text{O}_5)_{25}$.

Acknowledgement: The research leading to these results has received funding from Bulgarian NSF under grant No E02/3/2014. Participation of O. Koleva in RSE-SSE 5 has been made possible with the financial support of Bulgarian Ministry of Education and Science

REFERENCES

1. A. Barbucci, P. Piccardo, M. P. Carpanese, M. Viviani, Portable and Emergency Energy Sources, Z. Stoyanov, D. Vladikova (Eds.), Prof. Marin Drinov Publishing House, Sofia, 2006, p. 329.
2. D. Vladikova, Z. Stoyanov, G. Raikova, A. Thorel, A. Chesnaud, J. Abreu, M. Viviani, A. Barbucci, S. Presto, P. Carpanese, *Electrochim Acta*, **56**, 7955 (2011).
3. Z. Stoyanov, D. Vladikova, E. Mladenova, *J Solid State Electrochem*, **17**(2), 555 (2013).
4. M. Liu, *Fuel Cells Bulletin*, **11** p. 11 (2009).
5. J. Fleig, P. Pham, P. Sztulzaft, J. Maier, *J Solid State Ionics*, **113**, 739 (1998).
6. <http://www.fuelcelltoday.com/media/pdf/surveys/2007-SOFC-Survey.pdf>
7. Z. Stoyanov, D. Vladikova, Differential Impedance Analysis, Prof. Marin Drinov Publishing House, Sofia, 2005, p. 1.
8. M. Viviani, S. Presto, A. Barbucci, M. P. Carpanese, R. Amendola, A. Torel, A. Chesnaud, J. Abreu, R. Costa, Z. Ilhan, S. Ansar, D. Vladikova, Z. Stoyanov, MRS Online Proceeding Library 01/2011; 1330:1-12. DOI: 10.1557/opl.2011.1338 (2011)
9. F.H. ElBatal, Y.M. Hamdy, S.Y. Marzouk, *Materials Chemistry and Physics*, **112**, 991 (2008).
10. D. Carta, D. M. Pickup, J. C. Knowles, I. Ahmed, M. E. Smith, R. J. Newport, *J Non-Cryst Sol*, **353**, 1759 (2007).
11. P.Y. Shih, S.W. Yung, T.S. Chin, *J. Non-Cryst. Sol.*, **244**, 211 (1999).

12. V. Dimitrov, Y. Dimitriev, Structural analysis, УСТМ, Sofia, 2009.
13. A. N. Murashkevich, A. S. Lavitskaya, T. I. Barannikova, I. M. Zharskii, *J. Appl. Spectrosc.*, **75** (5), 730 (2008).
14. F. Lefebvre-Joud, G. Gauthier, J. Mouglin, *J Appl Electrochem.*, **39**, 535 (2009).

ЗАВИСИМОСТ МЕЖДУ СТРУКТУРА И ПРОВОДИМОСТ НА $(\text{TiO}_2)_5(\text{V}_2\text{O}_5)_{70}(\text{P}_2\text{O}_5)_{25}$ ЗА НИСКОТЕМПЕРАТУРНИ ТОГК

О. Колева^{1*}, Д. Кошничарова^{1,2}, Е. Младенова¹, Т. Петкова¹, Д. Владикова¹

¹ *Институт по електрохимия и енергийни системи „Акад. Евгени Будевски“, Българска Академия на Науките, ул. „Акад. Г. Бончев“, бл. 10, 1113, София, България*

² *Химикотехнологичен и металургичен университет, Катедра по електрохимия, бул. „Св. Климент Охридски“ №8, 1756, София, България*

Получена на 3 февруари 2016; коригирана на 18 февруари 2016 г.

(Резюме)

Този труд е фокусиран върху търсенето на директна взаимовръзка между състав и структура, от една страна, и електрохимичното поведение (проводимост), от друга, на $(\text{TiO}_2)_5(\text{V}_2\text{O}_5)_{70}(\text{P}_2\text{O}_5)_{25}$ стъклообразен материал за приложение в нискотемпературни твърдотелни оксидни горивни клетки (ТОГК).

Синтезиран е обемен образец със състав $(\text{TiO}_2)_5(\text{V}_2\text{O}_5)_{70}(\text{P}_2\text{O}_5)_{25}$ по метода на застъкляване от стопилка. Проведеният рентгено-структурен анализ потвърждава аморфната природа на пробата; изследването на структурата чрез инфрачервена спектроскопия показва наличие на VO_5 групи и изолирани PO_4^{3-} (Q^0) структурни единици. Пробата проявява едновременно протонна и кислородна проводимост, регистрирана чрез електрохимична импедансна спектроскопия. Наблюдаваната промяна в импедансното поведение при 350 °C във водородна атмосфера се отдава на превръщането на аморфния материал в кристален.

Investigation of pitting corrosion by potentiostatic polarization measurements

M. H. Loukaycheva^{1*}

¹Technical University - Sofia, 8 Kliment Ohridski Blvd., 1756 Sofia, Bulgaria

Received October 15, 2015; Revised February 8, 2016

In the present study, two austenitic stainless steels (conventional Cr18Ni9 and high nitrogen Cr18Mn12N) are examined with the purpose of demonstrate applicability and sensibility of potentiostatic polarization method to pitting corrosion investigation. The experiments were conducted in 0.1 M Na₂HPO₄ + 0.5 M NaCl at room temperature and open air conditions.

According to cyclic potentiodynamic polarization method for stable pits development on the surface of nitrogen bearing steel lower anodic polarization is necessary in comparison with the nickel containing steel. The latter is acriterion for lower pitting corrosion resistance. However, the pitting potential values obtained potentiostatically are by 0.2 V more positive and what is more, the potentiostatic method reveals metastable pits on Cr 18Mn12N steel with longer incubation time. The combination of results from the both used methods revises the final conclusion for the pitting corrosion resistance in nitrogen bearing steel favour.

Key words: pitting corrosion, potentiostatic polarization, steel.

INTRODUCTION

The investigation of pitting corrosion is really important for evaluation of corrosion behaviour of stainless steels. The most used method of pitting corrosion studies is the cyclic potentiodynamic polarization method (CPPM). However, some of the corrosion parameters determined by it strongly depend from scan rate of potential even the experiments were performed at very low values of it [1, 2]. The other conditions influencing the pitting corrosion parameters obtained potentiodynamically are the surface state, i.e. the surface finishing, treatment and metallurgical factors [2]. Therefore, the use of additional electrochemical methods for proving and clarification of pits nucleation kinetic is recommendable.

One of these rarely used electrochemical methods is the potentiostatic polarization method (PPM) which serves as a basis of other investigation methods namely Potentiostatic scratch method, Pulse potentiostatic method, etc. [3]. However, Schwenk et al. [4] show that it is the most reliable way of evaluating susceptibility to pitting corrosion. The PPM could surmount the disadvantages of CPPM and obtain more real evaluation of pitting potential (E_{pitt}). The method consists in continuous polarization of the examined samples at potentials before and after the pitting and repassivation (E_{rp}) potentials previously

defined by CPPM. Some of the authors [5] accepted that pits start to appear when the resulting current exceeds 10 $\mu\text{A cm}^{-2}$. The time in which the current suddenly rise is called incubation or induction time (t_i). This is another important index which might be obtained only by PPM.

Potentiostatic polarization method was used and for assessment of the critical pitting temperature [6] applying fixed potential and continuously increasing the temperature until stable pits appearance.

In the present study, two austenitic stainless steels (conventional Cr18Ni9 and high nitrogen Cr18Mn12N) are examined with the purpose to demonstrate the applicability and the sensibility of PPM to pitting corrosion investigation.

EXPERIMENTAL

Two austenitic stainless steels: the conventional Cr18Ni9 and the high nitrogen steel, (HNS) Cr18Mn12N were investigated in 0.1 M Na₂HPO₄ solutions containing 0.5 M NaCl. All tests were carried out in a conventional three electrodes cell in open air conditions at room temperature with a platinum counter electrode and a saturated calomel electrode (SCE) as a reference electrode. All potentials were reported with respect to the SCE. Two electrochemical methods were used: (i) Cyclic potentiodynamic polarization method and (ii) Potentiostatic polarization method.

The electrochemical results were obtained with a Galvanostat/potentiostat (Princeton Applied

To whom all correspondence should be sent:
E-mail: loukaycheva@tu-sofia.bg

Research Model 263) and computer software Power Suite.

RESULTS

In order to determine the characteristic pitting potentials by CPPM, experiments with scan rate $1 \text{ mV}\cdot\text{s}^{-1}$ were carried out. The obtained dependencies are presented on Fig. 1. From these dependencies the values of pitting potentials (E_{pitt}) for both steels were established and pointed out on the figure. It is well expressed that the E_{pitt} of nickel containing steel is more than 0.2 V higher than the nitrogen steel one. Regarding these E_{pitt} values the Cr18Mn12N steel is more susceptible to pitting corrosion in this corrosion environment. If the pitting corrosion susceptibility is evaluated only by CPPM the Cr18Ni9 steel would be reported as the more stable one.

These potentials values were used to determine the potential range in which the potentiostatic polarization experiments to be performed as well as to compare the E_{pitt} values obtained by both used methods.

The typical potentiostatic dependencies obtained at the applied potentials around the previously determined by CPPM E_{pitt} are given in Fig. 2 and Fig. 3.

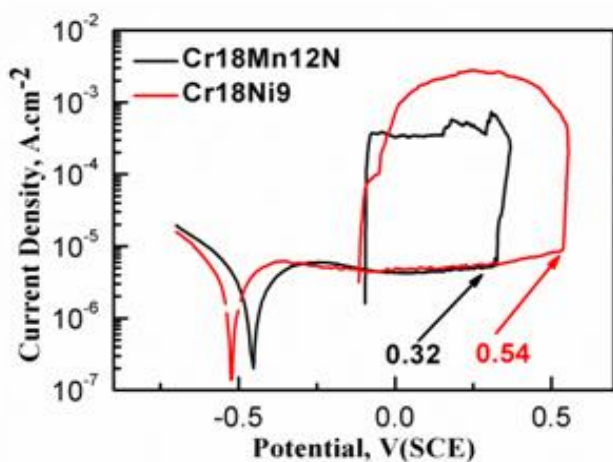


Fig. 1. Cyclic potentiodynamic polarization dependencies, $1 \text{ mV}\cdot\text{s}^{-1}$, 25°C .

From the dependencies at applied potentials more negative than pitting potential information about the passive films thickness and its stability could be drawn [7]. It is accepted that the lower current density means more stable (thicker) passive layer as the time necessary for passive film breakdown depends from the film thickness [8]. From Fig. 2 it is obvious that both steels are in passive state and what is more there are not significant differences between the reached steady current densities. However, the nitrogen steel has slightly lower steady current densities which might

be sign for more stable passive layer contrary to the results from cyclic potentiodynamic experiments.

The results obtained at more positive than E_{pitt} potentials reveal that the current densities differ for both investigated steels. Here, it is well distinguished that the nitrogen containing steel has lower current density than the nickel one at the same applied potential (i.e. 0.36 or 0.38 V(SCE)). Additionally, it is clear that the pitting potentials determined by potentiostatic method (about 0.36 V(SCE) for both steels) are not the same as these

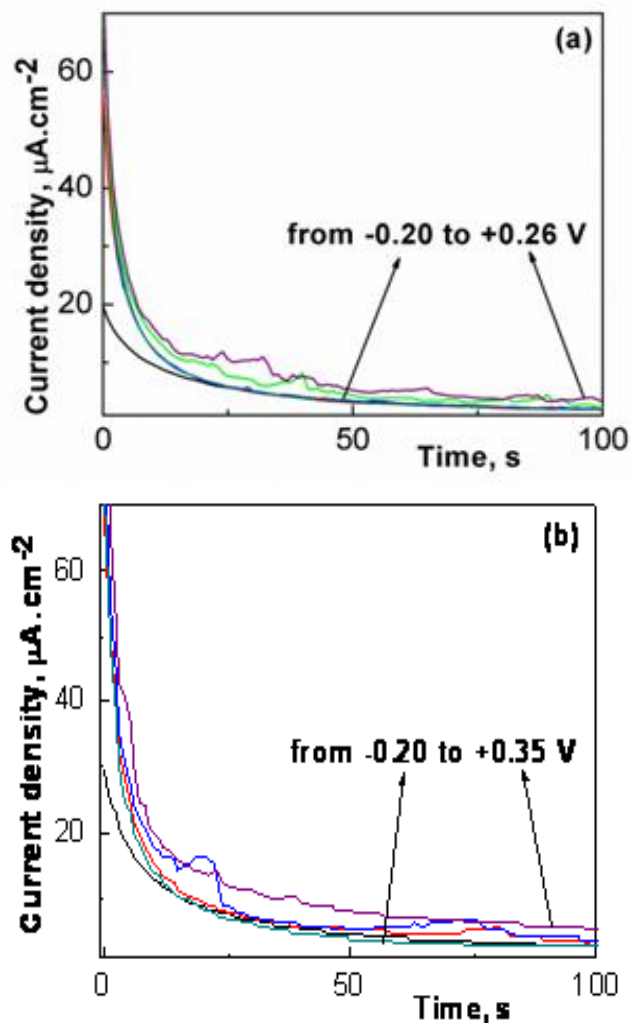


Fig. 2. Current density vs. time dependencies at $E_{\text{ap}} < E_{\text{pitt}}$: (a) Cr18Mn12N and (b) Cr18Ni9.

obtained by potentiodynamically polarization method (0.32 V(SCE) for Cr18Mn12N and 0.54 V(SCE) for Cr18Ni9). Thus, the both steels could have similar susceptibility to pitting corrosion in contrary to results presented on Fig. 1.

In addition, the dependencies for nitrogen steel at applied potentials 0.30 and 0.34 V(SCE) show that there is a metastable pits nucleation on the surface. It is expressed by small picks in the curve but the current density keeps its low value. Each

small fluctuation replies to pit initiation and repassivation [9-11]. These appeared and repassivated pits cannot be always registered by potentiodynamic measurements due to the limited resolution of the potentiostat. So, they must grow to a certain size before they can be registered. This growing needs time, and that is why they appear at more positive potentials in potentiodynamic measurements or the last registered only stable pits growing.

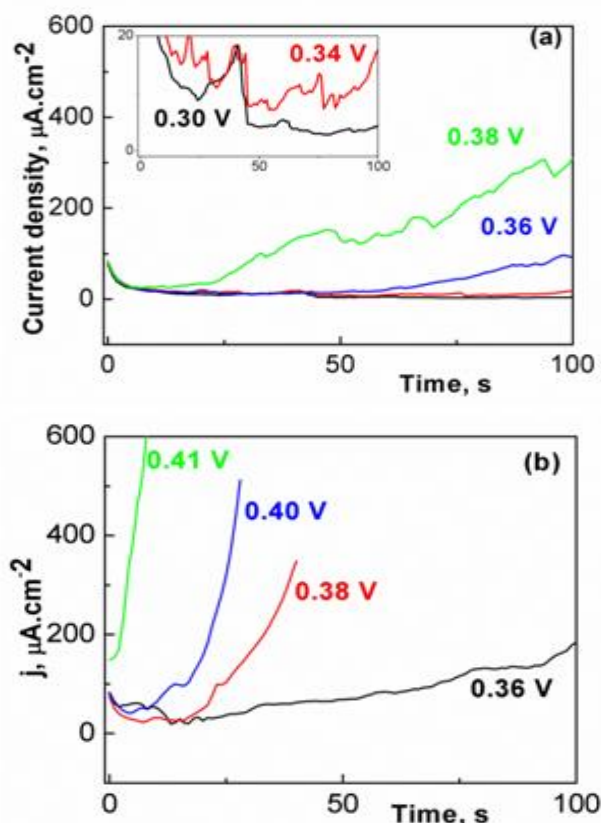


Fig. 3. Current density vs. time dependencies $E_{ap} > E_{pitt}$: (a) Cr18Mn12N and (b) Cr18Ni9.

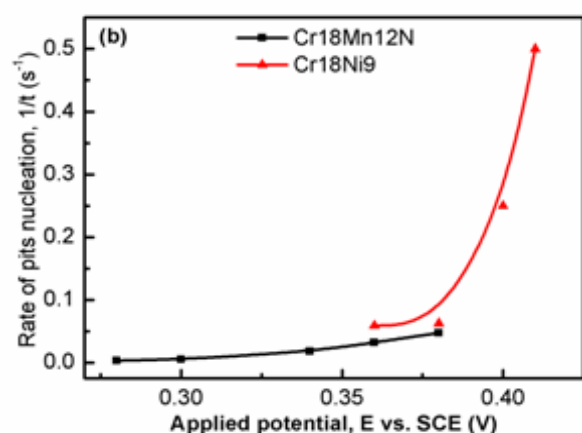


Fig. 4. Velocity of pits nucleation vs. applied potentials

An useful information which can be drawn from the potentiostatic results concerns the incubation time (t_i). This is the time at which after the initial decrease the current density suddenly rises, hence this is the time required for pits growth to start [12]. Comparing the dependencies obtained for both steels it is well expressed that the incubation time of Cr18Ni9 steel is significantly shorter than that of the Cr18Mn12N. This fact gives additional information about the stability of the passive films and cannot be established by the cyclic potentiodynamic method.

In addition, the rate of pits nucleation (expressed by $1/t_i$, s^{-1} [13]) vs. applied potential is shown in Fig. 4. The rate of pits initiation also gives valuable information. It is clear that the stable pits onto Cr18Ni9 steel surface appear at 0.36 V(SCE) and develop faster than pits on Cr18Mn12N steel surface which have rather metastable character.

Generalising the results obtained by potentiostatic polarization method it is well expressed that the Cr18Mn12N steel has similar corrosion resistance to pitting corrosion as Cr18Ni9 steel, which is completely opposite to the conclusion drawn from the results obtained by potentiodynamic method. Similar contradiction but in opposite direction was established and by Olefjord et al. [14] who studied Cr20Ni20Mo6N0.011 and Cr20Ni20Mo6N0.19 steels in HCl solutions. In the same way, they established that even the potentiodynamic dependencies do not show difference in the steel's behavior the potentiostatic dependencies at the same applied potential differ significantly. These inconsistencies of the results obtained by both methods suggest that the choice of method for pitting corrosion investigation must be made depending on the corrosion media on the one hand and the investigated material on the other hand. The choice of different study method has to depend on different properties of the formed in different corrosion environment passive films and on different surface conditions related to the pits nucleation. These surface conditions include different active sites for pits nucleation on materials (metallurgical defects, finishing, etc.). So, the potentiostatic results could be great supplement and verification to the results of potentiodynamic polarization method.

CONCLUSIONS

Taking into consideration all written above it can be concluded that:

1. During electrochemical studies of pitting corrosion the using of potentiostatic experiments

after cyclic potentiodynamic polarization measurements will provide really important and useful information for the susceptibility of materials to pitting corrosion and the type of the appeared pits.

2. The use of only potentiodynamic polarization method for determining and comparing the behaviour of various materials in a given environment is not sufficient.

3. The evaluation of properties of the passive layers could be made using the potentiostatic polarization method.

4. The choice of appropriate method for evaluation of corrosion behaviour of materials strongly depends from the materials themselves and from the concrete corrosion environment.

REFERENCES

1. A. Broli, H. Holtan, M. Midjo, *Br. Corros. J.*, **8**, 174 (1973).
2. G. Saivago, G. Fumagalli, *Corros. Sci.*, **33**, 985 (1992).
3. M. Dornhege, C. Punckt, J.L. Hudson, H.H. Rotermund, *J. Electrochem. Soc.*, **154**, C24 (2007).
4. D. Sinigaglia, B. Vicentini, G. Taccani, G. Salvago, G. Dallaspezia, *J. Electrochem. Soc.*, **130**, 991 (1983).
5. D. E. Williams, J. Stewart, P. H. Balkwill, *Corros. Sci.*, **46**, 1213 (1994).
6. A. Pardo, M.C. Merino, A.E. Coy, F. Viejo, R. Arrabal, E. Matykina, *Corros. Sci.*, **50**, 1796 (2008).
7. J.J. Park, S.I. Pyun, *Corros. Science.*, **45**, 995 (2003).
8. M.S. De Sa, C.M. Rangel, C.A.C. Sequeira, *Br. Corros. J.*, **23**, 186 (1988).
9. M. Lakatos-Varsányi, F. Falkenberg, I. Olefjord, *Electrochim. Acta*, **43**, 187 (1998).
10. J. Pan, C. Karlén, C. Ulfvin, *J. Electrochem. Soc.*, **147**, 1021 (2000).
11. W. Tian, N. Du, S. Li, S. Chen, Q. Wu, *Corros. Sci.*, **85**, 372 (2014).
12. E.A. Abd El Meguid, N.A. Mahmoud, S.S. Abd El Rehim, *Mater. Chem. Phys.*, **63**, 67 (2000).
13. M. A. Amin, S. S. Abd El Rehim, E. F. El Sherbini, *Electrochim. Acta*, **51**, 4754 (2006).
14. I. Olefjord, F. Falkenberg, L. Wegrelius, A. Velon, in *Mechanisms of Localized Corrosion (Eurocorr'96, Nice, 1996)*.

ИЗСЛЕДВАНЕ НА ПИТИНГОВА КОРОЗИЯ ПОСРЕДСТВОМ ПОТЕНЦИОСТАТИЧНИ ПОЛЯРИЗАЦИОННИ ИЗСЛЕДВАНИЯ

М. Х. Лукайчева^{1*}

¹ Технически университет – София, бул. Кл. Охридски 8, 1756 София, България

Постъпила на 15 октомври, 2015 г.; коригирана на 8 февруари, 2016 г.

(Резюме)

В настоящата работа са изследвани две аустенитни неръждаеми стомани (конвенционалната Cr18Ni9 и високо азотната Cr18Mn12N) с цел да се демонстрира приложимостта и чувствителността на потенциостатичния поляризационен метод при изследване на питингова корозия. Експериментите са проведени в 0.1 MNa₂HPO₄ + 0.5 MNaCl при стайна температура.

Според цикличния потенциодинамичен поляризационен метод за развитието на устойчиво нарастващи питинги на повърхността на азотната стомана е необходима по-ниска анодна поляризация в сравнение с тази при никеловата стомана. Последното е критерий за по-ниска устойчивост към питингова корозия. Обратно, потенциалите на питингообразуване получени чрез прилагане на потенциостатичния поляризационен метод са с 0.2 V по-положителни, нещо повече потенциостатичният метод открива метастабилни питинги върху стомана Cr18Mn12N, развиващи се след по-продължително инкубационно време. Съвместното разглеждане на резултатите от двата използвани метода променя крайното заключение за устойчивостта към питингова корозия в полза на азот-съдържащата стомана.

CONTENTS

10th International Symposium on Electrochemical Impedance Analysis, 2014

<i>Editorial</i>	5
<i>O.I. Gichan, V.V. Pototskaya</i> , Can a form of electrode/electrolyte interface change the ranges of dynamic instabilities?.....	7
<i>T. Günther, P. Büschel, O. Kanoun</i> , Multispectral impedance measurement in embedded systems.....	13
<i>A. Survila</i> , Equivalent circuits for electrochemical reaction involving consecutive charge transfer steps.....	18
<i>M.P. Carpanese, A. Giuliano, M. Panizza, E. Mercadelli, A. Sanson, A. Gondolini, A. Bertei, A. Barbucci</i> , Experimental approach for the study of SOFC cathodes.....	23
<i>M.Tanovska, L.Vladimirova-Mihaleva, K.Bachev, V.Kochev</i> , Electrochemical impedance investigation of cholesterol enriched supported films of lipids.....	30
<i>F. Wendler, P. Büschel, O. Kanoun</i> , Efficient parameter estimation for spectral sensor data by a linear transformation.....	34
<i>E. Mladenova, Z. Stoynov, D. Vladikova</i> , Comparative studies of polarizable dielectric fluids in yttrium-doped barium cerate by permittivity spectroscopy.....	39
<i>S.G. Avramov, E. Lefterova, H. Penchev, V. Sinigersky, E. Slavcheva</i> , Comparative study on the proton conductivity of perfluorosulfonic and polybenzimidazole based polymer electrolyte membranes.....	43
Sofia Electrochemistry Days, 2015	
<i>N.D. Boshkova, P.D. Petrov, V. Chukova, L.Lutov, S.D. Vitkova, N.S. Boshkov</i> , Surface morphology and corrosion behavior of zinc and zinc composite coatings with Cr(III) based conversion films.....	53
<i>H. Nichev, B.Georgieva, M. Petrov, K. Lovchinov, V. Georgieva, L.Vergov, G.Alexieva, D. Dimova-Malinovska</i> , Effect of quartz plate roughness on ZnO/QCM response to NO ₂	60
<i>G.P. Ilieva, M.H. Loukaycheva, B.R. Tzaneva, L.T. Gekova, L.B. Fachikov</i> , Corrosion behavior of nitrogen stainless steel inringer's solution.....	66
<i>M. Monev</i> , Hydrogenation and cracking of nickel coatings electrodeposited in the presence of brighteners.....	73
<i>T. Valkova, I. Krastev</i> , Influence of glycine on the electrochemical deposition of Sn-Co alloy from gluconate electrolyte.....	78
<i>K. Maksimova – Dimitrova, E. Lefterova, S. Atanasova – Vladimirova, E. Slavcheva</i> , Influence of metal loading on morphology and performance of oxide supported cobalt electrocatalysts.....	85
<i>B. Tzaneva, T. Petrova, J. Hristov, L. Fachikov</i> , Electrochemical investigation of cementation process	91
<i>R.A. Andreeva, E.A. Stoyanova, A.S.Tsanev, D.S. Stoychev</i> , Corrosion behavior of anodically formed oxide films on aluminum, sealed in cerium-ions containing solutions.....	96
<i>A. Gyozaova, I. Krastev, L. Petkov, Ts. Dobrovolksa</i> , Electrodeposition and structure of binary alloys of silver, tin and antimony.....	103
<i>O. Koleva, D. Kochnitcharova, E. Mladenova, E. Lefterova, T. Petkova, D. Vladikova</i> , Structure-conductivity correlation in(TiO ₂) ₅ (V ₂ O ₅) ₇₀ (P ₂ O ₅) ₂₅ glass for low-temperature SOFC.....	110
<i>M. H. Loukaycheva</i> , Investigation of pitting corrosion by potentiostatic polarization measurements...	115

СЪДЪРЖАНИЕ

10-ти Международен симпозиум „Електрохимичен импедансен анализ“, 2014 г.

<i>О.И. Гичан, В.В.Потоцкая</i> , Може ли формата на интерфейса електрод/електролит да промени обхватите на динамичните нестабилности?.....	6
<i>Т. Гюнтер, П. Бюшел, О. Каноун</i> , Мултиспектрални импедансни измервания във вградени системи.....	12
<i>А. Сурвила</i> , Еквивалентни схеми на електрохимична реакция включваща последователни стъпки при преноса на заряд.....	17
<i>М.П. Карпанезе, А. Джулиано, М. Паница, Е. Меркаделли, А. Сансон, А. Гондолини, А. Бертеи, А. Барбучи</i> , Експериментален подход при изследване на катоди за твърдооксидни горивни клетки (SOFC).....	22
<i>М. Тановска, Л. Владимирова-Михалева, К. Бачев, В. Кочев</i> , Електрохимично импедансно изследване на обогатени с холестерол поддържащи липидни филми	29
<i>Ф. Вендлер, П. Бюшел, О. Каноун</i> , Оценка на ефективни параметри на спектрални сензорни данни чрез линейна трансформация.....	33
<i>Ем. Младенова, Здр. Стойнов, Д. Владикова</i> , Сравнителни изследвания на диелектрични полярни флуиди в итриево дотиран бариев церат чрез диелектрична спектроскопия.....	38
<i>С.Г. Аврамов, Е. Лефтерова, Х. Пенчев, В. Синигерски, Е. Славчева</i> , Сравнително изследване на протонната проводимост на перфлуоросулфонирани и полибензимидазол базирани полимерни електролитни мембрани.....	42
Софийски електрохимични дни, 2015 г.	
<i>Н.Д. Божкова, П.Д. Петров, В. Чукова, Л. Лютов, С.Д. Виткова, Н.С. Божков</i> , Повърхностна морфология и корозионно поведение на цинкови и цинкови композитни покрития с конверсионни защитни филми на база тривалентен хром.....	59
<i>Хр. Ничев, Б. Георгиева, М. Петров, К. Ловчинов, В. Георгиева, Л. Вергов, Г. Алексиева, Д. Димова-Малиновска</i> , Влияние на повърхностната грапавост на кварцови подложки върху сорбционните свойства на ZnO/QCM към NO ₂	65
<i>Г.П. Илиева, М.Х. Лукайчева, Б.Р. Цанева, Л.Ц. Жекова, Л.Б. Фачиков</i> , Корозионно поведение на n-съдържащи неръждаеми стомани в разтвор Ringer	72
<i>М. Монеv</i> , Наводородяване и напукване на никелови покрития електроотложени в присъствие на блясъкообразуватели.....	77
<i>Т.Вълкова, И.Кръстев</i> , Влияние на глицин върху електрохимичното получаване на сплав Sn-Co от глюконатен електролит.....	84
<i>К. Максимова-Димитрова, Е. Лефтерова, С. Атанасова-Владимирова, Е. Славчева</i> , Влияние на каталитичното натоварване върху морфологията и работните характеристики на кобалтови електрокатализатори, отложени върху оксиден носител.....	90
<i>Б. Цанева, Т. Петрова, Й. Христов, Л. Фачиков</i> , Електрохимично изследване на цементационни процеси.....	95
<i>Р.А. Андреева, Е.А. Стоянова, А.С. Цанев, Д.С. Стойчев</i> , Корозионно поведение на анодно формиран оксиден филм върху алуминий, уплътнени в разтвори, съдържащи цериеви йони.....	102
<i>А. Гъзова, Ив. Кръстев, Л. Петков, Цв. Доброволска</i> , Електроотлагане и структура на бинарни сплави от сребро, калай и антимон.....	109
<i>О. Колева, Д. Кошничарова, Е. Младенова, Т. Петкова, Д. Владикова</i> , Зависимост между структура и проводимост на (TiO ₂) ₅ (V ₂ O ₅) ₇₀ (P ₂ O ₅) ₂₅ за нискотемпературни ТОГК.....	114
<i>М. Х. Лукайчева</i> , Изследване на питингова корозия посредством потенциостатични поляризационни изследвания.....	118